Conductance Switching in Ensemble Molecular Devices

Based on Liquid Crystal-Inspired Molecules

Julian Matthias Dlugosch, MSc.

Vollständiger Abdruck der von der *TUM School of Computation, Information and Technology* der Technischen Universität München zur Erlangung des akademischen Grades eines
Doktors der Ingenieurwissenschaften (Dr.-Ing.)
genehmigten Dissertation

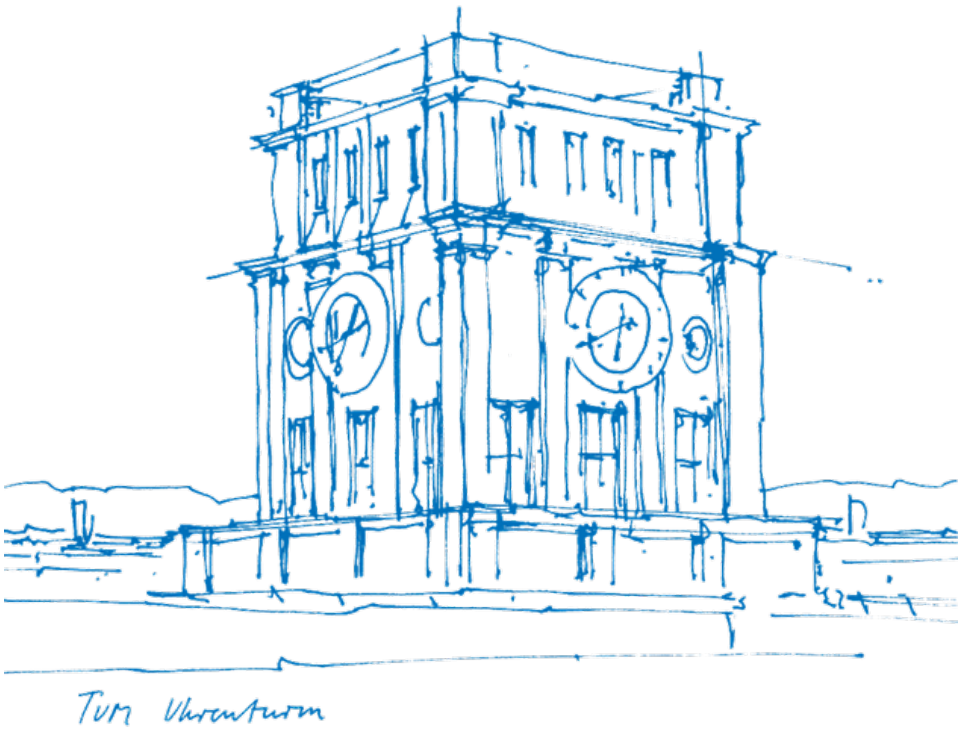

TUM School of Computation, Information and Technology

Conductance Switching in Ensemble Molecular Devices

Based on Liquid Crystal-Inspired Molecules

Julian Matthias Dlugosch, MSc.

Vollständiger Abdruck der von der TUM School of Computation, Information and Technology der Technischen Universität München zur Erlangung des akademischen Grades eines

Doktors der Ingenieurwissenschaften (Dr.-Ing.)

genehmigten Dissertation.

Vorsitz: Prof. Dr.-Ing. Christian Jirauschek
Prüfer*innen der Dissertation:

1. Prof. Dr. rer. nat. Marc Tornow
2. Prof. Dr. rer. nat. Peer Kirsch

Die Dissertation wurde am 14.06.2022 bei der Technischen Universität München eingereicht und durch die TUM School of Computation, Information and Technology am 27.01.2023 angenommen.

Abstract

To meet the ever-increasing demand of computational capabilities, novel computing paradigms beyond von Neumann computers are currently being developed. With many of them greatly dependent on the performance of memory devices, novel material systems that exhibit conductance switching in a reliable, energy efficient fashion are highly sought after.

This work presents a feasibility study of using self-assembled monolayers (SAMs) of liquid crystal-inspired (LCI) molecules within ensemble molecular devices (EMD) as conductance switching moieties. Conductance switching was intended to occur through the re-orientation of molecular dipoles within a SAM and the resulting change of the dipole-induced, conformation-dependent tunneling barrier modification.
To this end, three major objectives were pursued. First, the SAM formation as well as the electrical characteristics of SAMs of phenyl cyclohexane based phosphonic acids with an aliphatic linker was studied in great detail. Then, a novel, reliable contacting scheme to yield EMDs with phosphonic acids sandwiched between two conductive layers was developed and studied. Lastly, conductance switching characteristics of a variety of LCI molecule based EMDs were measured, some structure - property relationships were observed and multi-state conductance switching was demonstrated for a difluorphenyl cyclohexane based molecule.

First, self-assembly of LCI molecules was studied on aluminum substrates. Monolayer formation was confirmed using a multitude of surface characterization techniques, including XPS, NEXAFS, water contact angle and ellipsometry. These techniques revealed presence of XPS absorption peaks characteristic for carbon bound fluorine, an average orientation angle of an aromatic moiety (β = 23°), a surface modifcation-induced increase of water contact angle (from 84° for the bare substrate to 108° for the grafted one) as well as the presence of an organic layer on top of the substrate. Electrical characterization via the recording of current density-voltage (J-V) traces of EMDs featuring a Al/Al_xO_y/SAM/Pb/Ag stack revealed a pronounced hysteretic conductance switching for fluorinated LCI molecules, while no hysteresis was observed for the non-fluorinated reference compound. The maximum ON/OFF conductance ratio was found to be approximately 300. Hysteresis in J-V traces was observed for 7 devices and for 100 voltage cycles in one device. This constituted preliminary evidence, that the effect was both repeatable and stable. Calculations on single molecule (density functional theory DFT and TranSIESTA calculations), molecular ensemble (molecular dynamics) and device level (expansion of a well-established tunneling model) were performed to investigate the switching mechanism. Combining the results from these three models, compelling evidence pointing towards the re-orientation of dipoles within the SAM to be the governing mechanism in conductance switching was found. Additionally, molecular dynamics simulations revealed a dependence of the conductance switching effect on surface density of the molecules as well as on maximum applied electrical field across the SAM. The device model revealed a pronounced relationship between ON/OFF conductance ratio and effective charge carrier mass.
The need to replace the lead-based contacting scheme to improve stability of the devices and to avoid the use of toxic materials was also addressed. Alkylphosphonic acids (APAs) were utilized as model system to develop

a novel contacting scheme. Following the argument, that device malfunction is often due to migration of the top contact atoms through the SAM, the combination of TiN anchoring layer and Ti top contact was chosen for further study. Water contact angle, AFM scratching, elipsometry, XPS as well as FTIR spectroscopy confirmed successful grafting of a series of APAs on TiN covered substrates.
Studying J-V traces of EMDs featuring a series of APAs sandwiched between TiN as bottom and Ti/Au as top contact revealed tunneling attenuation factors β within the range of literature consensus. For instance, $\beta(V = -0.2$ V)=1.0/nC was calculated from J-V traces of devices of 15 x 15 μm^2 area and molecules with 6-12 carbon atoms. Injection currents in the range of J_0 =1-13 mA/cm^2 were further observed. Both tunneling attenuation factor β and injection current J_0 were found to increase with increasing magnitude of the evaluation voltage - a fact that, while contradicting the Simmons model, has been repeatedly observed by others. Analyzing the J-V data of individual devices, using an expansion of the Simmons tunneling model revealed physically sound values (e.g., ideality factor $\alpha = 0.71 - 0.85$, barrier height $\Phi = 3.0$ eV, electrically active area 10%).

The novel **TiN/phosphonic acid/Ti/Au** contacting scheme was ultimately transferred to the study of LCI-based EMD. To study the impact of molecular design on device performance, EMDs were fabricated with molecules featuring a variety of molecular motifs. Devices featuring the previously studied LCI molecule in the novel contact scheme revealed an increased current density (by approximately 4 orders of magnitude), but a lower on/off conductance ratio maximum of ≈ 13.
Three different molecules with a difluoro phenylcyclohexane dipolar unit were found to yield devices with maximum ON/OFF conductance ratios of $\approx 10 - 20$, while devices featuring a molecule with a difluoro dibenzofuran dipolar unit exhibited maximum ON/OFF conductance ratios of ≈ 135.
To further investigate the potential multi-state conductance switching, maximum sweep voltage dependent conductance was measured for LCI-EMD featuring one type of difluorphenylcyclohexane molecule. Current densities at a fixed evaluation voltage increased from 0.0027 mA/cm^2 to 0.0038 mA/cm^2 in the LRS and from 0.0022 mA/cm^2 to 0.0038 mA/cm^2 in the HRS when the maximum applied voltage across the junction was varied from 2 to 10 V. In total, 14 conductance states with at least 0.1 μA/cm^2 separation were observed. This points towards the general applicability of LCI-based EMDs to computational paradigms built on multi-state memory devices.

Overall, a novel contacting scheme for ensemble molecular devices was developed and compelling evidence for utilizing molecules with a conformationally flexible dipolar unit to achieve (multi-state) conductance switching was found.

Zusammenfassung

Um die stetig wachsende Nachfrage nach Rechenleistung zu befriedigen, werden derzeit neuartige Rechenparadigmen jenseits der von-Neumann Architektur entwickelt. Da viele von ihnen in hohem Maße von der Leistung von Speicherbausteinen abhängen, sind neuartige Materialsysteme, die eine zuverlässige und energieeffiziente Leitfähigkeitsschaltverhalten zeigen, sehr gefragt.
In dieser Arbeit wird eine Machbarkeitsstudie über die Verwendung von selbstorganisierenden Monoschichten (SAMs) aus flüssigkristall-inspirierten Molekülen in molekularen Ensemble-Bauteilen (EMBs) als Leitfähigkeitsschalter vorgestellt. Die Leitfähigkeitsumschaltung erfolgt hierbei durch die Neuausrichtung molekularer Dipole innerhalb einer SAM und die daraus resultierende Änderung der dipolinduzierten, konformationsabhängigen Modifikation der Tunnelbarriere.
Zu diesem Zweck wurden drei Hauptziele verfolgt. Zunächst wurden die SAM-Bildung sowie die elektrischen Eigenschaften von SAMs aus Phenylcyclohexan-basierten Phosphonsäuren mit einem aliphatischen Linker eingehend untersucht. Dann wurde ein neuartiges, zuverlässiges Kontaktierungsschema zur Herstellung von EMBs mit Phosphonsäuren zwischen zwei leitenden Schichten entwickelt und untersucht. Schließlich wurden die Leitfähigkeitsschaltcharakteristiken einer Reihe von EMDs auf der Basis von LCI-Molekülen gemessen, einige Beziehungen zwischen Struktur und Eigenschaften beobachtet und die Leitfähigkeitsschaltung in mehreren Zuständen für ein Molekül auf der Basis von Difluorphenylcyclohexan demonstriert.
Zunächst wurde die Selbstorganisation von LCI-Molekülen auf Aluminiumsubstraten untersucht. Die Bildung von Monolagen wurde durch eine Vielzahl von Oberflächencharakterisierungsverfahren bestätigt, darunter XPS, NEXAFS, Wasserkontaktwinkel und Ellipsometrie. Diese Techniken zeigten das Vorhandensein von XPS-Absorptionspeaks, die für kohlenstoffgebundenes Fluor charakteristisch sind, einen durchschnittlichen Orientierungswinkel der aromatischen Einheit ($\beta = 23°$), eine oberflächenmodifizierungsbedingte Vergrößerung des Wasserkontaktwinkels (von 84° für das reine Substrat auf 108° für das modifizierte) sowie das Vorhandensein einer organischen Schicht auf der Oberseite des Substrats. Die elektrische Charakterisierung durch die Aufzeichnung von Stromdichte-Spannungs-Kurven (J-V) von EMDs mit einem Al/Al_xO_y/SAM/Pb/Ag-Stapel ergab eine ausgeprägte hysteretische Leitfähigkeitsschaltung für fluorierte LCI-Moleküle, während für die nicht fluorierte Referenzverbindung keine Hysterese beobachtet wurde. Das maximale ON/OFF-Leitfähigkeitsverhältnis wurde zu etwa 300 berechnet. Hysterese in den J-V-Kurven wurde für 7 Bauelemente und für 100 Spannungszyklen in einem Bauelement beobachtet. Dies ist ein erster Hinweis darauf, dass der Effekt sowohl wiederholbar als auch stabil ist. Berechnungen auf Einzelmolekül- (Dichtefunktionaltheorie DFT und TranSIESTA-Berechnungen), molekulares Ensemble- (Molekulardynamik) und Bauelementebene (Erweiterung eines etablierten Tunnelmodells) wurden durchgeführt, um den Schaltmechanismus zu untersuchen. Die Kombination der Ergebnisse dieser drei Modelle ergab überzeugende Hinweise darauf, dass die Neuorientierung von Dipolen innerhalb der SAM der maßgebliche Mechanismus für das Schalten der Leitfähigkeit ist. Darüber hinaus zeigten Molekulardynamiksimulationen eine Abhängigkeit des Leitfähigkeitsschalteffekts von der Oberflächendichte der Moleküle sowie vom maximal angelegten elektrischen Feld. Das Bauelementemodell zeigte eine ausgeprägte Beziehung zwischen dem ON/OFF-

Leitfähigkeitsverhältnis und der effektiven Ladungsträgermasse.
Die Notwendigkeit, das Kontaktierungsschema auf Bleibasis zu ersetzen, um die Stabilität der Bauelemente zu verbessern und die Verwendung giftiger Materialien zu vermeiden, wurde ebenfalls addressiert. Alkylphosphonsäuren (APAs) wurden als Modellsystem verwendet, um ein neuartiges Kontaktierungsschema zu entwickeln. In Anlehnung an das Argument, dass eine Fehlfunktion von SAM basierten Bauteilen häufig auf die Migration der Atome des oberen Kontakts durch die SAM zurückzuführen ist, wurde die Kombination aus TiN-Verankerungsschicht und Ti-Kontakt auf der Oberseite für weitere Untersuchungen ausgewählt. Wasserkontaktwinkel, AFM-Kratzen, Ellipsometrie, XPS sowie FTIR-Spektroskopie bestätigten die erfolgreiche Aufbringung von APA SAMs auf TiN-bedeckte Substrate.
Die Untersuchung der J-V-Kurven von EMBs mit einer Reihe von APAs, die zwischen TiN als unterem und Ti/Au als oberem Kontakt liegen, ergab Tunneldämpfungsfaktoren β, die im Bereich des Literaturkonsenses liegen. So wurde beispielsweise $\beta(V = -0,2\ \text{V})$=1,0 nC^{-1} aus J-V-Kurven von Bauteilen mit einer Fläche von 15 x 15 μm^2 und Molekülen mit 6-12 Kohlenstoffatomen berechnet. Weiterhin wurden Injektionsströme im Bereich von J_0 =1-13 mA/cm^2 beobachtet. Es wurde festgestellt, dass sowohl der Tunneldämpfungsfaktor β als auch der Injektionsstrom J_0 mit zunehmender Größe der Auswertungsspannung ansteigen - eine Tatsache, die zwar dem Simmons-Modell widerspricht, aber von anderen bereits wiederholt experimentell beobachtet wurde. Die Analyse der J-V-Daten einzelner Bauelemente unter Verwendung einer Erweiterung des Simmons-Tunnelmodells ergab physikalisch sinnvolle Werte (z.B. Idealitätsfaktor $\alpha = 0,71 - 0,85$, Barrierenhöhe $\Phi = 3,0$ eV, elektrisch aktive Fläche 10%).

Das neuartige **TiN/Phosphonsäure/Ti/Au**-Kontaktierungsschema wurde schließlich auf die Untersuchung von EMBs auf LCI-Basis übertragen. Um die Auswirkungen des Moleküldesigns auf die Charakteristiken der Bauelemente zu untersuchen, wurden EMBs mit Molekülen hergestellt, die verschiedene Molekülmotive aufweisen. Bauelemente mit dem zuvor untersuchten LCI-Molekül in dem neuartigen Kontaktschema zeigten eine um etwa 4 Größenordnungen erhöhte Stromdichte, aber ein niedrigeres maximales Ein/Aus-Leitfähigkeitsverhältnis von etwa 13. Drei verschiedene Moleküle mit einer dipolaren Difluorphenylcyclohexan-Einheit ergaben Bauelemente mit maximalen Ein/Aus-Leitfähigkeitsverhältnissen von $\approx 10 - 20$, während Bauelemente mit einem Molekül mit einer dipolaren Difluordibenzofuran-Einheit maximale Ein/Aus-Leitfähigkeitsverhältnisse von ≈ 135 aufwiesen.
Um die potentielle Erreichbarkeit von mehr als zwei Zuständen weiter zu untersuchen, wurde der maximale, von der Sweep-Spannung abhängige Leitwert für LCI-EMD mit einer Art von Difluorphenylcyclohexan-Molekül gemessen. Die Stromdichten stiegen bei einer festen Auswertungsspannung von 0,0027 mA/cm^2 auf 0,0038 mA/cm^2 im LRS und von 0,0022 mA/cm^2 auf 0,0038 mA/cm^2 im HRS, wenn die maximal angelegte Spannung von 2 bis 10 V variiert wurde. Insgesamt wurden 14 Leitfähigkeitszustände mit mindestens 0,1 $\mu\text{A/cm}^2$ Abstand beobachtet. Dies deutet auf die allgemeine Anwendbarkeit von LCI-basierten EMDs für neuartige Computerparadigmen hin, die auf Mehrzustandsspeicherbauelementen aufbauen.

Insgesamt wurde ein neuartiges Kontaktierungsschema für molekulare Ensemble-Bauelemente entwickelt, und es wurden überzeugende Hinweise für die Eignung von Molekülen mit einer konformationsflexiblen dipolaren Einheit zur Erzielung von (Mehrzustands-)Leitfähigkeitsschaltungen gefunden.

Contents

1 Introduction

Historically, from a physical perspective, the capabilities of computational systems have mainly been improved by driving down feature sizes. Since power efficiency and the speed of electronic devices approach their physical and economical limits, new materials, devices and computing paradigms are needed to further scale computational performance. In the past, most computing systems have been built on the combination of complementary metal oxide semiconductor (CMOS) technology and the von Neumann (VN) computing architecture. [1]

The road map for decreasing feature sizes of CMOS transistors has been famously described by Moore's law. [2] It proposes a doubling of transistors per area every two years in order to cope with future demands of computational capabilities. Driving innovation in computing for decades, Moore's law is believed to soon reach its scaling limitations. [3] In the widespread von Neumann computing architecture, data and instructions are stored in memory. The central processing unit (CPU) fetches instructions from memory and performs basic controlling, logic and arithmetic functions on data according to these instructions. Both, data and instructions are stored in memory that is addressed over a common bus. This enables the 'stored program' paradigm and makes computing systems based on this architecture highly flexible. Its word-at-a-time thinking renders the speed of memory and bus the limiting factors in computational power. This limitation is commonly referred to as *von Neumann bottleneck* and is particularly disadvantageous for data-centric applications. When much data has to be analyzed by a von Neumann machine, much time and energy is spent to move around data. Several computing concepts have been proposed to overcome these limitations. Among them are spike time-dependent plasticity learning, deep neural networks, quantum computing and in-memory computing. They each have their unique advantages for unique challenges of computational systems and a parallel existence of all of them in the future is to be expected. [4] Those novel computing paradigms are, as more established ones as well, deeply embedded around memory devices. Their efficiency and computational capabilities are therefor highly dependent on fast, efficient and reliable memory devices. Even though many of the novel computing paradigms can be implemented in CMOS, they require a large number of transistors and passive components, consuming considerable space and dissipating a large amount of heat on a chip. Hence, a power- and area-efficient physical implementation of future computing paradigms requires the simultaneous development of materials and devices.

With both the basic devices and the computing architecture approaching their ultimate limitations, new materials, devices and computing principles have to be developed in conjunction with each other to further decrease cost and power consumption as well as to increase computational capabilities of future electronics.[5] Among the emerging memory technologies, resistive random access memory (RRAM) devices have gained huge attention for next-generation computational applications. RRAMs operate on the mechanism of changing an active material's resistance between a high resistive state (HRS) and low resistive state (HRS), sometimes even several resistive states, upon an external stimulus. Therefore, their resistance (or conductance) can be used as entity for information storage and computation. As potential *universal memory*, collapsing the memory

storage hierarchy, they might open up new ways from processor-centric to memory-driven computing. Devices featuring multiple conductive states might even result in a direct, physical implementation of neuromorphic and neural networks. [1]

This great potential impact of memristive devices has been a major driving force to find and develop conductance switching materials. While most these efforts focused on inorganic systems, more recently, organic systems have come into focus. Specifically, state changes in self-assembled monolayers (SAMs) have more recently been studied, due to their potential to offer a solution to continue the scaling of electronics and to implement new electronic functions more deliberately and efficiently. With lengths that often do not exceed few nanometers, electrically functional molecules promise the ultimate miniaturization of electronics.
Ensemble molecular devices, that utilize the electronic functionality of organic molecules in form of SAMs promise cheap, scalable production through solution processing, small volume consumption on chip, bio-compatibility, potential 3D stacking capability and the ease of tailored property design. Molecules can also be designed to feature multiple required properties in one layer, potentially eliminating the need of peripheral electronic devices, such as the selectors commonly used within RRAM memory arrays. [6–11]
Molecular based memory devices that utilize the change in conductance arising from different physical states of the molecule (or monolayer) to store and express information, have recently been explored. Among the strategies to change the conductance of a molecular junction through an external stimulus are changes in molecular geometry [12, 13], redox reactions [14–16], charge migration [11] magnetic field [17, 18], wavelength of light [19, 20] and electric current [11, 21].

This work aims at adding another, novel strategy of conductance switch to this plethora of choices. Specifically, using the re-orientation of molecular dipolar units within a SAM via an applied electrical field to asymmetrically modify the tunneling barrier, is proposed and studied. To this end, SAMs of liquid crystal inspired molecules as well as ensemble molecular devices based on them were characterized and models from single molecule to device level theory will be used to investigate the proposed conductance switching effect. Since these molecules do not undergo any kind of chemical reaction during operation, i.e., no bond breaking, change of redox state or electronic excitation, ensemble molecular devices with them show great potential for slow degradation and high stability.

Fabrication of simple sandwich junction architectures with a molecular monolayer embedded in-between two solid-state conductive layers (contacts) is crucial for industrial translation, yet still remains a challenging task. [22] This is mostly due to the intrinsic challenges of fragility and reactivity of organic molecules, potential diffusion of contact atoms through the SAM and surface roughness of contacts on the order of magnitude of the length of molecules. Due to this difficulty of solid top contact formation, today, only few specific anchoring layer/molecule/solid top contact combinations have been reported and systematic variations of specific functional groups of a molecule within such an ensemble molecular device are reported even less often. [23] The latter would be crucial to study the structure-process-property relationships for ensemble molecular devices. In this work, a previously studied fabrication method to deploy top contacts, namely the physical vapor phase deposition of lead at a low deposition rate, is first used to study the general concept of conductance switching using liquid crystal inspired molecules. Then, a novel concept of fabricating reliable solid-state ensemble molecular devices is developed and transferred to the further study of conductance switching in

ensemble molecular devices.

The impact of variation of structural motifs of the molecules on charge transport characteristics of ensemble molecular devices featuring these within the novel contacting scheme will finally be studied.

The overall structure of this thesis is as dipole-induced:

In **Chapter 1** a brief introduction on the main aspects of ensemble molecular devices is given. In particular, self-assembly of molecular monolayers, the challenge of electrically contacting them as well as theoretical and computational aspects of charge transport through SAMs are covered.
Chapters 2 and **3** provide a comprehensive overview of the characterization and fabrication methods deployed in this work.
Chapter 4 details the substrates and molecules used.
In **Chapter 5**, details on the intial chip layout as well as on its improvement are presented.
Chapter 6 provides a first study of the feasibility of using liquid crystal inspired molecules as the basis for conductance switching ensemble molecular devices. It includes comprehensive characterizations of SAMs of a difluoro benzyl cyclohexane derived molecule on aluminum oxide surfaces (XPS, AFM, NEXAFS, contact angle, ellipsometry) as well as DC electrical characterization and analysis on single molecule (via density functional theory), molecular ensemble (via molecular dynamics) and device (via a newly device model) level of theory.
Chapter 7 outlines the steps taken to develop a novel, lead-free, solid-state contacting scheme for alkylphosphonic acid based SAMs. It includes comprehensive surface characterization of alkylphosphonic acid monolayers on titanium nitride (water contact angle, atomic force microscopy, atomic force microscopy scratching, x-ray photoelectron spectroscopy, fourier transform infrared spectroscopy) as well as DC current density voltage measurements and the comparison of the measured current densities to the simplified and an adjusted Simmons model.
In **Chapter 8** the two prior Chapters are brought together and ensemble molecular devices based on liquid crystal inspired molecules, using the newly developed contacting scheme, are electrically characterized and some observation about molecular structure - device performance relationships is given.
Chapter 9 summarizes the results obtained in this work and gives an outlook on possible future improvements on fabrication scheme, measurement methodologies and experiments.

2 Theoretical Background

The following chapter will provide an introduction to ensemble molecular electronics. This includes self-assembled monolayer (SAM) formation, the advantages of using phosphonic acids for SAMs, the challenge of electrically contacting SAMs, charge transport models, density functional theory & the TranSIESTA approach as well as the fundamentals of molecular dynamics simulations.

2.1 Ensemble Molecular Electronics

With organic molecules comes also the ease of tailored property design through the use of organic synthetic chemistry. Molecules can potentially be tailored to show any specific charge transfer characteristics when a voltage is applied across them. For instance, as proposed by *Aviram and Ratner* in 1974 a molecule that has a donor-insulating barrier-acceptor structure shows rectifying transfer characteristics and can hence be used as molecular diode.[24] Molecular interconnects with varying resistances can be realized with conjugated molecules. Putting these two basic, passive, structural elements of diodes and interconnects together, logic functions like AND or OR become possible. This in turn enables the construction of higher computational functions, like a full adder, simply by combining these building blocks to one large molecule. This approach to building a circuit *bottom up* is much less area-consuming and requires fewer structuring processes as doing the same with conventional semiconductors. In addition to passive components, molecules can also be designed to exhibit characteristics of active components, i.e., components whose charge transfer characteristics can be modulated via an additional external stimulus. For molecular length scale electronics, tunneling is often found to be the dominant charge transport mechanism. Hence, small perturbances, e.g., in lengths or energy levels, are directly translated into nonlinear electrical responses. Since molecules can be designed to react to a variety of stimuli, such as ion transfer, photon absorption, isomerization, oxidation and reduction as well as heat, electronic devices built on them can potentially be tailored to achieve what is often referred to as 'virtually unlimited device functionality'. [6, 25]

However, connecting those single molecular electronic circuits to electrical interconnects to provide an input/output and the connection to a voltage source, requires specialized approaches that have an inherent scaling limitation. Single molecules and molecular circuits are often connected through *mechanically controlled break junctions* or analyzed using conductive atomic force microscopy (C-AFM) or scanning tunneling microscopy (STM) methods. These methods are perfect testbeds to analyze the function of molecular building blocks and circuits on a small scale, but cannot be used on a larger, integrated scale and especially not in consumer electronics. Another drawback making the use of single molecules in practical devices unlikely is, that transport through one molecule is in its nature stochastic. Electronic devices on the other hand, need a certain degree of reproducibility. Since the current across a multitude of parallel molecules is the sum of many electron transfer events through those individual molecules, current measurements across self-assembled monolayers (SAMs) are much more reproducible than the ones carried out on single molecule junctions. This and the possibility to scale are the most important reasons, why SAMs may promise sooner realization of

integrated, functional devices than single molecule junctions. Since SAMs present an *ensemble* of molecules in contrast to a *single* molecule, devices utilizing SAMs as electronically active component are often termed *ensemble molecular devices*. Consequently, the study of electronics based on these devices is termed *ensemble molecular electronics*.[6–8]
SAMs are formed by the immersion of a substrate into a solution containing a molecule with a reactive end group that binds to the surface of the substrate. Since this reactive end group reacts exclusively with the surface and not with the end group of other molecules present in the solution, the self-assembly on the surface is self-limited and results in a monolayer of the molecule attached to the surface (or *anchoring layer*).
The intentional design of the molecular backbone of the SAM forming molecule enables the modification of the physical and chemical properties of surfaces and interfaces. Self-assembled monolayers have for example been used to modify wetting behavior [26, 27], adhesion of bio-molecules and cells [28, 29] and corrosion protection [30]. Technological uses of SAMs within electronic devices, include SAMs that reduce the injection or extraction barrier for organic light emitting diodes and organic photovoltaics.[31–35] Only recently, research interest in the field of ensemble molecular electronics, where the SAMs themselves are used as passive or active electronic component, has grown. SAMs have for instance been studied as active layers in self-assembled monolayer field effect transistors (SAM-FETs) [36] or electrical-field controllable switches.[10, 11]

In contrast to single molecule electronics, the charge transfer and reaction to external stimuli in ensemble molecular devices can differ significantly from those calculated for single molecules. One reason for that is, that the SAM might not be perfectly packed which opens up through-space transport as a secondary transport channels. Also, *inter*molecular interactions can influence the overall electronic configuration and hence influence the overall charge transfer. [6, 37] Additionally, barrier height and barrier width might follow a distribution rather than being confined to a singular value. *Miller et al.* have shown that this distribution can significantly alter tunneling characteristics of area devices. [38] When the electronic functionality builds on conformational changes of the molecules, *inter*molecular forces, governed e.g., by the distance between the molecules, have also been shown to have great impact on device performance. [39] The study of ensemble molecular electronics hence also includes the study of *inter*molecular interactions as well as molecule-substrate interactions governing the formation of the electronically functional SAM.
In the following, a general introduction to the field of ensemble molecular electronics is given. For more details on specific aspects, the reader is refered to a recent, comprehensive review by *Liu et al.* [25].

2.1.1 Self-Assembled Monolayers

Bare metal and metal oxide surfaces are known to readily adsorb organic materials since they lower the free energy of the interface between the surface and the ambient environment. [40] Surfaces that are unintentionally covered with adsorbed molecules might posses advantageous properties but are ill-defined; they do not present intended functionalities or reproducible physical properties. [37]

Self-assembled monolayers of organic molecules present a facile tool to exploit the advantageous property change of metal or metal oxide surfaces in an intentional, flexible and reproducible fashion. SAMs are organic assemblies formed by a controlled adsorption of molecular constituents presented to a pristine surface. Molecules that form SAMs posses a chemical functionality with an affinity towards the substrate. This chemical functionality - often termed *headgroup* - sometimes shows a particular high affinity for the surface and can

hence displace already adsorbed organic molecules from the surface. In contrast to other organic thin film deposition techniques, grafting SAMs on a surface is frequently connected with a covalent bond between SAM molecules and surface. This may be preferred for long-term stability of the organic layer. [41]
A number of headgroups that bind to specific semiconductors, metals and metal oxides have been studied. For instance, the adsorption of molecules with a thiol headgroup on noble and coinage metals has been studied to a great extent [37, 42–52]. Silanes are another headgroup that has been extensively studied to form covalently bound monolayers on silicon [53] and silicon oxide [54]. Lesser studied is the formation of self-assembled monolayers of phosphonic acids (PA) on metal oxide surfaces. For all headgroups, molecules that consist of the headgroup and an alkyl chain of varied length are often used as benchmark system, since the formation of monolayers of alkyl chain molecules has been extensively studied both theoretically and experimentally.

To form a SAM on a substrate, the substrate is immersed into a solution containing a molecule with a reactive end group that binds to the surface of the substrate. Since this reactive end group reacts exclusively with the surface and not with the end group of other molecules present in the solution, the self-assembly on the surface is self-limited and results in a monolayer of the molecule attached to the surface (or *anchoring layer*). During the self-organization of the molecules at the surface, *inter*molecular interactions between adjacent molecules and solvent-molecule interactions drive the SAM towards an overall energetically favorable state. For molecules with a long alkyl chain this typically leads to a highly ordered structure of the SAM where the molecules are typically tilted by a tilting angle Θ with respect to the surface normal. This in turn results in a SAM thickness d that differs from the molecule length l. This tilting angle is defined by:

$$\Theta = \arccos \frac{d}{l} \tag{2.1.1}$$

The local structure of molecules, including the packing density, within the SAM is governed and can be influenced by choice of solvent, temperature, and concentration of the SAM-forming molecule within the solution as well as by physical properties of the substrate surface. Since molecular monolayers are at or below the resolution limit of many surface characterization techniques, often several characterization methods are combined to analyze the *quality*, i.e., the degree of order and reproducibility, of a SAM. Water contact angle is often used to determine the polarity of the ambient facing moiety, atomic force microscopy is used to analyze surface morphology and to visualize multi-layer or larger pin-holes. Infrared spectroscopy can be used to detect presence of the intended molecule, surface bound head groups and compare the quality of the SAM to well-studied reference systems. Ellipsometry, x-ray photoelectron spectroscopy attenuation, atomic force microscopy (AFM) scratching as well as transmission electron microscopy (TEM) imaging of a cross-section of the SAM can be used to determine the SAM thickness and other properties. These measurement methods are covered in more detail in Chapter 3.

Phosphonic Acid SAMs

Phosphonic acids are molecules of general formula RPO_3H_2, where R is an organic rest component. They are known to react with a variety of metal salts, semiconductors and oxides. [41, 55, 56] In particular, phosphonic acids have been shown to form stable self-assembled monolayers on a variety of substrates such as aluminum oxide [57–61], titanium oxide [62–66], zirconium oxide [62, 66], zinc oxide [67, 68] and silicon

oxide [69–72].[73] When it comes to the fabrication and stability of SAMs, phosphonic acids come with several potential advantages over silanes, thiols, carbocylic acids and alkenes, some of which will be outlined below.

Several anchoring groups depend on a specific surface termination to form a covalent bond to the surface. Hydrosilylation for instance requires hydrogen-terminated surfaces wheras silanization, depends on hydroxyl-terminated surfaces. Phosphonic acid chemistry is different from that in that it has been proposed that the formation of organophosphonate monolayers requires surface OH groups only as initial bonding sites, and does not depend on them for full coverage. It has also been shown that water contamination of the surface does not preclude phosphonic acid grafting. Thus, the self-assembly of phosphonic acids is a robust process and can be achieved even if the introduction of OH groups on the substrate can only be partially achieved. This may simplify fabrication of self-assembled monolayer of phosphonic acids and also makes them feasible candidates for monolayer formation on any oxide material.[41, 74]

Simple immersion of oxide surfaces in phosphonic acid solutions may result only in physisorption through hydrogen bonding and van der Waals forces. Subsequently annealing the adsorbed phosphonic acid film at temperatures between 120°C and 140°C, is widely considered to achieve covalent bonding.[71] During annealing, stable P-O-M linkages (where M is the metal atom of the metal oxide) form through deprotonation of both phosphonate hydroxyl groups. These covalent bonds greatly improve the stability of the monolayer. A schematic of this process, leading to *bidentate* binding of the phosphonic acids is shown in Figure 2.1.1. Dissolution and precipitation are however also processes increasingly occurring with increasing temperature and may compete with the formation of covalent bonds to the surface. Reaction conditions, such as temperature, concentration, pH, nature of the solvent and sequence of heating and immersion processes are therefore to be taken into account, when optimizing SAM formation. An additional P-O-M bond may be formed from the phosphoryl oxygen to the metal. This might either be through coordination [75] or through an acid-promoted condensation reaction [76]. Phosphonate SAMs on various oxides have in fact been shown to favor the formation of tridentate coordinates, which might be the reason for the exceptionally high stability of phosphonic acid based self-assembled monolayers as compared to e.g., thiols. [76–81]

Molecules with some particular head groups suffer from potential dimerization of the headgroup. Examples are the formation of disulfides from thiols [82] as well as the homocondensation of silanes [83]. This can lead to the formation of aggregates within the solution and ultimately multilayers on the substrate surface as well as to significantly altered adsorption dynamics. Phosphonic acids, in contrast, do not rapidly homocondense and are hence likely immune to aggregation issues. [75, 84]

In addition to the above presented advantages, the phosphonic acid surface bond has shown to be exceptionally thermally and aquatically stable on a variety of substrates. [66, 85] *Wan et al.* have for instance shown that while for a variety of phosphonic acids the anchoring groups were hardly affected by annealing up to 773 K, breakup of the bond between anchoring group and the rest of the molecule was observed at much lower temperatures. [85]

An overview by *Queffélec et al.* [86] details synthetic routes and deposition methods to yield phosphonic acid grafted surfaces.

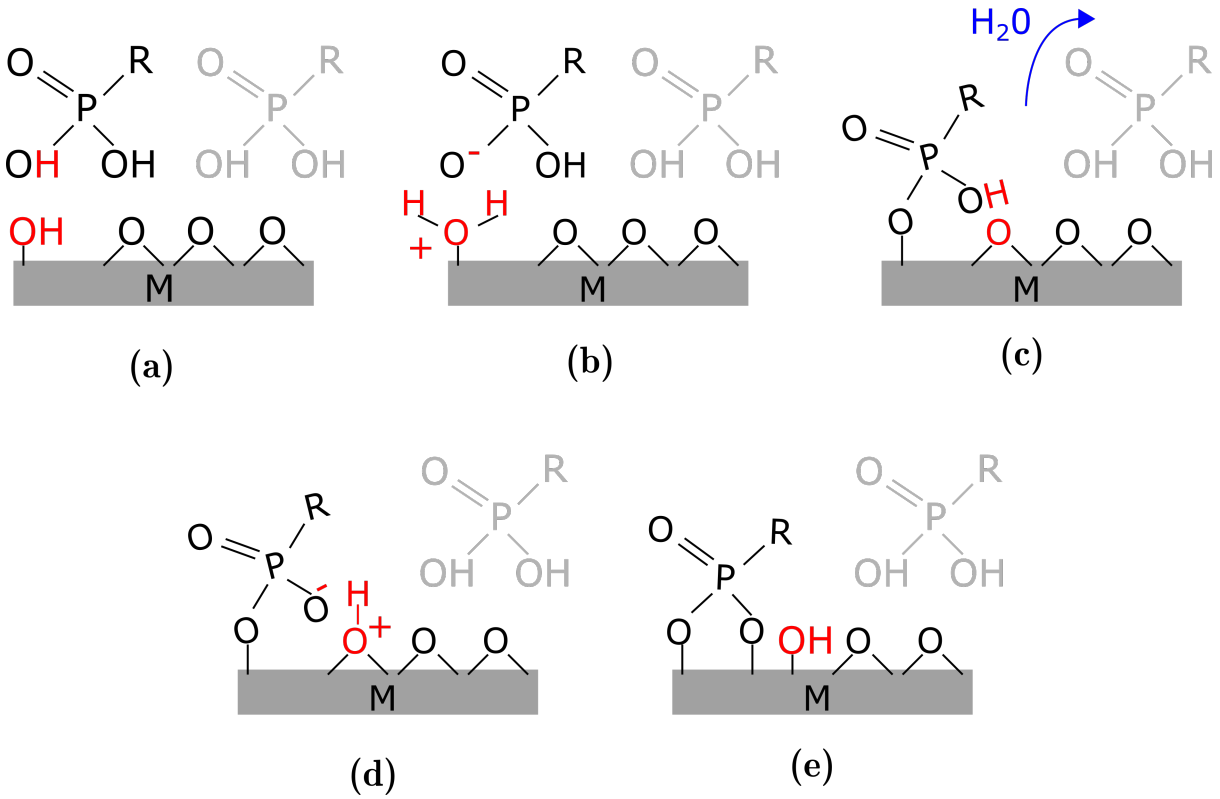

Figure 2.1.1 Proposed binding mechanism of phosphonic acids to metal oxide surfaces. M:metal, O:oxygen, P:phosphor, H:hydrogen, R: residue, + and - denote positive and negative charge. Second phosphonic acid is greyed out for clarity. a) Initial situation with phosphonic acids physisorbed to a metal oxide layer, that presents one adsorbed hydroxyl group at the solid-ambient interface. This hydroxyl group is sufficient to initiate monolayer formation. b) Deprotonation of the first hydroxyl group and proton transfer to the OH group at the surface resulting in surface bound H_2O. c) H_2O disassociates from the surface and evaporates (as sufficient temperature), phosphonic acid forms first bond to the surface, resulting in a monodentate complex. d) Deprotonation of the second hydroxyl group and proton transfer to the oxygen of the oxide. e) Open oxygen binds to the metal, yielding a bidentate complex and a surface bound hydroxyl group. Since this resembles the situation in a), the same process can continue with the next phosphonic acid that is physisorbed to the surface (grey). Theoretically one hydroxyl group might hence be enough to form a covalently bound monolayer of phosphonic acids on a metal oxide surface. Self-assembly might hence be independent of achieving high surface coverage of OH prior to exposure to the SAM forming molecule. In practice, the surface is often nevertheless enriched with OH to increase the efficiency and quality of SAM formation. Ordered monolayer formation is further driven by dispersion interactions between neighbouring organic moieties. Adapted from [41]

2.1.2 Electrical Contacting Schemes

Within the field of molecular electronics, wiring the self-assembled monolayers to the outside world in a reliable, stable and reproducible fashion remains one of the biggest technical challenges. This challenge has been present for almost half a century with *Mann and Kuhn* being the first to report having found a reliable contacting scheme with permanent, solid contacts in 1971. [87] Up until today, a truly reliable, universal method has not yet been found. This has hindered progress in fundamental understanding of structure-property relationships and ultimately technological advances.
While the assembly of monolayers onto conducting substrates or thin oxides is well established, the application of top-contact electrodes remains a daunting challenge. In the following, a selective overview of methods that have been proposed as contacting schemes for molecular monolayers is presented. For a more detailed discussion of various contacting schemes the reader is referred to [6, 7] and [88].

Temporary Contacts

Damaged induced by depositing the top contact is often thought to be the major limitation in forming top-contact electrodes. One possible remedy is to use temporary contacts that are less destructive to the molecules.
Well-established techniques to study charge transport with temporary contacts of other materials can readily be transfered to the study of molecular monolayers. This includes scanning probe techniques, such as conductive atomic force microscopy (C-AFM) as well as scanning tunneling microscopy (STM). While they are mostly deployed to study single molecular junctions, wider probe tips can also be used to contact molecular monolayers, yielding devices that include a small number of molecules sandwiched between two contacts. [89–92]
Another way to form temporary contacts is the use of highly conductive liquids. Most prominently, mercury (Hg) drop electrodes and eutectic gallium indium (EGaIn) electrodes have been used to contact monolayers.
A mercury drop electrode is formed by pushing a defined volume of Hg from a reservoir through a capillary. The high surface tension of Hg then leads to the formation of a droplet, that deforms when coming into contact with an other surface, forming a circular contact area. Molecular monolayers can then be contacted by contacting the substrate and the Hg reservoir. Many molecular junction experiments using a mercury top-electrode have been reported. [57, 72, 93–95] While the high surface tension prevents direct diffusion of mercury through the monolayer, the vapor pressure of Hg at room temperature is very low. Thus, Hg vapor can diffuse through the monolayer, and potentially react with the bottom contact material. Since Hg is is reactive towards many common substrate materials, such as gold, silver and II-VI semiconductors, amalgamation strongly limits the usefulness of contacting monolayers on these substrates with a mercury drop electrode, even though it works reasonably well for monolayers on oxides [96, 97]. This drawback and the fact that mercury is toxic lead to the development of an alternative temporary liquid contact. To date, mercury drop electrodes have widely been replaced by eutectic gallium indium (EGaIn, pronounced 'e-gain'). Mixtures of 75 wt.% gallium (Ga) and 25 wt.% indium (In) yield an *eutectic*. Eutectics are mixtures of materials that exhibit melting temperatures that are lower than those of all of their individual consitutents. For EGaIn the melting temperature is found to be at ≈ 15 °C. [98] This makes EGaIn a room temperature liquid metal alloy that exhibits high conductivity and can hence be used as soft contact to electrically characterize SAMs.[99] EGaIn contacts are formed via pushing a defined volume of the material through a metallic syringe and directly contacting that syringe. EGaIn is also a non-Newtonian liquid, which allows it to be moulded into cones with well defined contact area. As compared to Hg drops, EGaIn contact areas are smaller, biocompatible and do not penetrate through SAMs, independent of the substrate material. However, they are covered by an ill-defined gallium oxide film [99], which complicates

theoretical transport calculations.
Temporal contacts are a facile method to form a contact/SAM/contact sandwich configuration for multiple repeat measurements. General drawbacks include the comparatively large area of the contacts and a change of contact area with temperature. [100]. They are also limited to lab use. For industrial application of ensemble molecular electronics, permanent contacts are crucial.

Permanent Contacts

In order to apply a solid-state top contact to SAMs, several strategies have been pursued. One strategy is the introduction of a conductive interlayer. The following concepts have most prominently be researched so far:

- **Nanoparticle Interlayers**: SAMs are designed with an ambient facing head group that exhibits an affinity towards a material that is available in nanoparticle form. For instance, di-thiols can be grafted onto a gold surface, such that they exhibit an ambient facing thiol group. Subsequent incubation of the substrate in a gold nanoparticle dispersion immobilizes the nanoparticles on the SAM via S-Au bond formation. This in turn, makes evaporation of any top contact feasible, since the nanoparticles mitigate potentially destructive effects of the condensation of the evaporated material. [101–103] This method has shown to result in the successful formation of metal-SAM-metal junctions with high yields. [104] A variant of this method is the synthesis of metallic nanoparticles or nanoislands directly on the monolayer film from a single precursor. This thermally induced decomposition of an organo-metallic compound (TIDOC) is for instance realized by incorporating a thermally sensitive organic gold complex as ambient facing moiety. Annealing at moderate temperature after self-assembly then leads to the formation of gold nanoislands that can serve as seeding layer for electroless metal deposition or direct metal evaporation. [105, 106]

- **E-beam deposited carbon (eC)**: Focused electron beam induced deposition (FEBID) can be employed to fabricate carbon interlayers on top of molecular monolayers. In general, FEBID is a maskless lithographic technique that utilizes the electron beam-induced decomposition of molecules in the gas-phase to non-volatile compounds. An electron beam is scanned over a sample and precursor molecules are delivered by a gas-injection system to achieve localized deposition of the decomposition product. [107] It has been shown that this technique is suitable to graft e-beam deposited carbon (eC) from a naphtalene precursor without damaging the underlying monolayer. This technique is independent from ambient facing moiety that carbon is directly deposited on and the resulting carbon layer was found to be stable. [108, 109]

- **Spin-coated polymer interlayers**: Deposition of a conducting, organic polymer interlayer can be used to protect the monolayer. For instance, spin-coating the well-known conducting polymer poly(3,4-ethylenedioxythiophene) polystyrene sulfonate (PEDOT:PSS) on top of a self-assembled monolayer has been shown to avoid the formation of shorts upon the thermal deposition of gold. [110–112] However, contact formation between polymers and molecules in the monolayer is reported to be poor [113, 114] and also highly dependent on the ambient facing moiety of the SAM [112]. While the ease of fabricating polymeric interlayers speaks for them, the introduction of conducting polymers into an ensemble molecular stack, also introduces additional challenges that come with the use of conducting polymers in general. This includes their often poor conductance as well as their poor stability under

ambient conditions. [111, 115]

- **Atomic layer deposition of interlayers**: Atomic layer deposition (ALD) presents another potential route to utilize specific ambient facing moieties to deposit an interlayer on molecular monolayers. In ALD, atomic monolayers of materials are deposited through repeated exposure of typically two separate precursors. The two precursors that react to the desired product are never simultaneously present within the chamber, except at the deposition surface. First, the chamber is flooded with the first precursor and a self-limiting reaction with the surface occurs, leaving surface bound reaction products. The chamber is then pumped and flooded with an inert gas before it is flooded with the second precursor, that in turn reacts with the reaction product of the first precursor such that the surface is primed for the first precursor again. Since the reaction of the first precursor typically depends on an ambient facing moiety, that the second precursor generates on the surface, SAMs with that particular moiety can also be used as a starting point. Atomic layer deposition of metal oxides (namely Al_2O_3, ZnOx and MnOx) on SAMs with ambient facing functional groups OH, COOH, and SH has been shown to be feasible at temperatures <100°C. [116, 117] Ensemble molecular devices using this fabrication scheme have also been demonstrated. [116] While being compatible with CMOS processes and large scale production, low temperature ALD of metal oxides introduces an additional oxide layer in the ensemble molecular device, increasing its complexity and decreasing the conductivity of individual junctions. Within this work, a first attempt to grow TiO_2 on SAMs of alkylphosphonic acids with an ambient facing carboxyl endgroup have shown first successes (see Appendix).

Most of these contacting schemes are, however, incompatible with current fab scale nanofabrication techniques or increase device fabrication time and device complexity and decrease device conductance. A simple method of forming an electrically conductive top contact to SAMs is still highly sought after. This issue and a potential solution to this challenge will be elaborated further in Chapter 8.

2.2 Charge Transport through Self-Assembled Monolayers

Understanding the charge transport mechanisms through molecular monolayers is crucial to developing an understanding of ensemble molecular devices. However, despite the decades long study of charge transport through molecular monolayers, the study of molecular junctions and devices still lacks a widely accepted, generic description of the current-voltage characteristics. A detailed discussion of transport models is, for instance covered in works by *Vilan et al.*, most prominently in [6, 118] and [119].
To analyze the charge transport across a molecular monolayer, several charge transfer mechanisms have to be considered. Most notably, tunneling and hopping have been considered as dominant transfer mechanisms through single molecules and molecular monolayers of various molecules.
A clear distinction between those two mechanisms is often difficult. However, temperature dependence of transport is often considered a distinguishing property of hopping transport. [120] As will be derived below, tunneling is in general not inherently temperature dependent. However, this distinction through temperature dependence alone can become more complex, when taking temperature dependent energy broadening effects into account. For one, broadening of the Fermi-Dirac distribution in the electrodes with increasing temperature may change the relative alignment between the molecular frontier orbital and the Fermi level, i.e., the tunneling barrier height. Hence, an increasing temperature might decrease the effective barrier. This can lead to an increased conductance with increasing temperature, even for pure tunneling transport. [121] Further, physical properties of SAM anchoring layers, such as oxides, that might influence charge transport in a direct or in an indirect way might also be temperature dependent. Recently for instance, the permittivity of TiO_2 was found to increase with decreasing temperature. [122] Assuming a dual layer capacitor for an oxide/SAM system, this would decrease the electrical field across the SAM with decreasing temperature, ultimately resulting in a decreased tunneling current at a fixed voltage.
Since a very clear distinction between hopping and tunneling does most likely not perfectly reflect any experimental situation, a more realistic view would include a continuous transition between those extremes. In order to practically model transport and compare charge transfer across multiple types of molecular junctions, the following, more practical distinction is frequently assumed: The type of transport is governed by the difference between the Fermi level and the frontier orbital (LUMO for electron transport, HOMO for hole transport). When this difference is small, hopping conduction may take place. When it is large, charge transport occurs predominantly by tunneling. [120] Since for all molecules studied in this work, the difference between Fermi level of the electrodes and HOMO/LUMO is comparatively large, the dominating charge transfer process was assumed to be tunneling.

2.2.1 Tunneling

Tunneling is an illustrative term for the quantum physical effect that a particle can move from one side of a barrier of finite height to the other, even if its energy is insufficient to overcome the barrier. To quantitatively decribe it, the wave function of said particle has to be considered. The wave function ψ of a quantum-mechanical system, e.g., a charge carrier, is a complex-valued probability amplitude that the possible results of measurements made on the system can be derived from. The probability density $\rho = |\psi|^2$ gives the probabilities of locations of the particle. Since the wave function is governed by the Schrödinger equation, solving it for a moving charge

carrier within a potential landscape, including a barrier, allows one to calculate tunneling probabilities. In its one-dimensional, time-independent form, the linear partial differential equation reads:

$$H\psi(x) = E\psi(x) \tag{2.2.1}$$

Here, H is the Hamiltonian and E the energy of the particle. When considering moving charge carriers within a potential landscape, the following Hamiltonian is used:

$$H = -\frac{\hbar^2}{2m^*}\frac{d^2}{dx^2} + V(x) \tag{2.2.2}$$

Here, the first term describes the kinetic energy and $V(x)$ the potential. $\hbar$ is the reduced Planck constant, m^* is the effective mass and d^2/dx^2 is the second derivative with respect to the location x. Solutions to this equation describe the propagation of a single charge carrier within the potential $V(x)$. The solution of the Schrödinger equation for a free moving particle with the given Hamiltonian can be written as the superposition of right and left moving waves

$$\Psi(x) = A \cdot e^{jkx} + B \cdot e^{-jkx} \tag{2.2.3}$$

where k is the wavenumber that is related to the energy of the wave. With V(x), the effective mass of the carrier m^* and appropriate boundary conditions the Schrödinger equation can be solved and the probabilities of locations of the charge carrier can be calculated.
When analyzing a tunneling barrier in a one-dimensional system, the situation can be broken down into three regions: the region before the tunneling barrier, the tunneling barrier and the region behind the tunneling barrier. The probability of a charge carrier tunneling through the barrier is then described by the ratio of the absolute square of the wave function before and after the barrier. For a finite rectangular barrier and one charge carrier an analytical solution can easily be determined, as outlined below.
The situation becomes increasingly more complex, the more complex the potential landscape is and the more charge carriers are considered. Taking into account various effects that might be present in any given system, a myriad of tunneling models, that apply to specific situations and boundary conditions, have been developed.
In the following, an analytical solution to the rectangular tunneling barrier is derived to reveal some general observations with regards to charge carrier tunneling. More complex models that are often used within the field of molecular electronics will then be described to complete the picture. Specifically, the *Simmons model* and the *Gruverman model* will be given and their scope is briefly disussed. Lastly, a computational approach to deal with the complexity of a many electron system is presented. Namely short introductions to *density functional theory (DFT)* and the *non-equilibrium green function (NEGF)* approach that are used in combination within the TranSIESTA software package to calculate the electronic transfer properties from the chemical structure of molecules based on first principles, will be given.

Rectangular Barrier

A rectangular potential barrier can be described by:

$$V(x) = \begin{cases} V_0 & \text{for } x \in [-a, a] \\ 0 & \text{else} \end{cases} \tag{2.2.4}$$

This potential landscape can be divided into three regions I: before the barrier, II: within the barrier, and III: behind the barrier. The wave function within the three regions is then defined by:

$$\psi_I(x) = e^{jkx} + Re^{-jkx} \tag{2.2.5}$$

$$\psi_{II}(x) = \alpha e^{kx} + \beta e^{-kx} \tag{2.2.6}$$

$$\psi_{III}(x) = \frac{|\psi_{III}|}{|\psi_I|} e^{jkx} = Te^{jkx} \tag{2.2.7}$$

$$\tag{2.2.8}$$

Here, R is the *reflection coefficient* describing the ratio of the amplitude of the wave that gets reflected at the barrier, T is the transmission coefficient describing the ratio of the amplitude of the wave that gets transmitted into the barrier, α, β, A and B are parameters describing the wave propagation and have to be solved for. The wave function k is related to the energy of the charge carrier E via the dispersion relations:

$$k(E) = \begin{cases} \frac{\sqrt{2m^*(V_0-E)}}{\hbar} & \text{for } x \in [-a, a] \\ \frac{\sqrt{2m^*E}}{\hbar} & \text{else} \end{cases} \tag{2.2.9}$$

Here, $\hbar$ is the reduced Planck's quantum, V_0 is the barrier height, E the energy of the wave and m^* the effective carrier mass. The functions ψ_{I-III} have to be continuous and differentiable at the mutual boundaries of two adjacent regions. Therefore:

$$\psi_I(-a) = \psi_{II}(-a) \tag{2.2.10}$$

$$\psi_{II}(a) = \psi_{III}(a) \tag{2.2.11}$$

$$\frac{d}{dx}\psi_I(-a) = \frac{d}{dx}\psi_{II}(-a) \tag{2.2.12}$$

$$\frac{d}{dx}\psi_{II}(a) = \frac{d}{dx}\psi_{III}(a) \tag{2.2.13}$$

With these boundary conditions and using the identity $\sinh(a) = \frac{1}{2}(\exp(a) - \exp(-a))$ the tunneling probability $\tau(E)$ becomes:

$$\tau(E) = \frac{|\psi_{III}|^2}{|\psi_I|^2} = \left(1 + \frac{V_0^2}{4E(V_0 - E)} \sinh^2 \kappa(E) d\right)^{-1} \tag{2.2.14}$$

$$\text{with: } \kappa(E) = \frac{\sqrt{2m^*(V_0 - E)}}{\hbar} \tag{2.2.15}$$

This result exemplifies important characteristics of tunneling:

1. $\tau(E) > 0 \forall E$: There is tunneling at all energies. Most notably, charge carriers can tunnel through the barrier even if their associated energy is lower than that of the barrier.

2. $\tau(E) < 1 \forall E$: Even if the energy of a charge carrier is higher than that required to overcome the barrier, the probability of charge transport from one side to the other is not 1. This means that some charge carriers are reflected by the barrier, even if their energy is sufficient enough to overcome the barrier in a classical model.

3. The tunneling probability decreases exponentially with barrier thickness.

4. The tunneling probability is temperature-independent.

Realistic tunneling barriers are, however less ideal than the assumptions within this model. More complex models are hence needed to describe more complex system. [123]

2.2.2 WKB based models

If the situation of a metal-insulator-metal junction is considered, one approach to describe the net tunneling current density is to consider the tunneling probability $\tau(E)$ as well as the fermi-functions of the right electrode $f(E, E_{F,r})$ and the left electrode $f(E, E_{F,l})$. The net tunneling current density can then be calculated as the difference of tunneling from left to right ($L \rightarrow R$) and from right to left ($R \rightarrow L$):

$$J = J_{L\rightarrow R} - J_{R\rightarrow L} = \frac{4\pi mq}{h^3} \int_{E_{x,min}}^{E_{x,max}} \int_0^\infty \tau(E)[f(E, E_{F,l}) - f(E, E_{F,r})] dE_x dE_\perp \tag{2.2.16}$$

Here, m is the electron rest mass, q is the electronic charge, h is Planck's constant. E_x represents the total energy corresponding to the longitudinal momentum and $E_\perp$ represents the total energy corresponding to the perpendicular momentum. The terms *left* and *right* are arbitrarily chosen and interchangeable.
Using the *Wentzel–Kramers–Brillouin* (WKB) approximation of a slowly varying barrier, the tunneling probability $\tau(E)$ can be expressed as:

$$\tau(E) = e^{\frac{-4\pi d}{h}} \int_0^d \sqrt{2m^*(\phi - E)} dx \tag{2.2.17}$$

where m^* is the effective mass of the charge carrier in the barrier, d is the width of the barrier and ϕ is the barrier height.
Starting from these assumptions various models using additional assumptions about the shape of the barrier have been developed. Most notably *Simmons* derived a simple equation for tunneling through a barrier of trapezoidal shape at bias $V < \phi$:

$$J(V) = \frac{a}{d^2} \left[\left(\Phi - \frac{V}{2} \right) e^{-db\sqrt{\alpha(\Phi - \frac{V}{2})}} - \left(\Phi + \frac{V}{2} \right) e^{-db\sqrt{\alpha(\Phi + \frac{V}{2})}} \right] \tag{2.2.18}$$

Here, d is the tunneling distance (barrier thickness), V the applied voltage, Φ the barrier height, α the ideality factor and $a = \frac{e}{4\pi^2\hbar^2}$ as well as $b = 2\sqrt{\frac{2m}{\hbar^2}}$ with the reduced Planck's constant $\hbar$ and the electron rest mass m.[124] This can be further simplified to the *simplified Simmons Equation* $J = J_0 e^{-\beta d}$. J_0 is termed *charge injection current density*, β is called *tunneling attenuation factor* or *tunneling decay coefficient* and d is the thickness. This equation is particularily useful since d can be experimentally determined or varied (e.g., by increasing the number of repeating units in a molecule) and only two parameters β and J_0 are used to fit the data.
However, there is no theory for correlating molecular structure to experimental values of J_0 and β. In lack of a more developed theory, the Simmons equation has been adopted as quasi-standard for studying the charge tunneling across organic molecules. This is mainly due to that fact, that the reduction to the simplified Simmons equation $J = J_0 e^{-\beta d}$ reduces the modeling problem to the determination of just two parameters from experimental data and that these two parameters have proven to be useful in comparing contacting schemes

for ensemble molecular junctions. In particular, these values are often determined by simply measuring the experimental current density at a chosen evaluation bias for SAMs of varying alkyl chain length (in nC: number of carbons) and then fitting the above exponential equation to the $\beta(nC)$ data set. It has been shown, that the values for β determined this way, are in the range of $0.5 - 1.5\ nC^{-1}$ for a wide range of contacting schemes - including single molecule measurements, alkyl-thiols on gold or silver measured with both eutectic indium gallium [100, 125, 126] and mercury drop electrode [120, 127–129] It is important to note, that using the Simmons model to extract physically meaningful values from current voltage spectroscopy of SAMs is under debate. [6, 119, 130, 131] The model was developed for single molecules and may be inappropriate to model charge transport across monolayers, especially for those comprised of organic SAMs that have more complicated constituents than a simple alkyl chain. Nevertheless, more complex tunneling models can often be reduced to the form of the simplified Simmons equation with assumptions that are valid in the low voltage regime, effectively hiding more complex fitting parameters within J_0 and β. [131] The large number previously reported values for J_0 and β of specific molecule classes, together with the fact, that SAMs that were characterized by a plethora of techniques seem to exhibit very similar values of the experimentally determined values of β, justifies the usage of the simplified Simmons model as a tool to verify successful monolayer formation as well as to verify the feasibility of novel contacting schemes. This is particularly the case for alkylphosphonic acids.
Note that tunneling currents are often plotted on a `log10` scale in a semi-logarithmic plot before a linear regression is performed to yield β. To result in the same β as in the simplified Simmons equations, the data has therefore be fitted to $J = J_0 10^{-\beta \cdot d/2.303}$. Since $\log_{10}(e) = 0.434$ and $1/\log e = 2.303$, the slope determined from `log10` scale plots has to be multiplied by 2.303 to yield the correct β value.
In this work, the Simmons tunneling model has been implemented as model with the python package lmfit to fit and evaluate measurement data. The code is available at `https://github.com/JuMaD/TM-py` and is subject to change.

Asymmetric Barrier Shape

Brinkman, Dynes, and Rowell (BDR) have used the WKB approximation to develop a model describing tunneling through an asymmetric barrier. [132] *Asymmetric* refers to the situation in which the Fermi energies at both sides of the barrier differ before establishing equilibrium, which leads to a built-in potential. In particular that reflects the situation where both electrodes are made from materials exhibiting different work functions, ultimately leading to a trapezoidal barrier. Their model has been refined with the application of ferroelectric tunneling barriers in mind by *Gruverman et al.*[133], yielding the following expression for the direct (non-resonant) tunneling current I_{DT}:

$$I_{DT} = S \cdot C \cdot \frac{\exp\left(\alpha\left[(\phi_2 - \frac{eV}{2})^{\frac{3}{2}} - (\phi_1 + \frac{eV}{2})^{\frac{3}{2}}\right]\right)}{\alpha^2\left((\phi_2 - \frac{eV}{2})^{\frac{1}{2}} - (\phi_1 + \frac{eV}{2})^{\frac{1}{2}}\right)^2} \cdot \sinh\left(\frac{3eV}{4}\alpha\left((\phi_2 - \frac{eV}{2})^{\frac{1}{2}} - (\phi_1 + \frac{eV}{2})^{\frac{1}{2}}\right)\right) \tag{2.2.19}$$

With $C = -(32\pi e m^*)/(9h^3)$, $\alpha = (8\pi d\sqrt{2m^*})/(3h(\phi_1 + eV - \phi_2))$, where S, d, h, e, m^* are the area of the contact interface, the barrier thickness, Planck's constant, the elementary charge, and the effective carrier mass within the barrier, respectively, and ϕ_1 and ϕ_2 refer to the barrier heights on both sides of the barrier. The equation is only valid in the small voltage-regime ($eV/2 < \phi_i, \forall i$) and for comparatively thick barriers ($d \cdot ((2m/\hbar)^2 \cdot \phi)^{1/2} >> 1$)[133] Since the later assumption can not be satisfied by typical monolayer thicknesses

≈1-4 nm, the anchoring layer oxide and the self-assembled monolayer were considered as **one** effective barrier when this model was employed.

2.2.3 Embedded Dipoles

Self-assembled monolayers featuring dipolar units and the proposed charge transfer through them have been subject to recent studies. The introduction of dipole moments to SAMs has so far been most frequently done by the attachment of dipolar groups as ambient facing moieties. In contrast to that, molecules with an *embedded dipole* incorporate polar groups into the backbone of the SAM forming molecule. This comes with the advantage of decoupling the tuning of the electrostatic properties of a SAM from its ambient facing chemical identity. SAMs with an embedded dipole were found to alter workfunctions of substrates [134], charge transfer through a SAM [135] as well as transition dipole moments [136].

Tailoring the work function by introduction of a SAMs with a dipolar component has been widely employed for organic electronic devices. [37] Work function changes up to 0.9 eV have been experimentally verified. Work function and interfacial energy modifications utilizing SAMs have been demonstrated for metal surfaces [137], organic/metal and organic/organic interfaces [138] as well as oxide surfaces [139].

The Helmholtz Equation relates the average dipole moment in z-direction μ_z to a work function shift $\Delta\phi$. For a SAM with the surface density n it reads:

$$\Delta\phi = \frac{n\mu_z}{\epsilon_r \epsilon_0} \tag{2.2.20}$$

Here, ϵ_0 is the vacuum permittivity and ϵ_r the relative permittivity of the SAM.

Studies of SAMs with an *embedded* dipolar unit, so far focused on fixed orientation of the dipole per monolayer and varied the dipole direction as well as magnitude via varying the dipole inducing substituents in the aromatic unit of the molecule. The dipole induced changes in work function of surface [135] and conductance of SAMs [136] have at least in part been attributed to collective electrostatic effects of aligned dipoles affecting the delocalization of the frontier states of the individual molecules. [140] The orientations of the fixed dipoles in these monolayers can not be altered by an external stimulus and are assumed to be almost perfectly aligned.

The concept pursued in this work builds on embedded dipolar units, but goes beyond short, symmetric molecules as studied in the aforementioned work. The functionality of the envisioned ensemble molecular devices is ingrained in the chemical structure of the SAM constituents. The embedded dipolar unit is linked via a conformationally flexible linker to the substrate. This allows the dipolar unit to be reversibly reoriented in an electrical field, which potentially allows tuning the average dipole moment perpendicular to the substrate. Due to this flexible linker, the dipole SAM orientation is assumed to follow a distribution rather than being perfectly aligned. Further, the envisioned molecules are designed to feature a structural asymmetry that induces an asymmetry within a molecular junction and may result in different built-in voltage drops across such a junction. These two features potentially result in SAMs of this molecule acting as electrically switchable tunnel barriers. To use a simplified, descriptive picture: The goal is not to exploit the change in delocalization of the frontier states, but rather to provide a tunneling barrier with one part of the molecule and to utilize the work function altering capacity of embedded dipoles on one side of this tunneling barrier to flex-

ibly tune the height of the barrier on that side. This should ultimately allow tuning of the tunneling barrier shape.

2.3 Computational Methods

To evaluate whether experimentally determined current density - voltage traces fit to existing transfer models, this work utilizes different models on these three scales:

1. Single molecule: TranSIESTA approach
2. Molecular ensemble: Molecular dynamics simulations
3. Monolayer device including the oxide layer: Parallel plate, double-layer capacitor model combined with the Gruverman tunneling model

For the first two, computational methods are deployed and an introduction to the general concept behind them are outlined below. For calculations at the device level, the device is modeled as double-layer capacitor to calculate the voltage across the monolayer. Then, the Gruverman model that is described above is used to calculate the transfer current density. Details of this model are given in Chapter 7.

2.3.1 Density Functional Theory & TranSIESTA

TranSIESTA is both an *ab initio* method and a tool to calculate the electronic structure and forces acting on the atoms of multi-atomic systems that are connected to semi-infinite electrodes. It considers the influence an applied voltage bias and is also used to calculate electronic transport through molecules. TranSIESTA is built on SIESTA (**S**panish **I**nitiative for **E**lectronic **S**imulations of **T**housands of **A**toms), a method to perform efficient electronic structure calculations of molecules and solids based on density functional theory (DFT).[141] DFT is based on the theorems:

1. The ground-state properties of a many-electron system are determined by an electron density that depends only on three spatial coordinates.
2. The energy functional for this system is minimized by the ground-state electron density.
3. The many-body problem of interacting electrons in an external potential can be reduced to a problem of non-interacting electrons moving in an effective potential.

The latter effective potential typically includes the external potential, the effects of Coulomb interactions as well as exchange and correlation interactions.

An electronic state in an N-electron system can generally be described by the wavefunction $\Psi(\vec{r_1}, .., \vec{r_N})$ and satisfies the many-electron time-independent Schrödinger equation with the Hamiltonian $\hat{H} = [\hat{T} + \hat{V} + \hat{U}]$, where $\hat{T}, \hat{V}, \hat{U}$ are the kinetic energy, the potential energy and the electron-electron interaction energy, respectively, and $\vec{r_i}$ are the location vectors to all of the electrons within the system. The Schrödinger equation then reads

$$\hat{H}\Psi = [\hat{T} + \hat{V} + \hat{U}]\Psi = E\Psi \tag{2.3.1}$$

This many particle system is not separable into a simpler equation, mostly due to the fact that $\hat{U}$ includes the interaction between all electrons. Approximating the solution of this differential equation requires specialized methods - such as the Hartree-Fock method - which are connected with a large computational effort that increases with the number of electrons to be considered. It is hence virtually impossible to calculate these solutions for large, complex systems such as self-assembled monolayers.
Density functional theory (DFT) maps this multi-body problem to a single-body one by introducing the electron density $n(\vec{r})$ as a function of the wave function. Here $\vec{r}$ points at the location in space the electron density is calculated for. Since functions of functions are called *functionals* this method is called density *functional* theory. The introduction of this functional ultimately transforms one equation for many, interacting electrons into a system of many equations for one electron each. Introducing the functional $n(\vec{r})$ to equation 2.3.1 results in the so called *Kohn-Sham equations* that describe this auxiliary non-interacting system:

$$\left[-\frac{\hbar^2}{2m}\nabla^2 + V(\vec{r}) + \int \frac{n(\vec{r}')}{|\vec{r}-\vec{r}'|}d^3r' + V_{XC}[n(\vec{r})]\right]\phi_i(\vec{r}) = \epsilon_i\phi_i(\vec{r}) \tag{2.3.2}$$

Here, $i \in [0, N]$, $\hbar$ is the reduced Planck's quantum, m the electron rest mass, the first term in brackets is the kinetic energy, the second term is the external potential, the third term describes the electron-electron Coulomb repulsion and the last term corresponds to the exchange-correlation potential including all many-body interactions. Note that this equation has to be solved for each electron within the system and that i in the equation stands for the i-th electron. Solving these equations yields the orbitals ϕ_i which in turn make up the electron density:

$$n(\vec{r}) = \sum_{i=1}^{N} |\phi_i(\vec{r})|^2 \tag{2.3.3}$$

Since equations 2.3.3 and equations 2.3.2 are interdependent, the Kohn-Sham equations have to be solved iteratively after an initial well-educated guess for $n(\vec{r})$. Due to this iterative nature of the calculation, the result is always an approximation. [142]
Several expansions to this general concept exist. One of them, the so called *generalized gradient approximation* (GGA), is used to account not only for the electron density, but also its derivatives with respect to the location. To improve the accuracy of the solution, hybrid methods are applied. A common hybrid method, also used for calculations presented in this work, is called B3LYP. It combines GGA (a DFT method) with the Hartee-Fock method (a method to solve the Schroedinger Equation directly) to get more accurate solutions. [142, 143]

System under Bias

When adding electrodes and an external bias to the system under study, a constant perturbation is added to the right side of the Schrödinger equation 2.3.1 and the system is in non-equilibrium. This makes another expansion of the formalism necessary. The so called non-equilibrium Green's function (NEGF) formalism, which also uses a functional to get around the computational complexity of the many interactions, is typically used to deal with this perturbation.

TranSIESTA combines several of the above mentioned methods and more to yield high accuracy in transfer calculations while maintaining reasonable computational cost.[144–147] A more detailed discussion of

the NEGF formalism as well as the TranSIESTA formalism is beyond the scope of this work. The interested reader is referred to [148, 149] for more details on TranSIESTA and to [142] for a primer on DFT in general.

2.3.2 Molecular Dynamics

Molecular dynamics (MD) refers to simulations in molecular modeling in which the interactions between atoms and molecules as well as their motion in space are iteratively calculated. Since the computational effort to apply quantum mechanical methods for molecular systems, that typically consist of a vast number of atoms, is too large to yield results within reasonable time scales, MD simulations rely on numerical methods to approximate solutions . Most notably, *force fields* are used to describe the forces that act on each atom within the simulation volume.

The general procedure for MD simulations is as dipole-induced:
First, a volume element is populated with the atoms and molecules to study. Then, for each atom the forces acting on each atom due to its neighbors are calculated and the particles are moved in space according to these forces in very small time steps. After few iterations, the sample volume reaches thermal equilibrium. MD simulations are often carried out under periodic boundary conditions: each atom leaving the simulated volume on one side re-appears on the opposide side and all interactions take place across these boundaries as well. To this end, identical copies of the simulated volume are placed next to each other.
Force fields are a computational method to parameterize the potential energy landscape. When a specific force field is referred to, both the functional form of the force field as well as a specific (defined) parameter set are meant. Force fields often contain terms for contributions to the potential energy mediated by chemical bonds as well as terms for contributions that are not mediated by chemical bonds. A force field and its parameters are chosen such that they can reproduce certain aspects of the molecular system as accurately as possible. Force fields offer the advantage of modeling relatively large systems in a computational cheap way. The physical accuracy of the result from the simulation however crucially depends on how well the chosen parameter set fits the system under investigation. It is important to note that the initial description of a system will always be inaccurate to some degree and long MD simulations hence suffer from cumulative errors in numerical integration. [150–152]

MD simulations in this work have been carried out by Falk May (Merck KGaA, Darmstadt), making use of the GROMACS package. They have been performed for SAMs of the molecules QM15 and QM32. As a force field, a version of *Optimized Potential for Liquid Simulation* (OPLS) with an additional torsion potential was used. The atomic charges on the phosphonate group of the molecules was set to zero and the phosphonate atoms were replaced by H. The molecules were optimized by a variant of B3LYP to confirm that the employed force field reproduces the molecular dipole vectors correctly. The SAM was constructed within the simulation volume by placing 92 molecules in it, constraining the bottom phosphonate atoms in the x-y plane and calculating a starting point using the *packmol* package. [153] The SAM was then equilibrated for 20 ns using an isothermal-isobaric (NPT) simulation while constraining the phosphonate oxygens in the x-y plane, resulting in a density of n = 3.6 molecules nm^{-2}. In an NPT simulation the system is isolated from change in amount of substance (N), pressure (P) and temperature (T). The NPT simulation in this work was monitored using the total energy and surface density, which converged to within 1%. In order to prevent the molecules from aligning completely with the electrical field when it was applied, the three phosphonate oxygens as well as the top carbon were constrained

in their respective z positions during all following simulations. More details of the computational details of this model as well as simulations performed to check its validity are available in the supporting information of [154].

3 Characterization Methods

In this chapter, the characterization methods used in this work will be described. To image the samples, a variety of methods was used, namely atomic force microscopy (AFM), light microscopy, scanning electron microscopy (SEM) and transmission electron microscopy (TEM). Surface composition and thicknesses were probed via several spectrocopic methods, such as variable angle spectroscopic ellipsometry (VASE), x-ray photoelectron spectroscopy (XPS), fourier transform infrared spectroscopy (FTIR) and near-edge x-ray absorption spectroscopy (NEXAFS). Electrical characterization was carried out via current-voltage spectroscopy in a vacuum cryo probe-station.

3.1 Imaging Methods

3.1.1 Atomic Force Microscopy

To capture and analyze the topography of a sample down to nanometer resolution, *atomic force microscopy* (AFM) was used. For this purpose, a sharp tip at the end of a few micrometer long cantilever is brought very close to the surface. The cantilever is then put into oscillation near its resonant frequency. The interactions of the tip with the sample surface result in a change of amplitude and phase of the oscillation. This shift is measured as a deflection of a laser that is reflected from the cantilever to a photo detector. Using a feedback loop either frequency or amplitude are controlled to a fixed value when the sample is scanned below the cantilever. [155, 156] There are three modes of operations, most commonly used to capture the topography of a sample, namely:

1. **non-contact mode**: in which the tip never touches the surface and only short-range interactions of the atoms of the tip and the surface cause a the shift in phase and amplitude. To image the topography while avoiding destructive mechanical interactions between tip and surface, the lateral tip-surface separation is held at a fixed value.

2. **contact mode**: in which the tip is in soft contact with the surface and the cantilever is directly deflected by changes in height of the substrate. This significantly improves the resolution in z-direction. Typically, the force that the tip exerts on the surface is kept constant. Destructive interactions between tip and surface may occur.

3. **tapping mode**: in which the tip touches the surface with a low force at the end of each oscillation cycle. This intermittent method combines the advantages of non-contact and contact mode, resulting in a high resolution in z-direction with minimal mechanical interaction with the surface. [156]

Since the tapping mode is particularly useful to determine small roughnesses of mechanically "soft" surfaces, it is commonly deployed to determine the surface roughness of SAMs. If the surface roughness does not significantly vary between a measurement before and one after monolayer formation and the presence of molecules after

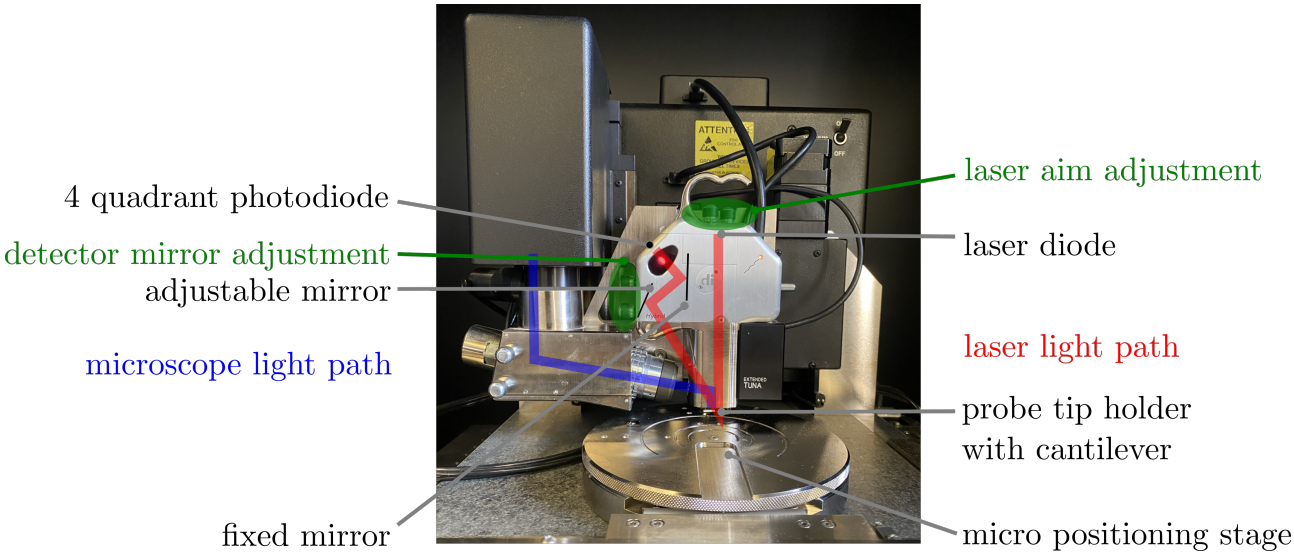

Figure 3.1.1 Atomic Force Microscopy - general working principle illustrated within a picture of the AFM system used in this work. Blue lines indicate the path light takes to the optical microscope that is used to navigate on the sample. Red lines indicate the laser light path. Starting from the light source (laser diode) the beam is guided via a two-mirror system to the tip of the cantilever on the probe holder. Then, light gets reflected and is steered via a two mirror system to the 4 quadrant detector, which then detects the amplitude and the phase of incoming light. When tips are exchanged, the laser has to be re-aligned using the two laser aim adjustment knobs to hit the tip. Then, the detection mirror adjustment knobs are used to correct for tilt in the tip orientation so that the beam hits the middle of the 4 quadrant detector again. Adjusted from [157]

monolayer formation can be confirmed through other methods - e.g., contact angle, XPS or FTIR, a dense layer of molecules covering the substrate can be assumed. In this work, unless specifically otherwise stated, all AFM topographies were taken using a *Bruker Nano Dimension V* AFM in tapping mode. AFM tips fabricated from diamond like carbon (DLC) of type TAP190DLC from *Budget Sensor* were used for all images. The experimental setup including a sketch of the AFM working principle is shown in Figure 3.1.1. Recorded topographies were analyzed using Bruker's Nanoscope Analysis software. The *plane fit function* was used to account for tilt within the image and level the images in x and y direction. The roughness of samples was analyzed using the root mean square roughness R_q value which is defined as:

$$R_q = \sqrt{\frac{1}{N}\sum_{i=1}^{N} y_i^2} \tag{3.1.1}$$

where N is the number of measurement points recorded within the area to be analyzed and y_i is the deviation of a measured height from the average within this area. Areas with exceptionally high deviation from the average height - i.e., potential dust particles on the surface - were treated as outliers and omitted from the determination of R_q by choosing a detection window that did not include those outliers.

AFM scratching

One method to determine monolayer thicknesses is AFM scratching. The general idea of AFM scratching is to use an AFM in contact mode with a drive amplitude that is effectively pressing the tip on the surface, scratching away any potential layer that can not withstand the force that acts on it. The region on the sample is then imaged

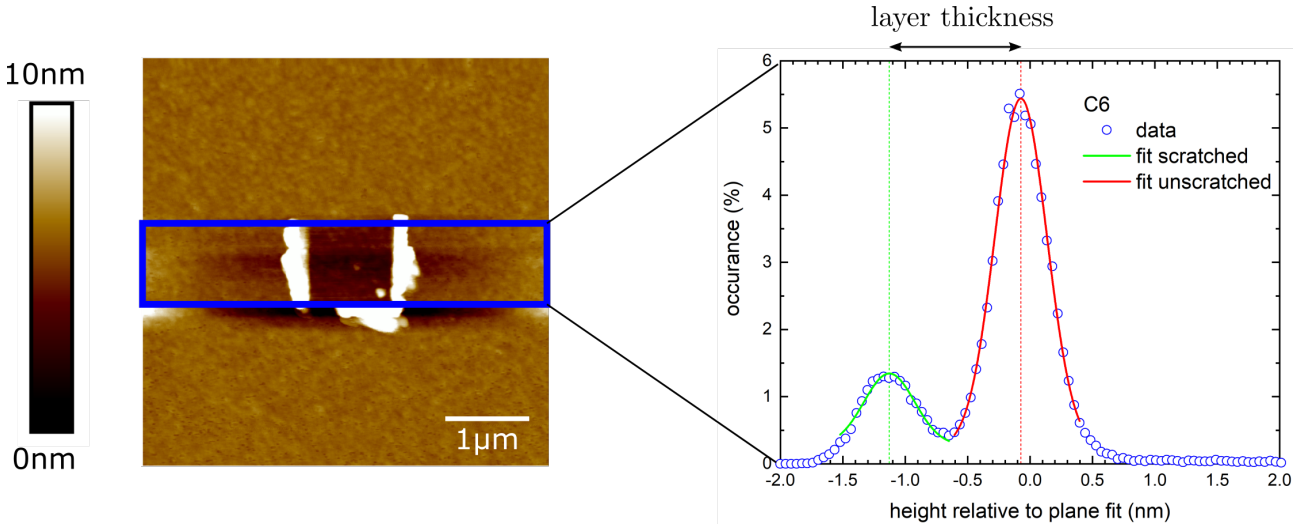

Figure 3.1.2 AFM scratching method - Topography on the left is taken in tapping mode after the smaller, quadratic area in the middle has been exposed to AFM in contact mode using a deflection set-point of 212 mV. A histogram of the data within the blue rectangle is shown on the right. *Open circles* indicate data points whereas *red* and *green* lines represent Gaussian fits of the two observable peaks. The difference in peak positions of those two fits is then reported as layer thickness. Scales of topography and histogram are shifted since for the topography a (color) scale starting at 0 with the lowest value is the most useful whereas in the histogram a scale relative to the plane fit height is useful to determine whether the plane fit and the average height of the monolayer coincide.

by AFM in tapping mode for a larger area, revealing the pristine as well as the scratched-away surface. After plane-fitting, a histogram of the height distribution of the region that has been scratched away as well as the laterally adjacent areas to the left and right is analyzed. Due to statistical variations the two dominant heights 'scratched away' and 'pristine' follow a Gaussian distribution. The maximum values of these distributions were fit using OriginLabs Origin's `Quick Fit -> Gaussian Fit` method and the distance between both maxima was reported as layer thickness. An example for the area typically used to determine the histogram as well as the Gaussian fits to the histogram are depicted in Figure 3.1.2. To ensure the substrate is not scratched in the scratching process, the maximum drive voltage of the cantilever before the substrate is scratched is determined separately. In general, AFM scratching can only be performed if the driving voltage that damages the substrate is well below the voltage, that allows scratching of the layer on top. Scratching experiments with DLC tips on bare TiN surfaces to determine the maximum drive voltage for the AFM scratching experiments were performed by Gagandeep Singh. The maximum driving voltage that did not damage the substrate was found to be 212 mV. All AFM scratching of SAMs on TiN was therafter performed at this voltage.

3.1.2 Light Microscopy

To magnify objects with dimensions in the microscale, optical microscopes are often used. They achieve a magnification of an object through a relay lens system. The object to be imaged is placed in focus of the objective lens that creates a magnified image of the object. The eyepiece is then focused on the resulting image, magnifying it and relaying it to the eye of the observer or a camera. In modern compound microscopes, objective and eyepiece consist of multiple lenses in order to correct for imperfections in image formation, as for instance chromatic aberration, spherical aberration and field curvature. [158] To image the surface on a strongly absorbing surface, the sample is illuminated from the top. Illumination path and imaging path often overlap inside a microscope.

The microscopic method that includes all light reflected from the surface is called *bright-field microscopy*. Contrast in bright-field images comes from differences in reflection and absorption across the sample. Contrary to that, in *dark-field microscopy*, contrast is due to scattering. The unscattered light from the sample is excluded and only the scattered light is imaged. This is achieved by illuminating the sample with light that is not collected by the objective. Due to the dark background, this method can also be used to detect the presence of particles below the diffraction limit. In the dark-field image, light scattered from smaller particles can appear as a larger dot or disc in the image. [159]
Bright-field and dark-field microscopy are complementary methods with different strengths and weaknesses. What is apparent in a bright-field image may not be visible in dark-field and vice versa. In this work, bright-field microscopy was used to get a general overview of microscopic structures. Dark-field microscopy was used to judge the effectiveness of cleaning processes and to have a quick method of determining whether small particles that could induce shorts are present on the bottom electrode before dip-coating.

3.1.3 Transmission Electron Microscopy

The resolution of illuminated, diffraction-limited imaging systems is governed by the *Abbe diffraction limit*. It describes the minimum distance d_{min} two distinct features must have to still be distinguishable after optical imaging. It is given by:

$$d_{min} = \frac{\lambda}{2n \sin \Theta} \tag{3.1.2}$$

Where λ is the wavelength of light, n is the refractive index of the medium, in which light is traveling to the objective and Θ is the maximum *half-angle* of the cone of light that can enter or exit the objective. Refractive index and half-angle are often described together as the *numerical aperture* NA = $n \sin \Theta$ of the optical system. Hence, the resolution of an imaging system can be improved by either increasing the numerical aperture of the optical system or by reducing the wavelength. An increase in NA is for instance typically achieved by immersing specimen and objective in a transparent oil of high refractive index. [158, 159]
As discovered by *DeBroglie*, electrons have an associated wavelength that is much smaller than that of ultra-violet light. At the same time, this associated wavelength means that similarly as light, electrons can be diffracted and the general concept of magnification through diffraction, that a light microscope utilizes can be transferred to electrons. Using electrons instead of photons drastically improves the resolution that can be achieved with a microscope. Taking relativistic effects into account, the associated wavelength of an electron is

$$\lambda_e = \frac{h}{\sqrt{2m_e E(1 + \frac{E}{2m_e c^2})}} \tag{3.1.3}$$

where h is Planck's constant, c is the speed of light, m_e is the rest mass of the electron and E is its kinetic energy. Typical acceleration voltages of modern TEMs are between 100kV and 300kV and therefore result in electron wavelengths between 3.7 pm and 2 pm. Compared to the minimum photon wavelengths typically used in light microscopy, this results in an increase in resolution by approximately five orders of magnitude.
In a *transmission* electron microscope, *transmitted* electrons are imaged. Since electrons get scattered easily the sample to be imaged has to be very thin - often below 100 nm. To image a cross-section of a vertical stack of layers, a focused beam of gallium ions is typically used to mill through the layers and cut and lift out a thin slab, often referred to as TEM *lamella*. This thin slab is transferred to a TEM window that acts as a larger scale

physical support of the lamella while not adding to the scattering cross-section. The slab is then often further thinned with the ion beam until it becomes transparent to electrons.
The TEM microscope itself operates on a general principle that is very similar to that of an optical transmission microscope: An electromagnetic field is generated, condensed to illuminate the sample in a homogeneous way and after transmission, absorption and refraction through the sample again focused to an image recording system. In case of a TEM, the field is generated by an emission source that is connected to a high voltage, emitting electrons by thermionic or field emission. The condenser and objective lens systems are realized using electrical and magnetical fields.
The objective lens focuses elastically scattered electrons that leave the specimen under the same angle on the same point. Using an aperture, scattered electrons can be excluded from the image and only non-scattered end up forming the image.
The elastic, incoherent scattering of electrons is goverened by *Rutherford scattering*. It describes the cross section for elastic scattering as a function of atomic number Z of the scattering atom. Since the cross section increases with increasing Z and the number of scattering events increases with the thickness t of the specimen, the intensity at the detector decreases with increasing t and Z. Hence, contrast in TEM imaging is achieved by atomic number and object thickness. Consequently, it is often referred to as *mass thickness contrast*. This mechanism is illustrated in Figure 3.1.3.

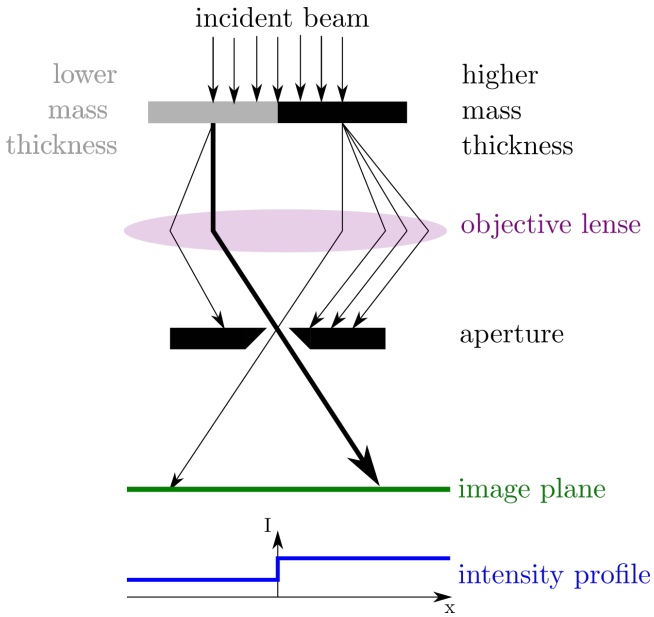

Figure 3.1.3 Mass thickness contrast in a transmission electron microscopy image. Both thicker and higher-Z areas of the specimen (right part of the image) scatter more electrons off axis than thinner or lower-Z ones (left part of the image). Consequently, fewer electrons from these areas pass the aperture and reach the imaging plane making these areas appear darker in the final image. Adapted from [160]

In the case of imaging TEM lamellas of amorphous layers, all layers are of the same thickness. This allows for a simple distinction of layers with a high contrast in atomic number. Table 3.1 lists the atomic numbers of all atoms present in the layers imaged via TEM in this work. Since the atomic numbers of atoms present in the organic layer are much lower than that of the metals used as contacts, a high contrast between those layers is to be expected. In this work, TEM imaging of devices with Pb top contact was performed by *Samurai Semiconductor Services*, Japan. There, a Hitachi High-Tech HD-2300A with an acceleration voltage of 200 kV was used. Lamellas were prepared at a thickness of 80 nm. Images of crossections of a device with Ti

Table 3.1 Atomic numbers of atoms predominantly present in the stacks imaged via TEM in this work.

Atom	Atomic Number
Ag	47
Al	13
Au	79
C	6
F	9
H	1
N	7
O	8
P	15
Pb	82
Ti	22

top contact were taken by Oscar Recalde, *Technical University Darmstadt*. There, a JEOL ARM200F with an acceleration voltage of 200 kV was used. Lamellas were prepared at a thickness of 60 nm using a JEOL JIB-4600F dual-beam FIB.

3.1.4 Scanning Electron Beam Microscopy (SEM)

Scanning electron beam microscopy is a surface characterization method that does not require thin samples. For SEM imaging, the specimen is irradiated with a focused electron beam and the interactions of the impinging electrons with the sample surface are then analyzed. The three most prominent interactions of surface and electrons are:

1. **Backscattering of primary electrons**. When high energy electrons hit a surface, some of them are elastically back-scattered by atoms at the specimen surface. Similarly to TEM imaging, contrast is achieved by chemical composition of the surface via the atomic number of surface atoms.

2. **Ejection of secondary electrons**. Beam electrons eject secondary electrons from conduction or valence bands of the atoms at the surface of the specimen. Since those electrons are typically of low energy - orders of magnitude lower than that of the beam electrons, applying some sort of a filter to collect only low energy electrons is necessary to achieve a good image quality. This is the most common imaging method for SEM.

3. **X-ray radiation**. Some of the secondary electrons generated by incident x-ray radiation stem from lower energy levels within the surface atoms. When the incident electron beam passes through the sample creating secondary electrons, it leaves multiple of the sample's atoms with vacancies in the electron shells where the secondary electrons used to be. If these vacancies are in inner shells, the atoms are not in a stable state. To stabilize the atoms, electrons from outer shells drop into the inner shells. To dissipate the excess energy the outer shell electron has with respect to the lower vacancy state x-rays are emitted. These x-rays can subsequently be measured and analyzed.

Since these interactions occur within the interaction volume of electron beam and surface and its diameter is limited, the beam is scanned over a fixed area of the surface and measurement results are stitched to form an image of the surface. SEM does not require an optical system to make up an image and is thus not limited by the diffraction limit that applies to optical microscopy and TEM. It is rather only limited by the smallest spot diameter that can be achieved when focussing the electron beam. [161]

SEM imaging shown in this work was performed with help from Sabrina Artmeier at the *Zeiss NVision 40 Dual Beam* SEM system at the *Zentrum für Nanotechnology und Nanomaterialien* in Garching. There, the in-lens detector, located inside the beam column, was used to detect low-energy back-scattered secondary electrons originating from the interaction volume at the top of the sample surface.

3.2 Variable Angle Spectroscopic Ellipsometry

Variable angle spectroscopic ellipsometery (VASE) was used to determine the thickness of various inorganic and organic layers. Ellipsometry measures the change of polarization of light upon reflection on a surface and compares it to a model based on the Fresnel equations.
In an ellipsometer, light emitted by a light source gets linearly polarized by a polarizer. It is then focused on the sample. After reflection, the light passes a rotating second polarizer and then reaches a detector. This way, the complex ratio ρ of the reflection coefficients r for p- and s-polarized light can be measured. Since any polarization state can be described by the combination of these two orthogonal linear polarizations, any change in polarization can be measured this way. The combination of two orthogonal linear polarizations with random phase and amplitude results in *elliptical* polarization. This is what gave *ellipsometry* its name. [162]
The working principle is illustrated in Figure 3.2.1.
After measurement, ρ is commonly expressed in terms of the ellipsometric quantities Ψ and Δ, that are defined

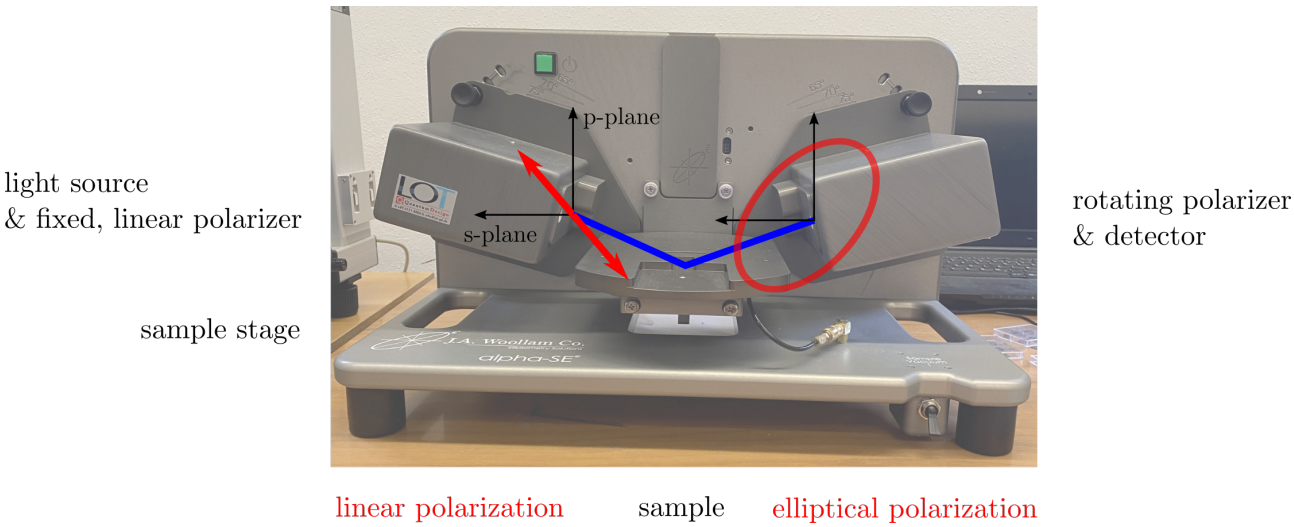

Figure 3.2.1 Working principle of ellipsometry as an overlay over the Alpha SE system deployed in this work. Red lines indicate polarization direction, blue light indicates light path. Light is linearly polarized behind the light source. The orthogonal components of light are in phase. When the light interacts with the sample, s- and p-polarized light are reflected differently. This results in a random phase relationship between s- and p-components and hence in elliptical polarization that can be measured by a rotating, linear polarizer. Since the reflection coefficents for s- and p-polarized light depend on layer thickness, optical constants and layer sequence, using an optical model enables non-contact measurement of these entities. Adapted from [163].

by the following equation:

$$\rho = \frac{r_p}{r_s} = \tan(\Psi)e^{j\Delta} \tag{3.2.1}$$

The reflection coefficient r is the ratio of the reflected wave's electric field complex amplitude and that of the incident wave. Likewise, the transmission coefficient t is the ratio of the transmitted wave's electric field complex amplitude and that of the incident wave. Ψ accounts for the amplitude ratio of incident and reflected wave whereas Δ is related to the difference in phase between s- and p-polarization. Only in an ideal bulk material, ρ can be directly inverted to yield the optical constants. For any multi-layered system, the measured data has to be compared to a model. The model considers the optical constants, thicknesses and layer sequence of the sample. Parameters of that model are then iteratively varied and the resulting ellipsometric quantities are calculated using the Fresnel equations until the calculated values sufficiently match with the experimental data. This optimization problem is often solved using regression. However, using regression on all parameters in the model quickly becomes too computationally expensive or can fail to find the global minimum. Therefore fixing multiple parameters to known or physically reasonable values before regression is important. Sometimes, a grid-search is applied to find the global minimum. In a grid search a set of values for each parameters is used to define a full-factorial grid as starting points for multiple regressions. Minimum errors of all starting points are then compared to yield their global minimum.

For each iteration of the regression, Ψ and Δ have to be calculated using the Fresnel equations. They describe the transmission and reflection of light incident on an interface between different media, depending on its polarization. A plane wave that is incident at an angle of θ_i is transmitted at an angle θ_t and reflected at an angle θ_r. In the case of an ideal dielectric material, with an extinction coefficient of $\kappa = 0$, the Fresnel equations relate reflection r and transmission coefficents t for s- and p-polarized light to the refractive indices n of both materials that the wave propagates in and the angles θ_i and θ_t:

$$r_s = \frac{n_1 \cos(\theta_i) - n_2 \cos(\theta_t)}{n_1 \cos(\theta_i) + n_2 \cos(\theta_t)} \tag{3.2.2}$$

$$t_s = \frac{2n_1 \cos(\theta_i)}{n_1 \cos(\theta_i) + n_2 \cos(\theta_t)} \tag{3.2.3}$$

$$r_p = \frac{n_2 \cos(\theta_i) - n_1 \cos(\theta_t)}{n_2 \cos(\theta_i) + n_1 \cos(\theta_t)} \tag{3.2.4}$$

$$t_p = \frac{2n_1 \cos\theta_i}{n_2 \cos\theta_i + n_1 \cos\theta_t} \tag{3.2.5}$$

If light is incident on two or more parallel interfaces, multiple transmissions and reflections occur. The light reflected from a sample with multiple parallel interfaces is therefore always a combination of multiple, interfering reflections and transmissions. Since the thickness of each layer can be expressed in terms of the phase change it induces, the phase-dependent interference of light connects the measured ellipsometric quantities to the layer thicknesses. The measured quantities r_s and r_p are calculated from a superposition of many internal reflections. These multiple reflections are the reason why the measured quantities are not directly invertable and why regression quickly becomes time consuming.

Alternatively to fixing as many parameters as possible to physically sound values, parameter sparse models can be used to model layers with unknown optical constants or thicknesses. One such simple approximation of the

variation of the refractive index of a material with wavelength is given by the Cauchy equation and represented as *Cauchy layer* within the data analysis software. It is typically given as:

$$n = A + \frac{B}{\lambda^2} + \frac{C}{\lambda^4} \tag{3.2.6}$$

Here, $A.B$ and C are parameters of the model, whereas λ is the wavelength of light. The Cauchy approximation does not necessary fulfill the Kramers-Kronig relation that connects refractive index n and extinction coefficient κ via a Hilbert transformation. In practice this means that after fitting of A, B and C, both optical constants have to be checked for physical consistency.

As outlined above, optical models of ellipsometry depend on a multitude of parameters. It is therefore beneficial for the physical accuracy of the model to measure as many quantities as possible. This is typically done by varying the angle and wavelength at which the ellipsometric quantities are recorded, effectively overdefining the optical model.

In this work, all VASE measurements were performed using a *J.A. Woollam* Alpha SE system, that utilizes wavelengths from 300 to 900 nm and allows measurements at three angles of incidence (65°, 70° and 75°). Data analysis was performed using the CompleteEase software package, also supplied by J.A. Woollam Alpha. Whenever possible, available text book data for optical constants was used to model layers. Readily available data was used directly for Si and SiO_2 [164]. For TiN layers, the Lorentz oscillator model within CompleteEase was used as a starting point, transformed into a B-Spline model and then fit to TiN reference samples [165]. Organic layers were modeled as a Cauchy layer with $C = 0$ and $k = 0$. This is an idealized assumption of no absorption within the layer that is valid for large band-gap materials or ultra-thin layers with neglectable absorption, such as self-assembled monolayers. [163]. For aluminum samples, available spectroscopic data [166] was used as a starting point for a Cauchy layer where A and B were fitted using a multi-sample analysis. This means that while the thicknesses of several substrates were allowed to vary independently, the values for A and B were kept constant across all samples, but were at the same time fit to achieve the best mean square error for all data across all substrates.

In literature, it has been common practice to determine a molecular monolayers thickness via ellipsometry using a measurement at one fixed wavelength and at one fixed angle. The refractive index (or the A parameter within the Cauchy model) is then assumed to be a fixed value in the range of 1.4 to 1.6. [57, 163, 167]. No further dispersion of the refractive index is typically taken into consideration.

Using multiple angles as well as multiple wavelengths leads to more data points that are more complicated to fit with such a simplistic model and therefore less prone to over-fitting. Self-assembled monolayers provide some particular challenges for the application of ellipsometry. For one, at very low thicknesses, if both n and d are parameters in the model, they become highly correlated. It is then safe to say that the optical thickness nd is accurate, but deviations of d from expected values can be directly connected to a small change in n. [168] This alone combined with the consenus range of assumed refractive index of SAMs can account for thickness variations > 14%. Additionally, interface effects at the interface of substrate and SAM can have a crucial impact on ψ. Missing or incorrect modeling of the SAM-induced variations in ψ can lead to a significant overestimation of the SAM thickness.[169, 170] Taking these limitations into account, VASE is still a useful building block in routine self-assembled monolayer analysis, especially when combined with complementary methods for determining the thickness of the layer. In particular, it presents a simple, fast and non-destructive quality control method, when analyzing similar SAMs on the same type of substrate.

Since liquid crystals exhibit an anisotropic refractive index, modeling of liquid crystal self-assembled monolayers

might depend on the orientation of the molecule on the surface. In fact, others have shown, that advanced VASE methods, can yield useful information including ordinary and extraordinary refractive index, twist distribution and tilt angle distribution of the liquid crystal moiety for liquid-crystal thin films. [171, 172]

3.3 Spectroscopic Methods

Spectroscopic methods study the physical and electronic structure of matter on an atomic or molecular level by observing the interaction between matter and electromagnetic radiation. In this work, spectroscopic methods based on the absorption of electromagnetic radiation have been used.
The general principle of absorption spectroscopy is based on the principle that radiation gets absorbed by matter, if its energy fits the energy difference between an occupied and a not fully occupied energy level within that material. Irradiating material with radiation of a known spectrum and then measuring the spectrum after interaction of that radiation with the sample enables the determination of energy level differences within the sample. Combined with theoretical calculations or reference measurements, individual atoms, molecules or binding states can be identified.

The energy E of electromagnetic radiation is inversely related to its wavelength λ:

$$E = \frac{hc}{\lambda} \tag{3.3.1}$$

where h is Planck's constant and c is the speed of light. Hence, different physical modalities require different forms of radiation to be probed. For example, the fine structure of atoms has to be probed with x-ray radiation whereas the energy separation generated by stretching vibrations of two or three atoms that are covalently bound require infrared radiation to be probed. [173]

3.3.1 Fourier Transform Infrared Spectroscopy (FTIR)

Infrared spectroscopy is used to study molecules or functional groups of molecules, since the vibrational frequency of molecular bonds is in the range of the frequency of infrared light. It is a well-developed tool to identify substances. Within the field of self-assembled monolayers it is also a well-established tool to quantify the order of a molecular monolayer, since CH stretching vibrations of alkyl chains are very sensitive to packing density and presence of defects. In particular, the asymmetric CH_2 stretching vibration at $k \approx 2918$ cm^{-1} is a useful indicator for this order. It has been shown, that a more ordered SAM, the more the CH_2 stretching vibration peak shifts towards lower frequencies. A SAM of a molecule with an alkyl chain that exhibits the asymmetric CH_2 stretching vibration at or below 2917 cm^{-1} is considered of exceptional quality, between 2918 cm^{-1} and 2926 cm^{-1} it is considered to have a high quality and above that the SAM is considered heavily disordered. [174, 175] Some of the vibrational modes that are present in many molecules used for molecular monolayers of this work are listed in Table 3.2.
In a **F**ourier **T**ransform **I**nfra**r**ed spectrometer, the fact, that location and frequency are connected via a Fourier transformation is exploited to translate the technical challenge of high resolution in frequency domain to an easier one within the location domain. Light from a broadband source is passed through a specimen and then through an interferometer, for instance a Michelson interferometer, as depicted in Figure 3.3.1. Then, the resulting intensity is recorded. By shifting one of the mirrors in the interferometer, an intensity profile $I(d)$,

Table 3.2 Frequency range for modes of particular interest for molecules used in this work. ν for vibration, δ for in-plane bending. Adapted from [173]

vibration	characteristic frequency (cm^{-1})	relative intensity
νCH	3100-2800	strong
νOH	3650-3000	strong
νC=C	1900-1500	weak
νC=O	1820-1680	very strong
δCH_3	1370-1470	medium
νC−F	1400-1000	strong
νP−OH	950	-
νP−O	1132	-
νP=O	1280	-

where d is the translation of the mirror compared to its initial state, is recorded. Applying the Fourier transform to $I(d)$ yields $I(f)$, where f is the frequency of light. Comparing this measurement to a measurement without a sample in the light path, results in the absorption spectrum of the sample, typically expressed in wavelength. The three main advantages of FTIR compared to regular IR spectroscopy are

1. **Multiplex advantage**: Since information of all wavelengths is collected simultaneously, for a given scan time the signal-to-noise ratio is increased. Similarily, at given resolution the scan-time is decreased.

2. **Throughput advantage**: Compared to a dispersive instrument, no entrance or exit slits are necessary. This way, the throughput in a FTIR spectrometer is limited only by the diameter of the beam coming from the source right after a circular aperture. Since this circular aperture lets more light through than a slit, the resulting measurement has a higher signal-to-noise ratio.

3. **Wavelength accuracy advantage**. The wavelength scale can be calibrated by a coherent laser beam passing through the interferometer. This calibration method is more stable and accurate than calibration methods that rely on mechanical movement of diffraction gratings as used in dispersive spectrometers. Hence, generally speaking, the wavelengths are more accurate in an FTIR spectrometer than in a dispersive spectrometer.

Self-assembled monolayers are often bound to substrates that are not sufficiently transparent to infrared light. Hence, placing the substrate covered with a monolayer into the beam path is not feasible. Instead, a method called *attenuated total reflection* (ATR) is deployed. The infrared light is guided through an optical waveguide by total internal reflection. The evanescent field behind the reflecting interface can then interact with a sample brought into close proximity of the surface. The light inside the waveguide gets attenuated through these interactions, hence the name *attenuated total reflection*. The penetration depth of the evanescent field into the specimen in contact with the ATR waveguide decreases with increasing difference of refractive indices of waveguide and specimen. For a large refractive index crystal the penetration depth into almost any other material is therfore very short. This is particularly advantageous for self-assembled monolayers, because the background of the substrate becomes less relevant. Attenuated total reflection also enables the measurement of absorption characteristics of thin layers on substrates that absorb in the infrared, since transmission of the

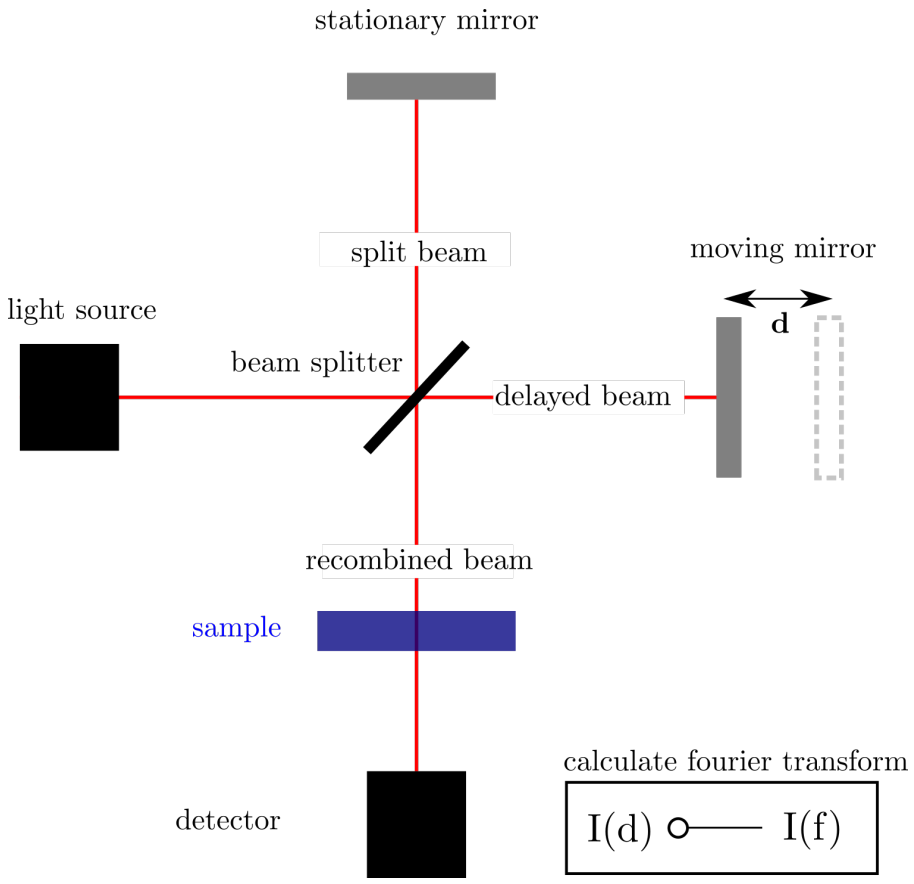

Figure 3.3.1 Working principle of a Michelson interferometer-based Fourier transform interferometer. Light from a source is split into two paths using a beam splitter (BS). The resulting two beams are reflected back from one mirror each and interfere at the beam splitter that in turn re-directs the combined beam through the sample to a detector. Moving one of the mirrors by distance d results in an interference pattern I(d) at the detector. This interference pattern can then be Fourier transformed to yield I(f). Comparing I(f) for measurements with and without sample results in the infrared absorption spectrum of the sample.

probing radiation through the substrate is not necessary.

To analyze an FTIR spectrum, the peaks in a spectrum are compared to reference values of known substances, that can be found in a multitude of reference tables. Since peak positions depend on the local surroundings of the molecule, reference values are often given in a broader range, termed *characteristic frequencies*. To identify unkown substances several algorithms that looks at identifying features first and then searches for support of the first hypothesis within the spectrum are used. [176] Peak positions of the CH_2 stretching vibrations as well as their width are important information in determining the quality of a self-assembled monolayer. Peaks in infrared spectra are most commonly determined by fitting a region of interest to the Voigt function. The Voigt function $V(\tilde{\nu};\sigma,\gamma)$ is defined as the convolution of a Gaussian $G(\tilde{\nu};\sigma)$ and a Lorentzian function $L(\tilde{\nu};\gamma)$. Here, $\tilde{\nu}$ is the wavenumber, σ is the standard deviation of the Gaussian function and γ is the full-width-half-maximum (FWHM) of the Lorentzian. The Voigt function allows to fit broadening effects, that are accounted for through either the Gaussian function (Doppler broadening) or Lorentzian function (natural and collision broadening) as well as in any combination of them. Taking into account all of these broadening effects leads to a lower mean square error of the fit and more accurate values of peak position and width than Gaussian or Lorentzian fits to the same data.[177] All fits to ATR-FTIR data in this work were performed using OriginLabs Origin's *quick fit function* with a Voigt function as objective function. Regions of interest were adjusted until a convergence

of $\chi^2 < 1 \cdot 10^{-9}$ was achieved. Here, $\chi^2 = \frac{1}{\mathrm{DOF}} \sum_{\forall i} (d_i - f_i)^2$ with the degrees of freedom DOF (number of datapoints - number of parameters of the model), values from measurement d_i and values as predicted by the model f_i. ATR-FTIR measurements were performed at a *Bruker Vertex 70v* system at Walter Schottky Insitute, Garching.

3.3.2 X-Ray Photoelectron Spectroscopy

In x-ray Photoelectron Spectroscopy (XPS) the photoelectric effect is exploited to characterize the elemental composition of a surface. Typically, a monochromatic x-ray beam is directed on a surface where the x-ray photons remove characteristic, inner core-shell electrons from the atoms of the surface under investigation. The ejected electrons leave the sample with a kinetic energy W_{kin} that is the difference between the energy of the incoming x-ray W_{xr} and the binding energy of the electron within the atom W_b. When the electron hits the detector, this energy is further reduced by the workfunction difference between sample and detector $\Delta\Phi$. In total:

$$W_{kin} = W_{xr} - W_b - \Delta\Phi \tag{3.3.2}$$

Ejected electrons are typically collected via a system of lenses and analyzed by a *hemispherical electron energy analyzer*. It consists of two conductive hemispheres that bend the trajectories of incoming electrons through an electric field that is applied between the two hemispheres. The radii of electrons then depend on their kinetic energy when entering the hemisphere. The detector at the end of the hemispherical electron energy analyzer then provides a mapping between the position of the arriving electrons and their kinetic energy. Typical x-ray photon energies of lab-scale XPS devices are between 100 and 200 eV, whereas synchrotron sources may reach much higher energies. Since XPS spectra are recorded at fixed photon energies, higher energies may reveal stronger bound electrons, but may also lead to irreversible damage of the surface. At high energies, the measurement spot size of the impinging beam and the spectra acquisition time are optimized to yield enough ejected electrons for the sensitivity of the detector while avoiding noticeable damage to the samples caused by radiation load.

An XPS spectrum is mainly constituted of a series of narrow peaks that correspond to certain core-levels. These levels can be shifted, when elements are in different binding configurations.
Some of the peaks in XPS data are not due to the ejection of an electron by direct interaction with the incident photon. One example are the Auger peaks that present in a spectrum due to the decay of a more energetic electron into the vacant hole created by the x-ray photon, together with the emission of an electron with an energy matching the difference between the states involved in the spectrum. In this work, the *KLL* peaks of O1s and C1s are observed. They are termed KLL since these peaks are present due to the filling of the 1s state (K shell) by an electron from the L shell coupled with the ejection of an electron from an L shell.[178]

Spectra on insulating surfaces are shifted by charging effects. These spectra are therefore commonly charge-corrected by using a well-known binding energy as reference. [179] The binding energy scale of the spectra measured at Walter Schottky Institute, Garching, were calibrated to the hydrocarbon C1s peak at 284.8 eV whereas the spectra measured at the Helmholtz Zentrum Berlin were calibrated using the Al2p emission line of the underlying substrate at 74.1 eV.
Binding energy spectra can also be used to determine the thickness of an organic layer. It can be derived from

the attenuation of a signal that is connected to an atom at the bottom of this layer. Photoelectrons at the interface are subject to inelastic scattering events when passing through another solid. As long as the inelastic mean free path of photoelectrons, typically in the nanometer range [180], is longer than the layer thickness, the attenuation of the intensity can then be used to calculate the layer thickness. The photoelectron attenuation within a solid obeys the Lambert-Beer law [181] which reads:

$$\frac{I(d)}{I_0} = e^{-\frac{d}{\lambda(E_{kin})}} \tag{3.3.3}$$

Here, I_0 is the intensity at the interface, $I(d)$ is the intensity at a point where the photoelectrons travelled a distance d through the material and $\lambda(E_{kin})$ is the inelastic mean free path of the photoelectrons, which is energy- and material-dependent. For molecules with an alkyl backbone on Au [182] and Si[183] , the empirical inelastic mean free path has been previously determined to be

$$\lambda(E_{kin}) = 0.9\ \text{nm} + 0.0022\ \frac{\text{nm}}{eV} \cdot E_{kin} \tag{3.3.4}$$

Since to the best of the author's knowledge no empirical values for phosphonic acids on oxides are available, the above formula was also adopted for alkylphosphonic acids on TiN. The Ti2p peaks were used to perform these calculations. Intensities were determined as integrated intensities of the respective binding energy peaks.

In this work, XPS spectral analysis was performed at two different setups. XPS spectra of alkylphosphonic acids on TiN were acquired by Domenikos Chryssikos at Walter Schottky Institute using a home-built setup equipped with a non-monochromized XR50C-ray source and a Phoibos 100 hemispherical analyzer under a pressure of $6 \cdot 10^{-9}$ mbar, a voltage of 12.5 kV and an emission current of 20.0 mA. Survey spectra were aquired at a step size of 1.0 eV and with a dwell time of 0.5 s using a single scan. Single-peak spectra where then acquired at a step size of 0.1 eV with dwell times of 1 s. A pass energy of 30 eV was consistently used.
XPS spectra of $QM15^F$ and QM32 on aluminum oxide on silicon oxide were acquired by Christian Seim at the HE-SGM beamline at the synchrotron radiation facility BESSY II within the Helmholtz Zentrum Berlin. [184] A moderate photon flux provided by this beamline is well suitable for radiation-sensitive samples. To diminish the radiation load of the samples, the spectra acquisition time was minimized by reducing the spot size to 2 mm x 0.2 mm. Measurements were performed at a base pressure of $2 \cdot 10^{-9}$ mbar. Survey spectra were acquired at photon energy 750 eV to cover the predicted monolayer elements and silicon substrate region. The energy resolution was 0.3 eV. High Resolution X-Ray Photo-Electron Spectra (HR-XPS) of Al2p, P2p, C1s at 350eV excitation energy and F1s at 750eV excitation energy were also acquired at the same beam line.

3.3.3 Near-Edge X-Ray Absorption Fine Structure (NEXAFS) Spectroscopy

Near-edge x-ray absorption fine structure (NEXAFS) spectroscopy can be used to determine the orientation of molecules on a surface. Similarly to XPS, NEXAFS utilizes x-ray irradiation of a surface to draw conclusions about its constitution. In contrast to XPS, NEXAFS is not generating photo electrons, but stimulating electrons to higher energy levels and then monitoring the decay of electrons to this newly vacant level. When electrons from a higher level fill up the vacancy, their excess energy is released either via the emission of a photon or transferred to an other electron in the same atom that then leaves the atom. These electrons are called *Auger electrons*. In NEXAFS, either the emission of x-ray photons or emission of Auger electrons is monitored to determine the absorption spectrum of the sample. Due to experimental reasons, monitoring the emission of

Auger electrons has become the more common method. [185] For NEXAFS spectroscopy first, the *absorption edge* is determined by increasing the energy of the impinging x-ray beam. Since an x-ray photon can only be absorbed if the energy is at least sufficient for the electron to reach a higher, unoccupied state, for any given atom or molecule, the x-ray absorption remains zero up until this characteristic edge and then suddenly increases. The energy value at which this sudden increase occurs is called the *absorption edge*. In the energy region close to it, absorption depends on how many unoccupied states are available for the electron. Hence, absorption spectroscopy in this energy regime is particularly useful to determine the fine structure of a surface. This is also what gives NEXAFS its name. Since the Auger electrons generated by this process have a decay length of few nanometers, NEXAFS spectroscopy only probes a few nanometers at the surface of a substrate. Since the energy of the excitation beam is scanned in NEXAFS, a synchrotron source is required to perform these measurements. [185] NEXAFS is very sensitive to the bonding environment of the absorbing atom and is commonly used especially to characterize different fine structures for carbon in different molecular groups.
The absorption of x-rays by molecules depends on the orientation of their transition dipole moment with respect to the electric field vector of the incident beam. This difference in absorption of perpendicular and parallel polarized radiation is called dichroism. It is particularily pronounced in aromatic moieties and hence enables probing the average tilt of these within a SAMs. Hence, NEXAFS can contribute to a better understanding of self-assembled monolayers. Specifically the ability to probe the orientation of functional units within monolayers is crucial when the electronic functionality of monolayer devices depends on this orientation. This information can then be used to validate molecular dynamics simulations that in turn contribute to a deeper understanding of structure-function relationships in ensemble molecular electronics.[186]
Due to the dichroic effect, the intensity of the NEXAFS resonances I relates the angle of incidence of the polarized x-ray beam θ to the average tilt angle of the transition dipole moment α via the following equation

$$I(\theta) \propto Pcos^2(\theta)\left(1 - \frac{3}{2}sin^2(\alpha)\right) + \frac{1}{2}sin^2(\alpha) \tag{3.3.5}$$

Here, P denotes the degree of polarization of the x-ray beam. This equation can be re-written as

$$I(\theta) \propto Pcos^2(\theta)\left(cos^2(\alpha) + \frac{1}{2P}tan^2(\theta)sin^2(\alpha)\right) \tag{3.3.6}$$

In this form, it is immediately evident that for $\theta = \arctan(\sqrt{2P})$ the absorption is independent from the orientation of the transition dipole moment. For $P \approx 1$ this so called *magic angle* is $\theta \approx 55°$. The absorption intensity measured at this angle is crucial for data analysis, since it provides a scaling factor for all physical and experimental constants and allows the comparison of different measurements. Without any preferable orientation of molecules on a surface, recording NEXAFS spectra at this 'magic' angle is sufficient.[185] If a preferential orientation however, is to be expected, this orientation can be determined by determining the average tilt angle of the transition dipole moment of surface bound molecules. By measuring $I(\theta)$ at multiple angles of incidence and fitting the resulting data to the above equation, the average tilt angle of the transition dipole moment α can be determined. Since the transition dipole moment of the aromatic π^* level is orientated perpendicular to the molecular plane of the aromatic ring, the average tilt angle β of the aromatic ring can be calculated from α, as long as the so-called twist angle γ is known. The twist angle describes the rotation of the

aromatic moiety around its axis with respect to the plane spanned by this axis and the surface normal. [187, 188] The relationship between these three angles is [185]:

$$cos(\alpha) = sin(\beta)cos(\gamma) \tag{3.3.7}$$

If the twist angle is not known, reasonable assumptions have to be made. For the molecules under consideration in this work, a twist angle of $\theta \approx 0$ is set to simplify calculations. Polarized NEXAFS and polarized IR spectra complement each other and can be used to collectively determine γ and hence unambiguously calculate β. This method has been applied to various monolayers, especially for the tilt of aromatic moieties.[185, 189–194] In this work, the analysis is also focused on the aromatic rings since they contribute the majority of the overall transition dipole moment of the molecules that have been studied.

NEXAFS spectra to calculate the orientation of the polar group of $QM15^F$ and QM32 within a monolayer on aluminum oxide were recorded by Christian Seim at the HE-SGM beamline at the synchrotron radiation facility BESSY II within the Helmholtz Zentrum Berlin. The NEXAFS/XPS apparatus at the end-point of the synchrotron was designed and built by *PREVAC*, Poland. [188]

The spectra were recorded at the carbon K-edge in partial electron yield mode with retarding voltages of -150 V. As the primary x-ray source, linearly polarized synchrotron light with a polarization factor of 88% was used. The angle of incidence of the x-rays was varied between the normal (90°) and grazing (20°) incidence geometry in 10-20° steps. The energy resolution was 0.3 eV. The photon energy (PE) scale at the C K-edge was referenced to the pronounced π^* resonance of highly oriented pyrolytic graphite at 285.38 eV. [195] To extract quantitative information about the monolayers, the following normalization procedure was used additionally: First, the constant background signal without illumination was determined and later subtracted from the spectra. Then the spectrum of a substrate without monolayer was recorded and later subtracted from the spectra of the monolayer covered substrates. The spectra were corrected for the photoelectron dependence of the incident photon flux by division through the spectrum of gold and reduced to the standard form (zero intensity in the pre-edge region and the unity jump in the far post-edge region). This data analysis procedure reveals information that can be attributed exclusively to the monolayer on the substrate.

3.4 Current-Voltage Spectroscopy

All electrical measurements were performed using a Keithley 2635B source measure unit (SMU). Communication to the Keithley 2635B was established via the Virtual Instrument Software Architecture (VISA) protocol and the SMUs were connected via GPIB. First measurements were performed with a Python script based on the package pymeasure and later measurements were performed using LabView software *qMem* developed and continuously improved by Simon Schwarzkopf of *Merck KGaA*, Darmstadt. If not otherwise specified, the following conditions were used for IV-sweep measurements: Integration time: 400 ms, dwell time: 100 ms, step size: 50 mV. Here, integration time describes the duration of the current measurement at each voltage and dwell time is the time delay between applying the voltage and starting the current measurement. All voltages applied via the Keithley 2635B were done so in a 'floating' configuration. This means that there was no fixed ground on either of the two terminals and voltages are always relative to the other contact and not relative to a defined zero potential.

Electrical measurements were post-processed with a Python script, that is part of this work. It is mainly based on the Python packages Pandas, NumPy and PyPlotLib. The script re-arranges sweeps so odd and even

number sweeps are grouped. This is advantageous to cluster high and low resistive states when a memristive device is voltage sweeped. Furthermore the script automatically calculates and plots the on/off ratios, Fowler Nordheim Plots, normalized differential conduction (ndc) plots and current as well as current density vs voltage statistics. The comprehensivly documented code of this `datawrangling.py` script is available at `https://github.com/JuMaD/qmDataWrangling` and still subject to change after submission of this work.

3.4.1 Vacuum Cryo Probe-Station

Two-terminal electrical characterizations of solid state devices were performed using a vacuum probe station. Most characterizations were performed inside a *Lakeshore TTPX* probe station, that was later replaced by the for all two-terminal measurement purposes identical *Lakeshore CRX-6.5K*. Both probe stations consist of a vacuum chamber with four flexible probe-arms mounted to it and are themselves mounted on a shock-free table to minimize mechanical noise. The vacuum chamber is connected to a *Pfeiffer* vaccuum pump station that evacuates the chamber and a nitrogen supply that is used to flood the chamber and to keep water adhesion to the inside of the chamber to a minimum during sample exchange. To contact the contact pads on the fabricated chips, probes that have a tip of tungsten with diameter 25 µm mounted to a temperature stable ceramic.
The vacuum chamber itself consists of two layers: the outer vacuum chamber and the inner radiation shield. Probe tips are connected via mini coaxial cables to a feed-through coax to triax connector. The inner guard of the outside facing triax is connected to the probe station radiation shield. This way, the probe station itself is designed with following the principle of a triax cable, ultimately reducing the noise of measurements inside the probe station to a minimum. The sample stage that is made out of copper as well as the outer shell of the vacuum chamber are set to a common ground.
Quartz windows are incorporated in both radiation shield and outer shell and a long working distance microscope is mounted above the stage to allow magnified observation of samples and tips within the probe station. Imaging is facilitated via a ring light and the quartz windows were covered with a light blocking sheet during electrical measurements to avoid any potential absorption phenomena influencing the measurement.
The general setup of the probe station is illustrated within a picture of the LakeShore CRX-6.5K probe station in Figure 3.4.1 whereas the electrical configuration is shown in more detail in Figure 3.4.2.

At the TTPX probe station, a capillary below the sample stage is connected to gas in- and outlets to allow for cooling liquids, such as He and N_2 to cool down the stage to cryogenic temperatures. At the LakeShore CRX-6.5K probe station, the base is directly connected to a refrigerator that is cooled down using an external He compressor, forming a closed cycle system that can be cooled down below 10 K within approximately 4 hours. Temperature control for both probe stations is established through heating coils that are controlled via a Lakeshore 336 temperature controller. In both probe stations the probe mounts are thermally anchored to the stage, whereas the probe arm is thermally anchored to the radiation shield.
In this work, two terminal IV-measurements at the probe station were conducted at room temperature under a base pressure of $\leq 5 \cdot 10^{-6}$ mbar.

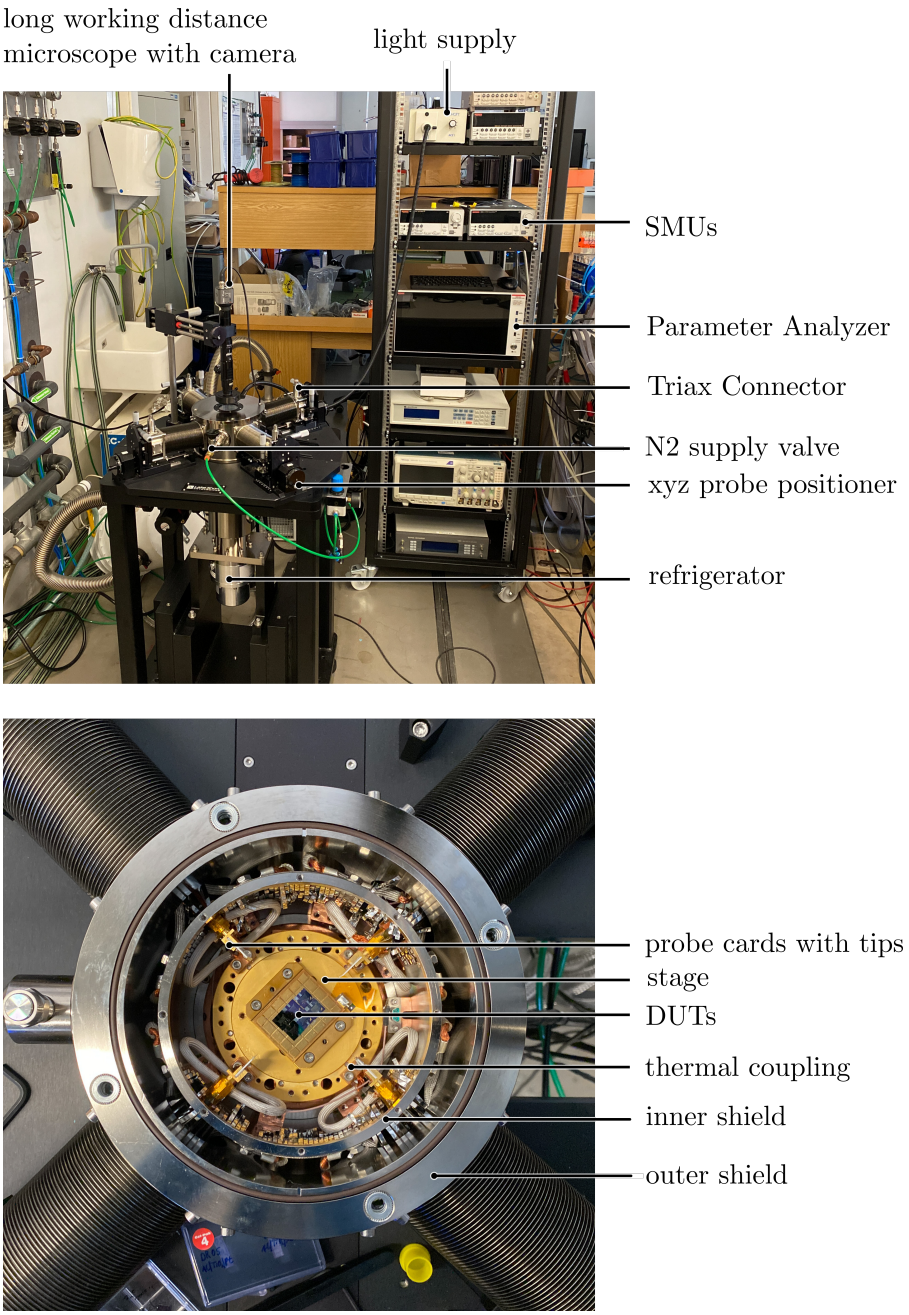

Figure 3.4.1 Cryo probestation measurement setup. *Upper image* shows the LakeShore CRX-6.5K cryo probestation together with the periphal measurement equipment. SMUs are connected to the probes via Triax Cables that are connected to the Triax connectors of the probestation. *Lower image* shows a closer look at the opened up probe station, showcasing the 4 probes, the measurement stage, the outer and inner shell as well as 6 devices under test (DUT).

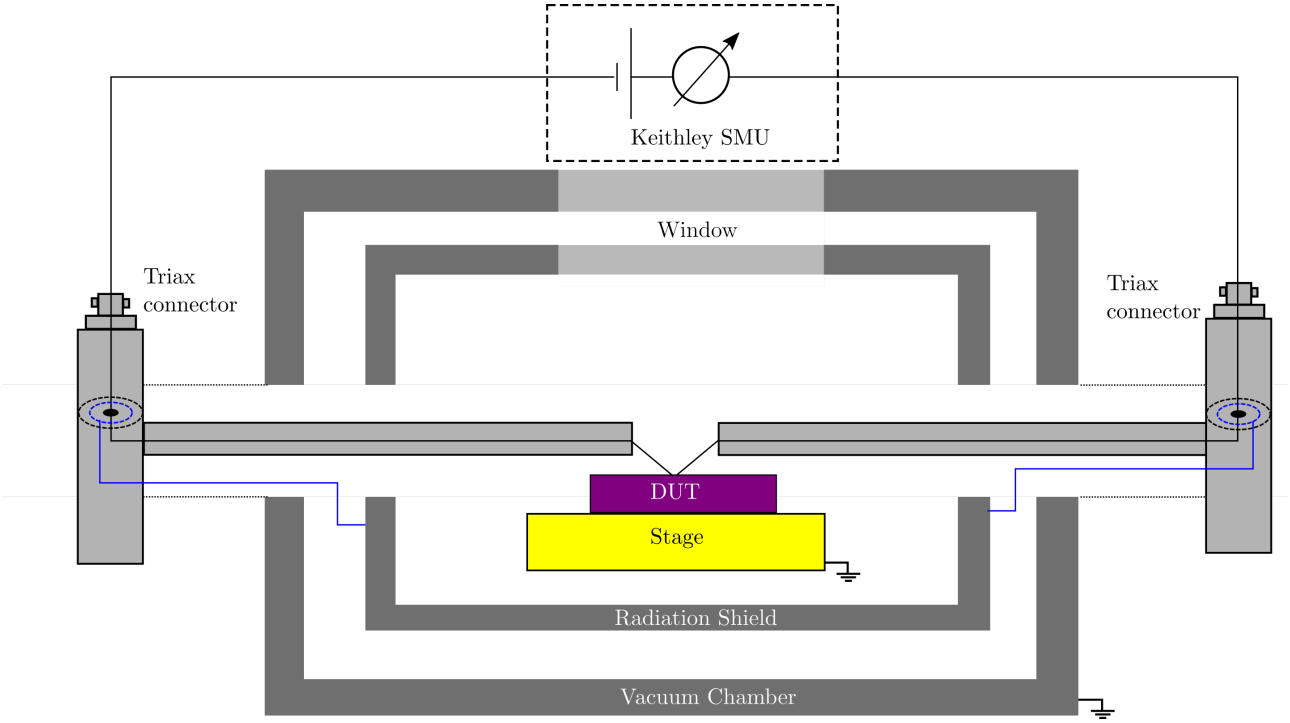

Figure 3.4.2 Crossection schematic of the probestation setup used for two terminal measurements. The sample is placed on a grounded Cu stage. Contacts on top of the sample are contacted via probe tips that are fed through the probearms to a triax connector that is then connected to a Keithley 2635 SMU. The SMU is then controlled via a LabView program. The sample stage is enclosed by a two-chamber system. The outer chamber functions as vacuum chamber, whereas the inner one acts as radiation shield that is connected to the inner guard of the triax connector (as indicated by the *blue* lines). *Dashed lines* inside the triax connector illustrate the inner and outer guard and the connections of the probestation parts to it.

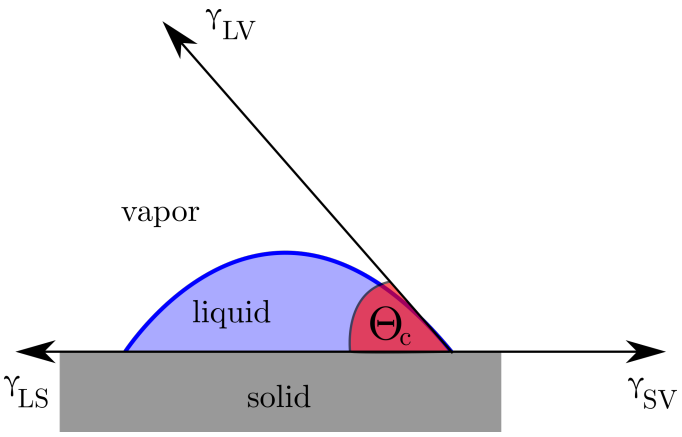

Figure 3.5.1 Definition of the contact angle of a liquid on a solid. When a droplet of a liquid is placed on top of a surface, an equilibrium contact angle Θ_c forms due to liquid-solid interfacial energy γ_{LS}, the solid-vapor interfacial energy γ_{SV} and liquid-vapor interfacial energy γ_{LV}. Adapted from [200].

3.5 Water Contact Angle

Measuring the water contact angle of a surface has been proven to be a quick method for quality control of self-assembled monolayers. [37, 57, 196–199] When a liquid drop comes into contact with a solid surface, cohesive forces within the liquid cause the drop to avoid contact with the surface and adhesive forces between the liquid and the solid cause the liquid to spread across the surface. When these forces come to an equilibrium, a droplet is formed on the surface. The angle between the tangent to the liquid's outline and the solid surface, determined at the position where the liquid-vapor interface meets the surface, is called contact angle. The definition of this angle is shown in Figure 3.5.1.

The equlibrium contact angle Θ_c is related to the liquid-solid interfacial energy γ_{LS}, the solid-vapor interfacial energy γ_{SV} and liquid-vapor interfacial energy γ_{LV} via the Young equation[201]:

$$\gamma_{LV} \cos\theta_c = \gamma_{SV} - \gamma_{LS} \tag{3.5.1}$$

Keeping the liquid and the vapor the same, the contact angle becomes a simple figure of merit for a change in interfacial energies at the liquid-solid and vapor-solid interfaces. Since the surface facing moieties of bare surface and monolayer often significantly differ with respect to their surface energy, a change in water contact angle is a useful measure to indicate successful monolayer formation.[202] Many experiments have determined the water contact angle of alkyl monolayers with ambient facing methyl moieties at >100° whereas for typically hydroxy-terminated oxide surfaces, contact angles of 50° have been reported. [203, 204].

The solid surface is termed hydrophilic, if the water contact angle is smaller than 90°, and hydrophobic, when it is larger than that. Clean oxide surfaces are therefore hydrophilic, whereas surfaces with a methyl terminated SAM are hydrophobic.[200] In the *sessile drop* method, a defined volume of the test liquid is dropped onto the surface, completely detaching from the syringe it is deposed off of.

In this work, static water contact angle measurements with the sessile drop method were recorded and analyzed at room temperature on a OCA-20 contact angle measurement system from *DataPhysics Instruments GmbH* (Filderstadt, Germany) with SCA20 analysis software. Reported contact angles are averages of 3 measurements on on each surface. De-ionized water from a Millipore system was used as a test liquid in all cases.

4 Fabrication

In this chapter, the fabrication methods deployed in this work will be briefly outlined. These include sputter coating, self-assembled monolayer growth, vacuum evaporation and optical lithography.

4.1 Thin Film Deposition

4.1.1 Sputter Coating

Sputter-deposition is a type of thin-film deposition that is mainly used for dielectrics and metals. The material to be deposited and the substrate are placed in a process chamber facing each other. After evacuation of the champer, a gas-mixture of argon and nitrogen is supplied as bleeding gas. An external field then induces a plasma within the chamber. Ar^+ ions inside this glow discharge plasma are then accelerated towards the target that is strongly negatively biased compared to the substrate. The accelerated ions hit the target surface, ejecting of the target material from the surface. Atoms with sufficient energy reach the substrate and are deposited there. [205, 206] In this work, sputter-deposition was performed by *Fraunhofer EMFT* to fabricate the TiN and Al coatings on the Si/SiO_2 wafers as well as to fabricate the AlSi reinforcement at the pad area of the 1D-crossbar.

4.1.2 Self-Assembled Monolayer Growth

Organophosphonic Acid Monolayer Fabrication

A detailed description of the self-assembly process of phosphonic acids is given in chapter 2.
Unless otherwise stated, monolayers in this work were grafted from 1 mM solutions of the respective molecules in tetrahydrofuran (THF). Dipcoating was performed in 20 ml glass vials that were filled close to the maximum and sealed air tight to reduce the potential influence of oxygen on monolayer formation. Samples were kept in the solutions at room temperature ($\approx$ 23 °C) for 72 hours before they were taken out, blown dry in a dry nitrogen stream and subsequently heated on a hotplate at 130 °C for 1 hour. Samples were subsequently left to cool down for 5 min and then rinsed for 20 s in a 1 ml/s stream of ethanol (EtOH), deposited from a glass syringe exlusively used for that purpose. This rinsing step was introduced to wash off potentially unbound molecules as well as excess THF. Samples were then blown dry in a dry nitrogen stream and heated on a hotplate at 130 °C for 10 s to remove residual EtOH.

4.1.3 Vacuum evaporation

In a vacuum evaporation process - also commonly referred to as*physical vapor phase deposition*, the source material is heated, typically within a crucible, under high vacuum. It then resublimates or condensates on the substrate. The substrate is placed upside down above the crucibles containing the material to be evaporated.The process is executed in vacuum to lower the melting and boiling points of the materials as well as to decrease the mean free path of atoms. Typically, the pressure is decreased to a value where the mean free path of the

evaporated atoms is much larger than the size of the evaporation chamber, resulting in a highly directional flux of atoms, that avoid scattering events with impurity atoms present in the chamber. [206]

Materials are heated either via supplying a high current through the crucible holder, effectively heating the crucible via joule heating, or via directing an electron beam onto the material inside the crucible. The former method is commonly referred to as *thermal evaporation* while the latter is commonly referred to as *e-beam evaporation*. E-beam evaporation has several advantages over thermal evaporation. Since the electron beam is typically focused to a small spot on the source material and the crucible is cooled by water, the heated area is confined to a small spot within the source material. This eliminates any unwanted contamination from peripherals that might be contaminated with materials other than the source material. Additionally, e-beam evaporation is expected to lead to less thermal load for the sample during evaporation. [207, 208] A shutter separates the source from the substrate and allows to control the start and end of the end point of the process. Using oscillating quartz crystals in close vicinity of the substrate, the layer thickness of the resublimated material can be tracked. In combination with the shutter, an exact adjustment of the layer thickness as well as the evaporation rate is possible. The material flux from source to substrate depends on the net evaporation rate, the angular distribution function of the material, the shape and material of the crucible as well as the geometry of the deposition chamber.

Within this work, the deposition of aluminium as bottom contact layer was performed within a *Leybold L560* system at *Walter Schottky Institute*, Garching. Two tungsten coils were placed in-between electrical contacts to form a thermal heater. Four 5 mm long jugs of 99.99% aluminum (supplied by Kurt J. Lesker) were placed inside the coils. Vacuum pressure was typically in the range of $6 \cdot 10^{-7}$ mbar to $6 \cdot 10^{-8}$ mbar. Liquid nitrogen was supplied to the double-walled cryogenic vacuum chamber in order to freeze out air moisture. Evaporation rate was kept between 2 nm/s and 4 nm/s.
The deposition of the Pb/Ag bi-layer was performed within a *Balzers* evaporator at the *Department of Hybrid Electronic Systems*, Munich. Tungsten boats placed in-between electrical contacts to form thermal heaters within the same vacuum chamber. Three to five ball-shaped jugs of lead and silver were placed inside the respective crucibles. Cold water was supplied to the double-walled vacuum chamber in order to 'freeze' adsorbates at the inner side of the chamber. Deposition rate was keept at ≈10 nm/s for Pb and at ≈ 5 nm/s for Ag. The substrate was moved from one evaporation source to the other without breaking the vacuum via a rotation mechanism inside the chamber.
The deposition of Ti/Au top contacts was performed within a *Leybold L560* system at the *Zentrum für Nanotechnologie und Nanomaterialien*, Garching. Ceramic crucibles were placed within a rotating revolver and filled with titanium jugs (supplied by Kurt J. Lesker) and gold jugs (supplied by Kurt J. Lesker) respectively. The materials were subsequently heated by exposure to an electron beam. Vacuum pressure was typically in the range of $1 \cdot 10^{-7}$ mbar to $2 \cdot 10^{-8}$ mbar. Liquid nitrogen was supplied to the double-walled cryogenic vacuum chamber in order to freeze out air moisture. Deposition rates were kept as low as possible - which corresponds to rates between 0.05 nm/s and 0.15 nm/s. At the Ti evaporation step, the shutter was kept in-between source and substrate after Ti started to evaporate (as observed by a slight pressure increase and the deposition rate from a QCM that was not shielded by the shutter) until the pressure inside the chamber stopped decreasing. The decreasing pressure was seen as an indicator for the reaction between Ti atoms evaporating from the source and potentially still present oxygen in the chamber. The steady state of pressure during evaporation of Ti atoms was seen as an indicator that oxygen within the chamber is likely 'used up' and the species reaching the substrate is

in fact Ti and not TiO_2.

4.1.4 Shadow Mask Evaporation

A shadow mask can be used to structure evaporated materials directly at evaporation instead of afterwards via a lithographic process. The mask is placed in-between the evaporation source and the substrate. It is comprised of a thin membrane with small windows. The evaporated material is then blocked by the membrane and locally deposited directly onto the substrate through the windows. Hence, the deposited layers are already structured on the substrate and no further processing of the substrate to structure the evaporated material is necessary. However, the mask has to be as close and as parallel to the substrate as possible in order to avoid any imaging effects, since the windows within the mask effectively act as aperture. [209] Shadow mask evaporation is beneficial for direct evaporation of metallic top contacts to self-assembled monolayers since it avoids any chemical, thermal or optical processes that would be necessary in a lithographic process and that might put the structural integrity of the monolayer at risk.
In this work, all top contacts were structured via shadow mask. The shadow masks used in this work were 10 µm thick nickel masks supplied by *Temicon GmbH, Dortmund*. The smallest feature on these masks was 5 µm wide. This was the minimum feature size available at a commercial manufacturer at the time. However, shadow mask evaporation is, in principle, not limited by this feature size. It has been shown, that substrate-aligned lines of 10-15 nm width can be structured using shadow mask evaporation and this process is - in principle - suitable for nano-sized devices. [210]
In this work, the nickel masks were aligned to the substrate using a custom-made shadow mask alignment kit (*Idonus, Hauterive*). A mask chuck and a substrate chuck including a connection to a vacuum pump hold the mask and substrate in place. These chucks are in turn fixated via screws within adapter plates, allowing them to be placed inside a *Karl Süss MA-6* mask aligner. Alignment markers on mask and substrate were aligned using the MA-6 system and brought into contact. The chucks were then fixed to each other using screws that were passed through one spring and one ball bearing each. Springs are used to keep the force at the four screwing locations similar, whereas the ball bearings minimize the rotational forces on the chucks while screwing. This reduction in external mechanical forces after alignment secures the alignment of the two chucks. The combined chucks were then separated from their adapter plates and the chucks were carefully wrapped in aluminum foil to prevent clogging of the movable parts through evaporated metal. A hole was carefully punched into the foil to reveal the substrate opening of the mask chuck. Figure 4.1.1 shows the mask aligner and all parts involved in the mask alignment process. Detailed images of the aligned chucks are shown in Figure 4.1.2.

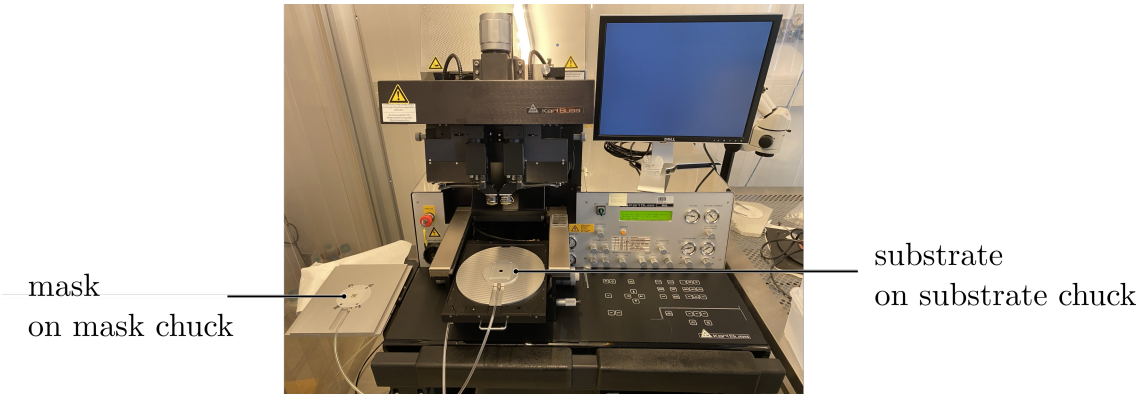

Figure 4.1.1 Image of the custom mask alignment setup including the Süss MA-6 mask aligner. Mask aligner is shown in the middle. In the left part of the image, the mask chuck that is screwed to its adapter plate is highlighted, wheres the substrate chuck screwed to its adapter plate is shown on the right. Both chucks are connected to the vacuum pump of the MA-6 in order to keep substrate and chuck in place. The left adapter plate is placed upside down in the mask aligner top part. The microscope of the mask aligner in conjunction with the micrometer positioning screws are used to move the substrate adapter plate with respect to the mask adapter plate to align the alignment markers on substrate and mask. The 'check alignment' feature is then used to bring mask and substrate into contact. Chucks are screwed together to fixate the alignment and the combined chucks are then removed from the mask alignment system.

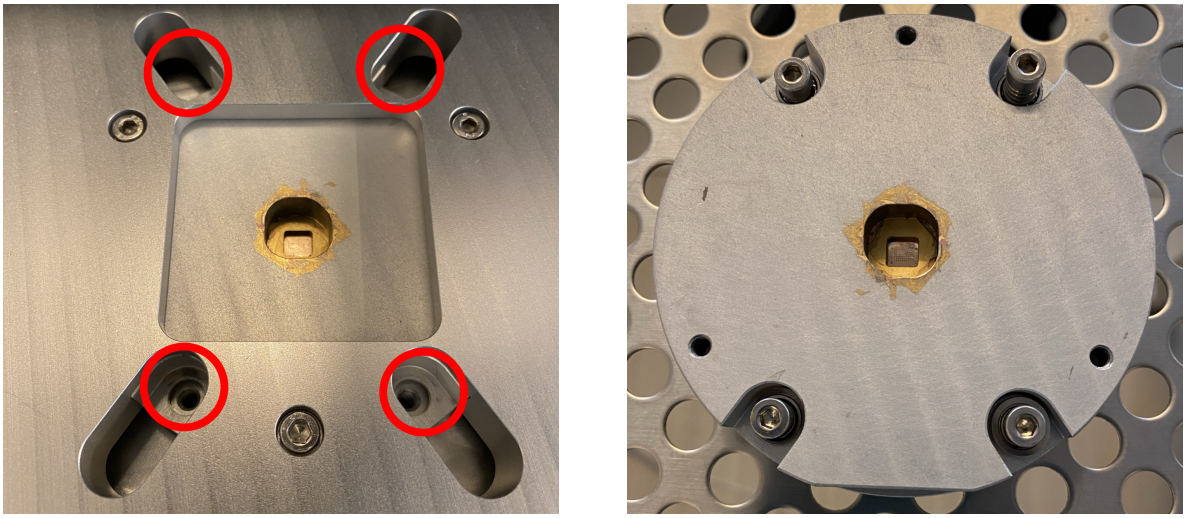

(a) **(b)**

Figure 4.1.2 Detailed picture of the shadow mask alignment kit. a) Picture of the chuck in the mask aligner where both chucks are still connected to their respective adapter plates. Threads of the substrate chuck where the screws with springs and ball bearings go to are highlighted in red. b) The combined substrate and mask chucks after alignment and after removal from the adapter plates. This setup is then wrapped in aluminum foil and a hole is carefully opened up at the position of the opening in the middle before being transferred to a PVD system. Gold coating at the position of the opening is clearly visible in both pictures, whereas the rest of the chucks remained uncoated, as intended.

Since mask aligner and Pb/Ag evaporation system were located across Munich, to reduce environmental impacts on the sample, the aligned chucks were placed in a plastic desiccator with water absorbing silica gel. Air was then removed from the desiccator using a membrane pump and the evacuated desiccator was placed inside a Styrofoam box, partially isolating it from temperature changes. An image of this transport system containing an aligned chuck is shown in Figure 4.1.3.

Figure 4.1.3 Shadow Mask Alignment kit transport box that was used to transport the aligned samples across the city. Stryrofoam box serves the purpose of keeping the temperature inside the box as constant as possible, whereas the desiccator and the silica gel inside the evacuated desiccator were introduced to reduce humidity inside. Foil and paper were added to provide additional thermal isolation. This transport system aims to prevent condensation of water on the sample that might happen due to repeated temperature changes when moving from a warm to a cold and then to a warm environment again.

4.2 Lithography

Lithography is a well-established method used to transfer patterns onto a substrate to protect selected areas of the substrate during subsequent processing steps. Substrates are coated with a resist that hardens or breaks down when exposed to specific radiation. In *photolithography*, resists are typically sensitive to UV light and change their chemical properties when exposed to light. Typically, surface to be structured are coated with thin films of resists within a yellow room where UV and blue light is filtered out. The thin film is then exposed to UV light that is structured either through a photomask or via a laser scanner. Locally changed chemical properties are then exploited using a developer. The developer removes either exposed or unexposed areas on the sample revealing the previously transfered pattern as photoresist material on the substrate. For a *positive* resist, the light exposed areas are removed in the development step, i.e., a positive of the mask remains on the substrate. For a *negative* resist, the light protected areas are removed in the development step, i.e., a negative of the mask remains on the substrate. A third category of resists are reversible resists that can be turned from a positive to a negative resist - or vice versa - via a specific stimulus, such as heating to a certain temperature.
Additional processing steps such as pre-heating the thin film before exposure (soft bake) or post-heating the pattern after development (hard bake) can be employed to improve the result of the pattern transfer and hardening the remaining pattern to make it more resistant to subsequent processing steps. [211]
Bottom contacts in this work were structured via photolithography and subsequent etching of the unexposed areas. The 1D crossbar chips fabricated at Fraunhofer were fabricated on a wafer scale using their standard procedure. They were sawed into 8 mm x 8 mm chips. Prior to sawing, wafers were coated in a resist to protect the surface from sawdust.
The crossbar aluminium bottom electrode chips were structured in a clean room using the following procedure: Reversible photoresist AZ5214E (*MicroChemicals*, Ulm, Germany) was spin cast (600 rpm, 6000 rpm/s, 40 s) on 8 mm x 8 mm chips and subsequently pre-heated at 100 °C for 100 s. Typical film thickness after spin coating was 1.6 µm. Pattern transfer was done via a chrome mask using a 200 W mask aligner. Samples were exposed to UV light for 20 s. The developer AZ351B (*MicroChemicals*, Ulm, Germany, 1 : 4 diluted with DI water) was used to develop the pattern. Development was stopped in DI water. Results were checked with a microscope and development was repeated until patterns were clearly developed. Then, a reversal bake was performed at 120 °C for 2 min and samples were exposed to UV light for 30 s without a mask. A following hard bake at 120 °C for 1 min was performed to further improve chemical stability. After cooling samples down to room temperature they were again immersed in the developer AZ351B. This was done to exploit the fact that the developer is KOH based and prolonged exposure of the samples lead to etching of the exposed aluminum on the surface, ultimately revealing the desired structure.

Before subsequent measurement or processing of the samples, all samples were cleaned using the following procedure:

1. **Dust removal**: Samples were immersed in a volume >50 ml of DI water and cleaned within an ultrasonic bath for 3 minutes. Samples were subsequently blown dry in a stream of dry nitrogen.

2. **Photoresist removal**: Samples were immersed in a volume >50 ml of acetone and cleaned within an ultrasonic bath for 5 minutes. Samples were transferred to a second beaker with fresh acetone and sonication was repeated for another 5 min.

3. **Removal of residual acetone**: To avoid straining effect of drying acetone, samples were directly transferred from the acetone beaker to a beaker with isopropanol, keeping a thin film of aceton on the chip during transfer. Samples were cleaned in an ultrasonic bath for 3 minutes and then blown dry in a stream of dry nitrogen.

5 Materials

In the following chapter, the materials used to fabricate monolayers and ensemble molecular devices within this work will be specified. This includes substrates, alkyl phosphonic acids and liquid crystal-inspired molecules.

5.1 Substrates

In this work, different types of silicon substrates were used.
Highly doped Si wafers (4 inch, p-type boron, ⟨100⟩ surface, $\rho < 0.005$ Ωcm, (525 ± 25)µm thickness, single-side polished) covered by a 50 nm thick layer of thermally grown silicon dioxide SiO_2 were purchased from *Active Business Company GmbH, Germany*. These wafers were diced into 8 mm x 8 mm chips and used as substrates for subsequent fabrication of the arrays of ensemble molecular devices, exclusively used in Chapter 7.
For contact angle and AFM measurements, Si(250µm)/SiO_2(850nm)/Al(50nm) substrates with sputter-deposited aluminum were obtained from *Siegert Wafer GmbH* (Aachen, Germany).
All 1D crossbars as well as surface characterizations of Al and TiN surfaces were fabricated on highly doped Si wafers (8 inch, (525 ± 25) µm thickness, single-side polished) covered by a 530 nm thick layer of thermally grown silicon dioxide SiO_2 that were purchased from *Fraunhofer EMFT, Germany*.

5.2 Alkyl Phosphonic Acids

Molecules with a long alkyl chain have been used as a universal test bed of (ensemble) molecular electronics. In this work, alkylphosphonic acids have been used to test phosphonic acid binding to native TiN surfaces and to test the feasibility of the **TiN/../Ti** contacting scheme. A series of alkyl phosphonic acids, namely hexyl- (C6), octyl- (C8), decyl- (C10), dodecyl-(C12), tetradecyl-(C14) and hexadecyl-phosphonic acid (C16) were obtained from *Sigma Aldrich*.

5.3 Liquid crystal-inspired molecules

Liquid crystals (LCs) are an additional phase (a so called *mesophase*) between liquid and crystalline solid phase. In this phase, the liquid consistency is maintained while a degree of long-range positional and orientational order can be observed. This phase was first observed by Friedrich Reinitzer in 1888. It was termed *liquid crystal* by Otto Lehmann in 1889 since it posseses characteristics of both a liquid, and a crystal. Liquid crystals became technologically relevant, when their optical anisotropy was discovered. Particularily technologically relevant is the combination of the possibility to align molecules within a liquid crystal by applying an external electrical field and their birefrigerence - the polarization and direction dependent refractive index. Sandwiching a layer of liquid crystals between two perpendicularily oriented linear polarizers allows the modulation of the

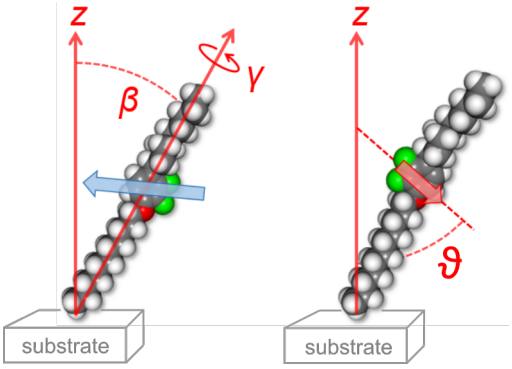

Figure 5.3.1 Concept of the electrical field induced dipole switching. Switching from anti (*blue*, left) to syn (*red*, right) conformation of the QM15 molecule is depicted as an example for the general concept. Atoms are color coded: *grey*: carbon, *white*: hydrogen, *red*: oxygen, *green*: fluorine. Electrical dipole orientation is displayed as a bold *blue* or *red* arrow with the arrow pointing from negative to positive charge. The dipole orientation with respect to the surface normal z (angle ϑ) is directly connected to the orientation of the carbon-fluorine bond. An applied electrical field induces orientation change of the molecule via coupling of the dipole to the field. Molecular orientations are described by tilt angle of the long molecular axis β. The orientation of the aromatic moiety is defined by the angle between its normal vector and z (angle α) as well as by its rotation around the long molecular axis by the angle γ. Here, α is perpendicular to the paper plane and not depicted. A change in the z-component of the dipole moment μ_z. Figure as published in [154].

transparency of this stack via an electrical field that is applied to the liquid crystal layer. This yields an electro-optical modulator that can, e.g., be used to modulate brightness of a pixel in a display or to quickly modulate the intensity of laser light without the use of movable parts.

Liquid crystals also exhibit dielectric anisotropy. This means that their dielectric constant ϵ depends on the direction of the external field. The dielectric constant can be split into two components: One that is parallel ($\epsilon_{\parallel}$) and one that is perpendicular ($\epsilon_{\perp}$) to the directional vector, often called *director*. The difference of the two components of the dielectric constant is then calculated via $\Delta\epsilon = \epsilon_{\parallel} - \epsilon_{\perp}$. Liquid crystals composed of materials with $\Delta\epsilon > 0$ are termed *dielectrically positive* liquid crystals, whereas materials with $\Delta\epsilon < 0$ are termed *dielectrically negative* liquid crystals. In this work, functional groups derived from common, dielectrically negative crystals have been used. [212, 213]

Recently, the interest in liquid crystals has expanded beyond their use in electro-optical modulators and displays. The have been shown to exhibit advantageous properties e.g., as active component of organic field effect transistors [214, 215]. However, to the best of the author's knowledge, this work is the first to demonstrate their use in molecular electronics in general and in ensemble molecular electronics with solid contacts in particular. The dipolar SAM molecules were inspired by dielectrically negative liquid crystals. Namely, the compounds QM15^F, QM69^F and QM85^F feature a difluorinated phenylcyclohexane unit, that is commonly used in liquid crystals. [212] The general concept of switching the dipole moment in the direction perpendicular to the substrate of a SAM is exemplified using QM15^F as an example in Figure 5.3.1. The molecules studied in this work are displayed in Figure 5.3.2. Liquid crystal building blocks were obtained from *Merck KGaA*, Darmstadt, Germany) and together with other reagents from *Specific Polymers*, Castries, France. The synthesis of all QM-labled substances was performed by *Colour Synthesis Solutions*, Manchester, UK. Details of the synthesis of QM15^F and QM32 are supplied in the Supplementary Information of [154].

For all conductance switching molecules the parameters that govern the charge transfer through them, namely thickness, dipole-induced energy shift in z-direction, HOMO and LUMO were calculated by *Peer Kirsch* using GAUSSIAN. All molecules were found to have two energetically stable conformers - consequently named *syn* and *anti*. From values resulting from the calculations, the differences between the two molecular conformers

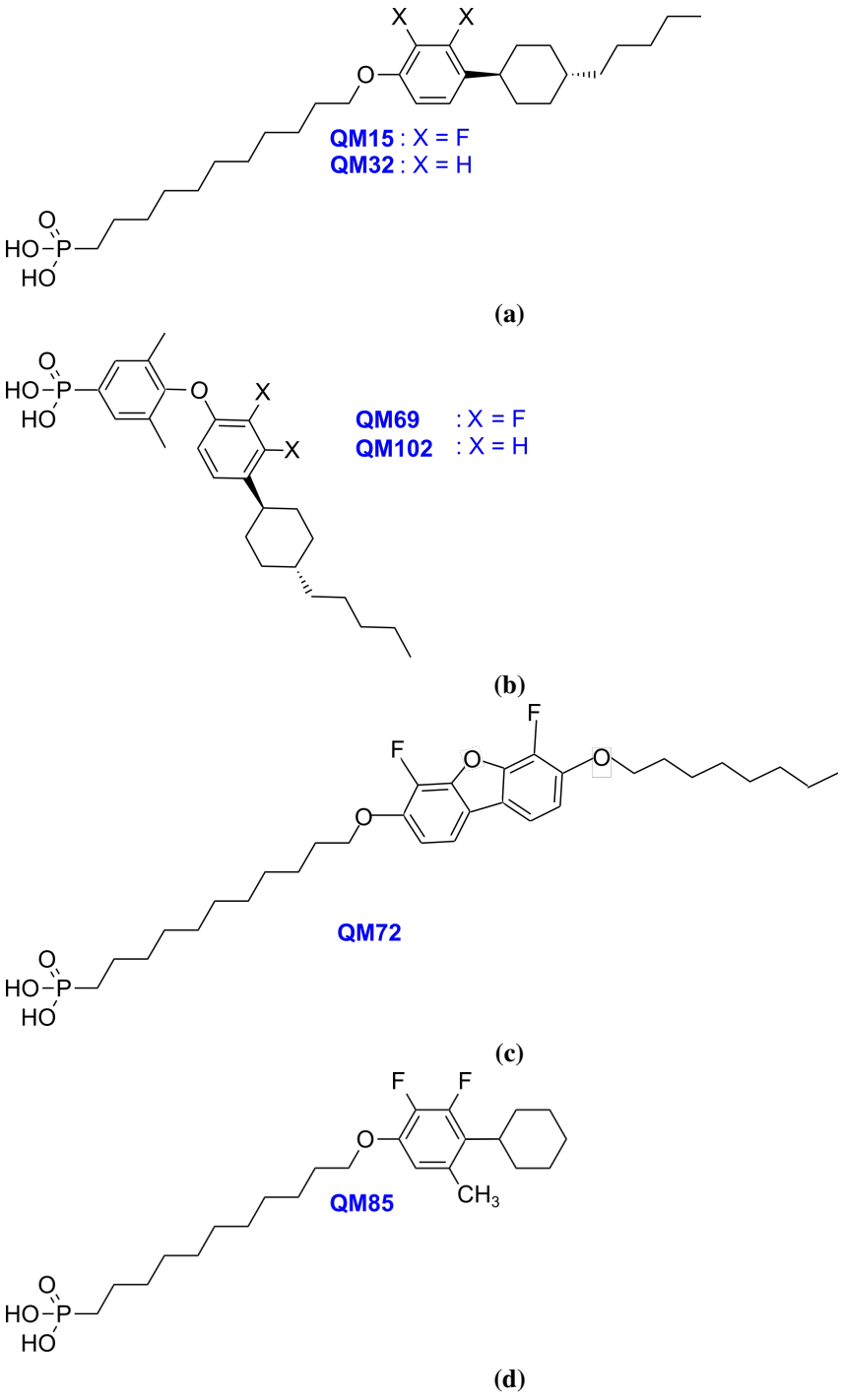

Figure 5.3.2 Structures of liquid crystal-inspired molecules used in this work. a) QM15 and reference compound QM32 are intended to investigate the general principle of using a conformationally flexible dipolar unit as conductance switching moiety. b) QM69 and reference compound QM102 feature a decreased molecular length, an aromatic instead of an aliphatic linker between head and functional group and two methyl groups intended to increase the difference in dipole moment in z-direction between *syn* and *anti* state. c) QM72 features a dibenzofuran moiety as dipolar unit d) QM85 is a shortened derivative of QM15 that a methyl unit intended was added to.

were also calculated. Results for single molecules are listed in Table 5.1, whereas the differences between the conformers for each molecule are listen in Table 5.2. Note that the thickness was calculated from the contour length and the calculated tilt angle - that is the angle between the surface and the main axis of the molecule.
For the 'first generation' molecule QM15^F, the differences between the conformers are negligible for the parameters length, HOMO and LUMO. Only the dipole induced energy shift difference $\Delta\Delta\Phi$ has a significant value. For all molecules the HOMO and LUMO differences between the conformers are $< 0.02eV$ which is negligible for the tunneling models used to model transport later in this work.
The length differences however increase to potentially significant values between 0.1 nm (QM69^F) and 0.62 nm (QM72^F). The difference in dipole induced energy shifts calculated for single molecules range from 84 meV (QM72^F) to 915 meV (QM69^F).

5.3.1 Nomenclature

For reasons of confidentiality as well as brevity, liquid crystal-inspired molecules have been given unique identifiers (UID) that consist of the prefix `QM` and a two to three digit number. Since in this nomenclature it is not immediately evident, whether the molecule was designed to have a significant dipole moment, the unique identifiers were expanded by an additional letter corresponding to the atom responsible for that dipole moment in superscript if this was the case. Since all molecules presented in this work achieved their increased dipole moment by adding a difluoro unit to the aromatic moiety, all molecules designed to provide conductance switching functionality are signified by a capital F in superscript: ^{F}. The non-fluorinated molecules are identified by their UID only. In particular, no superscript is added.
Molecules with an intentionally increased dipole moment and their reference compounds (that only differ in that dipolar unit) are unfortunatly not identifiable through any systematic in their UID. However, in this manuscript, only comparisons between ^{F} molecules and their references as well as between several ^{F} molecules are made. Hence, it should be evident to the reader which molecules are the reference compounds of which fluorinated compounds.
Figure 5.3.2 also includes the nomenclature of all liquid crystal-inspired compounds used in this work. It serves as a dictionary to map the UID to the compounds.

Table 5.1 Calculated properties of molecules with a flexible dipole. Only properties that might have an influence on charge transfer are listed. $\Delta\Phi$ is the molecular dipole induced shift of the vacuum energy level calculated from the Helmholtz equation with surface density $n = 3.1$ and dielectric constant $\epsilon_r = 3$.

Compound		μ_z / D	$\Delta\Phi$ / meV	HOMO / eV	LUMO / eV	tilt angle / °	thickness d / nm	length l / nm
QM15	anti	0.02	9	-5.91	0.09	31.59	2.57	3.02
	syn	-0.71	-275	-5.94	0.07	34.95	2.41	2.94
QM69	anti	-1.62	-630	-6.35	-0.93	47.94	1.21	1.80
	syn	0.73	285	-6.25	-0.74	47.90	1.22	1.82
QM72	anti	0.47	184	-5.42	-0.69	41.43	2.55	3.40
	syn	0.26	100	-5.42	-0.69	19.63	3.12	3.31
QM85	anti	0.23	89	-5.80	0.15	32.06	2.06	2.43
	syn	-0.70	-274	-5.86	0.13	32.10	2.04	2.41

Table 5.2 Calculated property *changes* of molecules with a flexible dipole between their two stable conformers. $\Delta\Delta\Phi$ is the difference in induced energy change between the two stable conformers of the molecule *anti* and *syn* ($\Delta\Delta\Phi = \Delta\Phi$ (anti)-$\Delta\Phi$ (syn), where $\Delta\Phi$ are calculated from the Helmholtz equation). Δ HOMO and Δ LUMO are the differences of HOMO and LUMO between the two conformers and Δd is the change in layer thickness between the two conformers.

	$\Delta\Delta\Phi$ / meV	ΔHOMO / eV	ΔLUMO / eV	Δ tilt angle / °	Δd / nm	Δl / nm
QM15	284	0.03	0.02	-3.36	0.16	0.08
QM69	915	-0.10	-0.19	0.04	-0.01	-0.02
QM72	84	0.00	0.00	21.80	-0.57	0.08
QM85	363	0.06	0.02	-0.04	0.01	0.01

6 Chip Layouts

In order to clearly and distinctively describe the experimental setup, some nomenclature is necessary. Unfortunately, in the field of devices based on molecular monolayers, depending on the author, different words for the same entities are used and a common nomenclature is lacking. One example to illustrate this, is the difficulty of naming the physical entity comprised of a monolayer sandwiched between two electrical contacts of any sort. There is often no clear distinction between *device* and *junction*. To describe the fact, that a self-assembled monolayer is studied, the words self-assembled monolayer, monolayer, molecular, molecular-array, large-area molecular and ensemble molecular are often combined with either *device* or *junction*. The sometimes added *based* concludes the word kit that leads to a vast number of descriptors for the same entity.
In this work, the nomenclature, coined by Vilan et al. is adapted. A physical entity comprised of a self-assembled monolayer sandwiched between two contacts of any sort will be termed *ensemble molecular junction* (NmJ) which is in contrast to the single molecular junction (1mJ). To stress the fact that the monolayer is sandwiched between solid contacts that are connected via leads to either other junctions or contact pads, the term *ensemble molecular device (EMD)* - or simply *device* - is used. [6]
The vertical sequence of materials that constitute a junction will be referred to as *stack*. The entirety of contacts, devices and interconnections and their positions and orientations on the substrate will be referred to as *chip layout*.

6.1 Initial Chip Layout: 8 x 8 Crossbar Array

The initial chip layout was conceived by *Achyut Bora*. It features 8 x 8 crossbar arrays for 6 different junction areas. Eight leads for the bottom contacts are placed in parallel to each other and in perpendicular to 8 leads placed in parallel for the top contacts. Each lead is connected to its own contact pad on one side of the lead. This way, 64 junctions of square area are formed between the intersecting leads of each junction area. For the three larger areas - with edge length 50 µm, 35 µm and 20 µm leads are of rectangular shape. For the three smaller areas - with edge length 15 µm, 10 µm and 5 µm the leads were kept at 35 µm and only dented in the area close to the supposed junctions. This was intended to keep the lead resistance low. A three dimensional illustration of the crossbar array concept is shown in Figure 6.1.1a. A detailed sketch of dented junctions is provided in Figure 6.1.1b.

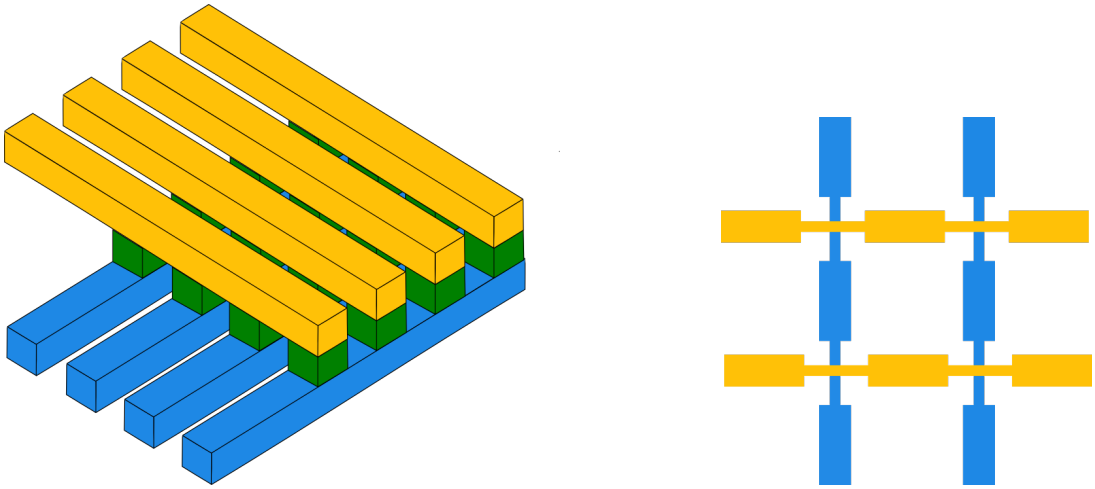

(a) (b)

Figure 6.1.1 Crossbar Array: a) Three dimensional sketch of the basic concept of a crossbar array. Top contact leads (orange) and bottom contact leads (blue) are placed in perpendicular and together with each volume directly between them (green) form a junction. b) Detailed sketch of 4 dented junctions in an array. At the area of overlap of top and bottom contact, a small edge-width can be achieved with bigger leads by denting the leads in vicinity to the junction position.

6.2 Improved Layout: 1D Crossbars

The initial layout comes with several draw-backs that were addressed in an improved chip layout.
In the initial layout, an electrical short in one device would render a whole row and a whole column of devices unable to be characterized. Depending on the distribution of electrical resistances of the devices within an array, so called *sneak paths* could also be present. A sneak path is a path for the current to flow from one contact to the other through more than one device. Since all sneak paths can be seen as resistors in parallel to the desired path, they have to be of much higher resistance to not alter the measurement in the desired path significantly. This situation is illustrated in Figures 6.2.1a and 6.2.1b. Typically, the effect of sneak paths is mitigated by introducing an additional *selector* in series with each device. These selectors can be passive - diodes - or active - transistors. They are used to intentionally decrease the conductance of all nodes within the grid that are not addressed as compared to the resistance of the addressed node. Within the field of memristors, resulting junctions are then termed *1D1R* or *1T1R*, where *D* stands for diode, *R* for resistor and *T* for transistor. [161] While asymmetric placement of an aromatic unit along an aliphatic chain might induce an asymmetry that might in fact already provide enough rectification, this rectification would be dependent on molecular design. To decouple the potential rectifying property ingrained in the different molecular designs explored in this work from their functionality as molecular switches, sneak paths should be avoided.

In order to avoid both, the sneak path and the device malfunction problems described above, the chip layout was re-designed under the constraint of not adding complexity in fabrication or measurement. This can be achieved by a layout where each device has a unique pair of contacts. To achieve this in an area efficient fashion, contact pads for bottom and top contacts were placed in two parallel rows. Both rows share the same spacing between contact pads in the same row and off-set by half of the spacing between each other. Each contact pad was connected to two perpendicularly oriented, rectangular leads. In the upper contact pad row the leads point to the right and down and in the lower contact pad row they point up and to the right. This way, between each pair of top and bottom contact pad, there is only one device while at the same time the number of contact pads is minimized. This also has the advantage, that characterizing a sequence of devices requires movement of

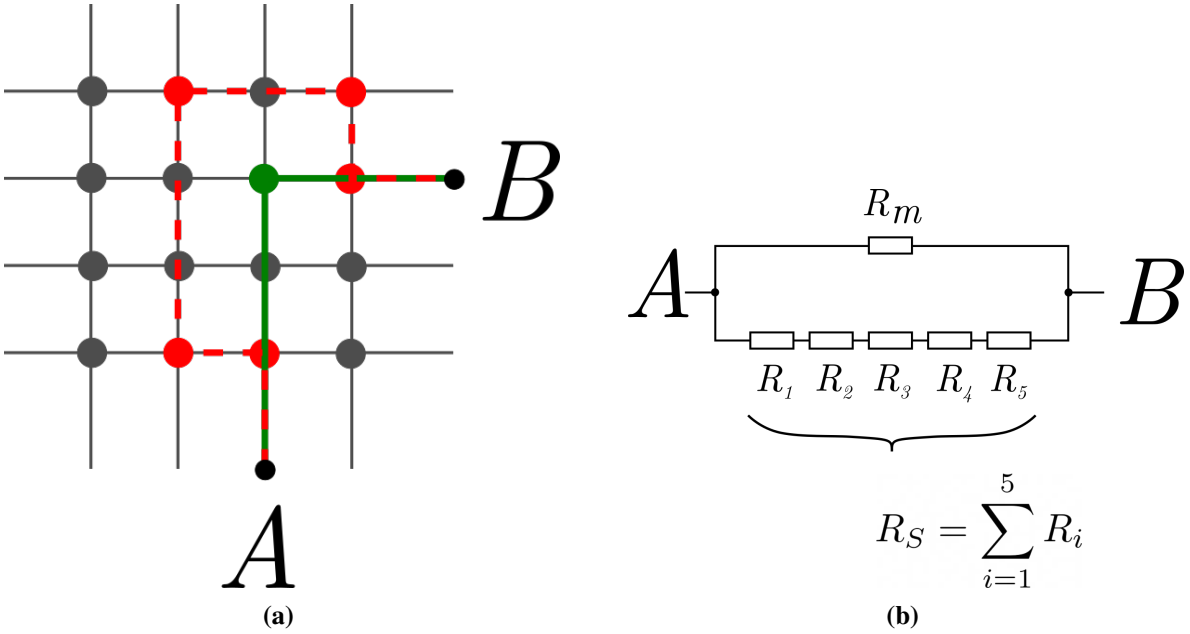

Figure 6.2.1 Sneak path in an array a) Desired path (green) and example sneak path (red). Every node in the grid is a memristor, black lines are leads. b) Equivalent circuit of a), only considering the displayed sneak path. All junctions in a sneak path have an equivalent resistance R_i that is connected in parallel to the memristor resistance R_M, hence influencing the overall resistance between points A and B. Adapted from [216]

only one probe tip in only one direction at a time. Compared to the initial layout this speeds up the contacting process, reduces wear on the pads and would allow using an automatic prober - even if that probe could only move automatically in one direction. Figure 6.2.2 illustrates the concept of this *1D crossbar*.

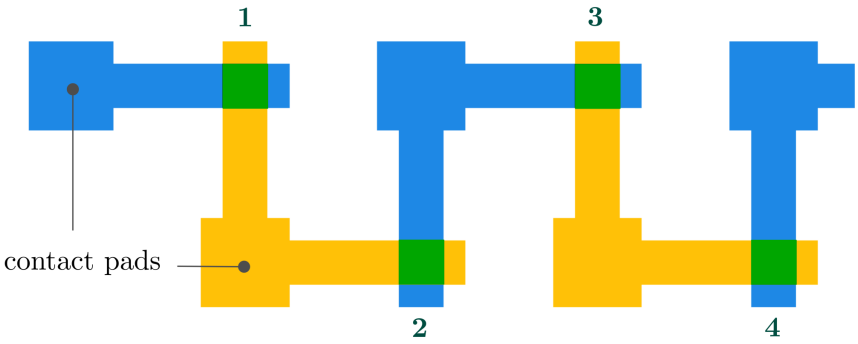

Figure 6.2.2 1D crossbar concept: Top (orange) and bottom (blue) contact are reinforced by a larger contact pad. The areas of overlap constitute the devices or junctions (green). Devices are numbered from left to right. This layout is continued to the right for a total of 20 devices and to the bottom for a total of 6 junction areas.

With a lower aspect ratio of the leads as compared to the initial layout, the use of dented leads is also redundant and was therefore dismissed. This renders the layout more robust to alignment errors when aligning the shadow mask to the substrate. To enable the characterization of devices within an array, two crossbar arrays were placed on the chip: One 1x4 array and one 2x4 array.

In order to be able to experimentally determine the resistivity of the leads, *resistance bars* were also added. These resistance bars are contacted via contact pads on both sides and designed to match the widths present in the devices. Resistance bars for both, bottom and top contact material were added.

The alignment markers for the alignment of the shadow mask to the substrate were also improved by increasing

the margin between the markers on chip and mask. At the opposing edges of the chip a large-area square and a large-area triangle were added on the chip and shadow mask respectively. These visual orientation markers facilitate alignment and further handling of the chip without the need for magnifying equipment, hence also speeding up the alignment procedure and facilitating placement of the chips in a standardized way inside the probe station. Figure 6.2.3 shows the improved chip layout, including 1D crossbars, resistance bars, the two crossbar arrays, two different alignment markers and visual orientation markers.

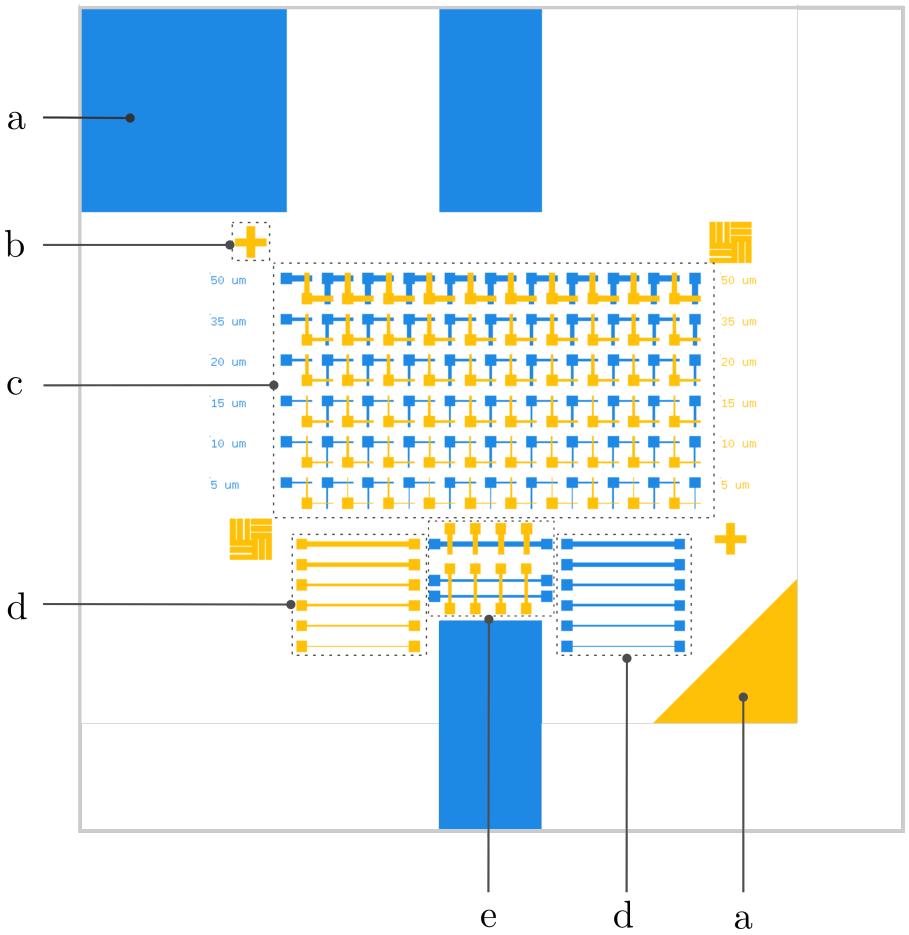

Figure 6.2.3 Improved Layout: Blue: bottom contact, orange: top contact. a) Visual orientation markers b) Alignment marker - only the top structure is visible since the bottom structure directly beneath it is slightly smaller c) 1D crossbars: 20 devices of 6 different junction areas d) Resistance bars e) Crossbar arrays. Boxes with dashed lines are to indicate different areas of the device in this illustration only and have no physical representation.

7 Conductance Switching in Liquid Crystal-Inspired Ensemble Molecular Junctions

In this chapter, the concept of utilizing ensemble molecular devices based on liquid crystal-inspired molecules as electrically switchable tunneling barrier is thoroughly investigated. Since both, aluminum oxide as substrate and lead as top contact metal to self-assembled monolayers [22] have been previously reported, the ***aluminum oxide / SAM / lead / silver*** *stack was chosen to fabricate solid-state devices. Successful SAM formation of the 'first generation' molecules QM15^F and QM32 on plasma-treated aluminum surfaces, was confirmed via AFM, WCA, VASE, and XPS. The orientation of the dipolar unit of QM15^F was probed via NEXAFS. Crossbar arrays with the aforementioned stacks were then fabricated and electrically characterized. Integrity of the monolayer after top contact formation was confirmed via TEM crossection imaging. Experimentally determined tunneling currents were finally compared to single molecule calculations, molecular dynamics simulations as well as to a device model based on the Gruverman model. This chapter closely relates to the work that is currently under review [154]. AFM, WCA and VASE measurements in this chapter were performed by Sebastian Resch, NEXAFS and XPS measurements were performed by Christian Seim and Alexei Nefedov at the HE-SGM beamline of synchrotron facility BESSY II (Berlin), TEM cross-section imaging was performed at Samurai Semiconductors (Japan), molecular dynamics simulations were performed by Falk May and TranSIESTA and GAUSSIAN calculations were executed by Peer Kirsch.*

The basic concept of conductance switching through liquid crystal-inspired molecules was conceived as dipole-induced: The potentially conductance switching molecule combines a tunneling barrier, implemented as alkyl chain, with an asymmetrically embedded dipolar unit, implemented as difluorophenyl cyclohexane. The dipole induced energy shift then alters the height of the tunneling barrier on one side of the barrier. Since the dipolar unit is placed on a flexible linker, it is able to align with an external field. Hence, the dipole direction and with it the magnitude in the direction normal to the attached electrodes, becomes electrical field controlled. Since this magnitude of the dipole moment is directly connected with the induced energy shift via the Helmholtz equation, the barrier on one side of the alkyl chain is expected to become electrical field controlled. The tunneling current through a barrier with two distinct barrier heights on each side of the barrier in turn depends on the height of both barriers as well as on the width of the barrier. Keeping the overal width as well as the height on one side constant and the barrier on the other side electrical field controlled should hence ultimately result in electrical field controlled conductance switching that is dominated by the effect of dipole reorientation.
In order to test the general feasibility of this concept within an ensemble molecular device, devices with QM15^F sandwiched between aluminum oxide and lead were conceived. On top of the lead electrode, silver was added as a capping layer to slow down potential oxidation of lead in air during post-fabrication transport,

measurement and storage. To provide electrical contact on both sides, aluminum, covered by a native oxide under ambient conditions, was chosen as bottom contact material.
First, surface grafting of QM15^F and its reference compound QM32 on plasma-oxidized aluminum (as well as on ALD-deposited Al_xO_y) was performed and resulting layers were analyzed using a plethora of surface characterization methods. Then, ensemble molecular devices with QM15^F and QM32 were fabricated and characterized by recording current-voltage traces and calculating current density-voltage (J-V) traces. Computations on single molecule, monolayer and device level to further the understanding of the conductance switching mechanisms were then performed and compared to experimental results.

7.1 Surface Characterization

First, the potential to form self-assembled monolayers of the two liquid-crystal inspired molecules QM15^F and QM32 was explored. To this end, substrates with ambient facing aluminum or aluminum oxide layer were treated with an O_2 plasma at 150 W for 1 min and then directly immersed in 1 mM solutions of the respective molecule. The coating vessel was sealed airtight afterwards and samples were immersed for 72 h at room temperature (T = 22 °C). Samples were then taken out of the solution, blown dry in a N_2 stream and subsequently heated on a hotplate at 120 °C for 1 h. They were left to cool down, rinsed in a steady stream of ethanol at ≈10 ml/s, blown dry with a N_2 stream and subsequently heated for another 10 min at 120 °C. Samples were then analyzed using high resolution XPS, NEXAFS, AFM and water contact angle. For each measurement method, different samples were used. Details on the types of aluminum or aluminum oxide surfaces used for each measurement modality are given in the respective sections below.
Water contact angle (WCA) analysis was performed as a first indicator of successful monolayer formation. Atomic force microscopy (AFM) measurements were performed to investigate the uniformity of the potentially formed SAMs. High resolution XPS spectra were recorded to confirm the presence of the respective molecules on the treated substrates. NEXAFS measurements at varying angles and the analysis procedure outlined in Chapter 3 were performed to determine the average tilt angle of the aromatic moiety within the monolayer.

7.1.1 WCA, AFM and VASE

For WCA, AFM and VASE analysis, Si(250µm)/SiO_2(850nm)/Al(50nm) substrates were treated with an 80 W oxygen plasma for 1 min to achieve a thin oxide layer on top of the substrate. Molecules QM15^F and QM32 were then grafted from 1 mM solutions in THF onto the substrate using the standard procedure outlined in Chapter 4.
Water contact angle measurements were performed using a MobileDrop GH11 (Krüss GmbH, Germany). For each measurement, 2 µl de-ionized water was dispensed manually. The contact angle on both sides of the droplet was measured, using the *Advance* software of the instrument. The angles were then averaged and the measurement was repeated at least two times per sample to yield the overall average WCA of the sample.
For atomic force microscopy, substrates were imaged with Park NX20 AFM system from Park Systems in non-contact mode at a scan rate of 0.7 Hz. PPP-NCHR tip (Park Systems) with nominal force constant 42 N m^{-1}, resonant frequency 330 kHz, and tip radius < 10 nm, typically 7 nm, was used.
VASE measurements of the layer thickness was performed using a Woollam M-2000 Ellipsometer (J. A. Woollam Co.), wavelength range 245-1000 nm. Measurements were performed at incidence angles of 65°, 70° and

Table 7.1 Surface characterization of various substrate-SAM combinations.

Surface	WCA /°	Roughness RMS /nm	SAM Thickness /nm
Al_xO_y	84 ±2	0.4	0
Al_xO_y/QM15^F	108 ±2	0.1	3.3±0.1
Al_xO_y/QM32	109±2	0.1	3.3±0.1

75°. Analysis was done fitting the Al_xO_y substrate with an optical model containing a Si substrate (Si_JAW model), a native SiO_2 layer (NTVE_JAW model) of 1.38 nm and an Al_xO_y layer (Al_xO_y (Cauchy) model) of 2.81 nm thickness, where the latter value was determined from fitting VASE measurements of pristine substrates to layers with the mentioned optical constants. For the SAM film a Cauchy model (A = 1.450, B = 0.01, C = 0) with Urbach absorption (k-amplitude = 0.01213, exponent = 1) was assumed. Two samples of each material were fitted simultaneously in a multi sample analysis and results were averaged. Due to the challenges of VASE with respect to measuring the thickness self-assembled monolayers, outlined in Chapter 3 and further evaluated in the next chapter, the determined values were taken as comparative measure rather than absolute value. For both types of molecules, the same parameters (A, B, C in the Cauchy model and Urbach absorption constants) were chosen.
Table 7.1 summarizes the results of the inital surface characterizations from WCA, AFM and VASE measurements.

The difference in water contact angle from 83.6° (Al_xO_y) to 108.4° (Al_xO_y/QM15^F) and 109.3° (Al_xO_y/QM32) can be ascribed to the surface facing moiety changing from hydroxyl on the bare substrate to methyl on both the SAM coated samples. The low surface roughness and measured thickness of the coated samples in the range of the length of the molecules confirm successful monolayer formation. The similarity of the result of the VASE measurement with the same optical constants also indicates a high similarity of the monolayers of both molecules with respect to all parameters that potentially influence the optical constants, such as, e.g., surface density.

7.1.2 XPS

X-ray photoelectron spectra were recorded for one sample per molecule. To that end, monolayers of QM15^F and QM32 were grown on ultra-thin ALD deposited aluminum oxide.
The substrates were prepared by deposition of a thin Al_xO_y layer on top of a boron-doped 6 inch silicon wafer. Silicon oxide was removed prior to Al_xO_y deposition by a short dip in aqueous hydrofluoric acid (1% v/v, DI water, 1 min, room temperature). Aluminum oxide was then deposited via atomic layer deposition. The resulting Al_xO_y layer thickness was measured by VASE and found to be ≈3 nm thick. The wafer was then diced into 8 mm x 8 mm chips. Two of these chips were then immersed in 1 mM solutions of QM15^F or QM32 in THF for 72 h. Samples were kept in air tight sealed vessels for 72 h, then dried in a N_2 gas stream, annealed for 1 h at 120 °C. They were then rinsed with 10 ml of ethanol and subsequently blown dry in a N_2 gas stream.
Figure 7.1.1 shows the XP survey spectra of both samples. Since both molecules share several characteristics in their chemical constituents, so do the recorded XP spectra.
Peaks and orbital splittings that are characteristic for the substrate can be observed for both samples. Specifically, they both show peaks at 74.1 eV (Al2p), an orbital splitting at 99.0 eV and 102.9 eV (Si2p) as well as at 120.3 eV (Al2s). These are typical for Al_xO_y and AlSiOx directly confirming the presence of a thin Al_xO_y layer on

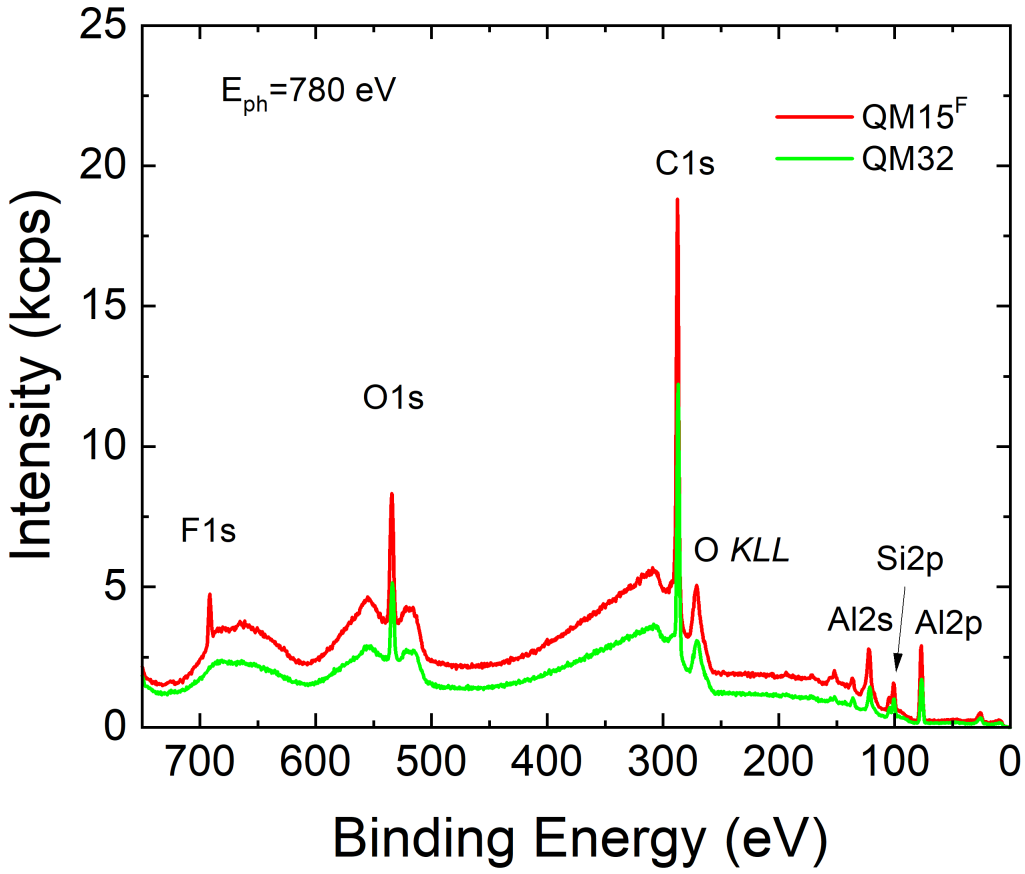

Figure 7.1.1 XPS spectra of the first generation of liquid-crystal inspired molecule grafted Al_xO_y surfaces acquired at 780 eV excitation energy. *Red*: QM15^F and *green*: QM32. Since both molecules differ only in the presence or absence of fluorinated carbon, their spectra only differ significantly at the carbon-bound fluorine peak at 689.9 eV. Similar figure submitted to [154]

top of the silicon substrate.

The presence of molecules with a phosphonic acid anchoring group was confirmed by a weak phosphorus signal at 133.2 eV (P2p), which is characteristic for a PO_3^- group and is expected for a surface-bound phosphonic acid group. The presence of organic constituents was confirmed via the presence of the C1s peak at 285.0 eV that is typical for both aliphatic and aromatic carbon. The O1s peak at 532.4 eV is expected for both, the mixed oxide layer and the oxygen atoms in the SAM itself. Together, these three peaks confirm the presence of a carbon based, surface-bound phosphonic acid on the samples.

Both molecules differ in the presence or absence of organic fluorine. This is also observed in the XPS spectrum. Only the sample grafted with QM15^F shows a F1s signal at 689.9 eV, typical for organic fluorine. The data originating from QM32 does not show a peak at this position. This confirms the presence of the intended molecules on the studied samples.

To further investigate the differences between the two samples, High Resolution X-Ray Photo-Electron Spectra (HR-XPS) of Al2p, P2p and C1s at 350 eV excitation energy as well as F1s at 750 eV excitation energy were acquired. The results are displayed in Figure 7.1.2. The phosphorus and the aluminum spectra confirm the phosphonate binding for both samples with no significant differences between the spectra of QM15^F and QM32 grafted samples. The carbon and fluorine spectra highlight the subtle differences between the two samples. The C1s peak of the QM15^F sample shows a shoulder at ≈287 eV, most likely originating from the C-F bond within the molecule. The C1s peak of the QM32 sample shows no such shoulder. The F1s is only present in the

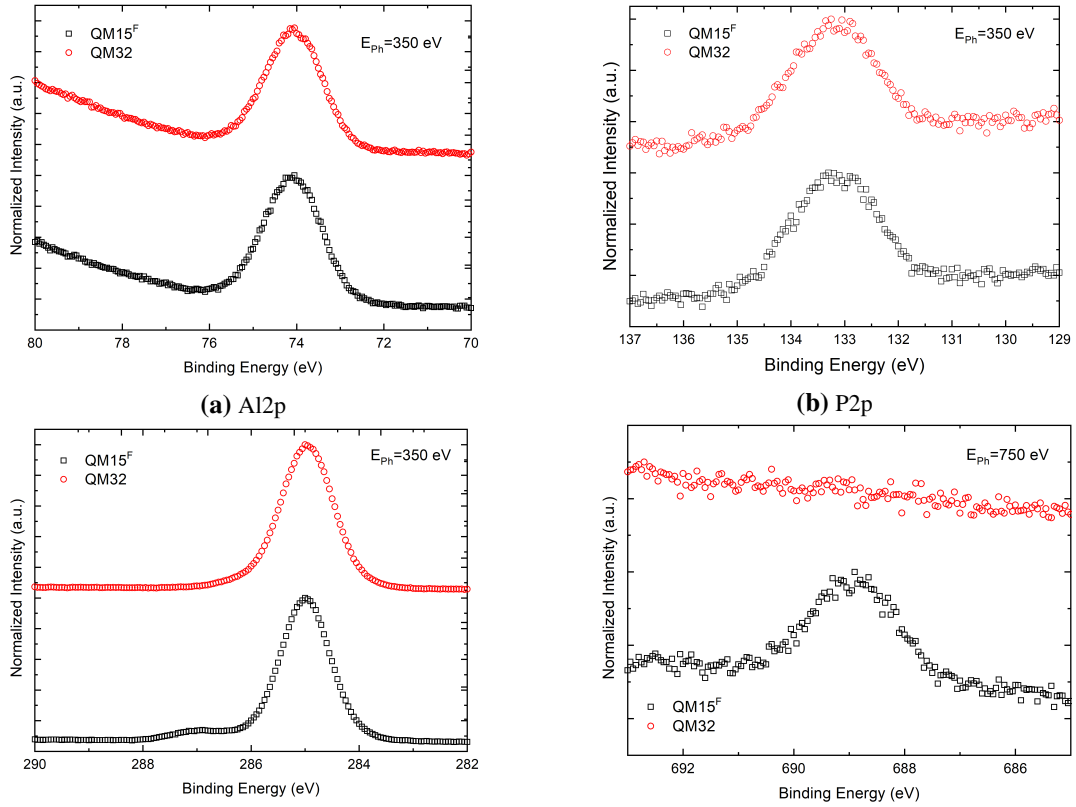

(a) Al2p **(b)** P2p **(c)** C1s **(d)** F1s

Figure 7.1.2 High resolution XPS spectra of QM15^F and QM32 grafted Al$_x$O$_y$ surfaces at positions characteristic for a) Al2p b) P2p c) C1s and d) F1s. Red open circles: QM32, black open circles: QM15^F. Excitation energies were 750 eV for the F1s signal and 250 eV for all others. Al2p and P2p signals are highly similar whereas C1s and F1s signals show characteristic differences for the two SAM forming molecules. In the C1s signal, only for QM15^F grafted surfaces the C-F shoulder at ≈287 eV is visible. The F1s signal is nearly flat for QM32 and shows a signal for QM15^F. These results point towards the intended molecules being present on the corresponding substrates. Figures submitted to [154]

spectrum from the QM15^F sample and clearly absent in the spectrum of the QM32 sample.
Overall, the XPS spectra qualitatively confirmed the presence of the intended molecules on the respective surfaces and point towards successful monolayer formation.

7.1.3 NEXAFS

Near-edge absorption fine structure measurements with polarized X-ray radiation were performed for the samples that were previously analyzed using XPS. The carbon K edge was chosen as absorption edge for further analysis. Measurements were performed and referenced as described in Chapter 3. Figure 7.1.3 displays the NEXAFS spectrum at several angles of incidence, including the magic angle $\theta = 55°$.
The electronic structure of the unoccupied molecular orbitals can be derived from the spectrum taken at the magic angle to eliminate the influence of orientation effects. The dominant resonances within the spectra for QM15^F and QM32 at ≈286 eV and ≈289 eV can be assigned to the C1s $\pi^*_{1,2}$ and $\pi^*_{3,4}$ transition. This orbital splitting is well known and described, for instance in [217]. Additional resonances can be found at ≈290 eV, ≈293 eV, and ≈300 eV. These are tentatively assigned to C1s σ^* transitions. [218]

In order to calculate the angle between the E-field of the incident x-ray and the average transition dipole moment of the molecules within the SAMs under investigation, the recorded spectra were analyzed using the procedure outlined in Chapter 3. To this end, the intensity of the first $\pi^*_{1,2}$ was plotted against the X-ray incidence angle for both molecules and the data was fit to $\sin(\alpha)$. The data as well as the fit are displayed in Figure 7.1.4. The fit resulted in a transition dipole tilt of $\alpha = 67°$. To calculate the average tilt angle of the aromatic ring β, the twist angle γ was set to 0°. Given that $\cos(\alpha) = \sin(\beta)cos(\gamma)$ this yields $\beta = 23°$.

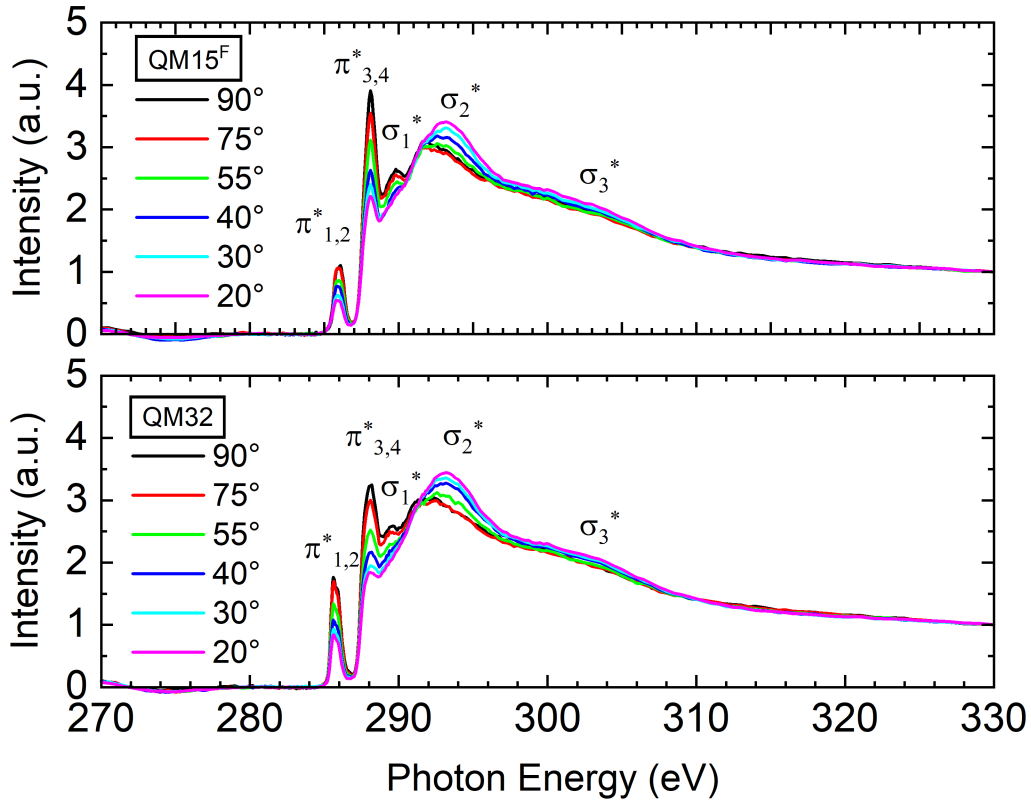

Figure 7.1.3 C-K edge NEXAFS spectra for QM15^F (*upper panel*) and QM32 (*lower panel*) for different X-ray angles of incidence, including the magic angle 55°(*green*). The assignment of resonances is noted above corresponding peaks. Spectra at angles other than the magic angle significantly differ from that at the magic angle, indicating the presence of an aromatic moiety with a preferential orientation on the surface. Similar figure submitted to [154]

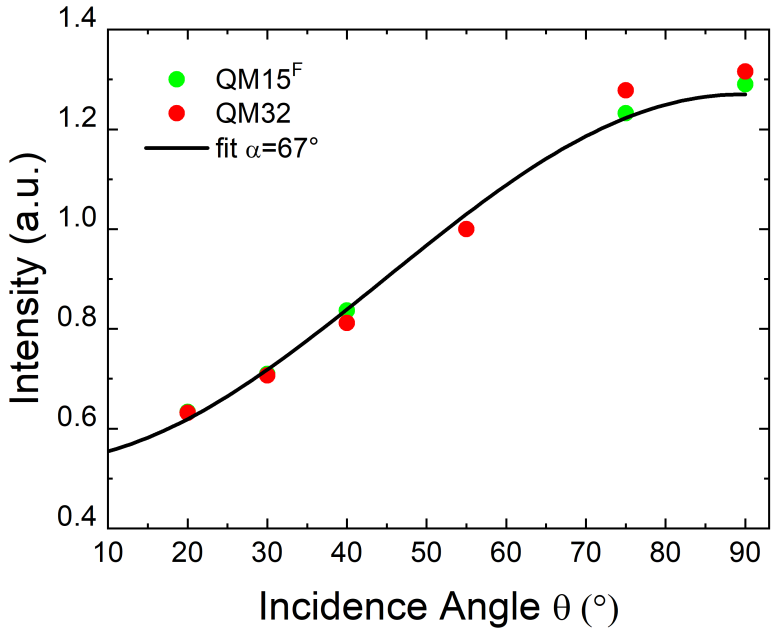

Figure 7.1.4 Intensities of the first $\pi^*_{1,2}$ resonance versus x-ray angle of incidence for QM15^F (green) and QM32 (red), as well as a fit to equation 3.3.6 that yields $\alpha = 67°$, that ultimately determines the average tilt angle of the aromatic ring $\beta = 23°$. Figure submitted to [154]

7.1.4 Surface Characterization Summary

In summary, aluminum oxide surfaces immersed into 1 mM solutions of QM15^F and QM32 in THF exhibit:

- increased contact angles as compared to bare aluminum oxide surfaces,
- decreased roughnesses as compared to bare aluminum oxide surface,
- similar VASE-derived thicknesses,
- XPS resonances at energies that are characteristic for atoms within the molecules, and
- a clear x-ray angle of incidence dependence of the first $\pi^*_{1,2}$ resonances that dipole-induced a theoretically predicted trend in NEXAFS measurements.

Combined, these results strongly indicate the successful formation of self-assembled monolayers of QM15^F and QM32 on aluminum oxide surfaces.
Additionally, the average tilt angle of the aromatic ring, as calculated from the NEXAFS measurements, was found to be the same for SAMs QM15F and its reference compound QM32. This indicates a similar distribution of molecular orientations for both compounds. Hence, differences in electrical characterizations are unlikely to be the result of significantly different initial local surroundings induced by potentially different monolayer formation.

7.2 Ensemble Molecular Device Characterization

It has been shown by others, that monolayers of phosphonic acids can be grown on plasma-oxidized aluminum [219] as well as naturally oxidized aluminum [196] and that physical vapor phase deposited lead forms top contacts on methyl-terminated SAMs without compromising device functionality. [22] A **plasma oxidized aluminum/SAM/Pb/Ag** stack was hence conceived to measure the response of SAMs of liquid crystal-inspired molecular monolayers to an electrical stimulus. To this end, 50 nm of aluminum was vapor deposited on a previously cleaned Si/SiO_2 wafer, that was subsequently cut into 8 mm x 8 mm chips. The bottom electrodes were then structured using the procedure outlined in Chapter 4. Chips were then cleaned, exposed to oxygen plasma at 80 W for 60 s and finally immersed in 1 mM solutions of $QM15^F$ or QM32 in completely filled and sealed vials for 72 hours. Samples were then taken out from the solutions, heated at 120 °C for 1 h and subsequently rinsed in THF. After samples were blown dry in a N_2 stream, a shadow mask was aligned following the procedure outlined in Chapter 4. For the top electrode, 300 nm Pb and 100 nm Ag were physical vapor phase deposited without breaking the vacuum between the subsequent evaporation steps. To allow the sample to cool down in-between the evaporation steps, there was a 5 min break between those two steps. Samples were then transported in a desiccator filled with silica gel to the probe station in order to minimize the exposure time of the samples to ambient atmosphere.

7.2.1 Electron Microscopy

To confirm integrity of the monolayer after top contact evaporation, TEM crossectional imaging was performed for devices with $QM15^F$ or QM32 sandwiched between Al/Al_xO_y and Pb/Ag as well as for a reference device without any molecule. The resulting images of the FIB-cut lamellae are shown in Figure 7.2.1. The lamellae originating from devices with embedded monolayer exhibit a light layer in-between the two darker regions, whereas the lamella originating from the reference device (without monolayer) only shows the two darker regions. Since contrast in TEM images stems from mass and thickness and over the area of one lamella the thickness is constant, lighter areas indicate atoms with lower mass. Since the atom mostly constituting the SAM - carbon - has a much lower mass than the surrounding Pb and Al, the lighter region can be ascribed to the SAM. As can be seen in the image, the lighter region is intact over the whole imaging region. This indicates successful perseverance of the integrity of the monolayer after condensation of the Pb atoms on top. Measuring the thickness of the lighter region using the size reference within the image yields a SAM thickness of 3.4 ± 0.5 nm. This is in very good agreement with the thickness previously measured using VASE (3.3 nm) and the value calculated using geometric optimization in GAUSSIAN (*anti*:2.78 nm, *syn*:2.81 nm), taking the tilt angle of the molecule into account. Structural integrity of the top electrodes was investigated by taking SEM images of the finished device array and single junctions. Figure 7.2.2 displays colorized SEM images of both a whole crossbar array as well as a single junction. These images show structurally intact electrodes at the junctions as well as between junctions.

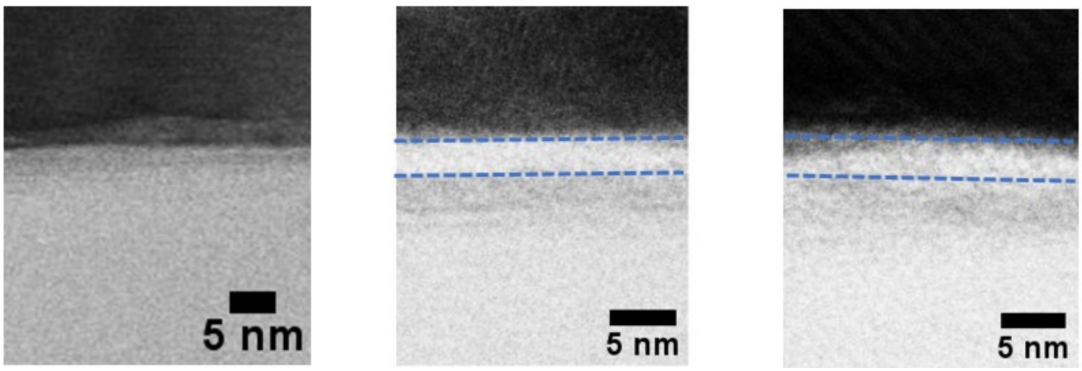

(a) (b) (c)

Figure 7.2.1 TEM images of FIB-cut lamellae of Al/Al$_x$O$_y$/../Pb/Ag stacks cut from 15 µm x 15 µm junctions a) without molecule, b) with QM15^F sandwiched between the electrodes and c) with QM32 sandwiched between the electrodes. Light grey horizontal stripes in b) and c) are indicative of an organic layer. Dashed blue lines are meant to guide the eye. Figure as submitted to [154].

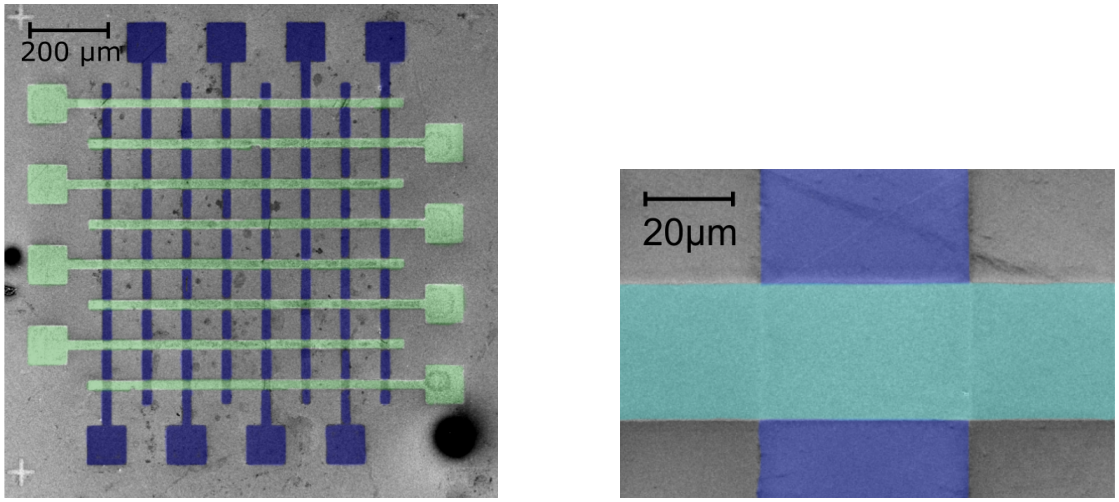

(a) (b)

Figure 7.2.2 Colorized SEM images of Al/Al$_x$O$_y$/QM15^F/Pb/Ag junctions of a) a crossbar array of 25 µm x 25 µm junctions (green: top electrode, blue: bottom electrode) b) a single 50 µm x 50 µm junction (turquoise: top electrode, blue: bottom electrode). Both show structural integrity of the electrodes both at and next to the overlap of top and bottom electrodes. Figure b as published in [154]

7.2.2 Current Voltage Spectroscopy

Ensemble molecular junction with embedded SAMs of QM15^F were electrically characterized by applying a voltage to the top versus the bottom contact and varying this voltage in a cyclic manner. Starting from zero, the voltage was first increased to 3.0 V. The sweep direction was then reversed until the maximum voltage of opposite polarity, before sweeping back to zero. This cycle was then repeated, typically until 10 cycles were complete. The sweep speed was 50 mV s^{-1}. Each cycle therefore corresponds to a measurement duration of 4 minutes. The maximum absolute sweep voltage was determined by ramping up the voltage on a 'sacrificial' device starting from 0 V to 10 V and observing a sharp increase in current at $\approx$ 3.1 V. This was considered the voltage at which the device exhibits electrical breakdown and the maximum voltage was chosen to be as close to it as possible without risking device failure. From the data obtained through cycling the voltage, the current density was calculated by dividing the current by the area of the device under test. Figure 7.2.3a displays the average and envelopes of these J-V traces for an exemplary device. The current densities show a pronounced hysteresis: depending on sweep direction and voltage history of the junction, a distinct high resistive state (HRS) and low resistive state (LRS) can be observed. The states do not show an abrupt switching as typically observed in other conductance switching material systems, such as, for instance electrochemical metallization cells. The ensemble molecular junctions rather exhibit a gradual change of conductance with bias voltage. At a reference voltage of -1.0 V the exemplary device shows a ON/OFF ratio of LRS-current density divided by HRS-current density in the order of 10^2. Figure 7.2.3b displays the J-V traces of a reference device of the same area, containing the non-polar, non-fluorinated reference compound QM32. Current densities are in range with the LRS of the QM15^F device. However, the reference junction does not exhibit such hysteresis. This presents preliminary evidence, that the embedded molecular dipoles are indeed responsible for conductance switching within the ensemble molecular devices.

To investigate whether this phenomenon can be observed repeatedly across multiple junctions, multiple devices of the same area on the same chip were measured. Figure 7.2.4 displays the average and envelopes of the averages from 6 different QM15^F devices as well as the ON/OFF ratios versus voltage. To calculate this average, the average currents of all devices were averaged. The average of six devices also shows a pronounced hysteresis that dipole-induced the trend described for the exemplary device. The ON/OFF ratio of this average of averages shows a clear voltage dependency with ON/OFF ratios of negative voltages consistently being higher than those at the same absolute voltage with opposite polarity. The ON/OFF ratio exhibits a maximum of 303 at -1.8 V.

The repeatability of the switching process of the monolayer junction was probed by cycling one device between the maximum voltages of opposite polarity for 100 times. The J-V traces of one 15 µm x 15 µm area device as well as the current densities of the HRS and LRS state in each cycle at evaluation voltage V=-1 V are displayed in Figure 7.2.5. On average, this device exhibited hysteresis for all 100 cycles. As shown in the figure, the envelopes do not overlap for applied voltages from -1 V to 0 V, but do overlap outside this voltage window. This means that for the 100 cycles presented here, only for voltages $\in [-1; 0]$ V two conductance states can be distinguished with a single measurement without knowing anything about the device's history. Current density versus cycle number was hence analyzed for a voltage within this window, namely V = -1 V. Current densities continuously decreased for the HRS from $6.5 \cdot 10^{-7}$ mA/cm^2 at the first cycle to $1.93 \cdot 10^{-7}$ mA/cm^2 at the 97th cycle. In other words, current density in the HRS decreased to 1/3 of its initial values after 100 cycles. Few outliers breaking with this general trend can be observed at cycles 11, 22, 61, 62, 64, 98-100. The LRS current

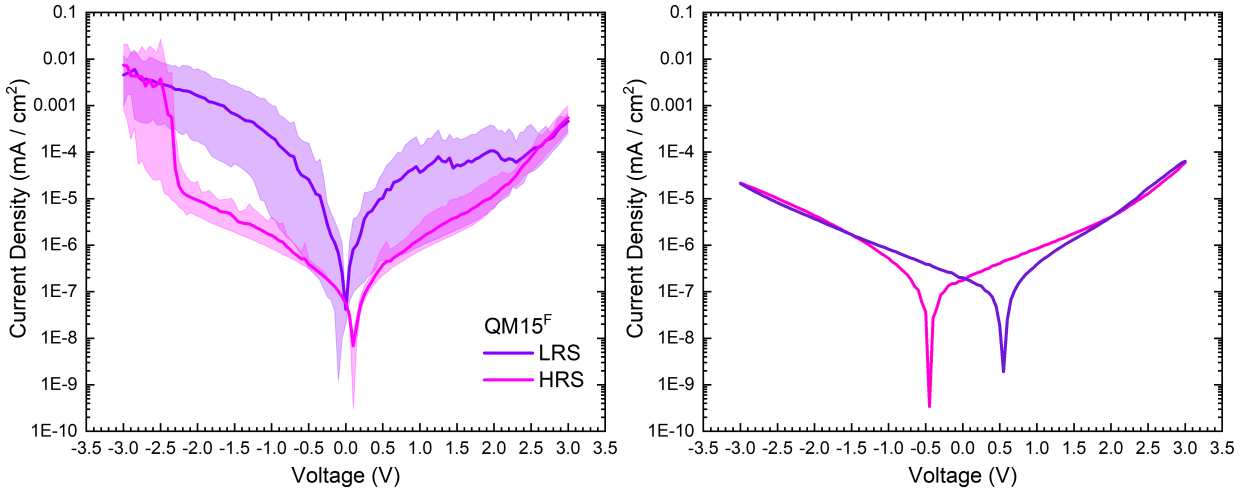

Figure 7.2.3 a) Semi-logarithmic representation of the absolute current density-voltage (J-V) characteristics of an **Al/Al$_x$O$_y$/QM15^F/Pb/Ag**, 25 µm x 25 µm junction. Bold curves show the average of 10 cycles: *light magenta* for the HRS and *dark violet* for the LRS. The thin curves below and above the average are the measured minimum and maximum current traces (envelopes). c) Reference J-V data for a reference junction containing QM32, showing the average of 10 cycles. Envelopes are hardly visible due to low sweep-to-sweep variability. The offset on the voltage axis can be assigned to capacitive charging currents. Adapted from figures published in [154]

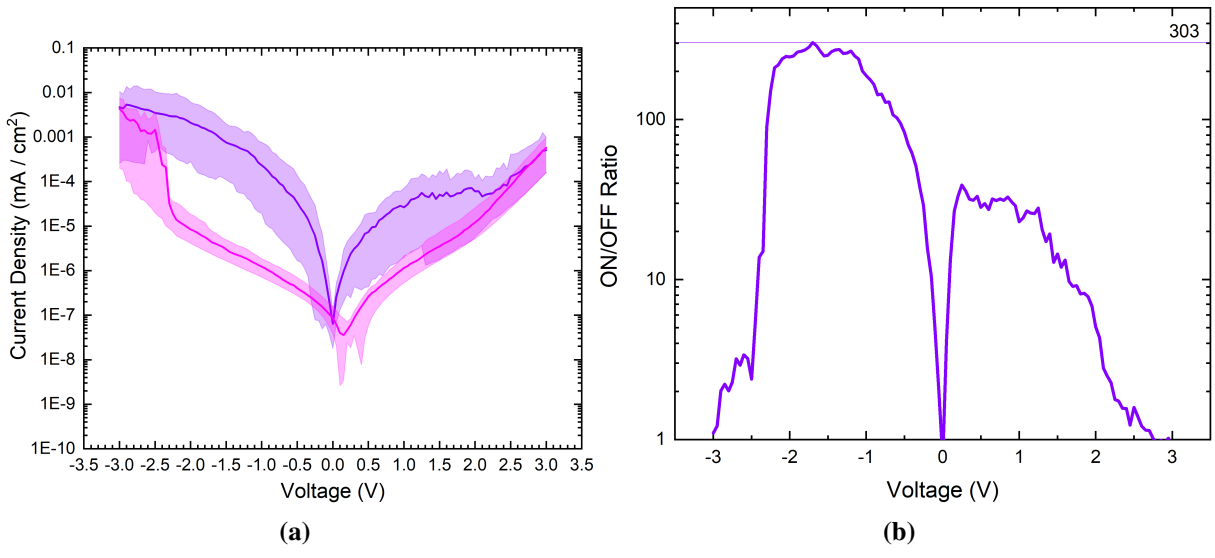

Figure 7.2.4 Average current density-voltage characteristics of 6 Al/Al$_x$O$_y$/QM15^F/Pb/Ag devices, each of area 25 µm x 25 µm. *Bold curves* show the average of 6 devices: *light magenta* for the HRS and *dark violet* for the LRS. The thin curves below and above the average are the measured minimum and maximum current traces (envelopes). b) ON/OFF ratios versus voltage calculated for the data shown in a. Horizontal line indicates the maximum value. a) is adapted from a figure submitted to [154]

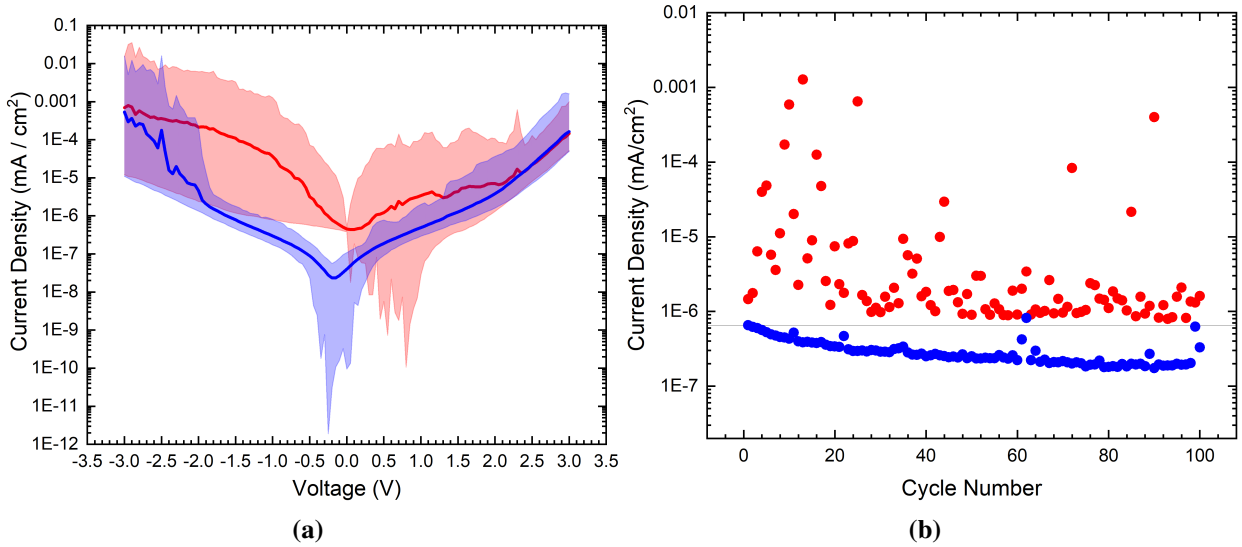

Figure 7.2.5 Electrical characteristics of a 100 cycle measurement of an Al/Al_xO_y/QM15^F/Pb/Ag device of area 25 µm x 25 µm. a) Current density-voltage characteristics. Bold curves show the averages: Red for the LRS and blue for the HRS. The thin curves below and above the average are the measured minimum and maximum current traces (envelopes). Envelopes of HRS and HRS overlap for V $\notin [-1;0]$V b) Current density at V=-1 V versus cycle number, extracted from the data summarized in a). Red for LRS and blue for HRS. Grey horizontal line marks the HRS current density of the first cycle. All but one of the data points for HRS are lower and all datapoints of the LRS exhibit a higher current density. HRS and LRS are therefore clearly distinguishable for all but one cycle.

density at -1 V on the other hand shows a high sweep to sweep variance with current densities ranging over almost four orders of magnitude ($8.1 \cdot 10^{-7}$ mA/cm^2 to $1.3 \cdot 10^{-3}$ mA/cm^2). For all but cycle 62, LRS and HRS are clearly distinct states. For practical applications of a conductance switching device, conductance states have to be clearly distinguishable for as many switches between the states as possible. Taking the first cycle's HRS current density as reference, in all but one cycle HRS current density is below that value while LRS current density is above it for all cycles. Overall this data suggests stable, repeatable switching between two clearly distinguishable conductance states for at least 100 voltage cycles.

In summary, the electrical characterization of ensemble molecular devices with QM15^F revealed a pronounced hysteresis for seven devices, a voltage dependent average ON/OFF ratio with a maximum of 303.03 at -1.8 V and consistent switching between two distinct conductance states for at least 100 cycles. In particular, this means that conductance switching is observed across several devices and across several cycles. Devices with unpolar, non-fluorinated reference compound QM32 did not show such hysteresis. As will be elaborated further in the following, the observed bi-stable, gradual conductance switching can since be assigned to conformational changes of the embedded molecular dipoles.

7.3 Theoretical Calculations

In order to investigate the microscopic mechanism of the observed pronounced hysteresis, the anticipated reorientation of the molecular dipoles in the external electric field is further studied.
First, to get an estimate of the energy required to switch between the two conductance states the intramolecular rotational barrier of the fluorinated molecule was calculated.
Transfer current simulations based on density functional theory of single molecules between two gold point contacts were performed for both conformers to examine the influence of electrical configuration change on tunneling current.
Molecular dynamics simulations were performed to get some insight into the distribution of dipole orientations of the molecule within a SAM and on the change of this distribution through the application of an external bias.
A model of the ensemble molecular device based on the Gruverman tunneling model was conceived and experimental data was compared to it, in order to analyze whether reorientation of molecular dipoles can account for the experimentally measured hysteresis.

7.3.1 Rotational Scan

The proposed microscopic mechanism of the observed pronounced hysteresis is an anticipated reorientation of the SAM molecular dipoles. To achieve two clearly distinguishable states, there have to be somewhat stable orientations of the 2,3-difluorophenylene unit, which presents the rotatable local dipole unit within the molecule, ultimately causing a two-state change in the fluorine-associated dipole in z-direction. To investigate whether QM15^F exhibits those energetic minima, a potential energy profile of an isolated model compound was calculated using density functional theory. The model compound which was used for these calculations as well as the definition of the dihedral angle is shown on the right in Figure 7.3.1. The relative energy with respect to the *anti* state was calculated for varying dihedral angles in Figure 7.3.1 using the M06-2X-D3/6-31G(d) level of theory within GAUSSIAN 16, Revision C.01, Version 3. For the minima from these calculations, an additional zero-point energy (ZPE) correction was performed. This is necessary since even at T = 0 K vibrational modes lead to a non-zero energy of the system. The ZPE is calculated from a harmonic oscillator model as a sum of contributions from all vibrational modes of the system and ultimately estimates the energy of the molecule in its lowest vibrational state at T = 0 K, where it does not possess any translational or rotational energy yet. Figure 7.3.1 displays the results of that potential energy profile. Two distinct minima can be observed. They are separated by intramolecular barrier of 1.41 kcal mol^{-1} (2.38 kT at 298K) from *anti* to *syn* and 2.10 kcal mol^{-1} (3.54 kT at 298 K) from *syn* to *anti*. For a single isolated molecule this means that relatively unhindered rotation can occur at room temperature. An important result from these calculations is, that while the single molecule was designed to provide the electrical function, i.e., a rotatable dipolar unit, the effect can only be utilized in devices at room temperature, when the molecule is used within an ensemble of molecules. *Inter*molecular forces are hence crucial for device performance.

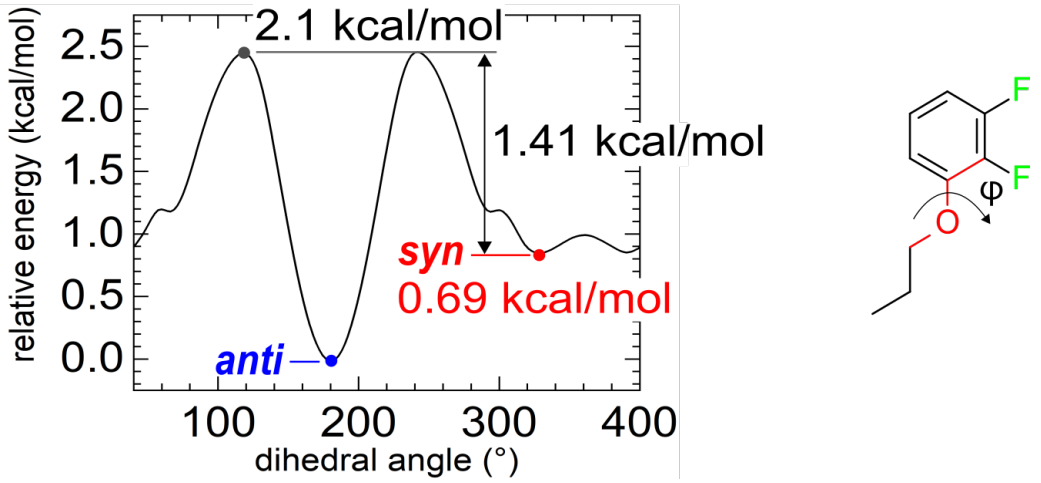

Figure 7.3.1 Calculated conformational energy scan for the rotation of a simplified model compound around the dihedral angle. Relative energy with respect to the energy of the *anti*-state (φ = 180°) versus dihedral angle. Relative energies of the maximum energy as well as of the *syn*-state (φ = 0°), as well as the resulting energy barrier that needs to be overcome to change the molecule from *syn* to *anti*-state are noted in the graph. While the solid line represents the calculated results without zero-point correction, the annotated values originate from calculations including the zero-point correction. Simplified model compound used to perform the calculations is shown on the right. *Red* color indicates the atoms and bonds that span the two planes that define the dihedral angle φ (marked *red*). Figure as published in [154]

7.3.2 Molecular Ensemble - Molecular Dynamics

Detailed molecular dynamics (MD) simulations were performed in order to investigate the potential reorientation of the dipolar unit of QM15^F within a densely packed SAM and the energetic landscape influenced by *inter*molecular forces connected with it.

Equilibration of the SAM

The SAM was set up with 92 instances of the QM15^F molecule within in the MD environment and the system was equilibrated in the NPT ensemble at T = 300 K, resulting in a surface density of n = 3.6 molecules nm^{-2}. As force field, a combination of OPLS and a torsion potential that was adapted to reproduce the rotational energy scan from the previous section, was used. More details are described in Chapter 2. Figure 7.3.2 displays a snapshot of the SAM with one molecule highlighted, including the definitions of tilt angle β, rotation angle around the long molecular axis γ and the aromatic unit orientation angle α. The distribution of of tilt angle β after equilibration is shown in the same figure.

Dipolar Reorientation with Electrical Field

The dipole reorientation within the SAM under the influence of an applied field was investigated using several different sequences of applied electrical fields. To ease comparison with experimental data, the electrical field was defined as positive, when a positive potential was applied to the top side of the junction. A positive field vector hence points towards the substrate whereas a negative field vector points towards the top contact. Three sequences of electrical fields were investigated. In summary, the SAM was simulated for 600 ns without an applied electrical field (sequence 1), a sequence consisting of a 100 ns positive electrical field pulse after 100 ns of no applied electrical field (sequence 2) and a sequence consisting of sequence 2 followed by 100 ns of no field applied and 100 ns of a negative electrical field. Sequence 2 and sequence 3 were both followed by an

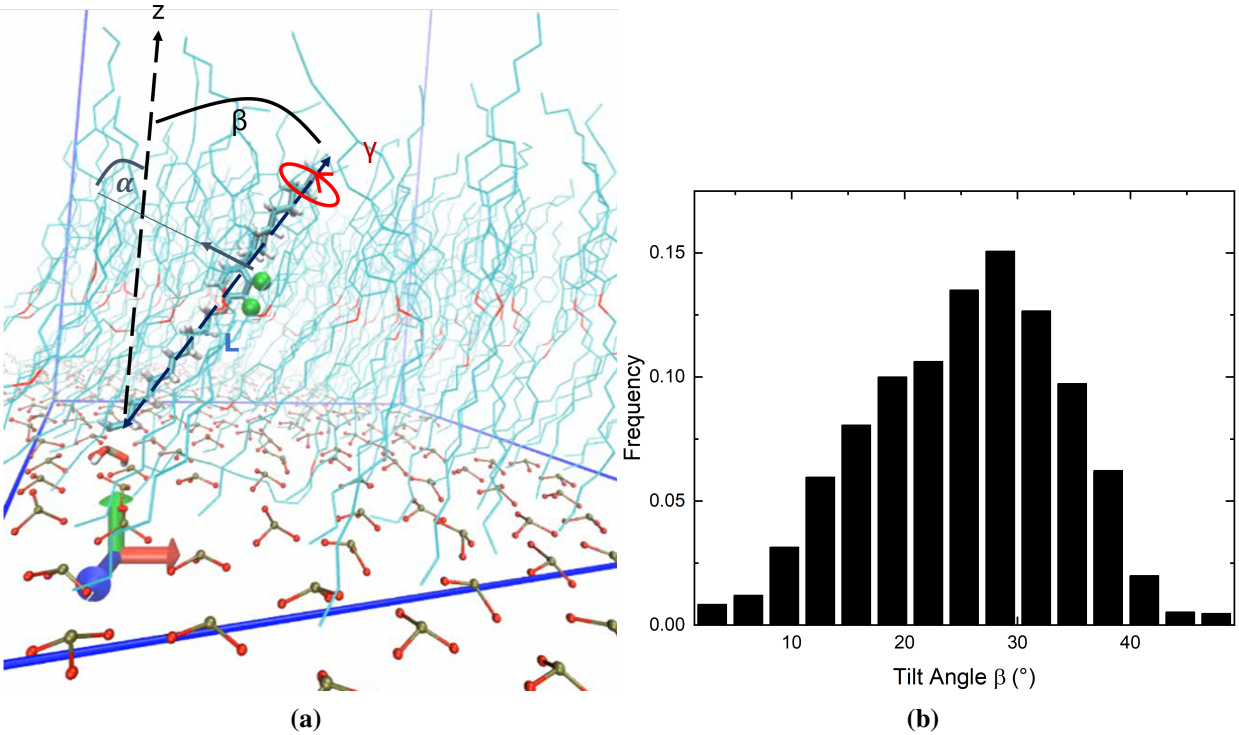

Figure 7.3.2 Equilibrated SAM of QM15^F. a) Snapshot including the definition of length L and tilt angle β, rotation angle around the long molecular axis γ and aromatic unit orientation angle α that is defined as the angle between the π-system's normal vector (*pink*) and the z-axis. b) Histogram of tilt angle β of the SAM after equilibration. Figures adapted from those submitted to [154]

additional 100 ns of the previously applied field (termed *under field*) as well as followed by an additional 400 ns (sequence 2) or 200 ns (sequence 3) of no applied field (termed *after field*). Hence, sequence 1 represents the SAM in its initial state over time, sequence 2 probes potential molecular reorientation under field - i.e., switching to a second conductance state - and the stability of this state after the field is turned off again and sequence 3 represents the proposed reversal of the reorientation, potentially leading to the initial conductance state again. As has been shown for the equilibrated SAM through exemplifying the distribution of the tilt angle β, the angles α, β and γ follow distributions within the SAM. This also leads to the dipole moment μ_z following a distribution. A detailed analysis of these distributions can be found in [154]. For the purpose of clarity, here, only the average dipole moment μ_z, per molecule, is displayed and analyzed.

For sequence 1, without an applied electrical field, the average dipole moment is μ_z = -0.1 D per molecule with $\approx$ 7% of the molecules in the energetically slightly favored anti-conformation. Neither the dipole moment nor this fraction significantly change over 600 ns of calculations, as long as no field is applied. This state is termed the *initial state*. After sequence 2, μ_z was found to saturate at -2.4 D per molecule when the field was still applied (*under field*). Already 100 ns after application of the electrical field, 90% of this saturation value was reached. This indicates fast switching of the molecular orientations. Turning the field off 100 ns after it was turned on, μ_z relaxed to -0.3 D after 100 ns and did not significantly change for the remaining 300 ns of the simulation. In this state *after field*, 64% of molecules were in the *anti*-state. This *switched state* is charaterized by 13% fewer molecules in *anti*-state and a difference of 0.2 D per molecule as compared to the initial state. In particular, this means that the switched state prevails after the field was turned off, and the average dipole moment per molecule of the SAM can in fact be switched by applying an electrical field.

After sequence 3 *under field*, μ_z was found to saturate after 10 ns at +0.7 D. Turning the field off again (the *after*

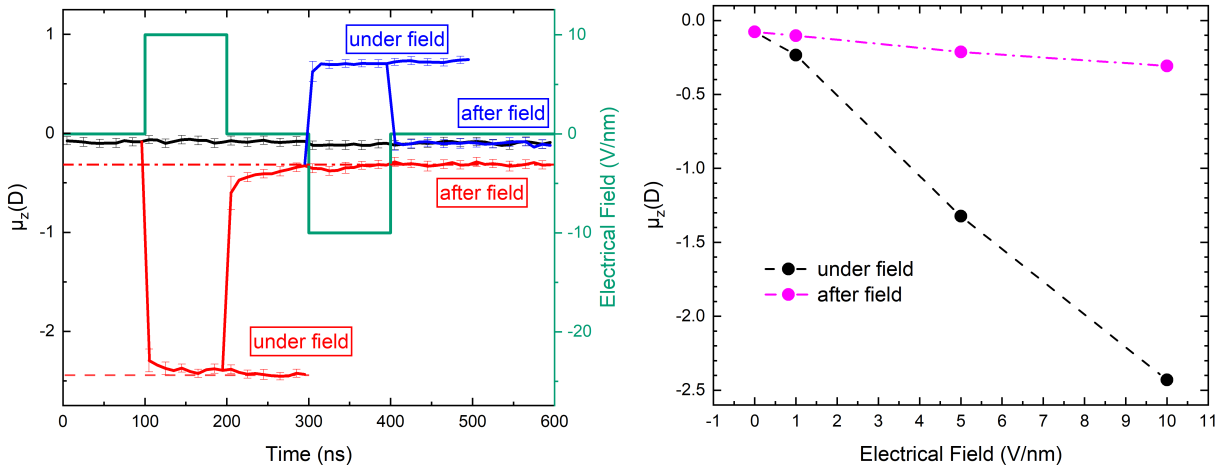

(a) **(b)**

Figure 7.3.3 Molecular Dynamics simulation of a pulse sequence. Dipole moment μ_z averaged per molecule (*left axis*) for electrical field pulses (*right axis*) over time t (error bars from fluctuations). *Black curve*: initial state without field. *Red curve* (sequence 1): +10 V nm^{-1} electrical field turned on at t = 100 ns and turned off at t = 200 ns until 600 ns. *Blue curve* (sequence 2): first 300 ns of sequence 1, then field same magnitude and opposing sign turned on t = 300 ns and turned off again at t = 400s, returning the SAM to initial state. Sequence 2 reveals a polarization hysteresis compared to the red state of $\Delta\mu_z$ = -0.2 D. b) Dipole moment μ_z from pulse sequences as in a), but with varied electrical field ampliudes $E_z \in [0; 1; 5; 10]$ V nm^{-1} *Dashed black line*: μ_z under applied positive field (averaged for 200-300 ns), corresponding to the situation marked by the dashed lower red line in a). *Dash-dotted pink line*: μ_z after the field is off (averaged for 300-400 ns), corresponding to the situation marked by the dash-dotted upper red line in a). Derived from figures submitted to [154]

field sequence) brought the SAM to a state with 74% of the molecules in *anti*-state, which is close to the initial 77%. The average dipole moment per molecule furthermore switched back to its initial value of -0.1 D.

Comparing μ_z of sequence one with the μ_z values for the *after field* situation of sequence 2 and 3 three reveals that a SAM of QM15^F can be switched from its initial state to a state with a lower μ_z and back to the initial value of μ_z, simply by applying electrical fields of opposite polarity. These simulations find a total polarization hysteresis between the inital and the switched state of $\Delta\mu_z = 0.2D$ for SAMs of surface density 3.6 molecules nm^{-2} and 10 V/nm electrical fields applied at room temperature.

This finding is in qualitative agreement with the experimentally determined hysteretic behavior, displayed in Figure 7.2.3a. Since both have most recently seen a negative field, the experimentally observed LRS state at 0 V and the simulated *switched* state at t > 300 ns are comparable. Following the same argument, the HRS state at 0 V from the experiment and the state of the SAM after sequence 2 are also comparable. A quantitive difference in the applied electrical field E_z of a factor of 10 between simulation and experiment still remains. Hence, sequence 1 was repeated for 1 V/nm and 5 V/nm. The resulting saturation values for μ_z *under* and *after field* are displayed in Figure 7.3.3. The dipole moment in z-direction for both, the *under field* and *after field* situation show a near-linear dependence of the polarization hysteresis on the applied field strength. From the assumption that distinct μ_z states result in distinct conductance states, this result suggests, that multiple conductance states within a SAM of liquid crystal-inspired molecules are accessible through varying the sign and magnitude of the previously applied field. This suggests possible future applications of this systems in the area of in-memory or neuromorphic computing.

Surface density dependence of average dipole moment change

The single molecule calculations revealing nearly unhindered rotation of the molecule at room temperature and the molecular dynamics simulations yielding stable SAM states, strengthens the previously mentioned hypothesis, that *inter*molecular forces govern device performance, in particular the achievable on/off ratio, but also retention.

Since the magnitude of *inter*molecular forces is a function of distance between the involved molecule, the surface density - or coverage - of the SAM might also have an influence on the dipolar hysteresis. To investigate whether this is in fact the case, molecular dynamics simulations of SAMs with varying surface densities were carried out. Two different sequences of applied electrical field were applied to the SAM. In the first sequence, SAM was simply left to equalibrate for 200 ns. As a second sequence, the SAM was left to equalibrate for 100 ns and then, an electrical field of 10 V/nm was turned on for 100 ns, turned off again, leaving the SAM for another 200 ns to equalibrate. Figure 7.3.4a displays the average dipole moment per molecule in z-direction following this simulation procedure. $\Delta\mu_{z,\text{under field}}$ was defined as the difference in saturation values of μ_z of the initial state (0 field) and the SAM under field, whereas $\Delta\mu_{z,\text{after field}}$ was defined as the difference in saturation values of μ_z of the initial state and the SAM after the field was applied and turned off again. Figure 7.3.4a displays the calculated values for varying surface densities. From these simulations, a near-linear decrease of $\Delta\mu_{z,\text{under field}}$ and a near linear increase of $\Delta\mu_{z,\text{after field}}$ can be observed. This is aligned with the image of *inter*molecular forces increasing the rotational barrier, since the energy required to change the state is expected to increase with increasing surface density. This should result in a lower probability of a state-change with increasing surface density. Under an applied electrical field, alignment of the overall dipole moment with the external field becomes less likely. After the field is turned off, re-orientation of the molecules also becomes less likely. Hence, increased molecular interaction, mediated by an increased surface coverage, results in a lower overall dipole moment of the SAM under field, but a higher one after field removal.

Overall, these results indicate that *inter*molecular steric interactions within the SAM are a determining factor for the polarization hysteresis, which can might be translated into an improved molecular design to achieve increased hysteresis and longer retention times.

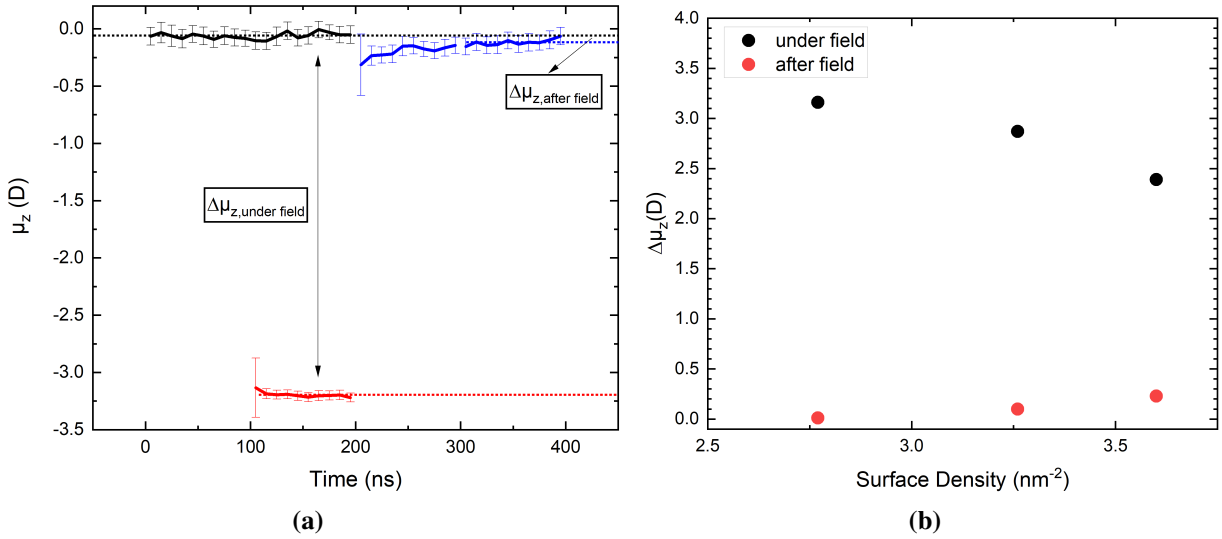

Figure 7.3.4 Surface density (n) dependence of average dipole moment change a) Average dipole change under an applied 10 V/nm electric pulse from 100 ns to 200 ns. Definition of $\Delta\mu_{z,\text{under field}}$ as difference between the average dipole moment of the SAM **while** the field is turned on and the average dipole moment of the SAM after equilibration. $\Delta\mu_{z,\text{after field}}$ is defined as difference of the average dipole moment of the SAM **after** the field is applied and the average dipole moment of the SAM after equilibration. b) $\Delta\mu_{z,\text{under field}}$ and $\Delta\mu_{z,\text{after field}}$ as calculated for three different surface densities (n = 3.60 nm^{-2}, n = 3.26 nm^{-2}, n = 2.77 nm^{-2}) show an approximately linear relationship for $\mu_z(n)$. Data also submitted in different form to [154]

7.3.3 Single Molecule Conductance - TranSIESTA

Since the orbital structure affects the molecular conductance, one additional effect that might lead to a different conduction between the *syn-* and *anti-* conformers could be a conformational change induced change of the electronic orbital structure. For other molecules, this effect has been investigated in a recent publication by Belding et al. .[220] To investigate whether this effect plays a significant role in liquid crystal-inspired molecules, single-molecule transmission calculations of simplified analogues were performed, using the TranSIESTA approach. For these calculations, the phosphonic acid head group was removed from $QM15^F$ to yield compound **1** and from QM32 to yield compound **2**. The model compounds were sandwiched between two gold electrodes and coupled to the central gold atoms of the electrodes via van der Waals contacts with the most remote, terminal hydrogen atoms. Using B3LYP/6-31G(d) level of theory, the frontier orbital energies were calculated to be -5.91 eV (HOMO) and 0.09 eV (LUMO) for *anti*-**1** (band gap E_G = 6.01 eV), and -5.94 eV (HOMO) and 0.07 eV (LUMO) for *syn*-**1** (Eg = 6.02 eV). Three dimensional sketches of the models as well as results of the calculated transmission currents through single molecules versus voltage are shown in Figure 7.3.5. For the two conformers of **1** the current at any given voltage differs by approximately one order of magnitude with the *syn*-conformer exhibiting the higher transfer current. The transmission of the non-fluorinated compound **2** yielded values very close to *anti*-**1**, indicating that the TranSIESTA method neglects any effects of the dipole moment μ_z.

Comparing the transfer currents of single molecules in full *syn-* and *anti-* state represents the two extreme cases. Since the molecular dynamics simulations showed a distribution of molecular orientations rather than SAMs in two distinct states, the conductance changing effect of a change in the electronic orbital structure can be expected to be less than the one obtained from the TranSIESTA calculations presented here. Albeit a change in conductance from this conformational change induced electronic orbital structure change can be assumed to occur, it alone can not explain the experimentally obtained orders of magnitude in conductance switching.

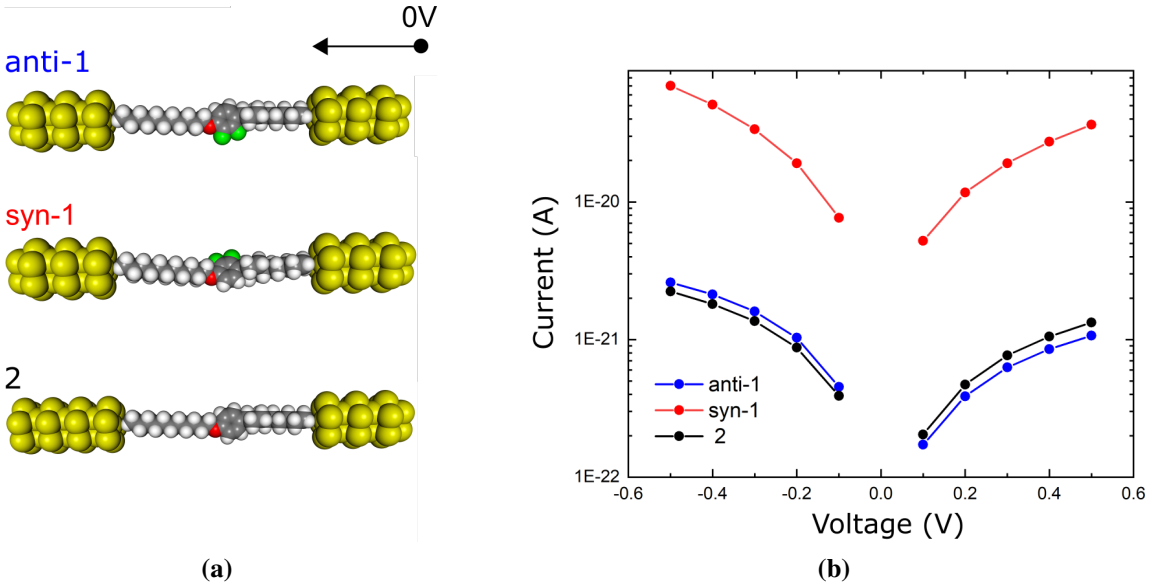

(a) **(b)**

Figure 7.3.5 Calculated single molecule currents of QM15^F simplified model compound 1 in *syn*-**1** and *anti*-**1** configuration as well as QM32 simplified model compound **2**, sandwiched between two gold electrodes. Phosphonic acid groups have been removed from QM15^F and QM32 for TranSIESTA calculations. Atoms are color coded. *Yellow*: Gold (Au), *grey*: carbon (C), *white*: hydrogen (H), *red*: oxygen (O), *green*: fluorine (F). a) 3D representation of the three studied model systems b) theoretical current-voltage characteristics through the three single molecule systems. *Red*: Fluorinated molecule in *syn*-state, *blue*: Fluorinated molecule in *anti*-state, *Black*: Non-fluorinated molecule. Figures as published in [154]

7.3.4 Ensemble Molecular Device - Device Model

To estimate the change in tunneling current induced by the conformational state change of the SAM, which results in a change of the shape of the asymmetric tunnel barrier, the following model was conceived: The **Al/Al$_x$O$_y$/SAM/Pb** stack was modeled as two-barrier system comprising the (amorphous) aluminum oxide and the organic layer as one effective tunneling barrier that has different barrier heights at both contacts, constituting an asymmetric trapezoidal barrier. Charging, interface polarization and band-bending effects are not taken into account in this model. Figure 7.3.6 depicts the approximated energy level diagram, assuming that the potential drop across the dipole layer is reflected in a change in barrier height at the electrode, which is in contact with the SAM. In order to model the direct (non-resonant) tunneling current I_{DT} of this system, the expression derived by Gruverman et al.[133] and shown in Chapter 2 was used. Due to the closer vicinity of the HOMO to the Fermi level, hole tunneling was assumed to be dominating [226] and therefore only the tunneling current through the trapezoidal barrier determined by the valence band edge of aluminum oxide and the HOMO of the molecule was calculated. On the aluminum side of the tunneling barrier, the difference of aluminum work function ϕ_{Al} and aluminium oxide valence band edge $VB_{\mathrm{Al}_x\mathrm{O}_y}$ constitutes the barrier height

$$\phi_1 = VB_{\mathrm{Al}_x\mathrm{O}_y} - \phi_{Al} \tag{7.3.1}$$

Since embedded dipoles are assumed to alter the shape of the tunneling barrier at the position where the induced dipole is located [25] and the dipolar unit is closer to the SAM/Pb interface than to the oxide/SAM interface, the barrier height on the Al$_x$O$_y$ side is kept constant within all following calculations. In contrast, on the Pb side,

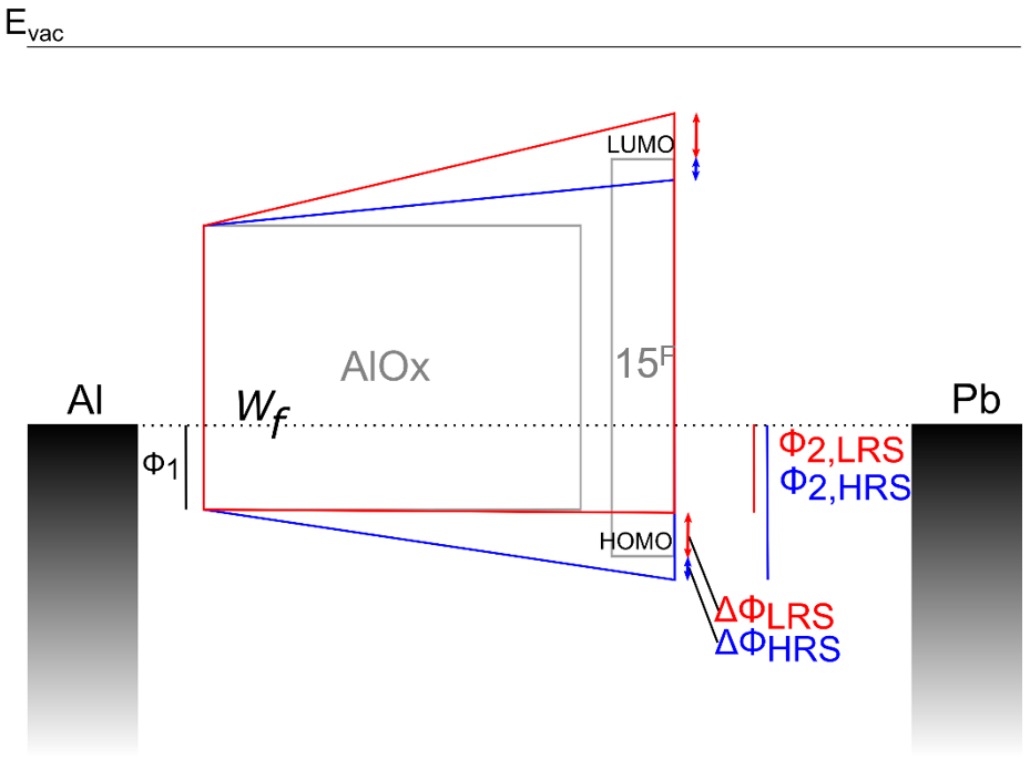

Figure 7.3.6 Simplified equilibrium energy level scheme of Al/Al$_x$O$_y$/QM15^F/Pb/Ag devices. *Red*: junction in LRS, *blue*: junction in HRS. Used parameters: Metal work functions $\phi_{Al} \approx \phi_{Pb} \approx 4.25$ eV, [221–223] aluminum oxide valence band edge $VB_{Al_yO_x} \approx -5.2$ eV [224, 225], HOMO and LUMO energies in both, the *syn* and *anti*-state: HOMO = -5.73 eV, LUMO = -1.26 eV, all with respect to the vacuum level E_{vac}. Barrier heights ϕ and changes in barrier heights $\Delta\phi$ are discussed in the text. Note that the vacuum level position in the barrier region is sketched with respect to the plain Al$_x$O$_y$ and molecular orbital energy levels (*light grey*), without dipolar contributions. W_f denotes the Fermi level. Figure as published in [154]

the difference between the Pb work function ϕ_{Pb}, the HOMO and the dipole orientation-dependent potential drop $\Delta\phi$ constitutes the barrier height ϕ_2:

$$\phi_2 = -HOMO - \phi_{Pb} - \Delta\Phi \tag{7.3.2}$$

Here, the energy shift induced by the dipole moment of the SAM in z-direction (μ_z) is reflected in $\Delta\Phi$. This shift is calculated using the Helmholtz Equation:

$$\Delta\phi = \frac{n\mu_z}{\epsilon_{r,SAM}\epsilon_0} \tag{7.3.3}$$

Here, n = 3.6 molecules nm^{-2} is the maximum molecule surface density from MD simulations, ϵ_0 is the vacuum permittivity and $\epsilon_{r,SAM}$ = 3 is the estimated relative permittivity of the SAM. The MD simulations yielded a linear relationship between μ_z and the magnitude of the applied electric field across the monolayer. Linearily interpolating the already calculated values yields:

$$\mu_{z,LRS} = 0.07\ \text{nm/V} \cdot E_{SAM} \cdot 3.33564 \cdot 10^{-30}\ \text{Cm} \tag{7.3.4}$$

$$\mu_{z,HRS} = (-0.05526 - 0.24029\ \text{nm/V} \cdot E_{SAM}) \cdot 3.33564 \cdot 10^{-30}\ \text{Cm} \tag{7.3.5}$$

Here, E_{SAM} is in V/nm, and the calculated μ_z is in SI units (Cm, 1 Cm $\approx 3 \cdot 10^{29}$ D). To further simplify calculations, the SAM is assumed to be in one of two distinct states: Either the state after the maximum (positive) voltage (V_{max} = 3 V) or the minimum (negative) voltage (V_{min} = -V_{max} = -3 V) has been previously applied. To calculate the absolute value of E_{SAM} for these voltages, the oxide and SAM are modeled as two capacitors connected in series. Assuming no charge accumulation at the SAM-oxide interface, the charges stored on both capacitors are equal ($Q_{Al_xO_y} = Q_{SAM}$) and therefore, the capacitances of oxide $C_{Al_xO_y}$ and SAM C_{SAM} are connected via the voltage drops across oxide ($V_{Al_xO_y}$) and SAM (V_{SAM}). Since $|V_{min}| = |V_{max}|$ and only the absolute value of E_{SAM} is of interest, calculations can be performed for V_{max} only. With $V_{max} = V_{Al_xO_y} + V_{SAM}$

$$V_{max} = \left(\frac{C_{SAM}}{C_{Al_xO_y}} + 1\right) \cdot V_{SAM} \tag{7.3.6}$$

The capacitance of a parallel plate capacitor is given by:

$$C = \frac{\epsilon_0 \epsilon_r A}{d} \tag{7.3.7}$$

Here, d is the distance between the conducting plates and A is the surface area of each plate. Since the area A and ϵ_0 are the same for both capacitors, they cancel out in the equation for V_{max}. This leaves an equation that connects the maximum voltage and the dielectric constants (ϵ_{r,Al_xO_y} = 9.84 [227] and $\epsilon_{r,SAM}$= 3) and thicknesses of the oxide and SAM layer ($d_{Al_xO_y} \approx 3$ nm, as derived from the TEM image shown in Figure 7.2.1 and d_{SAM} = 2.81 nm from MD simulations):

$$V_{max} = \left(\frac{C_{SAM}}{C_{Al_xO_y}} + 1\right) V_{SAM} = \left(\frac{\epsilon_{r,SAM} d_{Al_xO_y}}{\epsilon_{r,Al_xO_y} d_{SAM}}\right) V_{SAM} \tag{7.3.8}$$

$$V_{SAM} = \left(\frac{\epsilon_{r,Al_xO_y} d_{SAM}}{\epsilon_{r,Al_xO_y} d_{SAM} + \epsilon_{r,SAM} d_{Al_xO_y}}\right) \cdot V_{max} \tag{7.3.9}$$

With $E_{SAM} = \frac{V_{SAM}}{d_{SAM}}$:

$$E_{SAM} = \frac{V_{SAM}}{d_{SAM}} = \left(\frac{\epsilon_{r,\mathrm{Al}_x\mathrm{O}_y}}{\epsilon_{r,\mathrm{Al}_x\mathrm{O}_y} d_{SAM} + \epsilon_{r,SAM} d_{\mathrm{Al}_x\mathrm{O}_y}} \right) \cdot V_{max} \tag{7.3.10}$$

Using the Helmholtz Equation 7.3.3 and plugging in the linear interpolations of $\mu_{z,HRS}$ and $\mu_{z,LRS}$, shown in Equations 7.3.4 and 7.3.5, the two distinct hole barriers become:

$$\Phi_{2,LRS} = -HOMO - \Phi_{Pb} - \frac{n \cdot 0.07\, V_{max} \left(\frac{\epsilon_{r,\mathrm{Al}_x\mathrm{O}_y}}{\epsilon_{r,\mathrm{Al}_x\mathrm{O}_y} d_{SAM} + \epsilon_{r,SAM} d_{\mathrm{Al}_x\mathrm{O}_y}} \right) \frac{nm}{V} \cdot 3.33564 \cdot 10^{-30} Cm}{\epsilon_0 \epsilon_{r,SAM}} \tag{7.3.11}$$

$$\Phi_{2,HRS} = -HOMO - \Phi_{Pb} - \frac{n \cdot \left(0.05526 - 0.24029 \frac{nm}{V} \cdot V_{max} \left(\frac{\epsilon_{r,\mathrm{Al}_x\mathrm{O}_y}}{\epsilon_{r,\mathrm{Al}_x\mathrm{O}_y} d_{SAM} + \epsilon_{r,SAM} d_{\mathrm{Al}_x\mathrm{O}_y}} \right) \right) \cdot 3.33564 \cdot 10^{-30} Cm}{\epsilon_0 \epsilon_{r,SAM}} \tag{7.3.12}$$

Here, all values of d are inserted in nm. Using $\Phi_1, \Phi_{2,LRS}$ and $\Phi_{2,HRS}$ as derived above, the total thickness $d = d_{SAM} + d_{\mathrm{Al}_x\mathrm{O}_y} = 5.81$ nm, the effective mass $m^* = m_0$ as well as all other values as mentioned before in this section, the ON/OFF current ratio at V = -1 V was directly calculated using the Gruverman formula, yielding $I_{LRS}/I_{HRS} \approx 7.2$. This value is independent from the contact area A since it cancels out in the ratio.
This calculated ON/OFF ratio is significantly lower than the one observed from electrically characterizing actual devices. At the same voltage the experimentally observable ON/OFF ratio is ≈ 180. The quantitative difference between theory and experiment might, in part, be attributed to the simplifications made within model. Namely, charging, interface polarization and band-bending effects were not considered, but might have significant impact on device performance.

However, the analytical formula for the ON/OFF ratio critically depends on the numerical values of the molecular surface density n and the effective hole mass m^*. To illustrate this, ON/OFF ratios were calculated for multiple combinations of effective hole mass and surface density. The results are displayed as a contour plot in Figure 7.3.7. Due to the excessive computational cost of calculating $\mu_z(n)$, μ_z was assumed to be constant for all n within the calculations leading to the results displayed in 7.3.7. However, this does not critically dampen the strong dependence of the calculated ON/OFF ratio. In fact, taking it into account would rather intensify the strong dependence of the ON/OFF ratio on the surface density. The strong dependence of the ON/OFF ratio on effective hole mass becomes particularily evident comparing the previously assumed effective hole mass of $m^* = m_0$ to another one that is still in range of the reported values for alumina and organic compounds $m^* = 8m_0$. [224, 228] Then, the ON/OFF ratio calculated from the model derived above would be in range with the experimentally observed one. Assuming a specific value for the double barrier comprising amorphous alumina and liquid crystal-inspired molecules, however, would be pure speculation. This approach is therefore not pursued further here. However, it can be concluded that the experimental findings are qualitatively well in line with the simplified model, that is fully based on well-educated assumptions. Furthermore, the sensitivity of the ON/OFF ratio to the effective mass of the tunneling carrier might present an opportunity in later device optimization, since it might present an additional, molecule-independent variable to increase ON/OFF ratio. In particular, the choice of the oxide in this double-layer might influence the ON/OFF ratio of the resulting ensemble molecular device.

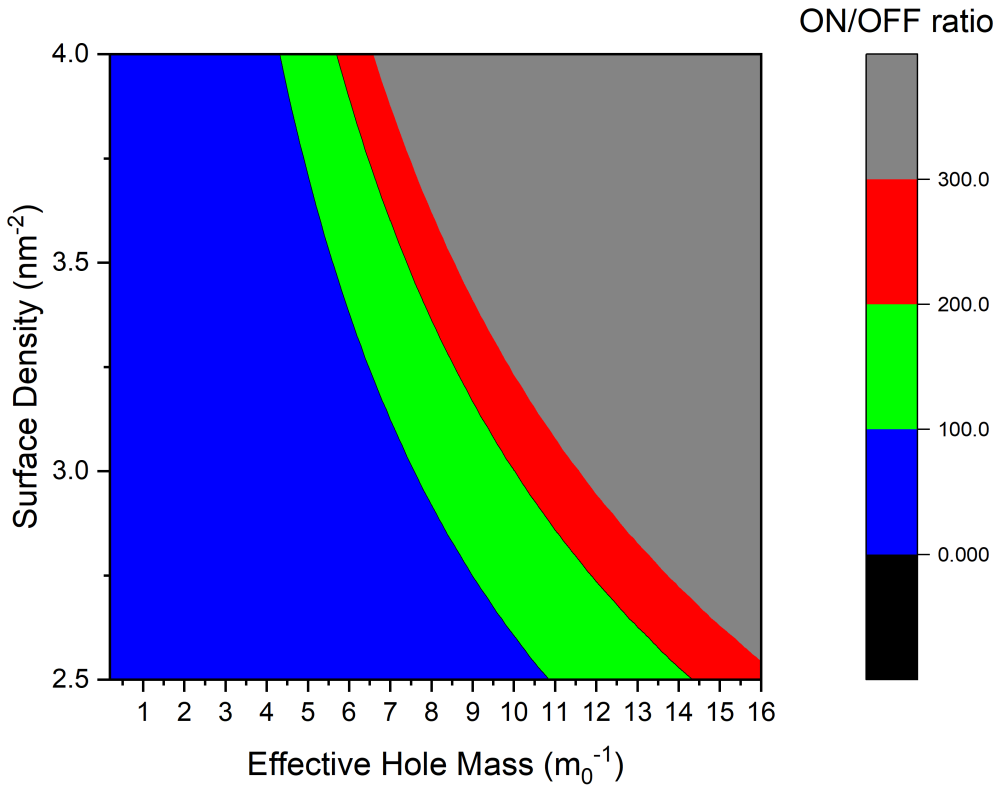

Figure 7.3.7 Dependence of the calculated ON/OFF current ratio on effective hole mass and surface density. The green area marks possible parameter combinations for an ON/OFF ratio comparable to the one obtained from experiments. Figure as published in [154]

7.4 Summary

Repeatable electrical-field induced conductance switching due to conformational reorientation of liquid crystal-inspired molecules within ensemble molecular solid-state devices has been demonstrated. Current density-voltage traces revealed a pronounced hysteresis that can be assigned to conformation-dependent varying shape of an asymmetric tunneling barrier. Experimentally determined ON/OFF conductance ratios were in the range of 10^2. The pronounced hysteris was found to be reproducible across seven devices as well as for 100 voltage cycles. The experimental data demonstrates the feasibility of exploiting the reorientaion of molecular dipoles in an external field as electrical field-driven switch.

Density functional theory based rotational energy scans revealed two energetic minima with energetic barriers that do not prevent the transitions between those two states at room temperature. Experiment and molecular dynamic simulations on the other hand revealed static states of the SAM. For this reason, *inter*molecular forces are likely responsible for the energetic barrier that is required for device functionality.

TranSIESTA calculations for single molecules revealed that the electronic structure change induced by the conformational change alone is not sufficient to explain the experimentally observed ON/OFF conductance ratios. Molecular dynamics simulations revealed distinct polarization states for SAMs after electric fields of opposite polarity were applied. Feeding the dipole moments of these two states, into a two-layer model based on the Gruverman model and using the Helmholtz equation to translate shifts in polarization to shifts in barrier height yielded ON/OFF ratios comparable to the experimentally determined values, assuming an effective

electron mass that is within the range of reported values for aluminum oxide. This device model, that is fully based on reasonable assumptions, also revealed a striking dependence of the ON/OFF ratio of conductance on charge carrier effective mass and molecular surface density. This dependency persists even for effective mass and molecular surface density independent polarization hysteresis, making both quantities potential design parameters for future devices.

Molecular dynamics simulations further revealed a dependency of the remnant polarization hysteresis on surface density of the molecules within the SAM as well as on electrical field strength. The dependency on surface density presents an additional argument that *inter*molecular interactions are an important parameter for device optimization. The dependency on electrical field strength means that the number of distinct conduction states is theoretically not limited to just two. The effect presented in this work hence has the potential to be exploited for applications built on multi-state devices, such as neuromorphic or in-memory computing devices as well as the physical implementation of pre-trained neural networks for edge-computing applications. [229, 230] First experimental data for similar molecules within an ensemble molecular device, that are presented in Chapter 9 strengthen this hypothesis.

8 Lead Free Metallic Solid State Top Contacts

This chapter briefly outlines the motivation to develop an alternative to the contacting scheme described in chapter 7 and gives the rationale behind the choice of combining titanium nitride as anchoring layer and titanium as top contact material. To explore the feasibility of the approach, first the formation of a monolayer of alkyl-phosphonic acids (APA) on titanium nitride (TiN) was confirmed using CWA, VASE, FTIR, AFM and XPS. Then, devices with monolayers of APA sandwiched between TiN and Ti were fabricated and electrically characterized by current-voltage spectroscopy. The tunneling attenuation factor was derived from data of devices with monolayers of APAs with varying chain length. The measured current density was further analyzed by fitting representative J-V data to the Simmons Model. This chapter relates to the work presented in [231]. Electrical measurements were in part performed by Deepthi Devendra in the framework of her Master's thesis. XPS measurements were performed by Domenikos Chryssikos.

As shown in chapter 7 the combination of an aluminum oxide anchoring layer and a lead top contact with a phosphonic acid monolayer sandwiched between them yields functional electronic devices. However, this **Al/Al$_x$O$_y$/SAM/Pb/Ag** stack comes with several drawbacks. For one, the native oxide on aluminum consitutes a large tunneling barrier that might be connected to an overall low current. With the aluminum work function 4.25 eV[222, 223], aluminum oxide valence band edge -5.2 eV [224] and the previously reported thickness of the oxide, current densities of the reference device featuring the native oxide surface and no molecule were below $1 \cdot 10^{-4}$ mA/cm^2 for absolute voltages up to 3 V. This corresponds to absolute currents below 0.1 nA for 25 µm x 25µm devices.

Aluminum Oxide Layer Thickness

To reduce the oxide layer's impact on magnitude of tunneling current, it would be beneficial to keep it as thin as possible. In order to analyze the impact of the plasma treatment of the aluminum/aluminum oxide surface on oxide thickness, an experiment exposing physical vapor phase deposited aluminum surfaces to variety of plasma treatment conditions was performed. Aluminum layers on substrates of silicon with a silicon oxide layer were fabricated via PVD as described in chapter 4. Plasma power was varied from 50 W to 150 W and plasma time was varied from 1 min to 10 min. Additionally, one sample was exposed to a 400 W oxygen plasma for 1 minute and one sample was not exposed at all. The resulting samples were analyzed with VASE and compared to an untreated sample. Figure 8.0.1 shows the results of VASE thickness fits of the oxide on the **Si/SiO$_2$/Al/oxide** stack. No significant change of oxide thickness with varying plasma treatment conditions was observed. The average oxide thickness of all plasma treated aluminum samples was 4.35 nm ± 0.34 nm, whereas the untreated reference sample was found to have an oxide thickness of 4.46 nm ± 0.43 nm. Others have previously reported values for native oxide thicknesses in the range from 3 nm to 5 nm [232]. All measured values fall in this region. It is therefore likely that the formation of a native oxide that occurs when exposing

the aluminum surface to ambient conditions could not be influenced by any of the processing conditions outlined above. However, others have found that the oxide thickness on PVD deposited aluminum films can be a function of plasma power and duration. Oxide thicknesses were found to increase with increasing power and duration. For instance *Geiger et al.* reported oxide thicknesses that were obtained from TEM imaging after oxygen plasma exposure of aluminum surfaces to vary from 4.3 nm (10 W, 30 s) to 7.3 nm (300 W, 30 s). They also found the thickness to saturate at a value of approximately 7 nm if the plasma duration was at least 30 s and the plasma power was at least 50 W. [233] The observation that all plasma exposed aluminum surfaces in this work show similar thicknesses is in agreement with their finding, since only plasma powers and durations that satisfy these conditions were applied. This is also in good agreement with the Cabrera-Mott model, describing self-limiting oxide-growth of aluminum oxide, mainly due to the small diffusivity of oxygen in aluminum oxide. [234] Notably, in contrast to *Geiger et al.*'s finding, the thickness of the native oxide observed in this work did not differ from the oxide thickness after plasma exposure. This difference might be explained by the fact that the time to transfer samples from fabrication to measurement was approximately two hours in this work and immediately after fabrication in the referenced work. This might have lead to oxide growth up to the self-limited value on the samples presented above. The difference in total value of the saturation thickness might be explained by the different measurement modalities and the strong model-dependency of derived film thicknesses for very thin layers in VASE.

In summary, the oxide thickness was found to be independent of plasma treatment conditions. The formation of the native oxide after exposure of the aluminum surface to ambient air seems to be the limiting factor for minimum oxide thickness. One potential solution to achieve a thinner oxide layer would be the removal of the native oxide layer and controlled re-growth of the oxide up to a certain thickness. This, however would require all subsequent fabrication and characterization steps to be in an inert atmosphere to avoid oxygen diffusion to the surface which could ultimately lead to an increase of oxide layer thickness up to the saturation value. Since an objective was to develop a fabrication scheme consisting of a short sequence of simple processing steps, other solutions on how to avoid a thick aluminum oxide layer had to be found.

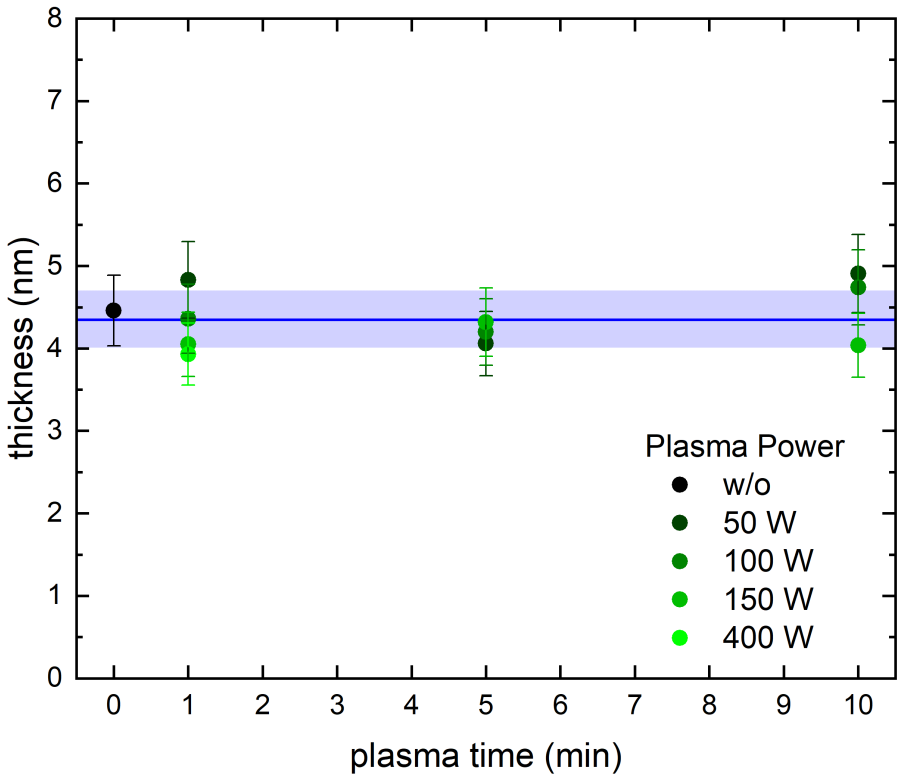

Figure 8.0.1 Aluminum oxide thicknesses after various O_2 plasma treatments of thermally evaporated aluminum layers on Si/SiO_2 substrates, as measured by VASE. Blue horizontal line indicates the average of all measurements, excluding the untreated sample (plasma time 0 min, plasma power w/o). Light blue area indicates the standard deviation of that average. Less than 1 nm thickness variation with change in plasma conditions can be observed. Data shows no clear trend of oxide thickness growth with either time or plasma power. Thus, oxide thickness on aluminum substrates is concluded to be independent of plasma treatment within the explored parameter space of plasma power and plasma duration.

Within the **Al/Al$_x$O$_y$/SAM/Pb/Ag** stack the use of lead as top contact material poses additional challenges. The two main challenges that need to be addressed are the toxicity and the stability of lead. The presence of lead represents a severe concern for commercialization, due to its toxicity and associated risks to human health and its environmental impact. Exposure to lead is especially harmful to the central nervous system. Additionally, lead is found to be toxic to renal organs and the reproductive system. The toxicity of lead and its salts is mainly a result of the increase oxidative stress. [235–237] Due to its toxicity, Pb is also often banned from shared physical vapor phase deposition facilities. In the context of this work, it was necessary to use a PVD system designated solely for potentially toxic substances including lead (see chapter 4 for details). With the age of the PVD system used, came a measurement and control system that allowed much lower accuracy of process control than would be possible on newer systems.

Pb/Ag electrode degradation

Another challenge that comes with the previously deployed Pb/Ag compound top electrode is its degradation over time. The SEM images shown in Figure 8.0.2 exemplify this degradation of Pb/Ag top contacts on a QM15^F monolayer. One sample was imaged one day after fabrication whereas the other sample was imaged after it was stored in a nitrogen cabinet for six months. The nitrogen cabinet supplied a nitrogen-rich and oxygen sparse environment, while still exposing samples to a limited amount of oxygen. On both samples, the day after fabrication, devices that showed the effects described in the previous chapter could be found. The sample imaged one day after fabrication revealed smooth top contacts, whereas the sample that was stored showed significant grain formation of the metallic components. This grain formation coincided with the junctions currents decreasing to values below the measurement threshold of the electrical characterization setup - regardless of sign or magnitude of the applied voltage up to $|V| = 20\ V$. Hence, it can be concluded, that the stability of Pb/Ag top electrodes is not sufficient for future commercial application. Potential reasons for this might be the oxidation of lead or the formation of a lead-silver alloy. A more in-depth investigation of the degradation was not carried out, as the observation outlined here already revealed that significant degradation of the contact is occurring and that a more stable alternative would be desired moving forward.

In summary, an alternative to the **Al/Al$_x$O$_y$/SAM/Pb/Ag** stack is desirable since

- the native oxide forms a high tunneling barrier, resulting in a low tunneling current.
- Pb and its salts are harmful to human health.
- the Pb/Ag top electrode degrades, leading to device malfunction after $\leq$ 6 months. This might potentially be avoided by replacing Ag with gold (Au), which is the more commonly applied capping layer material.[22] However, Ag was chosen over Au within this work, since the PVD system in which lead was allowed and two consecutive evaporation steps without breaking the vacuum were possible, exclusively featured thermal evaporation from tungsten boats. Gold is well known to form alloys with tungsten and was hence ruled out.

While the low current might not be a problem for niche applications, lead had to be replaced as top contact material in order to clear the path for potential future commercial scaling of the devices.

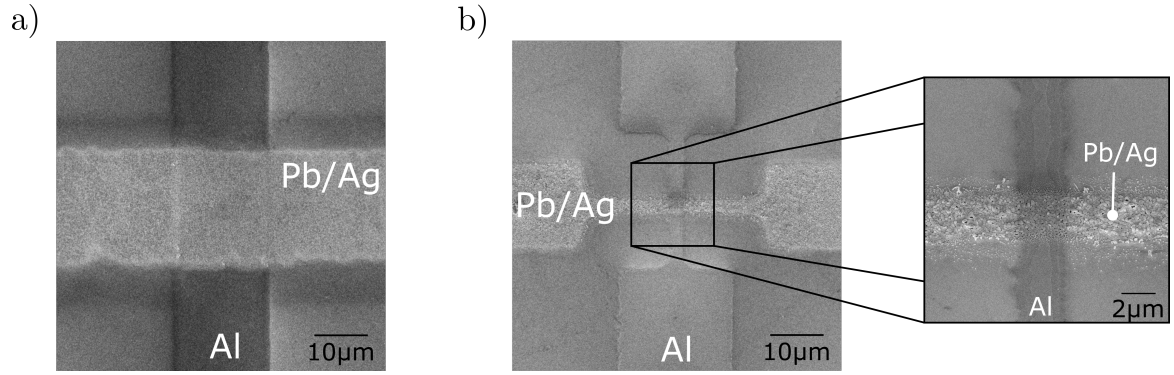

Figure 8.0.2 SEM images of Al/QM15/Pb/Ag devices exemplifying Pb/Ag electrode degradation. a) Device on a sample that has been imaged one day after fabrication b) Device on a sample that has been stored a nitrogen cabinet for 6 months. Right image shows a magnification of the indicated area, detailing the grain formation in the Pb contact. Images were rotated and cropped to align the Pb/Ag electrode with the horizontal and the Al electrode with the vertical axis for all images. Note: Images are from different samples and show different junction areas. The images shown here were motivated by devices on the stored sample not showing any electrical current with an applied bias after they did show pronounced hysteresis 6 months before. Hence, the grains shown in b) are likely to occur after some time and likely the reason for device malfunction.

Novel SAM Contacting Scheme

Identifying a potential fabrication scheme for ensemble molecular devices in a simple sandwich junction architecture with a molecular monolayer embedded in-between two conductive layers has been a critical challenge in the field of molecular electronics for almost half a century. Mann and Kuhn were the first to report having found a reliable contacting scheme with permanent, solid contacts in 1971.[87] However, a truly reliable, universal method has not yet been found. Over the last years, several causes of device failure have been identified. These include the reactivity of the organic molecules with the condensed metals, presence of defects in the SAM before top contact formation and diffusion of top contact metals through the monolayer.[6] Others have explored a myriad of fabrication schemes avoiding the physical vapor phase deposition (PVD) of the top contact.[238] Still, most of these schemes are currently incompatible with large scale, industrial fabrication. Hence, a method to deposit a metallic top contact on a SAM by PVD is essential for experiments leading to a better fundamental understanding of charge transport processes in self-assembled monolayer based electronic devices as well as for significant technological advances with these types of devices. To get to the fabrication of reliable top contacts by means of PVD, multiple concepts have been evaluated. These include: the reduction of the energy transferred to the monolayer by indirect evaporation,[239] the introduction of a protective interlayer on top of the SAM [112, 240] and the use of functional groups in the SAM constituting molecules that promote cross-linking of the molecules triggered by adsorbate atoms. [241] These concepts were developed to address the proposed most influential effect causing device failure: the energy transfer of atoms impinging on the SAM surface. Few experimental studies have proposed an alternative predominant reason for device failure. Namely, that the substrate and the anchoring group of the SAM determine the likelyhood of top contact metal atoms diffuse through the monolayer. This was for instance shown for the evaporation of different metals on alkyl SAMs on silicon and silicon oxide, [242] of lead on various SAMs on silicon [243] and for the evaporation of different metals on alkyl SAMs on gold (Au) [51]. Following these arguments, this chapter aims at providing a first contribution to extending the search for a simple contacting scheme of EMJs to different anchoring layers. Since studies of SAM-based electronic devices today are mostly limited anchoring layers of Au or Si, there is a dearth of data utilizing other materials as anchoring layer. Titanium nitride (TiN) as bottom electrode

material and titanium (Ti) as top contact have been chosen as a first contribution trying to help fill that research gap. Currently, TiN is widely used in complementary metal-oxide-semiconductor (CMOS) technology, e.g., as a diffusion barrier. This makes a potential **TiN/SAM/Ti** top contact device likely compatible with CMOS technology[244].The successful growth of phosphonic acid SAMs on TiN has been previously reported.[245] Phosphonic acids with their potential bi- or tri-dentate binding to the substrate are also known to be less mobile on the surface than thiols. [246] Since for thiol based SAMs this mobility has been proposed to contribute to the diffusion of top contact atoms to the head group, where energetically preferable complexes may be formed, reducing this mobility might contribute to hinder this process, ultimately supporting the successful fabrication of SAMs with a metallic overlayer.[247]

8.1 SAMs on TiN surfaces

In order to evaluate TiN as alternative anchoring layer for liquid-crystal inspired monolayer devices, the growth of alkyl-phosphonic acids on TiN was first investigated. Self-assembled monolayers that are constituted of molecules with a surface-binding head group and an alkyl chain are a well characterized model system to study the growth of monolayers. [6, 72, 113, 248–251] Results from a variety of measurement methods can therefore be compared to readily available data from literature. A variety of phosphonic acids has already been shown to for monolayers on TiN [245] as well as on TiO_2 [73, 252], that is potentially present as native oxide on TiN surfaces [65]. However, these studies are either limited on few, specific molecules, required for a specific, desired function, or limited to few characterization methods. A more general study with an otherwise well-known model system is still lacking and important to lay the foundation for electronic devices based on phosphonic acids on TiN. The following paragraphs aim to provide such a study.

A series of alkyl phosphonic acids , namely hexyl- (C6), octyl- (C8), decyl- (C10), dodecyl-(C12), tetradecyl-(C14) and hexadecyl-phosphonic acid (C16) was grafted on 50 nm thick, sputter deposited TiN samples as described in chapter 4 for all following measurements. Briefly: Cleaned silicon samples with a TiN overlayer were dipped in 1 mM solutions of the respective molecule in THF for 72 h, heated at 130 °C for 1 h, cooled down, rinsed in an ethanol stream for 10 s and heated again at 130 °C for 10 min. VASE, AFM and contact angle data was acquired using the same samples. To minimize the effect of potentially adsorbed water on the surface, contact angle measurements were performed last. Samples for XPS, AFM scratching and FTIR were freshly prepared using the substrates from the same wafer.
The change in water contact angle was used as a first indicator of successful orientation and binding of the molecule to the surface. AFM was used to characterize the uniformity of the SAMs on TiN surfaces. AFM scratching and VASE were used as complementary methods to analyze monolayer thickness and confirm that the formed films were monolayers. XPS was used to study the composition of native TiN surfaces as well as providing a third means of determining film thickness.
Infrared spectroscopy was used to study the potential binding of the constituents of the head group to the surface as well as the quality of potentially the formed SAM.
Lastly, the prediction that the **TiN/APA-SAM/Ti/Au** system is suitable to fabricate large-area molecular junctions comprised of a self-assembled monolayer (SAM) sandwiched between two solid state contacts was evaluated by fabricating 1D crossbar devices with the series of aliphatic phosphonic acids named above, and performing

cyclic IV measurements on these devices. Part of the recorded data was fit to a Simmons model and a tunneling attenuation factor β was determined and compared to literature values.

8.1.1 Water Contact Angles

The APA grafted TiN samples mentioned above were analyzed using a water contact angle measurement setup. To analyze the effect of solvent immersion on the water contact angle, a sample with bare TiN surface was additionally analyzed before and after 72 h immersion in THF. The bare TiN surface before and after immersion was found to be rather hydrophilic (WCA < 70°) whereas the APA modified surfaces were found to be more hydrophobic (WCA > 90 °). A 5 ° increase in water contact angle was observed after immersion of the bare TiN in THF. This is likely due to the partial adsorption of solvent molecules on the substrate. Immersion of substrates in solutions of aliphatic phosphonic acids resulted in a WCA shift greater than 20°. Since this a significantly higher increase than the increase by the solvent alone, it can be ascribed to the presence of the aliphatic phosphonic acids. This difference in WCA values is expected since the SAMs are terminated with non-polar, hydrophobic methyl groups, whereas the bare surface can be assumed to be hydroxyl-enriched and therefore hydrophilic. Hence, the increase of the contact angle by > 20 °indicates successful attachment of the APAs to the TiN surface. Figure 8.1.1 shows the water contact angles of the series of aliphatic phosphonic acids on TiN compared to the bare surface. Examples of pictures taken to determine the WCAs of the aforementioned surfaces are shown in the same figure. Note that the contact angle difference between bare TiN and alkyl-phosphonic acid treated surfaces is already visible from the images alone.
Overall, the WCA measurements of APA grafted TiN samples revealed a non-polar surface which strengthens the hypothesis of successful monolayer formation.

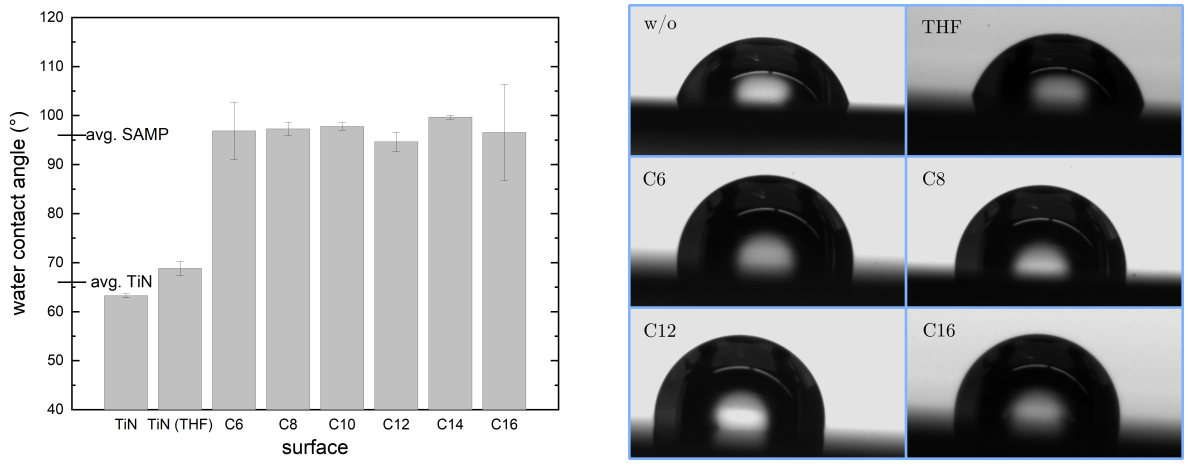

(a) **(b)**

Figure 8.1.1 Water contact angles of TiN surfaces after 72 h of treatment with varying solutions of alkyl phosphonic acids or THF. a) Contact angles as determined from one sample per surface and 3 measurements on each surface. Error bars indicate standard deviation. b) Optical microscopy images of typical water droplets on a bare TiN surface (w/o), on a solvent exposed TiN surface (THF) and on an alkyl phosphonic acid-functionalized surfaces visualizing functionalized surfaces being more hydrophobic than unfunctionalized ones.

8.1.2 Atomic Force Microscopy

The APA grafted TiN samples mentioned above were further analyzed using AFM topography. On each sample, 3 areas of 5µm x 5µm were imaged and the mean square roughness of the particle-free area was analyzed. The

resulting values as well as representative AFM images are shown in Figure 8.1.2. Cleaned TiN samples with no further treatment show a roughness of R_q = 0.24 nm±0.03 nm. The samples grafted with APAs have an overall mean roughness of R_q = 0.42 nm±0.32 nm. Since the average and standard deviation of C10 are with R_q = 1.00 nm ± 0.63 nm comparatively high, it is justified to treat this sample as an outlier. The increased roughness might be due to an only partial removal of unbound molecules during fabrication. These unbound molecules sticking out of the monolayer would slightly increase the observed roughness. The overall mean roughness for all APA grafted samples excluding C10 was R_q = 0.30 nm ±0.16 nm. Overall, the AFM images show uniform surfaces of APA grafted TiN with roughnesses comparable to the bare substrate. This indicates successful formation of a closed, uniform monolayer of APAs on TiN.
Note that the values reported here differ only slightly from previously reported values of R_q(TiN) = 0.4 nm and R_q(C8) = 0.4 nm that were measured on different samples, using the same fabrication and measurement scheme. [231] This points towards good reproducibility of our results.

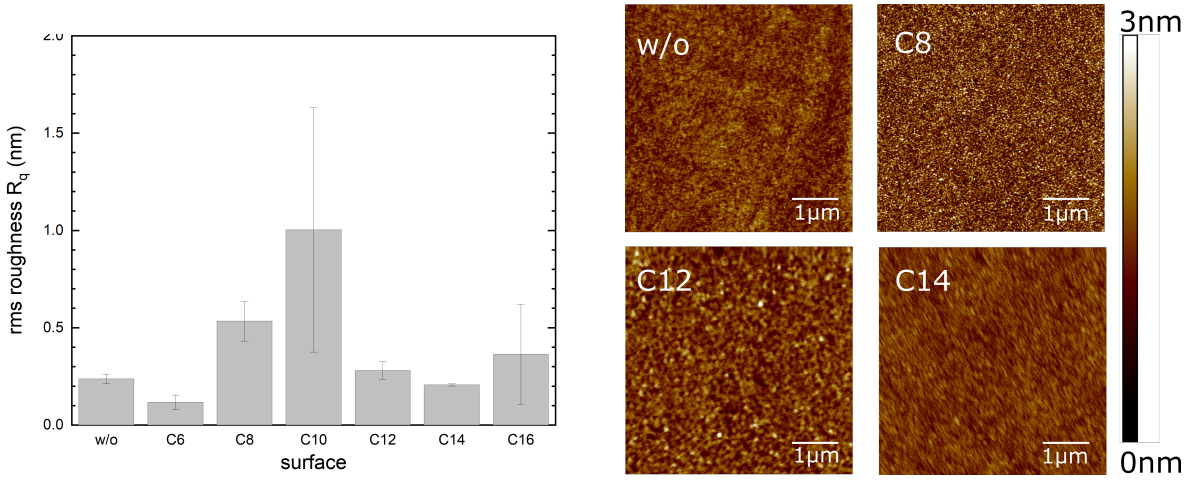

Figure 8.1.2 Atomic force microscopy of APA grafted TiN surfaces a) Root mean square surface roughnesses R_q of all surfaces. Error bars indicate standard deviation. Except C10 coated samples, all samples exhibit a roughness below 1 nm. Roughnesses of APA coated samples are in the same range as the roughness of the bare substrate. b) Surface topography of selected spots on four of the samples. All images have the same height scalebar. Images show a homogeneous surface for APA coated samples as well as the bare substrate (w/o). This indicates successful formation of a uniform, closed layer.

8.1.3 X-Ray Photoelectron Spectroscopy

The bare TiN coated reference samples were studied using XPS in order to analyze surface composition and gather information about potential attachment mechanisms of phosphonic acids to that surface. The surface of the reference substrate was found to be comprised of 17% TiN, 63% Ti(ON) and 20% TiO_2. This indicates that the TiN surface contains, in addition to the nitride compounds TiN and Ti(ON), a proportion of native oxide. This oxide in turn may allow the grafting of phosphonic acids on these samples.
To investigate the formation of potential monolayers on TiN, TiN substrates grafted with C6, C10 and C12 were also analyzed using XPS. In particular, the P2p region was studied to confirm presence of phosphor on the coated samples after the rinsing procedure. Figure 8.1.3a shows the P2p region for all four substrates. A clear peak can only be observed for the APA treated samples. There is no peak for the bare substrate. This confirms the presence of phosphor for all but the reference substrate and is another indicator for successful APA grafting on TiN. The peak intensity of C6 is the highest, followed by C12 and then C10. For the same number

of molecules per surface area, the P2p peak intensity is expected to increase with decreasing chain length, since the signal should get less attenuated when a shorter alkyl chain is present as compared to a longer one. However, the peak intensity also depends on the number of molecules present in the analyzed area. A higher number of C12 molecules per area as compared to C10 might explain the higher peak intensity of the P2p signal of C12 as compared to that of C10. This could, for instance, be the case, if the packing density was increased for C12 versus C10.

The intensity of the carbon signal is displayed in Figure 8.1.3b. It shows a clear increase in peak intensity from the bare substrate to the APA coated samples as well as an increase of the peak intensity with increasing chain length. This is another indicator that alkyl chains of increasing length are present on the coated samples.

Since the number of titanium atoms per area does not depend on the monolayer and titanium is an unlikely contaminant on the surface, the Ti2p signal attenuation was analyzed to calculate the APA layer thicknesses. The Ti2p signal intensities as well as the integrated intensities in the range of 452 eV to 467 eV are shown in Figure 8.1.4. The observed exponential decay of the Ti2p signal with increasing number of C atoms in the alkyl chain is in accordance with the expected behavior based on the Lambert-Beer law. The result of the thickness calculation is presented in the following section alongside thickness determinations via other measurement techniques.

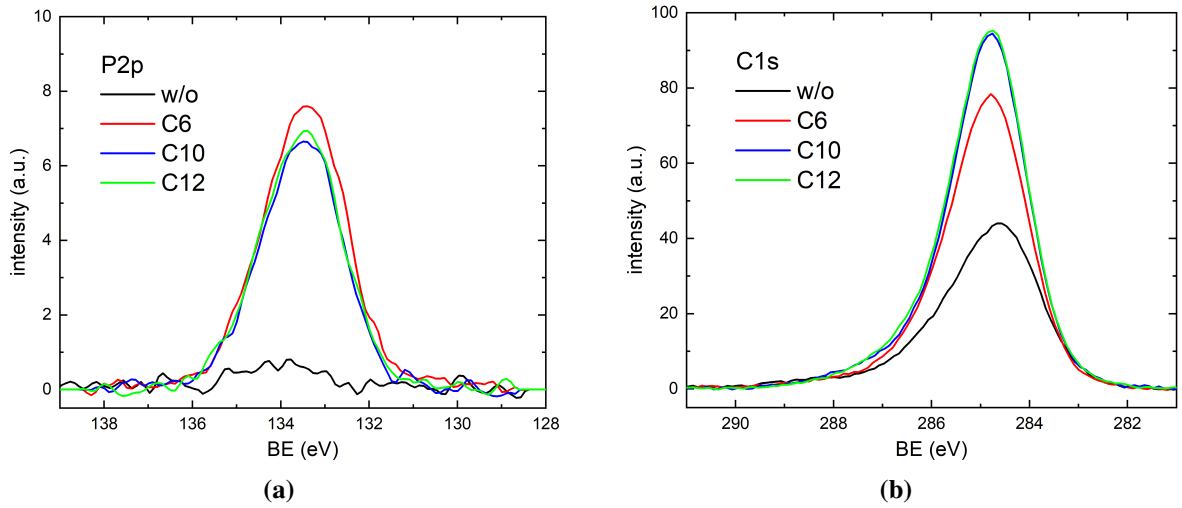

Figure 8.1.3 Background-corrected XPS spectra of APAs on TiN *Black line*: bare substrate, *red*, *blue* and *green line*: TiN substrates with alkyl-phosphonic acids with an alkyl chain of 6,10 and 12 carbon atoms, respectively a) Phosphor signal intensity. The bare substrate does not show any signal in the P2p region whereas the APA crafted samples show clear peaks. This confirms the presence of phosphor on the substrates after the dip coating procedure. b) Carbon signal. Non-zero signal of the bare substrate is likely due to contaminants introduced during sample transfer. Increasing peak value with increasing alkyl chain length indicates the presence of the expected alkyl chains. Graphs published in [231] ©2020 IEEE.

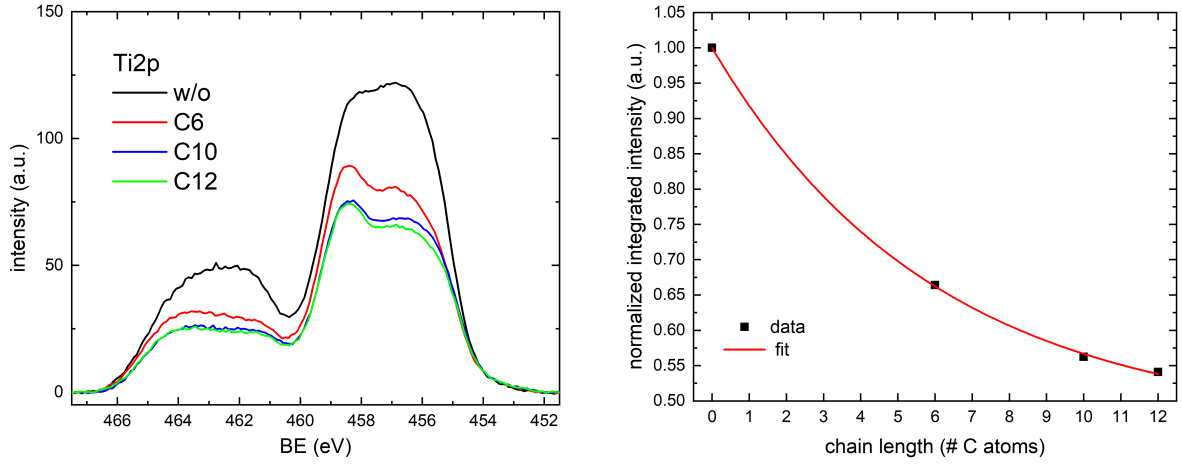

Figure 8.1.4 Ti2p signal attenuation a) Ti2p signal intensity. *Black line*: bare substrate, *red*, *blue* and *green line*: TiN substrates with alkyl phosphonic acids with an alkyl chain of 6,10 and 12 carbon atoms, respectively. The bare substrate exhibits the highest peaks whereas the signal from samples coated with APAs is attenuated. b) *black squares*: integrated intensity from 452 eV to 465 eV of the traces shown in a), plotted against number of C atoms in the alkyl phosphonic acid. *Red line*: Exponential fit to the data.

8.1.4 Thickness of the Surface Coating

AFM scratching, VASE as well as XPS were used as complementary methods to determine layer thicknesses of the series of APAs.
To determine the thickness via AFM scratching, samples treated with C6-C16 were scratched with a DLC tip at 212 mV drive amplitude over an area of 1 µm x 1 µm. Plane-fitted topographies of 5 µmx5 µm areas after scratching, with the scratched area in the center are displayed in Figure 8.1.5. Scratching was successful on all layers. Layer thicknesses were determined from height surveys in the scratching region by performing Gaussian fits to the two prominent peaks and determining the distance between the x-position of their maxima. Height surveys including Gaussian fits to the prominent peaks are shown in Figure 8.1.6.

To determine the thicknesses of C6, C12 and C14 from XPS data, the normalized integrated intensities of the Ti2p peaks were analyzed as described in Chapter 3.3.2. The empirical attenuation length $\lambda(E_{kin})$ was calculated using the maximum kinetic energy of the Ti2p E_{kin} = 470 eV, yielding $\lambda_{APA}(470\,\text{eV})$ = 1.93 nm. With I_0 determined from the untreated sample, the layer thicknesses were calculated.

To determine the thicknesses of C6-C16 via VASE the substrate was optically modeled as Si/SiO_2/TiN stack. Parameters of the resulting optical model were then fit to measurement results of an untreated Si/SiO_2/TiN substrate. The resulting model was fixed and the APA layer was added as Cauchy layer with A = 1.55 and B = 0.0 on top. Reported layer thicknesses are the result of fitting this model to the data until a mean square error <20 was reached.

The theoretical molecule length was calculated as optimized geometry of the molecules in GAUSSIAN 09 for isolated molecules in gas phase. These calculations were performed by Achyut Bora, TU München. Since APAs are expected to bind to the surface with an angle >0°, this length is expected to overestimate layer

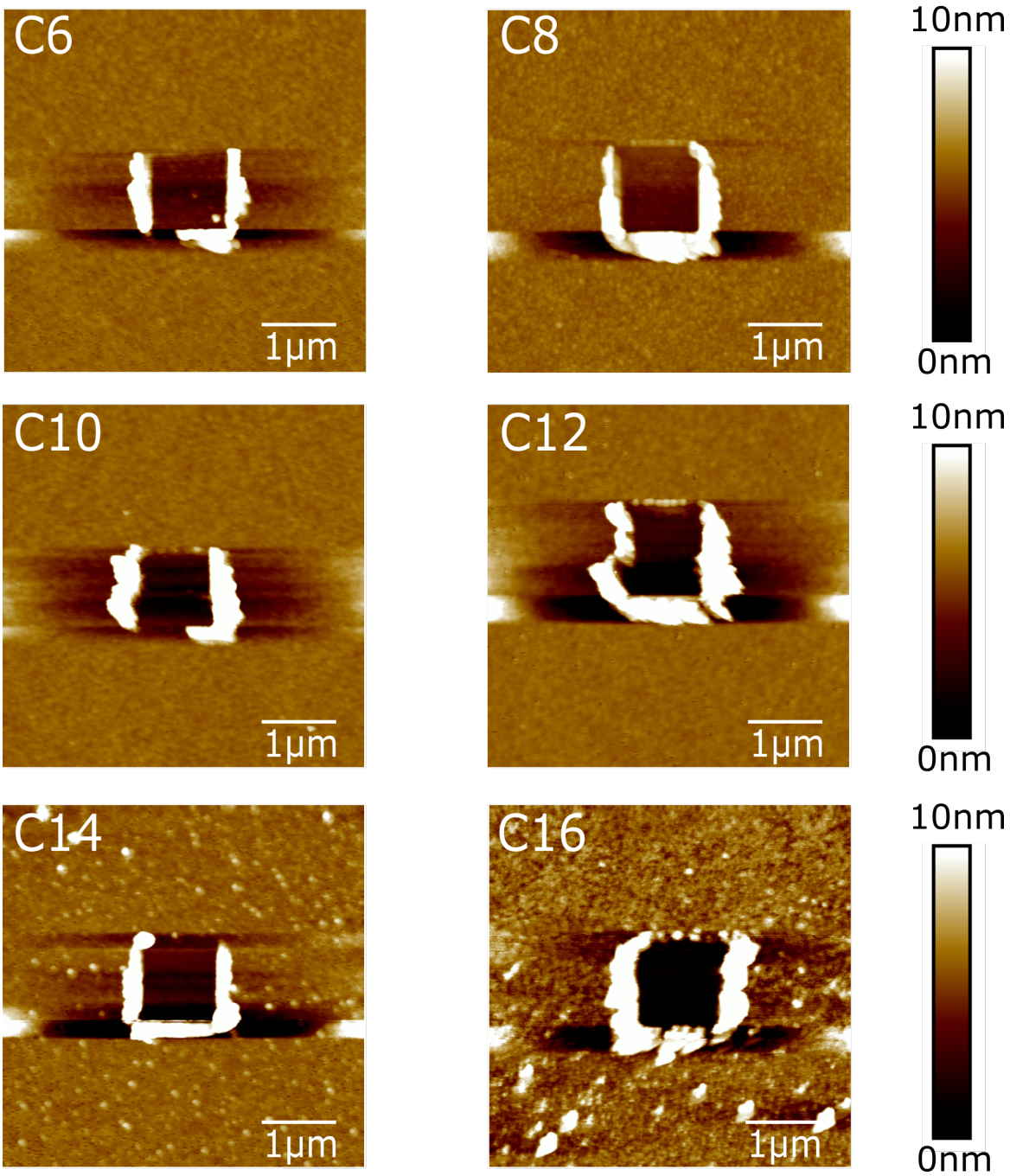

Figure 8.1.5 Plane-fitted topographies of APA coated TiN samples after AFM scratching. All images reveal a clearly defined square area of lower height in the middle, indicating successful removal of the SAM through the previous scratching step where a DLC tip was moved over an area of 1 µm x1 µm in the center of the 5 µm x 5 µm image while applying a 212 mV drive amplitude. White edges on the left and right side of the scratched area indicate areas where the height exceeds the scalebar. There, it is likely, that excess molecules that have been scratched away accumulated, since at these positions the AFM tip changed direction from right to left or vice versa.

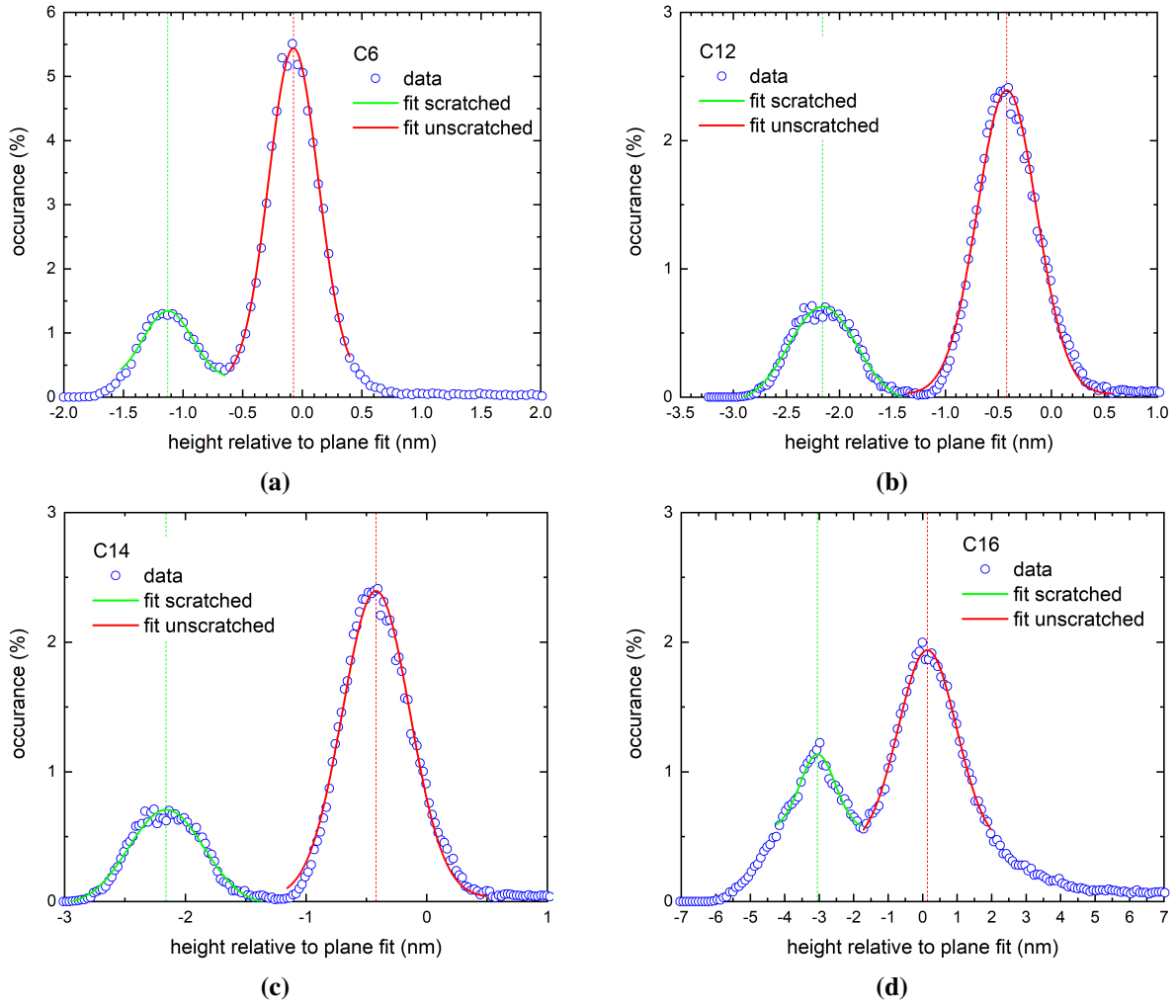

Figure 8.1.6 Height surveys of the AFM scratching topographies that are displayed in Figure 8.1.5. *Open blue circles*: Measured heights. *Green* and *red curve*: Gaussian fits to the prominent peaks representing the scratched and unscratched area of the image, respectively. *Dashed lines* indicate x-positions of the maxima of the Gaussian fits and hence the average relative height of scratched and unscratched area. The difference of those two values is the average thickness of the respective monolayer. Height surveys of a) C6, b) C12, c) C14, d) C16. Thicknesses of C8 and C10 were determined in the same fashion.

thickness. [253]

The results of all measurement methods as well as the calculated thicknesses of the monolayers are summarized in Figure 8.1.7. In total, a monotonically increasing layer-thickness with number of C atoms in the alkyl chain can be observed in the results from all measurement modalities. AFM scratching results are closest to the theoretically calculated values, VASE seems to overestimate the thickness while XPS Ti2p attenuation seems to underestimate it. This is likely due to the fact that the latter two methods depend on models that were not derived specifically for the self-assembled monolayers at hand. The thicknesses derived from XPS and VASE directly depend on a parameter that has to be estimated based on empirical data. For XPS, the attenuation length λ of the SAM has to be estimated, whereas the optical model of a SAM heavily depends on an estimate of the A parameter of the Cauchy layer. Both parameters are in turn highly dependent on the density of the monolayers, which are both uncertain and may vary with alkyl chain length. [6] If, for example, the gradient of 0.0022 nm/eV of the empirical, linear fit of the XPS attenuation length λ derived by *Laibinis et al.*[182] and *Wallart et al.* [183] was increased to 0.004 nm/eV, the normalized integrated intensity of the measurements shown above would yield layer thicknesses that are closer to the calculated values, namely $d_{XPS}(C6) = 0.95$ nm, $d_{XPS}(C10) = 1.37$ nm and $d_{XPS}(C12) = 1.42$ nm. Since the attenuation length depends on the structure of the SAM and the structure of the APA-SAM on TiN might differ from the thin organic layers used to determine the referenced empirical value, the empirical value proposed here might be more suited to describe APAs on TiN. Measurements the P2p signal of TiN surfaces treated with phosphonic acids of additional unique chain lengths might be used to improve and validate this new empirical value.

In total, all measurement modalities show the expected thickness trend for C6-C14. With the limitations of XPS and VASE mentioned above in mind, the thicknesses determined from XPS, VASE and AFM scratching provide compelling evidence for successful monolayer formation of C6-C14 on TiN. Thicknesses obtained from VASE and AFM scratching are inconclusive as to whether monolayers of C16 on TiN were formed, or in fact multi-layers of this molecule are present. In fact, Figure 8.1.2 shows several agglomerates outside the scratching region which can be seen as a first indicator for more than a monolayer being present on the sample.

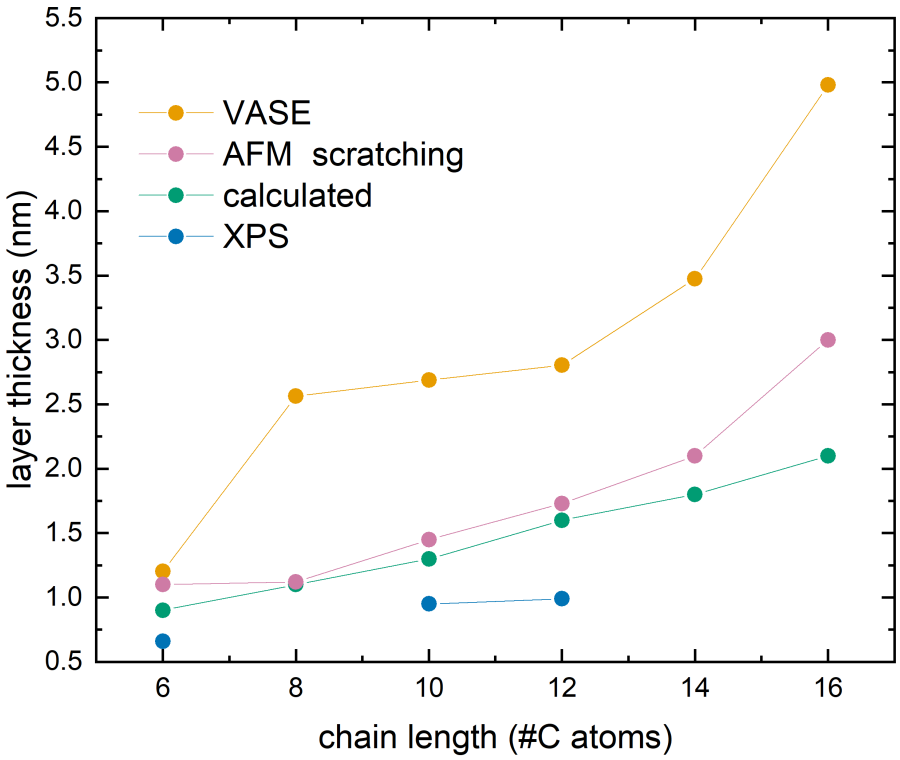

Figure 8.1.7 Layer thicknesses of alkyl phosphonic acids grafted on TiN as determined by XPS, VASE, AFM scratching as well as calculated contour lengths of the molecules. AFM scratching results are in very good agreement with the calculated thicknesses for C6-C14. For the same molecules, XPS and VASE show the expected trend, deviations are likely due to errors in estimated parameters in modeling. Data is inconclusive as to whether C16 forms mono- or multi-layers on TiN.

8.1.5 Infrared Spectroscopy

Infrared spectra of monolayers of APAs C6, C8, C10, C12, C14 and C16 on TiN were recorded using FTIR. The spectroscopic data was analyzed with two main objectives:

1. Confirm the presence of an alkyl chain on the substrate and analyze the quality of the monolayers through in-depth analysis of the position and full-width half maximum width of the symmetric and asymmetric stretching vibrations of CH_2.

2. Confirm the chemical bonding of the constituents of the phosphonic acid group to the substrate through analysis of the ν(P-OH) vibration, the symmetric as well as the asymmetric ν(P-O) stretching vibration, the ν(P=O) stretching vibration and the Ti-O-P skeletal vibration bands.

The full, background-corrected FTIR spectra of C6 to C16 are displayed in Figure 8.1.8. In this overview, all spectra show peaks at similar characteristic frequencies. Differences will be discussed in detail below. In general, the FTIR spectra of APA treated TiN surfaces are very similar for all molecules, which is expected. The region of interest to confirm presence of an alkyl-monolayer and characterize its quality as well as the region of interest to analyze chemical binding to the surface are highlighted in blue and orange, respectively.[86]

Figure 8.1.9 shows the characteristic frequencies of the CH_3 and CH_2 stretching vibrations. The presence of the four typical peaks associated with CH_3 antisymmetric (2965cm^{-1}), CH_3 symmetric (2875cm^{-1}), CH_2 antisymmetric (2925cm^{-1}) and CH_2 symmetric (2855cm^{-1}) stretching vibrations in the difference spectrum confirms the presence of alkyl chains in the measured, APA-grafted samples. From a look at the raw spectra, it is already evident, that the peaks become more pronounced with increasing chain length of the molecule.
The peak positions and full width half maximum widths of the peaks associated with the antisymmetric stretching vibrations of the CH_2 backbone were extracted using the Voigt function as fit function. The results are displayed in Figure 8.1.10. The peak position shows a clear trend towards lower frequencies with increasing chain length of alkyl phosphonic acid. This is in very good agreement with literature and often associated to the potential increase in order of the SAM with increasing chain length. Monolayers of alkyl phosphonic acids with chainlength $\geq$ 10 C atoms show an asymmetric CH_2 stretching vibration peak position that falls into a region that is commonly associated with a high to very high degree of order of the SAM. [174, 197, 254, 255] Those with shorter wavelength can be considered to be in a less ordered configuration.
Overall, peak positions from C10-C16 range from 2925 to 2918cm^{-1}, which is comparable to peak positions of the same molecules on aluminum oxide surfaces that range from 2928 to 2923 cm^{-1}. [57]
A second strong indicator for well-ordered SAM formation, is a comparatively low peak width (full-width-at-half-maximum) of the symmetric and asymmetric CH_2 vibrations of a spectrum. The FWHM values of phosphonic acids on TiN range from 10 to 20 cm^{-1} for the asymmetric and from 6 to 11 cm^{-1} for the symmetric stretching vibration. These values are lower than the values previously reported for alkyl phosphonic acids of similar length on aluminum oxide (FWHM$_{asymmetric}$ = 24−31 cm^{-1}, FWHM$_{symmetric}$ = 13−19 cm^{-1}).[57]

In total, the analysis of peak position and FWHM of CH_3 and CH_2 of the FTIR spectra above indicate the formation of well-ordered monolayers of APAs on titanium nitride. The peak analysis of FTIR data of APAs on TiN points towards SAMs of APAs on TiN having an even higher degree of order than those on aluminum oxide. Peak positions follow the expected trend indicating higher ordered monolayers for longer molecules.

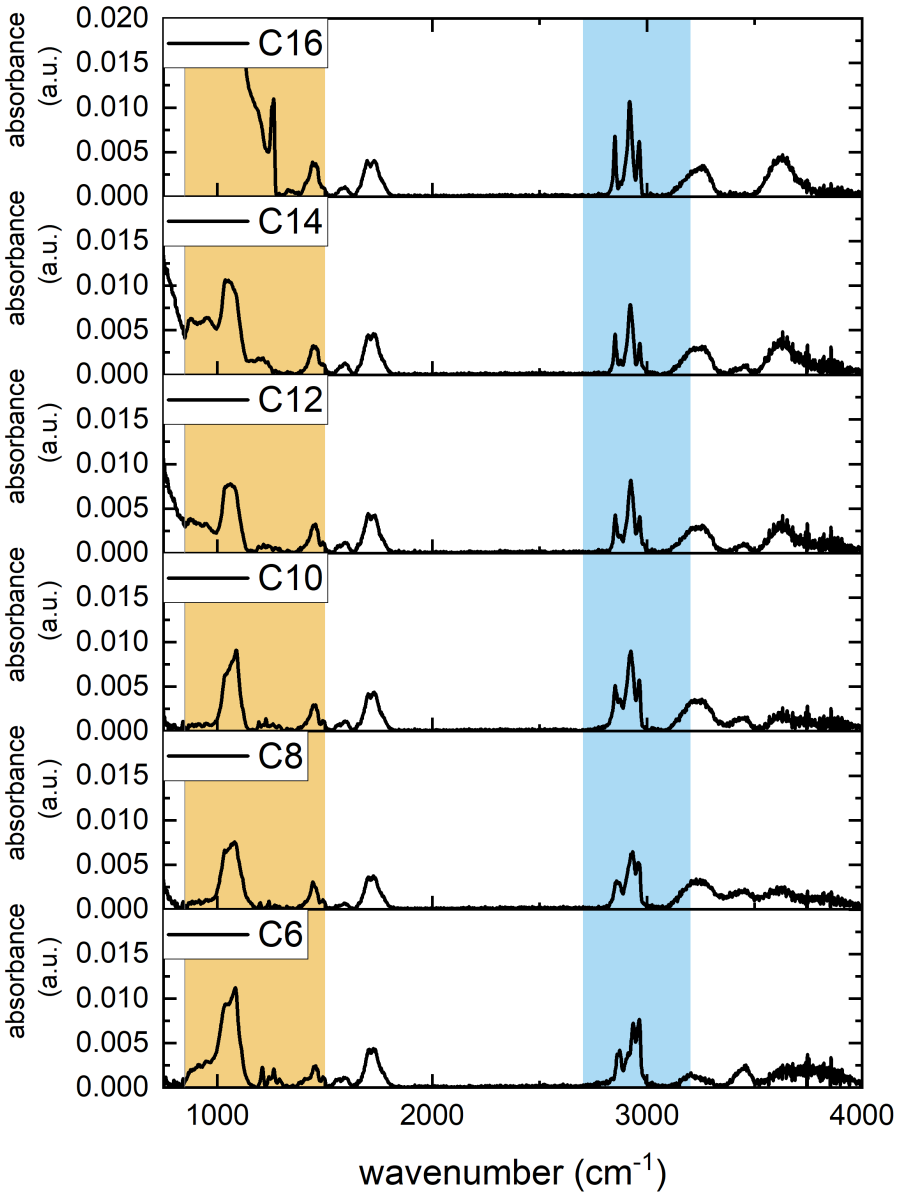

Figure 8.1.8 Infrared absorption spectrum survey of alkyl phosphonic acid grafted TiN samples. *Orange area*: 850-1500 cm^{-1} region, covering P-O, P=O, P-OH vibrational bands as well as Ti-O-P skeletal vibrations and $\delta(CH_2)$ deformation bands. *Blue area*: 2700-3200cm^{-1} region, covering CH_3 and CH_2 stretching vibrations. All samples exhibit similar absorption features.

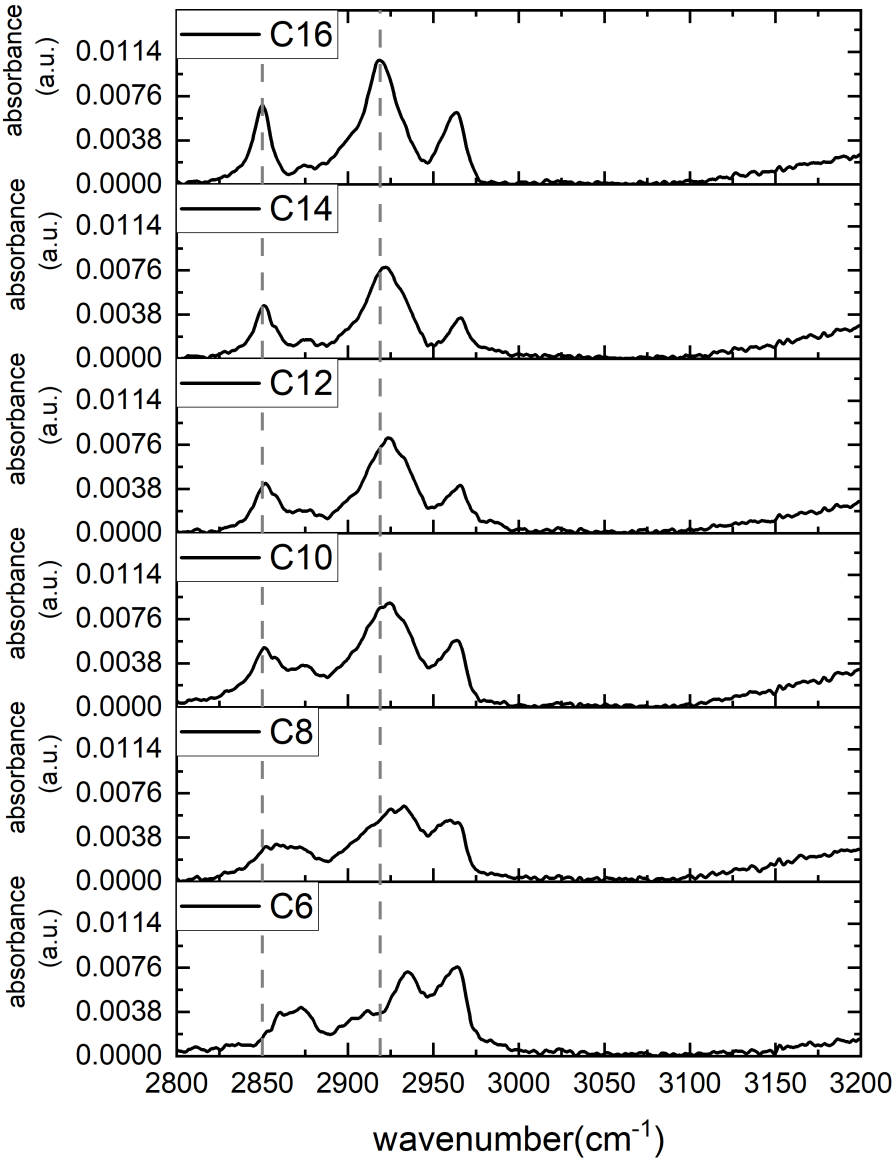

Figure 8.1.9 Spectral region of CH_2 and CH_3 stretching vibrations of potential APA SAMs on TiN. For all chain lengths, typical vibration bands of alkyl chains, namely the CH_3 antisymmetric (2963-2965 cm^{-1}), CH_3 symmetric (2872-2875 cm^{-1}), CH_2 antisymmetric (2918-2935 cm^{-1}) and CH_2 symmetric (2849-2855 cm^{-1}) stretching vibrations, are present. *Grey dashed lines* indicate the peak position of the CH_2 symmetric (2850 cm^{-1}) and the CH_2 antisymmetric (2919 cm^{-1}) stretching vibrations of C16 to facilitate the comparison of the same peak positions for the other chain lengths, since these characteristic frequencies are often used to judge the quality of a monolayer.

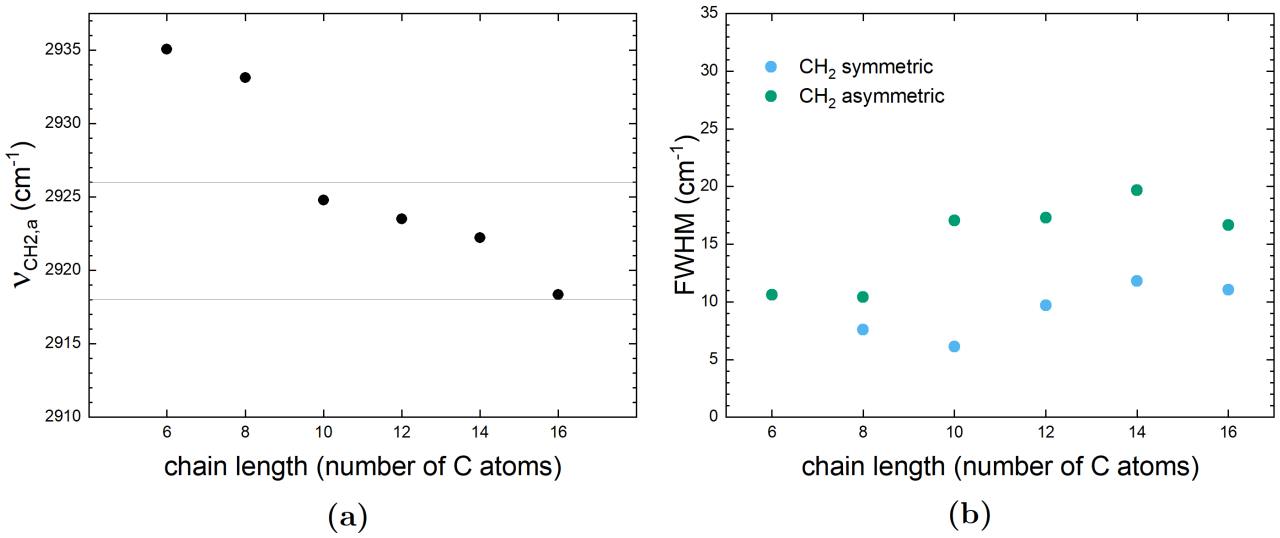

Figure 8.1.10 Peak position and FWHM of APA FTIR spectra determined from Voigt function fits to the raw data. a) Peak position versus chain length. *Light grey lines* indicate literature consensus for 'high degree of order'. Values above the upper line are considered to be connected with a 'low degree of order' whereas values below the lower line are considered to be connected with a 'very high degree of order'. b) FWHM for the symmetric (*blue*) and asymmetric (*green*) CH_2 stretching vibrations from the same fit.

To examine the binding of the phosphonic acid head group to the substrate the FTIR spectra were analyzed in the 850-1500 cm^{-1} region. The absorption bands of P=O, P-O and P-OH stretching vibrations, that lie in this region, are sensitive to the adsorption of APA molecules onto the potential metal oxide surface. If any of these groups is involved in forming a bond to the substrate, absorption peaks at their characteristic frequency are expected to disappear from the spectrum. [77, 78] Figure 8.1.11 depicts the FTIR spectrum of APAs grafted on TiN in the spectral range between 850 and 1500 cm^{-1}. The CH_2 deformations also fall into this region and can be observed as a weak peak at 1460cm^{-1}. This strengthens the evidence for alkyl chains being present on the analyzed samples surfaces.

Free phosphonic acid groups would show distinct peaks at the ν(P-OH) stretching vibration at 950 cm^{-1}, the anti-symmetric ν(P-O) stretching vibration at 1132 cm^{-1} and the ν(P=O) stretching vibration at 1280 cm^{-1}. These bands are marked red in Figure 8.1.11. Since for C6-C14 grafted samples, none of these bands shows a distinctive peak, bonding of the phosphonic acid group to the surface is confirmed and can be assumed to be tri-dentate. The C16 treated surface shows a peak at 1262 cm^{-1} which can be associated with a free P=O group. This could be either due to a bi-dentate binding of the molecules or due to molecules on the substrate that are not bound to the surface at all. One possible explanation would be the formation of a multi-layer. This is in agreement with the thickness measurements presented above, in particular with the AFM scratching results.

The band at 1093 cm^{-1} can be assigned to the symmetric ν(P-O) vibration. Together with the absence of a band at around 1253 cm^{-1} this is often associated with a surface bound phosphonic acid group. [256] Samples grafted with C6-C14 show a peak at the former and no peak at the latter position, which points towards a true monolayer of APA forming on TiN. Samples grafted with C16 show both peaks, which can be rationalized by the presence of a monolayer and additional, unbound molecules, which would be the case if there was a double layer.
The region between 1000 and 1050 cm^{-1} is commonly assigned to Ti-O-P vibrations.[252] All APA treated

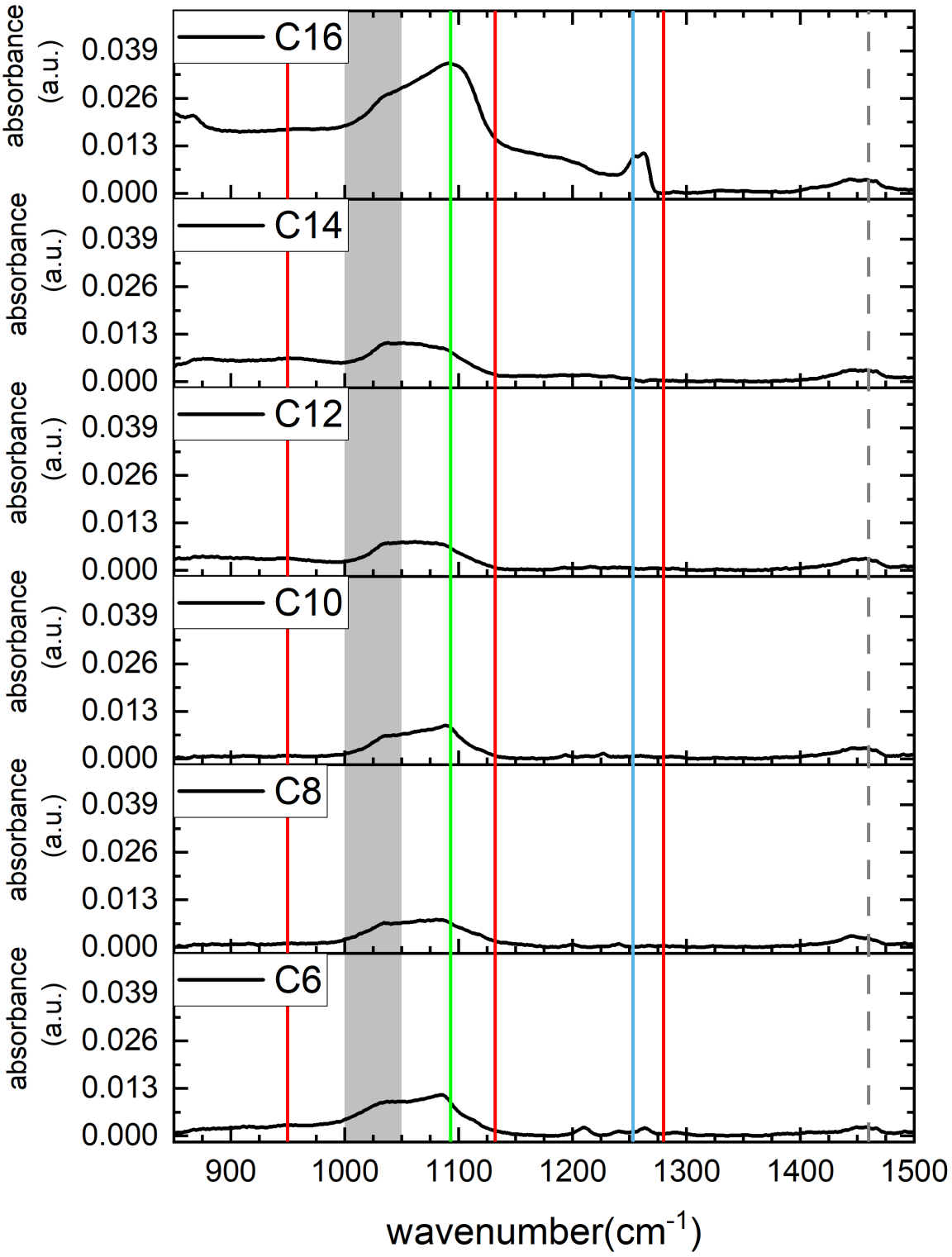

Figure 8.1.11 FTIR absorption spectra of APA grafted TiN surfaces at frequencies characteristic for bound phosphorous. *Red lines* indicate the characteristic frequencies of (from left to right): ν(P-OH) stretching vibration, the anti-symmetric ν(P-O) stretching vibration and the ν(P=O) stretching vibration, that would be present in unbound APA molecules, but are expected to be absent in surface bound APAs. *Green line* indicates symmetric ν(P-O) stretching vibration characteristic frequency, which together with the absence of a band at 1253 cm^{-1} indicates a surface bound PO_3^{2-}. The *blue line* marks the characteristic frequency of ν(P=O). The *grey area* indicates the range of characteristic frequencies assigned to Ti-O-P framework vibrations. The *dashed grey line* indicates the characteristic frequency of CH_2 deformations (1460 cm^{-1}).

TiN surfaces show a peak in this region as well, strengthening the hypothesis of surface bound phosphonic acid groups.

In total, the absence of bands associated with unbound phosphonic acid groups, together with the presence of bands associated with bound phosphonic acid groups, as well as the presence of Ti-O-P vibrations provide strong hints that the adsorption of alkyl phosphonic acids C6-C14 on TiN favours tridentate complexes. Together with the pronounced CH_2 vibration peaks, that are found at frequencies that indicate close monolayer formation, the infrared spectra of this series of alkyl phosphonic acid treated samples further give compelling evidence for successful formation of an alkyl phosphonic monolayer on TiN via dipcoating.

8.2 TiN/APA-SAM/Ti/Au Ensemble Molecular Devices

Samples with 1D crossbar devices consisting of a **TiN/APA-SAM/Ti/Au** stack were fabricated for a series of aliphatic phosphonic acids, namely hexyl- (C6), octyl- (C8), decyl- (C10), dodecyl-(C12), tetradecyl-(C14) and hexadecyl-phosphonic acid (C16) following the fabrication procedure outlined in chapter 4.
To confirm continuous layer formation on top of the SAM, SEM imaging was performed on some of the chips. A representative image of one junction with C12 sandwiched between TiN and Ti/Au is shown in Figure 8.2.1. The TiN resistivity was determined by measuring DC current-voltage characteristics of the 1 mm long

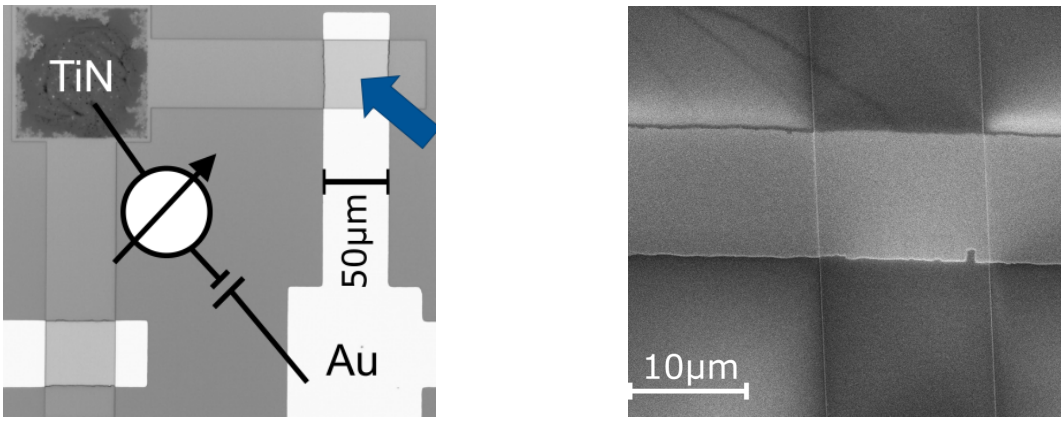

(a) **(b)**

Figure 8.2.1 Images of TiN/C12/Ti/Au 1D crossbars a) microscopic image of a 50 µm x 50 µm 1D crossbar (1D-XB) device depicting the contacting scheme. The darker color of the TiN contact pad originates from thicker metallization support. Blue arrow points at device under test. b) SEM image of a **TiN/C12/Ti/Au** 1D-crossbar shows homogeneity of top metal electrode.

reference bars of varying width. The experimentally determined value of $\rho_{TiN} = 1.1 \cdot 10^{-5} \pm 0.03 \cdot 10^{-5}\Omega$m is consistent with results reported in the literature. [162] These values being significantly lower than the resistivity expected from an alkyl chain monolayer, motivated omitting the lead resistivity in the further analysis.

DC current-voltage characteristics of ensemble molecular devices were measured up to ± 2V for at least 3 junctions per area and monolayer. An additional chip without any monolayer was also fabricated. The yield of devices with a conductivity in the expected range was between 20% (C6, 50 µm x 50 µm) and 100% (C12, 15 µm x 15 µm). A total number of 118 SAM-based devices with conductivity in the expected range was analyzed. Device-to-device variance was higher for shorter molecules and larger junction areas and lower for longer molecules and smaller junction areas.
In the following paragraphs, the results of these measurements will first be evaluated qualitatively to observe general trends. Then, the data will be compared to the Simmons model. To this end, tunneling attenuation factors β as well as the current density at V=0 V (J_0) will be determined and compared to literature values of similar systems. Finally, the data of individual, representative devices will be fit to the Simmons equation.

Figure 8.2.2 summarizes the current density-voltage (J-V) traces extracted from the above-mentioned measurements, averaged over 3 sweeps and 3 devices each, for each molecule length obtained for 15 µm x 15 µm area junctions. For fixed negative voltages, the current density dipole-induced a clear decreasing trend for increasing chain lengths from C6-C12. However, C14 and C16 break with this trend: For negative voltages ≥ -0.25 V their current densities are higher than those of C12 and still lower than C10. For

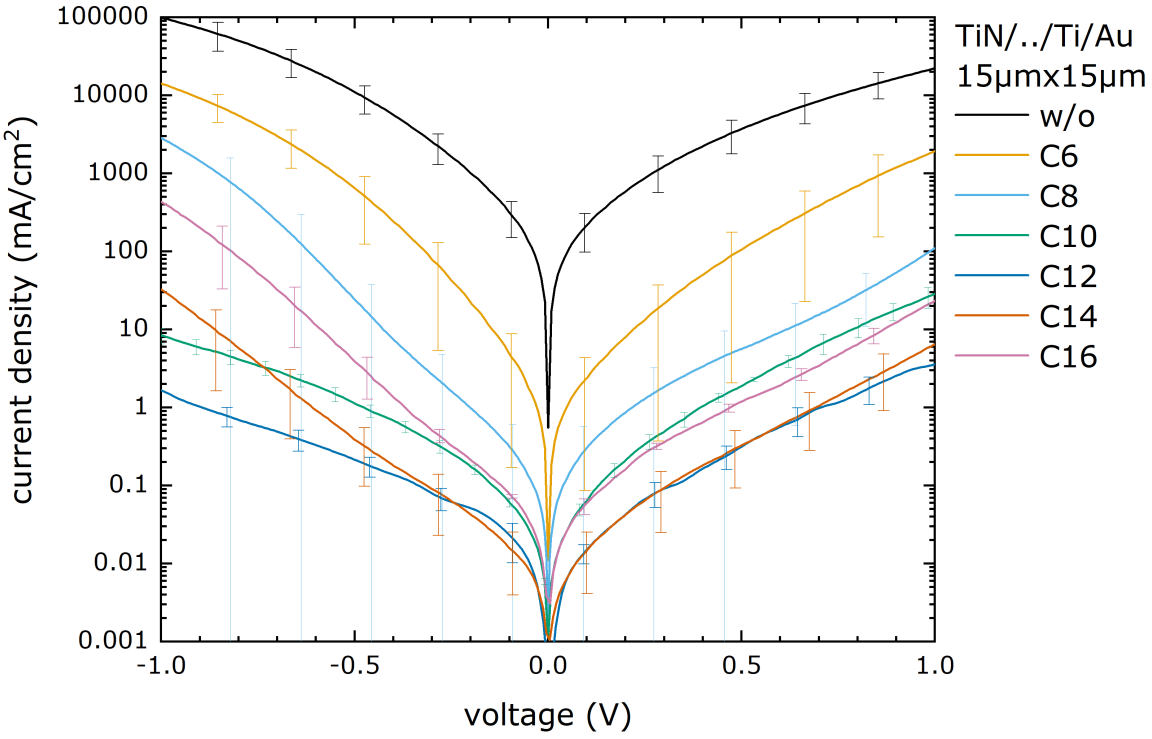

Figure 8.2.2 J-V traces for SAMs of alkyl phosphonic acids of different length. Averages over 3 sweeps and 3 devices per molecule length are shown. Error bars depict device-to device standard variation. Black curve (w/o) depicts the J-V trace for 3 devices without any monolayer sandwiched between the two contacts. Graph from [231]©2020 IEEE

voltages <-0.25 V the differential conductance of C14 and C16 devices is higher than that of C10 and C12 devices which ultimately leads to the current densities of C14 and C16 devices exceeding those of C10 and C12 devices at voltages ≤-0.75 V. In the positive voltage regime, the clear inverse relationship between molecule length and current density at the same voltage is preserved up to and including C12. Again, the devices with C14 and C16 sandwiched between the contacts break the trend. The average current density trace of the C16 devices differs only slightly from that of the C10 devices, whereas the C14 devices present a current density versus positive voltage characteristic which is almost identical to that of the C12 device.

In summary, the current density voltage characteristics of 15 µm x 15 µm area junctions with C6-C12 sandwiched between the contacts qualitatively follow a trend that is expected from tunneling devices with varying tunneling barrier widths - that is: a decreasing tunnel current density at fixed voltage with increasing chain length. In this first analysis, it is already observable that devices with C14 and C16 break this general trend and even inverse it at voltages beyond a certain absolute value.
One potential explanation could be a significant increase of packing density at these two chain lengths compared to monolayers composed of the shorter molecules. Over the area of a junction of a less than perfectly ordered monolayer, there are several parallel conduction paths that consist of varying amounts of through-space and through-molecule tunneling. [6] Since a molecule's HOMO and LUMO present lower tunneling barriers than the vacuum, a higher packing density that leads to an increase of conduction paths with more through-molecule tunneling would ultimately result in a higher current density. [57] In fact, layers made from longer alkyl chains (such as C14 and C16) are often reported to form more dense, ordered layers than those from shorter alkyl chains.[197] The FTIR spectra presented in the previous section point towards an increase of the degree of order of the monolayer with increasing molecular length, which is in support of this hypothesis.

8.2.1 J-V Traces for All Junction Areas

Expanding the analysis of J-V traces of the previous section to all 6 device areas for all 6 chain lengths leads to the study of the influence of both device area and chain length. To facilitate focusing on one at the time, the measured data is first grouped by chain length and then by device area. All data presented in this section was averaged over three cycles and three devices per molecule length and area.

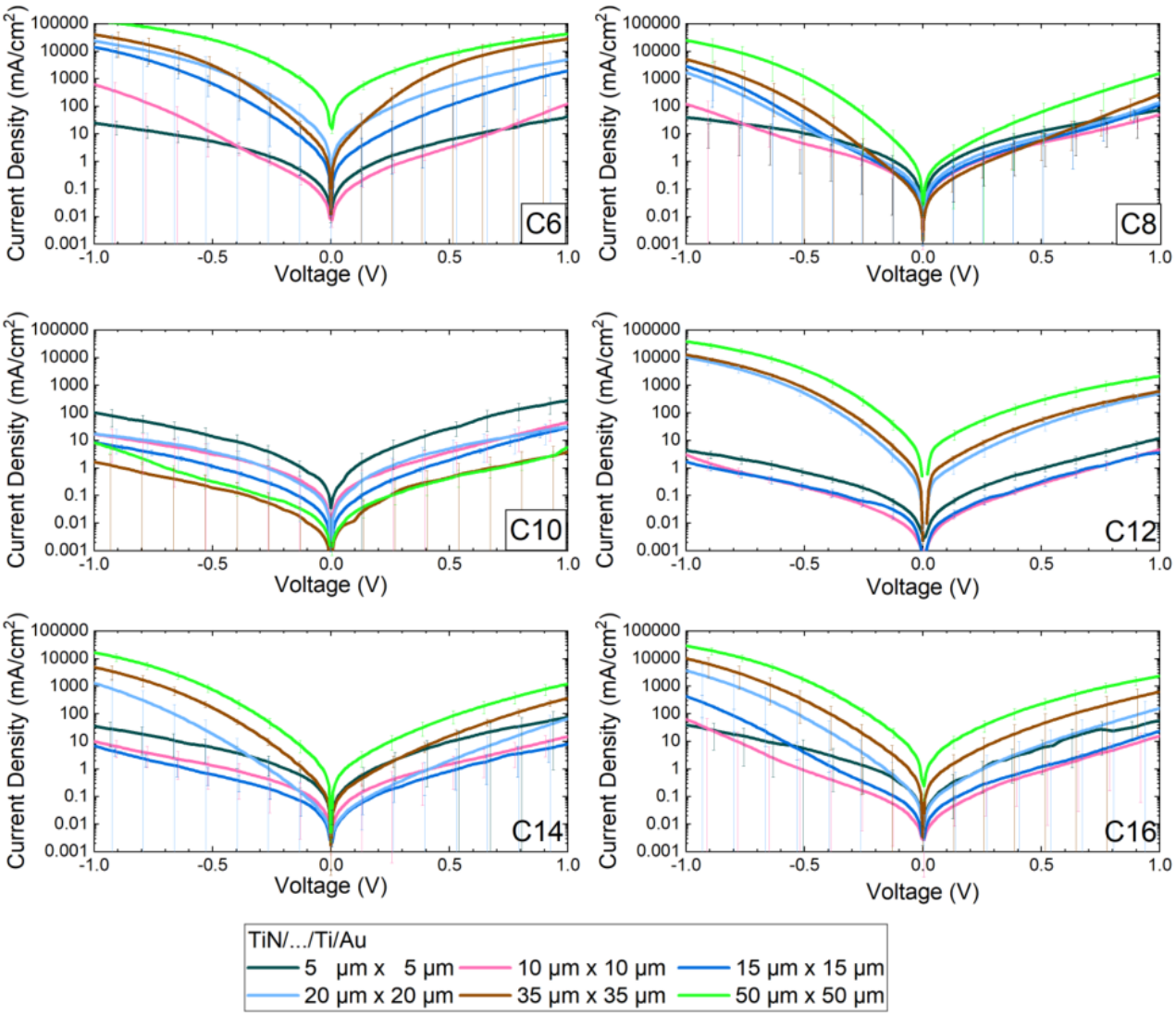

Figure 8.2.3 J-V traces for SAMs of alkyl phosphonic acids of different length and junctions of different areas, grouped by molecule length. Label in the lower right corner of each graph indicate the molecule. Averages over 3 sweeps and 3 devices per molecule length and per junction area are shown. Error bars depict device-to-device standard variation.

To analyze the area dependence of current densities, the averaged current density-voltage (J-V) traces were first grouped by molecule length. Figure 8.2.3 displays the J-V traces for each molecule length obtained for each of the six junction areas. This means that each graph corresponds to the data that originates from *one chip*. If the structure of the monolayer and the contacts were independent of surface area and homogeneous on the whole chip, the current density traces are expected to be indistinguishable for all areas. All of the graphs in Figure 8.2.3 show that this is not the case. For all molecule lengths it is evident that the current density varies with ensemble molecular junction area.

This deviation from the ideal assumption is not unexpected, since e.g., the occurrence of defects might scale

with area of the devices. However, a clear trend or relationship between conductance and device area can not be deduced directly from the data displayed in Figure 8.2.3. However, some features of the measured current density traces are clearly observable:

- For C10, C12 and C14 the current density traces split up into two groups. One consisting of the three larger area devices and one of the three smaller area devices. Within the former group the current density decreases with decreasing area. Furthermore the traces show similar differential conductances. Hence, their traces never cross within the measured range. In contrast to this, within the group of smaller device area, no clear trend of current density versus area is observable.

- for C12 the J-V traces of the three smaller device areas all exhibit current densities within one order of magnitude. The range of current densities between the three larger device areas is also approximately one order of magnitude. However, devices of larger areas show current densities of up to four orders of magnitude higher than devices of smaller area.

- All J-V traces show a slight asymmetry with respect to 0 V. For larger area devices ($\geq$20 µm x 20 µm) and shorter molecules (C6 and C8), J-V traces reveal a higher current density for voltages of negative bias as compared to the same absolute voltage of opposite polarity. This is particularily clear for devices with C12. For instance, devices of 50 µm x 50 µm area show a rectification ratio R = J(-1 V)/J(1 V) of $\approx$ 18. For devices with larger molecules (C12, C14 and C16) and smaller area devices ($\leq$15 µm x 15 µm), the opposite is true and the effect is less pronounced. 5 µm x 5 µm devices with C12 exhibit the rectification ratio 1/R = J(1 V)/J(-1 V) $\approx$ 2.1, which is approximately one order of magnitude lower than the rectification ratio of the larger area devices.

- All measurements show a short circuit current density of approximately 0 mA/cm^2. This means that no charging effects can be observed.

8.2.2 Molecule Length Dependence of Current Density for Varying Device Areas

Figure 8.2.3 depicts the same data as Figure 8.2.2, now re-organized such that each display item shows J-V traces of one junction area and of varying molecule length. This means that each display item groups data from 6 different chips. It corresponds to 8.2.2 plotted for all junction areas. Similar to the data grouped by molecule length, this representation does not clearly reveal any direct relationship. However, some trends can still be observed:

- For devices $\geq$ 35 µm x 35 µm area, J-V traces of all 6 molecules are clearly distinct, but follow no particular trend. At all voltages the current densities follow an increasing trend in the order C10-C8-C14-C16-C12-C6 and traces from C10 devices exhibit four orders of magnitude lower current densities than devices with all other molecules.

- For devices of 15 µm x 15 µm area, J-V traces follow a decreasing current density trend with increasing molecule length up to C12 at all voltages. Devices with longer molecules exhibit higher than expected current densities as well as a lower differential conductance (dJ/dV) than the rest of the devices.

- For devices of $\leq$ 15 µm x 15 µm area, J-V traces follow a decreasing current density trend with increasing molecule length up to C10 at all voltages.

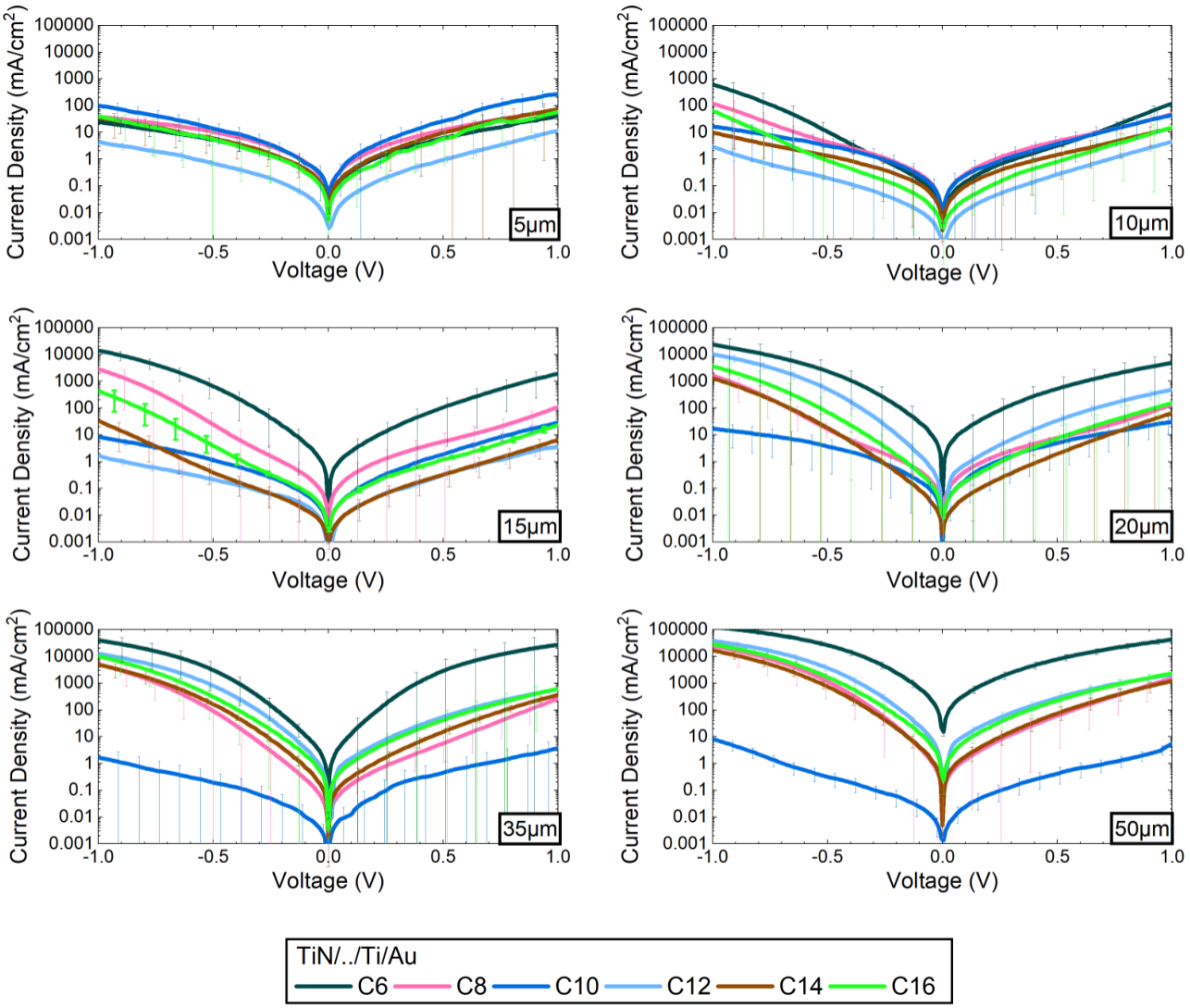

Figure 8.2.4 J-V traces for SAMs of alkyl phosphonic acids of different length and junctions of different areas, grouped by junction area. Label in the lower right corner of each graph indicates the edge length of square area devices. Averages over 3 sweeps and 3 devices per molecule length and per junction area are shown. Error bars depict device-to device standard variation. Legend below is valid for all graphs in this figure.

To further analyze the charge transport in these devices, the tunneling attenuation factor β was determined for all device areas at various evaluation voltages.

8.2.3 Comparison to the Simplified Simmons Model

Since the data presented above shows too much variance to justify averaging over device areas, current densities were sampled at fixed evaluation voltages for all J-V traces and then compared to the simplified Simmons model individually. To determine the tunneling decay constant β as well as the short circuit current density J_0 from a fit to the simplified Simmons equation $J = J_0 10^{-\beta \cdot d/2.303}$, the current densities averaged over three devices of all 6 junction areas at various evaluation voltages between -1 V and +1 V are first plotted as a function of alkyl chain length in Figure 8.2.6.

The following general trend can be observed: All averages from devices that feature areas ≥ 15 µm x 15 µm show monotonic, near exponential decay with increasing molecular chain length up to a defined molecular length. For 15 µm x 15 µm devices this trend is preserved until C14, for devices of larger area until C12. Longer alkyl chains showed an increase of current density from C12 to C16 between one order of magnitude for 15 µm x 15 µm devices and three orders of magnitude for 50 µm x 50 µm devices.

To calculate the tunneling decay constant β as well as the short circuit current density J_0, only current densities that followed the general trend of decreasing values with increasing alkyl chain length were considered when fitting the data. Specifically, for 15 µm x 15 µm area devices the data from C6-C12 was taken into account, data from 5 µm x 5 µm area devices was not fitted at all and for all areas, the data from C6-C10 was taken into account. The resulting values for β and J_0 are shown in Figure 8.2.6. Values for devices with junction area 10 µm x 10 µm to 20 µm x 20 µm fall into the consensus range in literature across different types of junctions β = 0.5-1.5 nC^{-1} (where nC is the **n**umber of **c**arbons in the alkyl chain). [100, 131, 197, 257–261] For larger areas, β is above this consensus area. This means that the current density falls off quicker with increasing molecule length for large area devices than would be expected. One potential explanation for this is, that the molecule length is not the only factor contributing to a decreased current density at increasing chain lengths and that at least one of these additional factors is particularly present in devices of larger junction area.

One of these potential factors might be that defects scale proportionally with area and inversely proportional with molecule length. Since generally speaking, the packing density of molecules in an alkyl SAM increases with increasing chain length, and the number of defects scales inversely with the packing density, a longer alkyl chain ultimately leads to fewer potential parallel 'defect' conduction paths in a device.[262] If these open spaces are filled by metal atoms during evaporation, they show higher conductivity than the electron transfer through a molecule. A decrease in the number of such pathways then leads to a decrease of the overall measured current. This in turn would decrease the current density more with increasing chain length than could be explained by the change in distance of the contacts alone. Since defects in the SAM seem to scale with area this effect would more profoundly show in junctions of large area than in those of small area. At the same time, J_0 seems to proportionally increase with increasing junction area at constant evaluation voltage. This is in support of the hypothesis since the presence of more parallel conduction paths with higher conductivity than the path through the molecule and the inverse scaling of their occurence with area of the device might also explain why the injection currents J_0 increase with increasing device area.

Another factor that might play a role is the electrically active area - the area through which current actually passes - of the devices. Comparing current densities instead of currents comes with the benefit of being able to compare junctions of different areas. However, determining the geometrical area A_{geo} of the junction might in

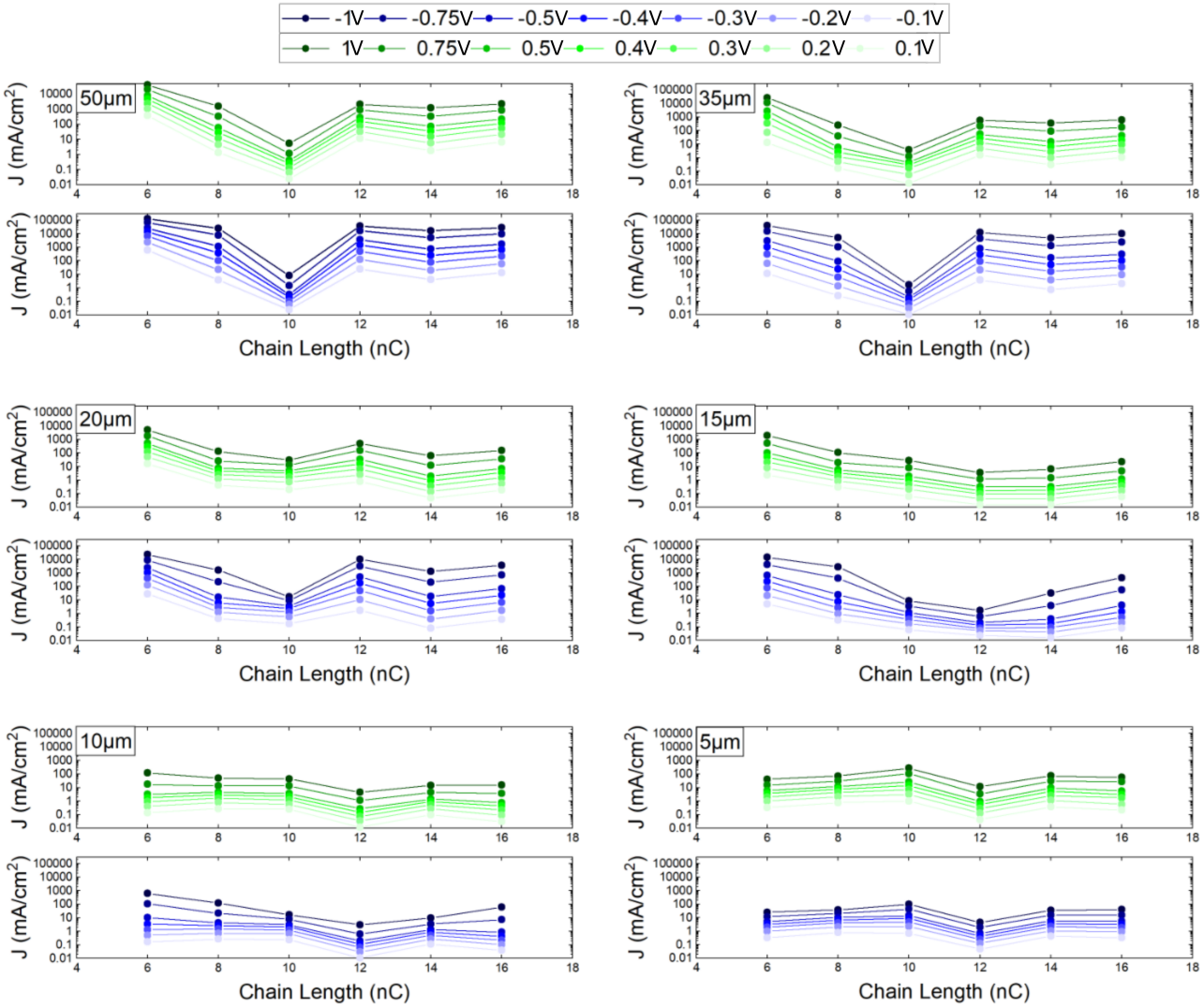

Figure 8.2.5 Semi-logarithmic representation of current densities at various evaluation voltages for all junction areas and plotted against alkyl chain length in number of carbon (nC). *Green* indicates positive voltage, *blue* indicates negative voltage. Increasing absolute voltage values are represented by increasing color saturation of the corresponding symbol and line. A clear close to exponential decrease of current density with number of carbon atoms can be observed only over a limited range of number of carbons.

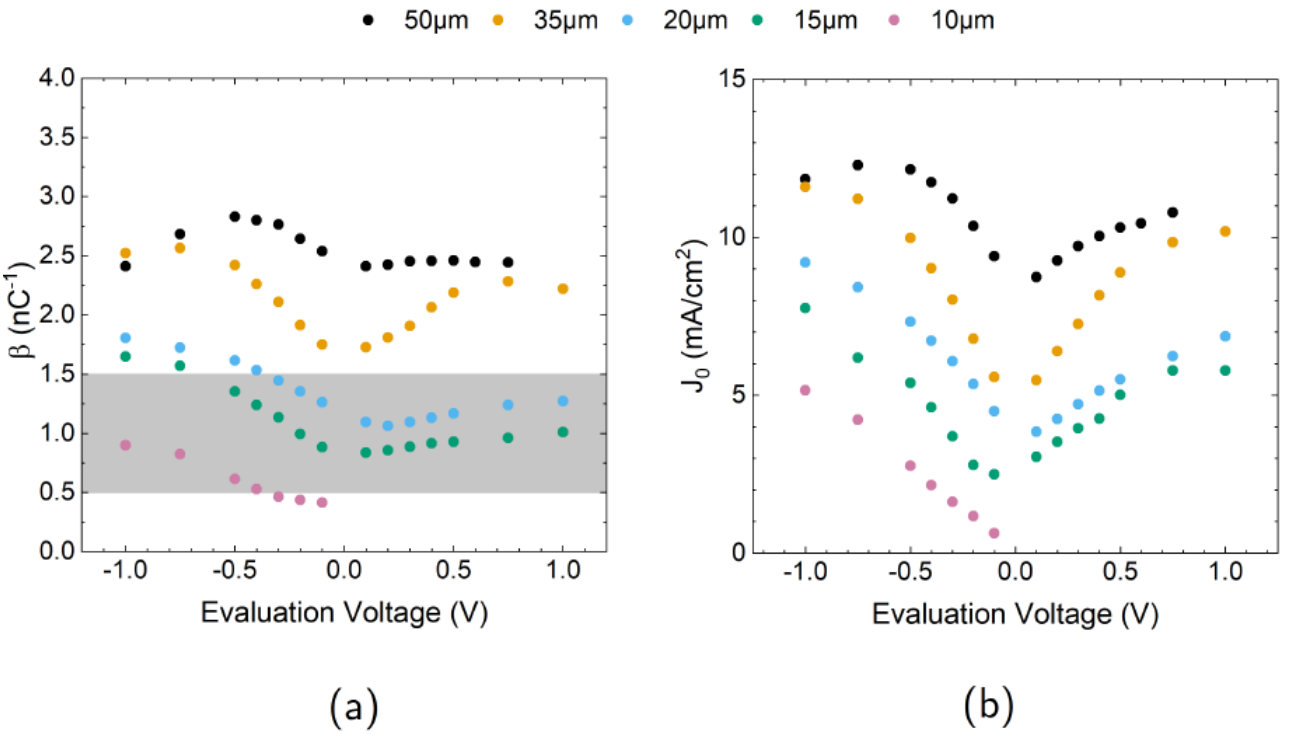

Figure 8.2.6 Tunneling decay constant β and injection current J_0 from a fit of the experimental data to the simplified Simmons equation $J(V) = J_0 10^{-\beta d/2.303}$ at evaluation voltages between -1V and 1V. a) Values of β. Colored points indicate calculated values, the *grey area* indicates literature consensus on the attenuation factor of alkyl chain SAMs. b) Values of J_0. Legend in the middle is valid for both figures. Both, the value for the decay constant and the injection current increase monotonically with area of the measured devices.

fact not be a suitable tool to determine the scaling factor used to calculate the current density. [131] The area, that the current is divided by to yield the current density is the electrically active area of the device A_{el} which is likely different from A_{geo}. This is mainly due to two reasons: Firstly, contact between two surfaces only occurs through asperities on these surfaces, since they always have a non-zero roughness. Secondly, only part of the physical contact area is known to be conductive. [263, 264] In literature, between 0.01-10% of A_{geo}, is often assumed to be the electrically active area. As long as the properties of the interfaces that determine A_{el}/A_{geo} do not change, the current density and the injection current density derived from A_{geo} are overestimated, but can be compared to each other. For the junctions discussed in this section however, these properties might change with chain length of the molecule. This might be due to the fact that the occurrence of defects and the packing density of the SAM might change with molecule chain length, ultimately making A_{el}/A_{geo} dependent on the molecule length.

The data presented in Figure 8.2.6 also shows a that β as well as J_0 mostly increase with magnitude of the evaluation voltage. For voltages $|V| \leq 0.5$ V and devices with $\leq$ 35 µm x 35 µm area, this increase is nearly linear. The full form of the Simmons equation predicts the opposite: a decrease of the β with increasing magnitude of bias. [124] Curiously, this trend for tunneling attenuation constant β and injection current J_0 has been previously observed by others. [92, 94, 126, 260] A possible explanation for this, suggested for instance by Frisbie et al. [260], Majda et al. [265], and Nijhuis et al. [126], is electrostriction, i.e., the deformation of the monolayer caused by the applied electrical field. It is noteworthy that the Simmons equation provides a very approximate treatment of tunneling through molecular barriers. Since it includes several simplifications, the

range of potential explanations for deviations from that model is large, including the influence of image charges [113], deformation of the SAMs [92] and changes in the mechanism of charge transport from chain-to-chain [266] to through-bond-tunneling [267]

While literature consensus of β for molecules with an alkyl backbone has been confirmed by many different techniques, the reported values of J_0 span more than eight orders of magnitude. [126] This suggests that the variations across different systems that might have an influence on β are not large enough to significantly alter its value. However, unlike β, J_0 requires extrapolation of the data over a large range and is hence, by definition, more sensitive to the choice of electrodes, interfaces and potentially present protective layers. Since the system presented here deviates strongly in these respects from previously reported systems, there are no consensus values of J_0 to compare the data to.

In total, the fact, that the tunneling decay constants at most evaluation voltages and junction areas lie within the consensus range for self-assembled monolayers with an alkyl chain and that $\beta(V)$ dipole-induced a previously reported trend, is a strong indicator that the measured devices are in fact tunneling devices with an alkyl-phosphonic acid monolayer sandwiched between the two contacts. In particular, the decay constants for 15 µm x 15 µm devices fall into the consensus region. For these devices, most chain lengths (C6-C12) were considered, when fitting the data to the model. The scaling of defects with junction area as well as the potential shift in electrical active area as function of the packing density for alkyl phosphonic acids with a chain length $\geq$ 14 C atoms have been discussed as potential sources for the current density of devices featuring longer chain alkyl phosphonic acids increasing with area and chain length.

Overall, the data from electrical measurements reveals some tunneling specific characteristics pointing towards the successful fabrication of molecular tunneling devices. However, the particularities breaking the trends for device area and molecule length are at this point not fully understood and would require more in-depth analysis of the contacting scheme and a much more detailed model of charge transfer across the junction.
For this contacting scheme to be a useful tool to characterize molecules with an electrically active functional group and to further develop ensemble molecular devices, understanding all particularities of the model system is not necessary. Moving forward, it was decided to focus on the analysis of devices of areas $\leq$ 20 µm x 20 µm, since their analysis yielded results expected from theoretical models.

8.2.4 Comparison to the Full Simmons Model

To further investigate the absolute current densities of the devices presented above, a quantitative comparison to the Simmons tunneling model was performed. To account for the fact, that the electrically active area may likely be a portion of the geometrical area, the Simmons model was expanded by a factor $K = A_{el}/A_{geo}$. The analytical formula for this adjusted Simmons formula then reads:

$$J(V) = K\frac{\alpha}{d^2}\left[\left(\Phi - \frac{V}{2}\right)e^{-db\sqrt{\alpha\left(\Phi-\frac{V}{2}\right)}} - \left(\Phi + \frac{V}{2}\right)e^{-db\sqrt{\alpha\left(\Phi+\frac{V}{2}\right)}}\right] \tag{8.2.1}$$

Representative sweeps from devices of 15µm x 15µm area with molecules C6, C8, C10 and C12 sandwiched between the conductive leads were chosen to perform fits to the Simmons model. This area and these molecules

Table 8.1 Fitted parameters resulting from fitting the adjusted Simmons tunneling model to single sweeps of representative 15 µm x 15 µm **TiN/APA-SAM/Ti/Au** devices.

Molecule	ideality factor α	monolayer thickness d /nm	ratio of electrical active / geometric area K
C6	0.71	1.15	0.1
C8	0.82	1.24	0.1
C10	0.75	1.30	0.1
C12	0.73	1.32	0.1

were chosen, since the tunneling attenuation factor analysis presented above showed that the decay with increasing chain length at low bias voltages, in which the assumptions of the Simmons model are valid, was found to be exponential for these particular combinations. For the optimization problem, current densities $J(V = 0V)$ were removed from the data since they seemed to cause computational errors. This is unlikely to affect the fitting procedure in a negative way. Generally, it has to be noted that the optimization problem featuring 4 free parameters leads to multiple local minima of the error function. To efficiently explore these and find solutions where α, d, ϕ and K are within the range of expected values, the following fitting procedure was executed: First, an exhaustive search was performed. Each parameter was set to 20 different values within a fixed range and the Simmons function was evaluated for all resulting $20^4 = 160,000$ possible combinations. The ranges of values for each parameter were:

$$\alpha \in [0, 1]$$
$$d \in [1\text{ nm}, 5\text{ nm}]$$
$$\phi \in [1\text{ eV}, 5\text{ eV}]$$
$$K \in [0, 1]$$

Out of the 160,000 results, the 50 candidates with the lowest mean square error compared to the measured data were chosen and further locally optimized using constrained optimization by linear approximation (COBYLA)[268] using the same constraints as before. Resulting parameter sets were then manually screened for sets where all parameters fall in a physically reasonable range. The barrier was anticipated to be invariant to molecule length and solutions that featured the same ϕ across data sets were hence preferentially chosen. This resulted in a barrier height of $\phi = 3.0$ eV which is physically reasonable for molecules with an aliphatic backbone. [154]

Figure 8.2.7 shows the low-bias J-V data of the representative sweeps together with the fits that yielded physically sound parameters. Note that all but one fit show an exceptionally good fit to the data with $R^2 = 0.99$. Only the fit of data from a device with C6 shows a worse fit with $R^2 = 0.88$. Looking at the raw data this is most likely due to the pronounced asymmetry of current densities at negative and positive voltages. A comparison with the sampled current densities in Figure 8.2.5 reveals that in fact, for +0.1 V and +0.2 V the sampled current densities follow an almost perfect linear trend whereas this is not the case for -0.1 V and -0.2 V. The parameters resulting from the outlined fitting procudure of individual sweeps are summarized in Table 8.1.

It is noteworthy that all fits presented here feature A_{el}/A_{geo}=0.1, suggesting that only 10% of the device area contribute to charge transport. This is in good agreement with what others have found across various types of ensemble molecular junction. [131] All fits are also characterized by an ideality factor $\alpha < 1$. This suggests

that the barrier does not have an ideal trapezoidal shape as assumed by the Simmons formula. This is likely due to the fact, that the tunneling barrier consists of two pieces: the molecule and the surface covering oxide. The shape of the barrier can then be assumed to be more step-like than trapezoidal. The monolayer thicknesses derived from this fitting procedure are monotonically increasing with number of C atoms. Compared to the values obtained by other methods however, they are smaller (compare Figure 8.2.4). This could be due to the fact that in the equation used to perform the fit, α and d are highly correlated. Another explanation might be that the evaporated titanium atoms might react with the SAM during condensation, ultimately forming a conductive complex or intermediate that could reduce the effective width of the tunneling barrier. However, without further analytics this remains speculative.

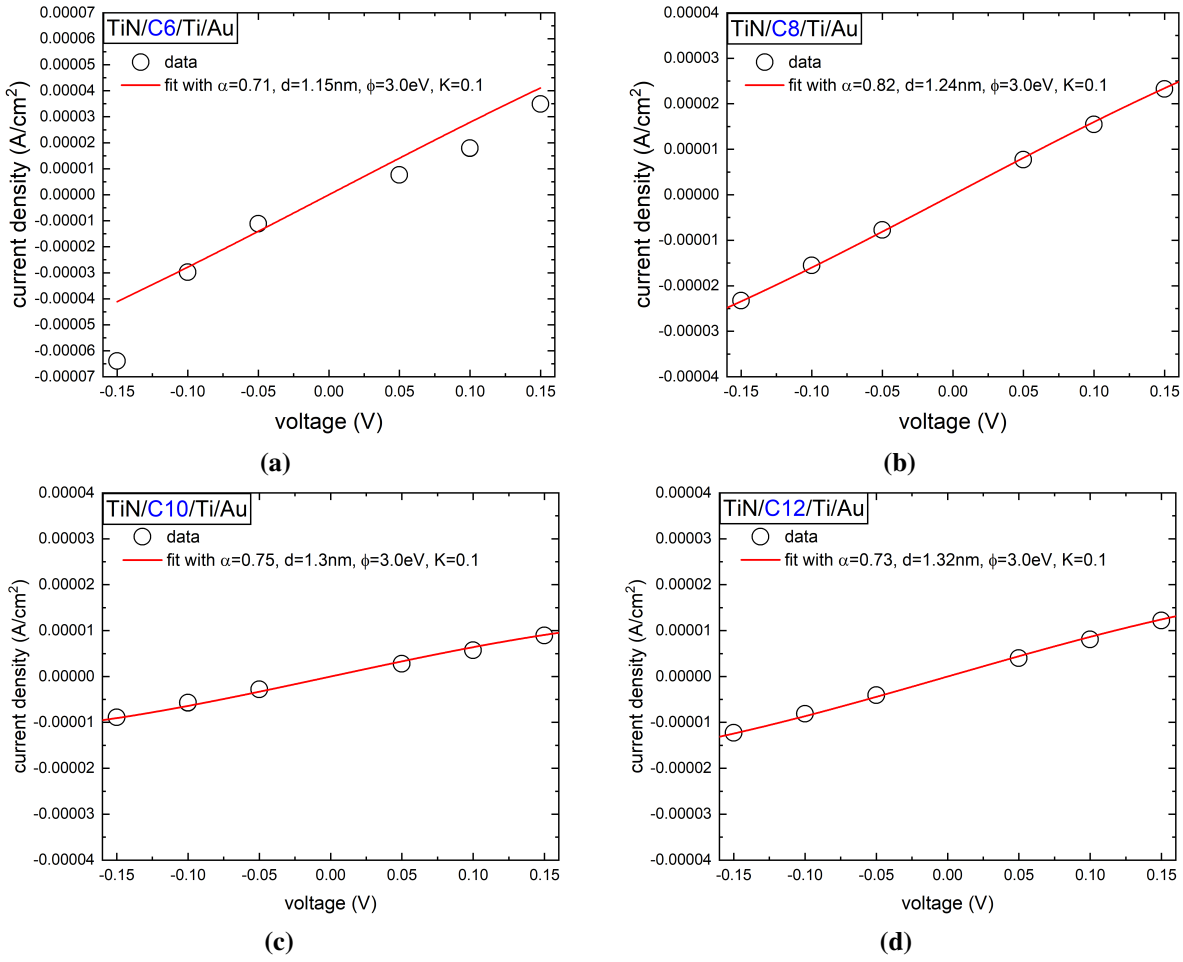

Figure 8.2.7 Fits of current densities to the adjusted Simmons formula. Subfigures a-d show the data (open circles) acquired from representative sweeps of junctions comprising APAs of length C6-C12 sandwiched between TiN and Ti/Au, as well as representative fits (red) to the data, using a global, then local optimization procedure. The fitting procedure yielded several potential fits with exceptionally good fit (R^2 = 0.99) for each dataset except for datasets of the C6 devices (best fit R^2 = 0.88). Fits that feature physically sound values for α and d, as well as a barrier height invariant to the molecule chain length (ϕ = 3.0 eV), were manually picked from the 50 best fits per molecule length.

8.2.5 Summary of Electrical Analysis

In total, the analysis of the recorded J-V traces of solid state devices of phosphonic acids of varying length sandwiched between TiN and Ti resulted in several observations that can not be explained at this point

with absolute certainty and require further study. Most notable, varying areas of the device are surprisingly connected with varying current densities at the same voltage. Also, the trend of decaying current density with increasing molecule length is, while generally true, broken for molecules with more than 12 carbon atoms.

From the analysis of the recorded J-V traces the following results point towards successful fabrication of **TiN/APA-SAM/Ti/Au** molecular tunneling devices:

- After top contact formation, the devices show a structurally intact, homogeneous layer on top of the SAMs.
- The tunneling decay parameter for devices of ≤ 20 µm x 20 µm area and evaluation voltages in the range of -0.5 to 0.5 V fall into the well established consensus range for tunneling through alkyl chains.
- Fitting the data of 15 µm x 15 µm devices with the molecules C6, C8, C10 or C12 sandwiched between TiN and Ti to the Simmons model results in physically sound parameters for the tunneling barrier (namely, ideality factor α, thickness d, barrier height ϕ and $K = A_{el}/A_{geo}$).

It is important to note that even though the electrical data supports the expected thickness trend, it does not allow to draw conclusions about the absolute thickness of the sandwiched SAM directly. Specifically, the data neither supports nor refutes the hypothesis that the highly reactive Ti might damage the terminal group of the monolayer. Others have found that the condensation of Ti on methyl-terminated SAMs can lead to a reaction yielding intermediate surface compounds at the interface. This is sometimes even found to be beneficial to prevent pin-hole formation. [51, 247, 269–272] From the analysis of single sweeps of representative devices, the thickness of the tunneling barrier was found to be thinner than expected, which could be a first indicator for this reaction playing a role in the fabrication of the devices presented above. As long as the devices under investigation show a low chip-to-chip and device-to-device variance and the desired device functionality is preserved, it is in fact not necessary to keep the SAM in its pristine state. *Haick et al.* have demonstrated that even discontinuous molecular films can yield functional electronic devices and have concluded that for ensemble molecular devices to find technological applications, achieving densely packed SAMs or perfect contact formation might not be necessary. [239] Having the application of SAM-based electronic devices in mind, a reproducible interface is found to be more important than an unaltered SAM surface. As long as the functional group providing the desired function is not affected, a fabrication scheme yielding reproducible results is sufficient. This is why a detailed study of the formation of the interface between SAM and Ti was left for others to explore and the promising electrical results were transferred to the study of ensemble molecular devices based on liquid crystal inspired monolayers.

8.3 Summary

To sum up the results from the analysis of monolayers of alkyl phosphonic acids on TiN as well as **TiN/APA-SAM/Ti/Au** ensemble molecular devices, the following was observed:

- An increase of water contact angle by >20°after APA grafting as compared to the bare substrate, indicating a change from hydrophilic to hydrophobic. This is in agreement with the expected change from a hydroxyl (bare substrate) to a methyl (SAM) terminated surface.

- Mean square surface roughnesses of the APA grafted samples are in the range of the roughness of the bare substrate ($\leq$ 1 nm), indicating closed layer formation.
- C1s XPS signal increase and exponential Ti2p XPS signal attenuation with increasing chain length, indicating the formation of a monolayer.
- Thicknesses calculated from three different measurement modalities, namely VASE, Ti2p XPS attenuation and AFM scratching, are in range with values calculated for single molecules using GAUSSIAN.
- In the IR absorption spectrum, peak positions of symmetric and asymmetric CH_2 stretching vibrations are found at characteristic frequencies typical for alkyl chains. FWHM values for Voigt fits to the CH_3 and CH_2 peaks in the IR absorption spectrum are low as compared to SAMs of APA on aluminum. Both results are commonly seen as indicator of closed monolayer formation.
- Absence of the IR aborption peak of the P-OH stretching vibration, presence of a peak characteristic for Ti-O-P framework vibrations as well as presence of a peak at the characteristic frequency characteristic of surface bound P-O. All indicate the successful, tri-dentate binding of the phosphonic acids to the clean, untreated TiN surface.
- From cyclic J-V measurements of devices with APAs sandwiched between TiN and Ti/Au, a trend of increasing tunneling current density with decreasing chain length was observed. Experimentally determined tunneling attenuation factors from these measurements are within the range of values previously reported by others.
- Tunneling attenuation factors β as well as injection currents J_0 were found to increase with increasing magnitude of the evaluation voltage. This also has been previously reported by others for tunneling across SAMs with an alkyl-backbone.
- Fits of the current density data of 15 µm x 15 µm devices to the Simmons model yielded physically sound values for thickness d, ideality factor α, barrier height ϕ and electrical active area A_{el}/A_{geo}.

These results, derived from a multitude of complementary methods, provide compelling evidence for successful formation of a self-assembled monolayer of phosphonic acids on native TiN surfaces and for the successful fabrication of ensemble molecular devices with SAMs sandwiched between TiN and Ti/Au.

Some questions with respect to the charge transport mechanism in **TiN/APA-SAM/Ti/Au** junctions still remain. Most notably, the surprising increase in current for the longest molecule chain lengths requires further study. The variation of tunneling current with device area that dipole-induced no clear trend is also left for further study. Molecular dynamics simulations that include an anchoring layer edge as well as locally resolved charge transfer measurements, e.g., using conductive probe AFM methods, on devices of varying area, may shed some light on these questions by investigating the potentially varying distribution of conductance channels across the junction area between devices with SAMs of different molecules. As reported by others [127, 273], defects in the SAM greatly influence device performance and could be further studied by impedance spectroscopy. [274]

In general, the ensemble molecular devices presented above capture details that are characteristic of charge transport through the sandwiched molecules. The electrical data presented hence strongly suggests that the novel combination of bottom contact, binding group and top contact is viable to yield functional electrical

devices based on self-assembled monolayers sandwiched between two solid contacts. In particular, grafting of TiN surfaces with alkyl phosphonic acids of varying length via dip-coating as well as the successful fabrication of ensemble molecular devices with a Ti/Au top contact have been achieved.
These results are also in support of the assessment most prominently supported by *Haynie et al.*, that device failure in ensemble molecular devices might be primarily governed by the choice of the material combination for anchoring layer and top contact [51] and thus encourages to broaden the search for such combinations. Preliminary results of the investigation of the feasibility of using NiO as anchoring layer for phosphonic acids are provided in the appendix of this work.

The contacting scheme developed in this work has since been successfully deployed for the study of charge transport through larger bio molecules that have been immobilized via short-chain phosphonic acids with a protein-binding head group. [275] As presented in the following chapters, the novel contacting scheme was also employed to investigate ensemble molecular devices with liquid crystal inspired molecules sandwiched between the contacts. The successful utilization of the general concept of the **TiN/phosphonic acid SAM/Ti/Au** stack using a variety of SAM forming molecules points towards its potential as a universal test bed to study charge transport in ensemble molecular devices. It might present a new, unspecific, facile route to non-destructive fabrication of top contacts for ensemble molecular electronics.

9 Variation of Molecular Motifs in Ensemble Molecular Devices

In this chapter, the results from the previous two chapters were brought together to yield conductance switching ensemble molecular devices within a ***TiN/../Ti/Au*** *contacting scheme. First, the contacting scheme was applied to the molecule presented in Chapter 7 (QM15^F) and the electrical characteristics of the resulting devices were compared to those of the devices presented in Chapter 7. Then, several structural motifs of the molecule were varied to explore chemical structure - device property relationships. For devices of all molecules, J-V traces of representative devices as well as multi-device averages were obtained and are presented in this chapter. Several figures of merit are then calculated and compared between devices featuring four different molecules. The aim of this chapter is not to provide an in-depth study about the detailed origins of the different observed device characteristics. It rather exemplifies the notion that this detailed analysis is always convoluted by many factors and would require many intermediate scale simulations to yield meaningful predictions. Below, a 'black box' approach is taken. Namely that of directly comparing the performance of conductance switching devices based on similar molecules. After this analysis, theoretically predicted multi-state conductance switching is probed for one of the devices based on QM85^F.*

9.1 Comparison of Contacting Schemes

To investigate whether the conductance switching observed for QM15^F monolayers sandwiched between Al and Pb/Ag is preserved within the **TiN/../Ti/Au** contacting scheme, ensemble molecular devices with QM15^F sandwiched between TiN and Ti were fabricated using the fabrication scheme outlined in Chapter 8.
Briefly: chips with pre-structured TiN bottom electrodes were immersed in a 1 mM solution of QM15^F in THF inside an air-tight container for 72 hours, then heated for 1 hour at 130 °C, rinsed in an ethanol stream and heated again for 3 minutes at 130 °C. A nickel shadow mask was then aligned to the substrate and 10 nm titanium and 40 nm gold were deposited via e-beam physical vapor phase deposition at rates of ≈ 0.1 nm/s.

After fabrication, thin lamella were cut out of one junction via FIB and cross-sectional TEM images of it were taken at TU Darmstadt, Germany. Figure 9.1.1 shows two of those images with varying magnifications. In both, all layers of the stack are clearly distinguishable. In particular, a bright, thin layer between two darker ones (here ascribed to TiN and Ti) is clearly visible in both images. No pinholes can be observed within the imaged regions. These images reveal that the SAM is structurally in tact after top contact formation. This further adds to the evidence presented in the previous chapter, that the **TiN/phosphonic acid-SAM/Ti/Au** stack presents a feasible, potentially universal route to fabricate ensemble molecular devices with solid state top contacts. Current density voltage (J-V) traces were then obtained for multiple devices on the chip, cycling the voltage between ±2 V three times, for a total of 6 sweeps. The maximum absolute sweep voltage for

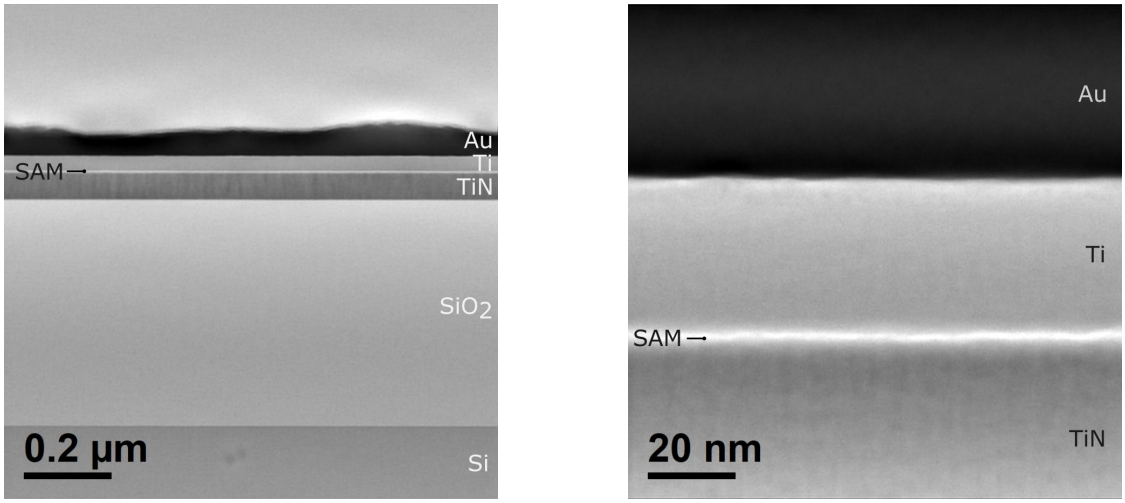

(a) **(b)**

Figure 9.1.1 Crossectional TEM images of a TiN/QM15^F/Ti/Au junction. a) Scanning TEM image indicates integrity of the SAM for > 1 µm lateral distance b) same junction imaged at a higher magnification. The atoms involved and their respective atomic numbers are carbon (6), nitrogen (7), oxygen (8), fluorine (9) titanium (22) and gold (79). This explains a decrease of brightness from the organic layer to Ti, TiN and Au.

TiN/QM15^F/Ti/Au was determined by sweeping one device in positive polarity, successively increasing the maximum voltage with each sweep until the current increased irreversibly by multiple orders of magnitude. The last voltage at which this 'break through' did not occur was then used as maximum absolute value for all successive devices. It was found to be 2 V.
For this chip, device yield was ≈ 48 %, i.e., 14 out of 29 measured devices showed pronounced hysteresis (ON/OFF conductance ratio >2). The 15 devices that did not show pronounced hysteresis exhibited current densities one order of magnitude higher than the others. This points towards the presence of additional conductance channels. In fact, 9 of these devices, did show a small hysteresis (ON/OFF conductance ratio ∈[1,3]), which might be a sign of competing conductance channels. Since their J-V traces significantly differed between each other and especially in comparison to the devices with pronounced hysteresis, they were omitted from further analysis.

The data from devices exhibiting pronounced hysteresis was then compared to the J-V traces of 6 devices with the **Al/../Pb/Ag** contacting scheme that were cycled between ±3 V (data of which was already shown in Chapter 7).
Figure 9.1.2 displays the J-V traces as well as the average ON/OFF ratio versus voltage for ensemble molecular devices with QM15^F within the two contacting schemes.

The average J-V traces exhibit a clear hysteresis for both contacting schemes. This is also reflected in the ON/OFF ratios that are ≥ 1 across the measured voltage range for both contacting schemes. Maximum ON/OFF ratio are 303 for the **Al/../Pb/Ag** contacting scheme and 18 for the **TiN/../Ti/Au** contacting scheme. Current density of the LRS at -1 V is in the 10^{-3}mA/cm^2 range for **Al/../Pb/Ag** devices and in the 10^2 mA/cm^2 for **TiN/../Ti/Au**.

In summary, moving from the **Al/../Pb/Ag** contacting scheme to **TiN/../Ti/Au** effectively decreased the maximum ON/OFF ratio by a factor of 17 and increased the current density by approximately 5 orders of

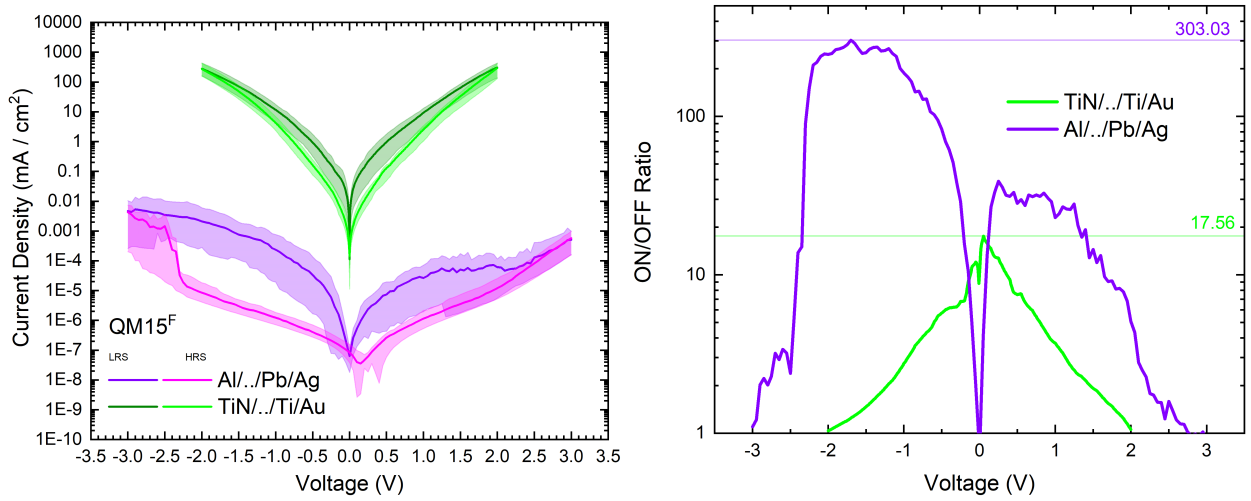

Figure 9.1.2 Device characteristics of QM15^F devices in Al/../Pb/Ag and TiN/../Ti/Au contacting scheme. a) Average J-V traces of six 25 µm x 25 µm devices (**Al/../Pb/Ag**) in crossbar array design compared to three 20 µm x 20 µm devices in 1D crossbar design. Minimum and maximum current densities at each voltage are shown as envelopes and the area between those is shaded. b) Average and minimum ON/OFF ratio versus voltage calculated from a). *Horizontal lines* mark the maximum values.

magnitude.

Since the work function of the electrodes of both devices are similar ($\Phi_{Al} \approx \Phi_{Pb} \approx 4.25$ eV [221–223], ($\Phi_{TiN} \approx 4.20$ eV [276, 277] and $\Phi_{Ti} \approx 4.33$ eV [278]), these differences are likely caused either by differences stemming from the oxide, the SAM that is formed on the oxide or by a different SAM - top contact interface. While the stack featuring an aluminum bottom contact has almost no built-in potential, the stack featuring TiN as anchoring layer has a built in potential of ≈ 0.1 eV, according to literature values cited here. However, the work function of TiN modulates over a large energy range 4.1-5.3 eV, depending on the processing conditions of the layer, the coupling to semiconductor or oxide substrate, as well as potential temperature treatments. [277, 279–282]

The surface density of molecules on the oxide may be a function of the underlying oxide anchoring layer. A higher surface density of the SAM on TiN as compared to the SAM on Al_xO_y would lead to an increased current density, since the proportion of through-space tunneling would decrease. However, an increase of through-molecule tunneling alone might not explain the five order of magnitude increase of the measured current density. Furthermore, the device model derived in Chapter 7 predicts an increased ON/OFF ratio with increasing surface density.

Thickness, charge carrier effective mass and dielectric constant of the oxide also differ between both contacting schemes. Thickness and dielectric constant of the oxide determine the magnitude of the electrical field across

the monolayer at any given voltage. As derived in Chapter 7 the electrical field across the monolayer E_{SAM} at a given voltage V is:

$$E_{SAM} = \left(\frac{\epsilon_{r,oxide}}{\epsilon_{r,oxide} d_{SAM} + \epsilon_{r,SAM} d_{oxide}} \right) \cdot V \tag{9.1.1}$$

$$= \frac{1}{d_{SAM} + \frac{d_{oxide}}{\epsilon_{r,oxide}} \cdot \epsilon_{r,SAM}} \cdot V \tag{9.1.2}$$

Hence, a decrease in oxide thickness and an increase in oxide dielectric constant result in a higher field across the SAM. This ultimately leads to a higher polarization after reorientation of molecules within the SAM under an electrical field. In other words, the average polarization per molecule of the SAM is inversely proportional to the ratio $r = \frac{d_{oxide}}{\epsilon_{r,oxide}}$ at any given voltage. Using the same parameters for the aluminum oxide and for the SAM as in Chapter 7 as well as d_{TiO_2} = 3 nm and ϵ_{r,TiO_2} [283, 284], the electric field across the SAM at 1 V is 5.49 V/nm for the device featuring aluminum oxide, and 2.94 V/nm for the device with titanium oxide. At the same voltage, the SAM within the **Al/../Pb/Ag** contacting scheme therefore exhibits approximately 1.9-fold magnitude of electrical field, than the same SAM within the **TiN/../Ti/Au** contacting scheme. Due to the linear relationship of the dipole moment in z-direction on the maximum field, at any given voltage, the difference in dielectric constant of the oxide alone can account for a factor of 1.9 in the ON/OFF conductance ratio.

To estimate the differences in barrier heights between the two contacting schemes, TiN was assumed to be covered with a TiO_2 layer and Al was assumed to be covered with a Al_2O_3 layer. This is a necessary simplification, since the exact surface composition an the resulting conduction and valence band edges have not been examined. Both surfaces are unlikely to feature perfectly stoichiometric compounds. In fact, the XPS characterization of TiN surfaces in Chapter 8 additionally pointed towards the presence of Ti(ON). Calculating the barrier heights at the bottom contact Φ_1, and at the top contact Φ_2 results in the values displayed in table 9.1. Here, bulk properties of Al_2O_3 and TiO_2 were used to perform the calculations. While at the Al/Al_2O_3 interface, the barrier for holes is 1.3 eV lower than that for electrons, at the proposed TiN/TiO_2 interface, the barrier for holes is 3.2 eV higher than that for electrons. At the top contact side both types of devices have very similar barriers, with electron barriers being approximately twice as high as hole barriers.
In total, for Al/Al_2O_3, hole barriers are approximately half as high as electron barriers. This leads to hole tunneling being the dominant charge transport in these devices. On the other hand, for TiN/TiO_2, the barrier at the bottom side is lower for electrons than for holes, while at the top contact the opposite is true. Charge transport through these devices is therefore likely a mixture of transport processes. One potential consequence from this is closely connected to the fact that in most materials, hole effective masses exceed electron effective masses. Since the ON/OFF conductance ratio was shown to increase with increasing effective carrier mass, a decrease in average effective carrier mass might lead to a lower ON/OFF ratio. To study this further, however, a device model featuring multiple parallel conduction channels would be required.

While the differences outlined above may lead to the described changes, a detailed study how their interplay influences conductance switching device performance is left for further, theoretical study. This is mainly due to the fact, that TiN layers can exhibit a variety of non-stoichiometric crystals and phase mixtures, characteristic to the individual processing conditions of the layer. The myriad of potential layer consitution results in a myriad of potential electrical and optical characteristics. Without much more in-depth study of the properties of the

Table 9.1 Barrier heights at the bottom contact side for both contacting schemes. Values for Al_2O_3 are calculated from the values presented in Figure 7.3.6. Values for TiO_2 are calculated based on the values provided in [285].

Oxide	Conductance Band Edge CB / eV	Valence Band Edge VB / eV	$\phi_{1,e}$ / eV	$\phi_{1,h}$ / eV	$\phi_{2,e}$ / eV	$\phi_{2,h}$ / eV
TiO_2	-4.2	-7.4	0	3.2	3.07	1.53
Al_2O_3	-2	-5.2	2.25	0.95	2.99	1.48

TiN layer and the surface covering TiON or TiO_2 layer, the source of identifying the differences between TiN and Al as bottom contact on device characteristics, would be highly speculative.
The following observations are, however relevant on a practical level: The device functionality, i.e., conductance switching, is preserved across the two contacting schemes. The ON/OFF conductance ratio is reduced by 94% for TiN/../Ti/Au devices as compared to **Al/../Pb/Ag** devices. Current densities increased by a factor of $\approx 10^5$ for **TiN/../Ti/Au** devices as compared to **Al/../Pb/Ag** devices.

In total, the objectives of preserving the hysteretic effect, increasing current densities and improved stability were achieved using the novel contacting scheme.

9.2 Variation of the Structural Motifs

One promise of molecular electronics is the supposed ease of device optimization via organic chemistry. Ideally, a direct relationship between molecule function and device characteristics can be derived from first principles and the molecule can be designed and synthesized to yield desired device characteristics. However, since as previously presented calculations have shown, characteristics of the monolayer are likely to influence device characteristics via *inter*molecular interactions, a direct, *ab initio* design of molecules would therefore be connected with tremendous computational effort. Another challenge is that the ON/OFF conductance ratio is also electrical field-dependent and the magnitude of the electrical field in turn depends on the thickness of the monolayer. Comparing molecules of different length at the same applied voltage hence compares two different 'states' of monolayers.

One approach to tackle this challenge is to vary functional units of the SAM-forming molecule and observe the changes in electrical characteristics, effectively skipping all intermediate scale considerations and calculations. Using this approach, changes in SAM characteristics that influence device characteristics become hidden variables, but a direct molecular structure-device performance relationship can still be determined and can be used to drive optimization of the molecular structure towards a desired electrical function.

Three molecule characteristics that might influence transfer characteristics as well as switching dynamics have been identified to provide a starting point into structure-property relationship investigations, namely:

1. **Length of the aliphatic linker and head group**. If the transport process across the monolayer is dominated by tunneling processes, the conductance of the device is a function of total molecular length. By decreasing this length the conductance is expected to increase. For two parallel plates, a reduced distance d between them also leads to a higher electrical field $E = V/d$ at a given voltage V. Based on the MD simulations presented in Chapter 7 and presented in [154] this is expected to influence the switching behavior of the SAM.

2. **Dipole moment change between the two conformers**. Both, the device model and the MD simulations presented in Chapter 7 point towards the change of the average dipole moment of the whole SAM being a determining factor for the ratio between low resistive and high resistive state of the junctions. A larger lateral dipole moment change is expected to result in a larger ON/OFF ratio. However, molecular dynamics calculations have also revealed for $QM15^F$ on aluminum oxide, that this average change crucially depends on the number of molecules that switch their confirmation within the SAM. This number in turn is influenced by molecule-molecule interactions. These interactions are also governed by magnitude and direction of dipole moments. Without detailed MD analysis it remains unclear whether an increased dipole moment change directly results in a higher ON/OFF conductance ratio.

3. **Type of linker between anchoring group and dipole unit**. Changing the linker between anchoring group to the dipole group might increase the intramolecular barrier between conductance states and hence influence the ON/OFF ratio as well as the overall switching dynamics of the SAM, e.g., switching speed and state retention.

These three basic considerations lead to the variation of several functional units of the $QM15^F$ molecule in order to potentially increase overall conductance and ON/OFF ratio of the resulting ensemble molecular devices, as well as the retention times of their conductance states. In $QM69^F$, the conformational flexible alkyl chain linker was replaced by a 3,5-Dimethylphenylen unit. For one, the change from an aliphatic to an aromatic

linker is expected to increase device conduction. Furthermost, the two methyl groups are thought to increase the intramolecular barrier between the two conformers and hence increase stability of the two states.
In QM72^F, the dipole unit of QM15^F was replaced by a difluorodibenzofurane unit. The resulting molecule hence exhibits smaller lateral dipole change ($\mu_{\text{z,anti}}(\text{QM72}^F) - \mu_{\text{z,syn}}(\text{QM72}^F) = 0.21\text{D}$) than QM15^F ($\mu_{\text{z,anti}}(\text{QM15}^F) - \mu_{\text{z,syn}}(\text{QM15}^F) = 0.73D$). The resulting ensemble molecular devices are hence expected to exhibit a lower ON/OFF conductance ratio as compared to devices with QM15^F.
For QM85^F, the pentyl head group was replaced by a hydrogen atom, and a methyl group was added to the 2,3- difluorophenyl cyclohexane unit. The shortening of the molecule is intended to increase the conductance, and potentially also the ON/OFF ratio, of the resulting ensemble molecular devices whereas the addition of the methyl group is intended to increase *inter*molecular forces, potentially increasing the retention times of the conductance states.

To compare device performance the following data was collected for devices featuring each type of molecule:

- 3 cycles of J-V traces for multiple devices. From this, average traces for HRS and LRS as well as their envelopes can be calculated.
- The average ON/OFF conductance ratio versus voltage. Here, the ratio of the average current densities of 3 devices and 3 cycles were used to calculate the ON/OFF ratio, since for invariant area A and voltage V, conductance ratio and current density ratio are equal. In particular, with the conductance G, the ON/OFF conductance ratio is

$$\frac{G_{LRS}}{G_{HRS}} = \frac{\frac{I_{LRS}}{V}}{\frac{I_{HRS}}{V}} \tag{9.2.1}$$

$$\text{with } I = J_i \cdot A: \tag{9.2.2}$$

$$= \frac{J_{LRS} \cdot A}{J_{HRS} \cdot A} \tag{9.2.3}$$

$$= \frac{J_{LRS}}{J_{HRS}} \tag{9.2.4}$$

  This ratio is a good indicator for conductance switching performance.

- 'LRS conductance change ratio' as a figure of merit for the retention of conductance states over time. For QM15^F and QM69^F, the zero bias resistance of the LRS was determined for one device each over >20 min. For QM72^F and QM85^F, both the LRS and the HRS were subsequently probed at a fixed voltage over the course of >30 min. To arrive at a comparable figure of merit, the 'LRS conductance change ratio' is defined as the average conductance change $G(20\text{ min})/G(0\text{ min})$ over 20 min. Following the rationale outlined above, this is equivalent to $J(20\text{ min})/J(0\text{ min})$ and via the identiy $G = 1/R$ also equivalent to $R(0\text{ min})/R(20\text{ min})$. This maps the measured resistances and current densities to a value that is comparable between these measurements. It is still noteworthy, that the resistances were calculated at zero bias and the current densities were obtained at V = 0.6 V.
- The 'envelope ratio' as a figure of merit for the repeatability of the conductance switching process. From here on out it is defined as $min(J)/max(J)$ at a fixed evaluation voltage and calculated sepeartely for LRS and HRS. It is calculated from 20 sweeps each. Dividing the minimum by the maximum value

ensures that all values are within [0,1] and that a higher value equates to a more desirable outcome, i.e., less maximum variation of one state over 20 cycles.

In the following sections, first an overview of the measured J-V traces and the calculated figures of merit is presented per molecule. J-V traces of each molecule are also compared to those of QM15^F, which was chosen as a mutual reference for all of them. Then, an overall comparison of the figures of merit listed above for all molecules is performed and some general chemical design - device property relationships are given.

9.2.1 3,5-Dimethylphenylene Linker Unit - QM69^F and QM102

The first variation of molecular motifs, intended to improve conductance switching ensemble molecular devices was the replacement of the aliphatic linker between anchoring group and dipolar unit by a shorter, aromatic one, namely 3,5-dimethylphenylene. This aromatic linker was introduced to increase current density and retention of conductance states. To compare the effect of swapping the linker unit on ensemble molecular devices, devices with QM69^F and its non-fluorinated reference compound QM102 were fabricated, using the same fabrication scheme as the devices presented in the previous section. The complete chemical structure of QM69^F and QM102 can be found in Chapter 5.

DC current-voltage characteristics of ensemble molecular devices were measured up to ± 2 V for at least 3 devices per molecule type. Figure 9.2.1 summarizes the current density-voltage (J-V) traces extracted from these measurements, averaged over 3 sweep cycles and 3 devices each, for each molecule and obtained for 20 µm x 20 µm area junctions. Data is compared to J-V traces of the previously characterized devices featuring QM15^F. From the average traces presented in this figure, the average ON/OFF conductance ratio was calculated at all voltages. The result is displayed in Figure 9.2.2.

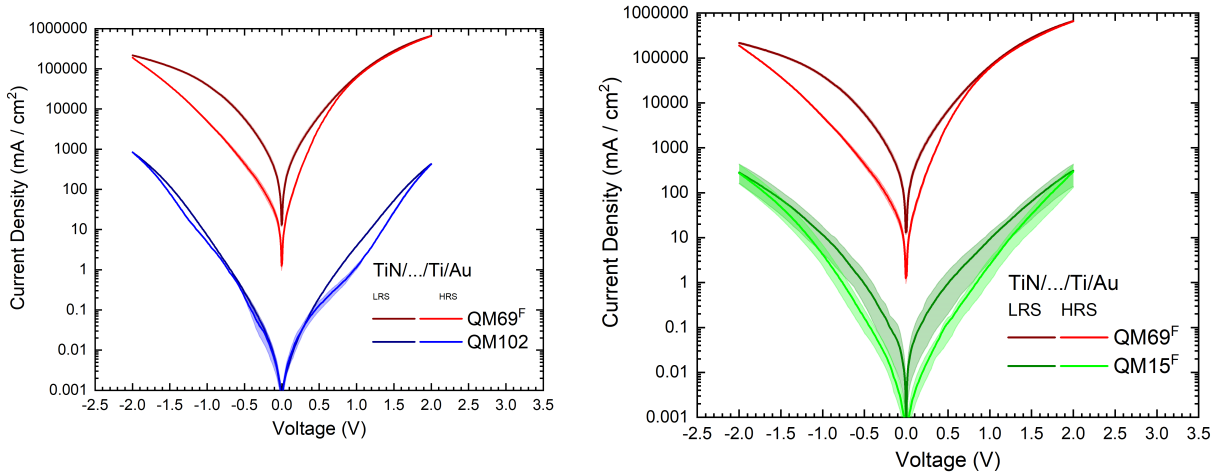

Figure 9.2.1 Electrical device characteristics of QM69^F devices in TiN/../Ti/Au contacting scheme compared to a) the non-fluorinated analogon QM102, and b) previously studied QM15^F. Averages for all molecules stem from 3 cycles and 3 devices. Minimum and maximum current densities at each voltage are shown as envelopes and the area between those is shaded. Shaded areas for QM69^F as well as QM102 are hardly visible since average traces varied only little over the three studied devices.

When comparing the results from devices featuring QM69^F to those featuring QM15^F, several differences can be observed:

Devices featuring QM69^F exhibit three orders of magnitude higher conductances than those featuring QM15^F, For example, at V= -1 V evaluation voltage, the ratio between the HRS current traces is $J_{HRS}(\text{QM69}^F)/J_{HRS}(\text{QM15}^F) \approx 1243$. This difference is even more pronounced for the LRS current traces, where $J_{LRS}(\text{QM69}^F)/J_{LRS}(\text{QM15}^F) \approx 3515$. An increase of current density was expected, since the molecule is significantly shorter and the linker between anchoring group and dipolar group is aromatic instead of aliphatic. However, J-V traces of reference compound QM102 also exhibited current densities three orders of magnitude lower than those of devices featuring QM69^F, being in range with those measured for

QM15^F. For example, at -1 V evaluation voltage, the ratio between the HRS traces of both molecules is J_{HRS}(QM69)/J_{HRS}(QM102) ≈ 995, J_{HRS}(QM69)/J_{HRS}(QM102) ≈ 5688.

As can be seen in Figure 9.2.2, QM69^F devices show a pronounced hysteresis for both voltage polarities, with ON/OFF ratios of negative voltages exceeding those at positive voltages, reaching a maximum of 13.33 at V = -0.5 V. In contrast, devices featuring the non-fluorinated reference compound QM102 show a non-zero, maximum ON/OFF conductance ratio of 3.35. This means that, most likely, multiple effects are responsible for the observed hysteresis. The larger aromatic interlayer may for instance present a conductive 'island' between the two tunneling barriers (the oxide and the aliphatic chain) that might act as a trap for charges, that is filled and emptied at specific voltages. The extend to which this can explain the observed hysteretic effect, however would be pure speculation and the details would need to be studied further. However, the hysteric effect is much more pronounced for the fluorinated molecule, than for the non-fluorinated one. Hence, the majority of the conductance switching that was observed, can be attributed to the proposed conductance switching effect.

The J-V traces also show exceptionally low device to device variance, which can be observed in a barely visible envelope of the J-V trace device average. The ratio of maximum divided by minimum current density of all three devices at any given voltage is lower than 1.9 for the low resistive state and lower than 2.0 for the high resistive state.

QM15^F devices in contrast show a higher device-to-device variance, resulting in clearly visible envelopes. The maximum ratio of maximum divided by minimum current density of all three devices at any given voltage is ≈ 378 for the low resistive state and ≈ 190 for the high resistive state.
Ultimately, this means that device to device variation of QM69^F devices was more than 100 times less pronounced than that of QM15^F.

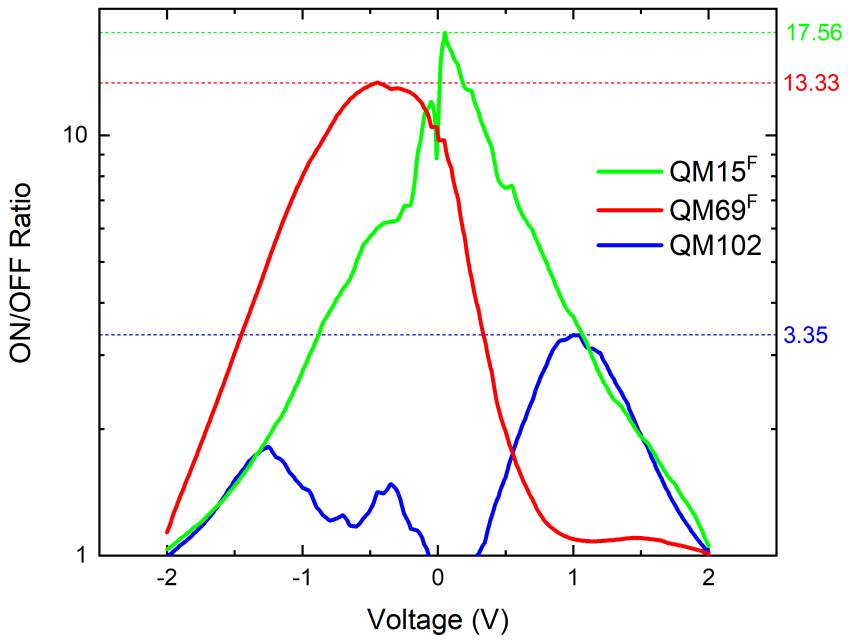

Figure 9.2.2 ON/OFF conductance ratio versus voltage for QM15^F, QM69^F and QM102. Ratios were calculated from the average data shown in Figure 9.2.1 and hence represent the averages of from 3 cycles and 3 devices per molecule. Dashed horizontal lines indicate the maximum ON/OFF ratio of the three types of junctions. Both fluorinated compounds exhibit a higher ratio than the non-fluorinated one for V ∈ [-1.2,1.1]. Maximum ON/OFF ratio is one order of magnitude higher for the fluorinated compounds than for the non-fluorinated one.

20 Cycle Measurement

A 5 µm x 5 µm device on the same chip with QM69^F - as the above presented devices - was cycled between ± 2.5 V for a total of 20 cycles. The J-V traces of this measurement as well as current density versus sweep number at the voltage of the highest ON/OFF conductance ratio (V = -0.45 V) are displayed in Figure 9.2.3. As can be seen in the J-V traces, the hysteresis remained clearly visible and sweep-to-sweep variation was low for the HRS and very low for the LRS. This becomes even more obvious in the current density versus sweep number representation, where the envelope ratio min(J)/max(J) was calculated to be 0.66 for the HRS and 0.76 for the LRS. Both conductance states remained clearly separable over the course of 20 cycles, i.e., their envelopes do not cross. This means that the two conductance states can be clearly distinguished without knowing the history of the device and suggests stable, repeatable conductance switching.

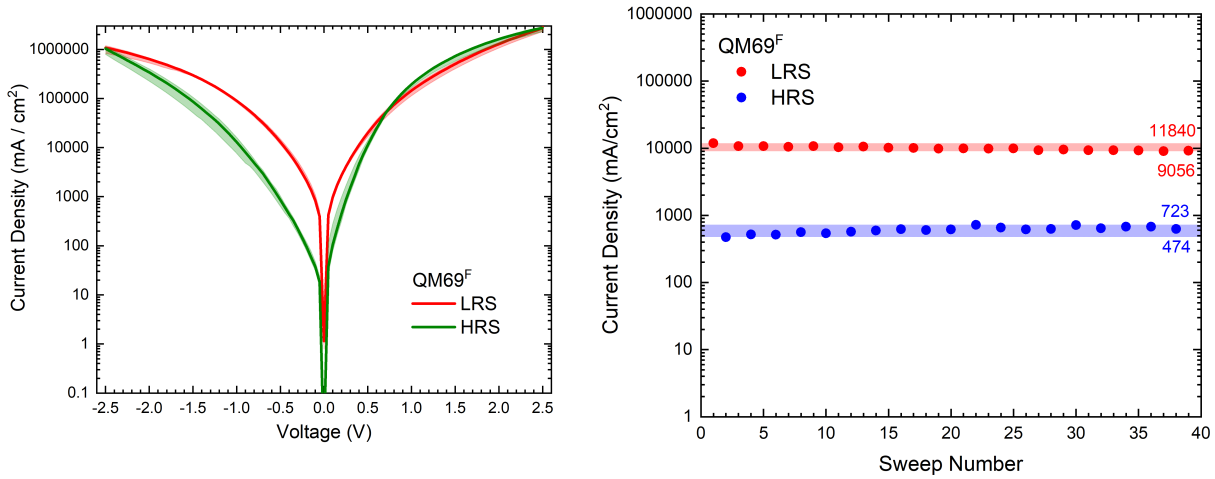

(a) (b)

Figure 9.2.3 Electrical characteristics of a 20 cycle measurement of a QM69^F device. Device area: 5 µm x 5 µm. a) J-V traces. Red: LRS, Green: HRS. Minimum and maximum current densities at each voltage are shown as envelopes and the area between those is shaded. b) Current density versus sweep number at the voltage at which the highest average ON/OFF conductance ratio is observed (V=-0.45 V). Annotated values correspond to the maximum and minimum values of the LRS and HRS, i.e., the envelopes at the given evaluation voltage. The area between those is shaded.

LRS Retention of QM15^F and QM69^F

In order to probe the retention of devices featuring QM15^F and QM69^F, the following measurements were performed on one exemplary device for each molecule: First, the device was set to its LRS state by ramping up the voltage to +2 V and back down to 0 V with 100 mV/s sweep speed. After ≈ 30 s, the *zero bias resistance* was then determined by sweeping the voltage between ±0.1 V three times in a row and fitting the resulting data to a linear function. The derivative dV/dI (where V is the voltage and I is the measured current) was then taken as the zero bias resistance Ω_0. Subsequently, Ω_0 was determined at random intervals between 2 and 8 minutes over the course of 21 minutes. The evolution of Ω_0 for both studied devices is shown in Figure 9.2.4. Zero bias resistances of both, the QM15^F and the QM69^F device increased with time, indicating a degradation of the low resistive state. Over the course of 20 min, resistance of the QM15^F device increased by a factor of ≈ 67 whereas the resistance of the QM69^F device increased by a factor of ≈ 5. In other words, the conductance of the QM15^F decreased to 1.5% of its initial value over 20 min, while the conductance of the QM15^F device decreased to 20.1% of its initial value. This indicates that the two methyl groups, added to the linker might in fact hinder a thermally induced rotation, significantly improving the retention of QM69^F based devices as compared to QM15^F based ones.

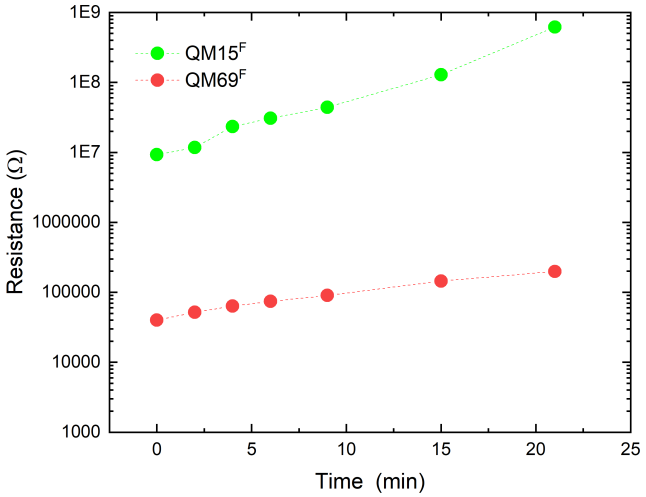

Figure 9.2.4 Zero bias resistance for QM15^F and QM69^F over time. Devices were put in LRS state via cycling the voltage from 0 V to 2 V and back to 0 V once. Resistance was then determined by sweeping between ±0.1 V three times in a row after 5 time intervals and then calculating a linear fit to the measured data points. The 0 minute data points come from a low bias cycle right after the first cycle 0-2 V.

9.2.2 4,6-Difluorodibenzofurane Dipolar Unit - QM72^F

The second structural variation of the SAM-forming molecule was the replacement of the dipolar unit by a 4,6 difluordibenzofuran dipolar unit. The whole structure of the resulting molecule QM72^F can be found in Chapter 5. No non-fluorinated compound was available.

Ensemble molecular devices featuring the molecule QM72^F were fabricated using the same fabrication scheme as utilized for all other devices presented in this chapter. DC current-voltage characteristics of ensemble molecular devices were measured up to ± 3.0 V. Figure 9.2.5 summarizes the J-V traces extracted from these measurements, averaged over 3 sweep cycles for one representative device of 15 µm x 15 µm area and compares them to the J-V traces of the previously measured QM15^F devices.

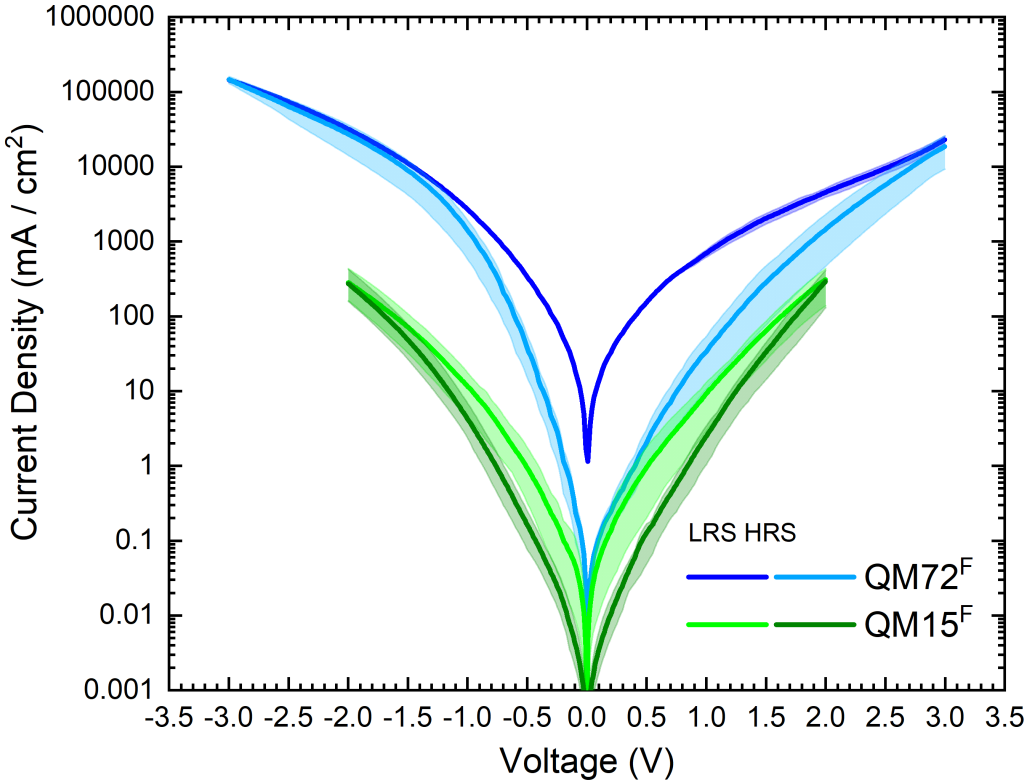

Figure 9.2.5 Electrical device characteristics of QM72^F devices in TiN/../Ti/Au contacting scheme compared to the previously studied QM15^F. Device area: 15 µm x 15 µm. Minimum and maximum current densities at each voltage are shown as envelopes and the area between those is shaded.

20 Cycle Measurement

Another 15 µm x 15 µm device on the same chip with QM72^F as the above presented device was cycled between ± 3.0 V for a total of 20 cycles. The J-V traces of this measurement as well as the current density versus sweep number at the voltage of the highest average ON/OFF conductance ratio are displayed in Figure 9.2.6.

As can be seen from the J-V traces, the hysteresis remained clearly visible on average, but the sweep-to-sweep variation was comparatively high. In fact, for all voltages except $V \in [-0.5, 0)$ the envelopes of HRS and LRS overlap. This means that during the observed 20 sweeps, a clear distinction of HRS and LRS would not be possible for all voltages outside this range, without knowing the device's history. However, within -0.5 V ≤ V < 0 V, LRS and HRS remain clearly distinct states with good repeatability of the switching process to the LRS and a large variance in the switching process to the HRS. This is also reflected in the current density versus sweep number representation, where the envelope ratio min(J)/max(J) was calculated to be 0.04 for the HRS and 0.29 for the LRS.

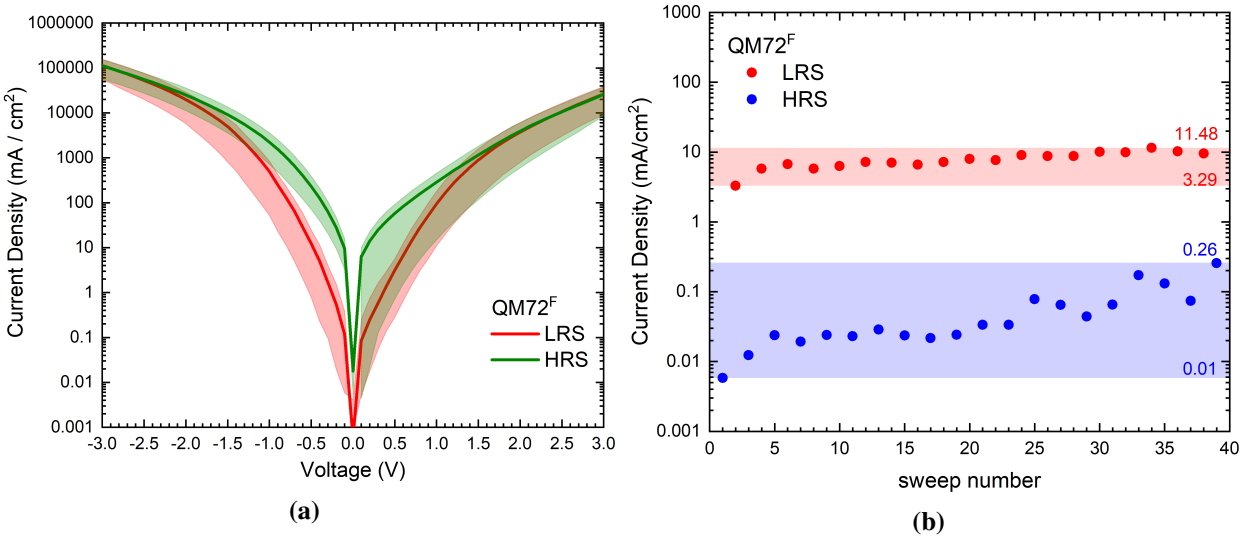

Figure 9.2.6 Twenty cycle measurement of a QM72^F device. Device area: 20 µm x 20 µm. a) J-V traces b) Current density versus cycle number at the voltage of the maximum average ON/OFF ratio V = 0.1 V. Annotated values correspond to the maximum and minimum values of the LRS and HRS, i.e., the envelopes at the given evaluation voltage. The area between those is shaded. Note that the annotated minimum value of the HRS is rounded and hence higher than the actual value that can be read out at the logarithmically scaled ordinate.

9.2.3 2,3-Difluoro-6-methyl-phenyl Cyclohexane Dipolar Unit - QM85^F

The third variation of chemical consituents of the SAM forming molecule was the replacement of the pentyl chain by a simple hydrogen atom as ambient facing moiety and the addition of a methyl group to the difluorphenyl cyclohexane dipolar unit. The full chemical formula of the resulting QM85^F molecule is displayed in Chapter 5

Ensemble molecular devices featuring the molecule QM85^F were fabricated using the same fabrication scheme as utilized for all other devices presented in this chapter. DC current-voltage characteristics of ensemble molecular devices were measured up to ± 2.8 V. Figure 9.2.7 summarizes the J-V traces extracted from these measurements, averaged over 3 sweep cycles for one representative device of 15 µm x 15 µm area and compares them to the J-V traces of the previously measured QM15^F devices.

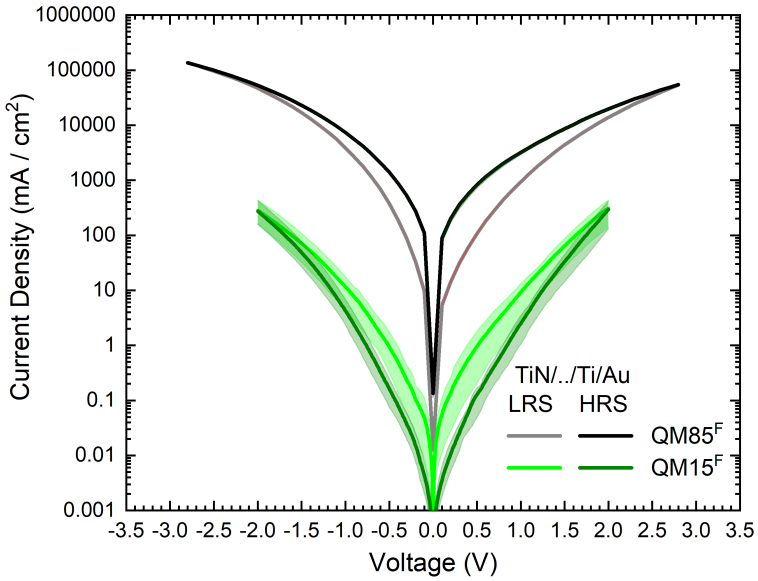

Figure 9.2.7 Electrical device characteristics of QM85^F devices in TiN/../Ti/Au contacting scheme. Device area: 15 µm x 15 µm. Black: LRS, Grey: HRS. Minimum and maximum current densities at each voltage are shown as envelopes and the area between those is shaded. Due to good sweep-to-sweep reproducibility, envelopes are hardly visibile.

20 Cycle Measurement

A 20 µm x 20 µm device on the same chip with QM85^F as the above presented device was cycled between ± 3.0 V for a total of 20 cycles. The J-V traces of this measurement as well as the current density versus sweep number at the voltage of the highest ON/OFF conductance ratio are displayed in Figure 9.2.8.

As can be deduced from the J-V traces, the hysteresis remained clearly visible and sweep-to-sweep variation was low for the HRS and very low for the LRS. This becomes even more obvious in the current density versus sweep number representation, where the envelope ratio min(J)/max(J) was calculated to be 0.58 for both, LRS and HRS.

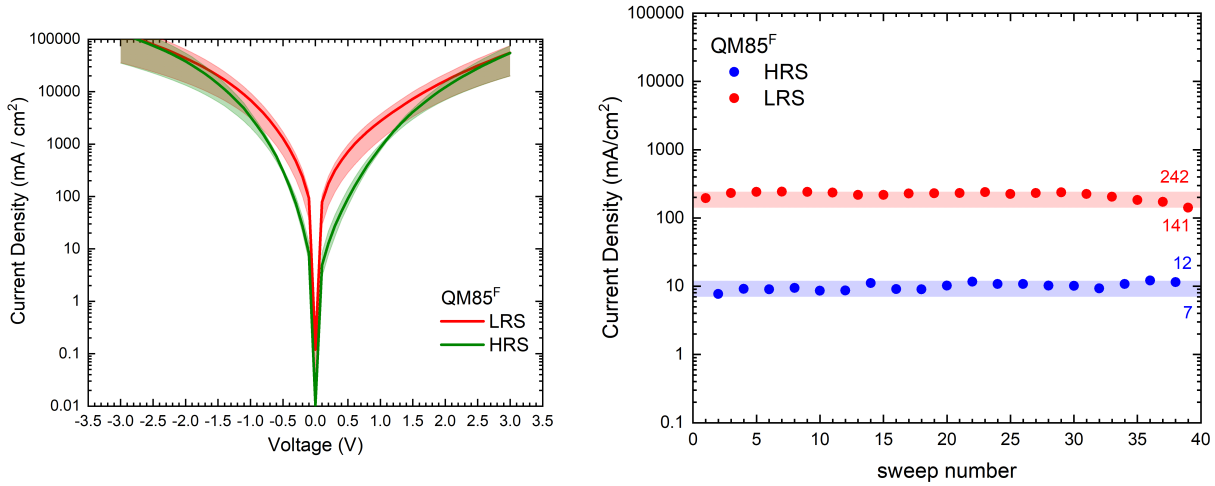

Figure 9.2.8 Twenty cycle measurement of a QM85^F device. Device area 20 µm x 20 µm. a) J-V traces b) Current density at 0.2 V versus sweep number. Annotated values correspond to the maximum and minimum values of the LRS and HRS, i.e., the envelopes at the given evaluation voltage. The area between those is shaded.

LRS and HRS Retention of QM72^F and QM85^F

The retention of both conductive states was determined for QM72^F and QM85^F using the following procedure for each: First, one device of 15 µm x 15 µm area, showing representative hysteresis was chosen. Then, the device was set to its LRS by sweeping the voltage to 3 V and back to 0 V once. Over the course of >30 min, the current density at V = 0.6 V was then read out in random time intervals between 3 and 5 minutes by applying a 500 ms pulse of constant voltage and averaging the current value over the duration of the pulse. After 32 minutes the devices were set to their LRS by sweeping the voltage to -3 V and back to 0 V once. Over the course of the next 32 min, the current density at V = 0.6 V was then read out in random time intervals between 3 and 5 minutes by applying a 500 ms pulse of constant voltage and measuring the current value.
Figure 9.2.9 depicts the outcome of these measurements, showing the evolution of the measured current over time.

For QM72^F the measured current in LRS decreased from $8.53 \cdot 10^{-8}$A at first measurement to $7.98 \cdot 10^{-9}$ at 20 min. This corresponds to an increase of the differential resistance (V/I at V = 0.6 V) from $7.03 \cdot 10^6$ Ω to $7.52 \cdot 10^7$ Ω (approximately an 11-fold increase). For the LRS, the differential resistance showed an approximately 3-fold increase. Most notably, after 21 min the current measured in the LRS state decreased to a value below that initially measured for the HRS. This means that at ≈ 21 min, HRS and LRS become indistinguishable without knowledge of the device's history. For QM85^F based devices in contrast, the LRS differential resistance increased by 54% over 31 minutes and the HRS resistance decreased by 38%. While this means that LRS and HRS are slowly approaching a value between the initial values of the two states, the very slow decay or increase means, that over the whole measurement period of 31 minutes, LRS and HRS stayed clearly distinguishable. Most of the conductance change occurred during the first 10 minutes. Over the last 15 minutes of measurement, the current values changed only by ≈ 2% (HRS) and ≈ 10%(LRS). This points towards much longer times until the two states may become indistinguishable, if at all.
Overall, the retention measurements presented in this section, showed that QM85^F based devices exhibited much lower degradation of the device's conductance states than QM72^F based ones.

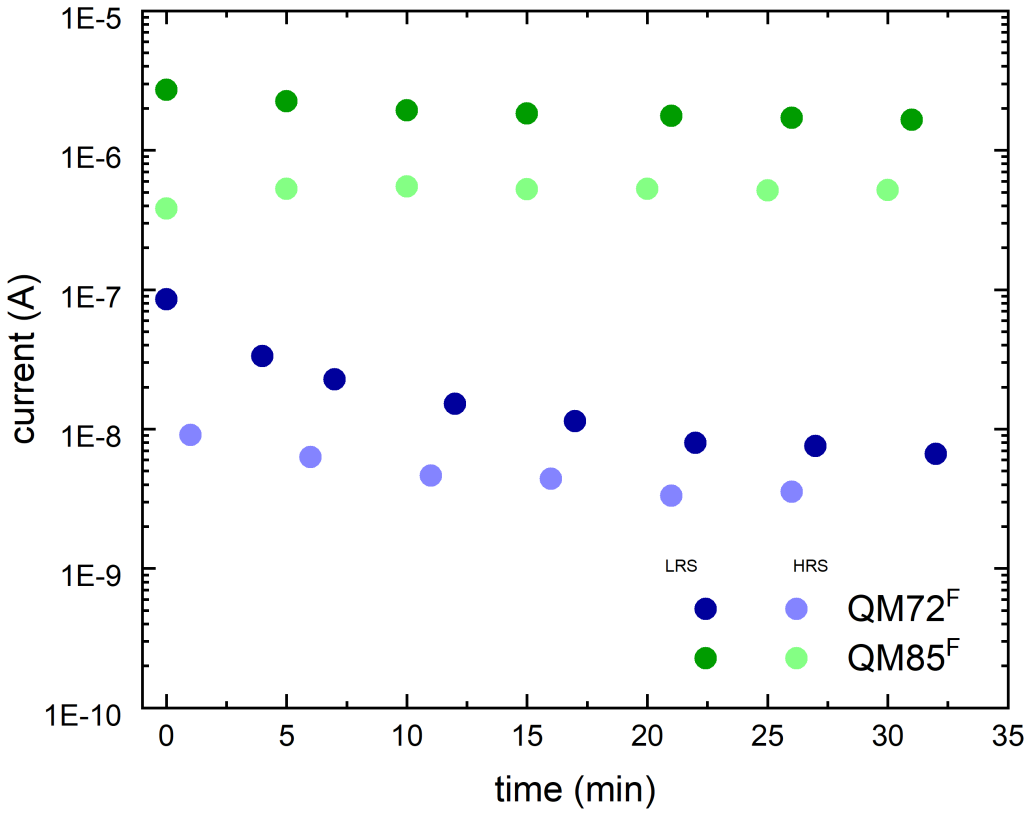

Figure 9.2.9 Temporal evolution of the LRS and HRS at fixed evaluation voltage for QM72^F and QM85^F. Devices were set to LRS first and the current at 0.6 V was manually read out every ≈5 min for ≈30 min. Devices were then set to HRS and currents were recorded every ≈5 min for ≈30 min again.

9.3 Comparison of Device Performance

The ON/OFF conductance ratios versus voltage of devices featuring the four molecules studied in this chapter are depicted in Figure 9.3.1. The displayed values are calculated by dividing the average LRS current density by the average HRS current density at each voltage and hence represent an average, voltage dependent device performance. Note that QM15^F and QM69^F devices were swept up to ±2 V, whereas QM85^F and QM72^F were swept up to ±3 V. Table 9.2 summarizes a variety of figures of merits for decices based on the four molecules. These are: the maximum of the ON/OFF conductance ratio (taken from Figure 9.3.1), the rectification r = J(-1 V)/J(1 V) for HRS and LRS, the *retention conductance ratio* g = G(20min)/G(0min) and the *envelope ratio* min(J)/max(J), calculated for HRS and LRS separately from a measurement with 20 voltage cycles.

Comparing the ON/OFF ratios for all molecules with a dipolar unit studied in this work, the following was observed.
QM72^F exhibited the maximum average overall ON/OFF ratio of 134.77. Devices with all other molecules exhibited similar maximum ON/OFF ratios within one order of magnitude: 17.56 for QM15^F, 16.02 for QM85^F and 13.33 for QM69^F. The latter three molecules were all designed with 2,3-difluorophenyl cyclohexane as dipolar unit, whereas QM72^F utilized a 4,6-difluorodibenzofurane dipolar unit. This indicates that the choice of dipolar unit governs the ON/OFF ratio of the resulting devices.
However, it is not immediately evident where this difference comes from. Among the herein studied molecules, QM72^F exhibits the lowest dipole moment change in direction of the electrical field, per molecule. Since the tilt angle changes the most between the two conformers, so does the calculated thickness (compare also Table 5.1). In fact, while all molecules with 2,3-difluorophenyl cyclohexane show a calculated thickness change $\leq$ 0.16 nm, QM72^F was calculated to change its thickness by 0.57 nm between the two conformers. This equates to $\approx$ 18% change in thickness of the monolayer and represents a significant change in the thickness of the tunneling barrier. While for single molecules this larger change in tunneling distance would be directly reflected in a larger change of transfer currents, it is unclear, what this may mean for ensemble molecular devices. If within the molecular ensemble not all molecules switch synchronously between *syn* and *anti* state, as MD simulations of QM15^F have shown, and the electrodes are considered fixed, within a monolayer of QM72^F multiple conductance channels would open up: One through the molecules in the thicker *syn* state, potentially directly connected to oxide and top contact, and one through the molecules in the thinner *anti* state and the potentially formed gap between the molecule and the top contact. While a decreased tunneling length in contact exponentially increases the tunneling current, opening up a gap would likely decrease the tunneling current, simply because the vacuum automatically presents a higher tunneling barrier than the molecule's HOMO and LUMO. How pronounced this effect would be reflected in the J-V traces would require much more detailed analysis - including a device model that considers a distribution of tunneling channels of varying width, as well as additional molecular dynamics simulations to determine the effect of electrical field induced molecular re-orientation on this distribution. Another potential origin of the higher than anticipated ON/OFF conductance ratio would be if molecules within the SAM were restricted by *inter*molecular forces, such that the surface angle of the molecule could shift less, while rotation of the dipolar unit would still occur. Then, the change in lateral dipole moment of the SAM could be bigger and with it $\Delta\Delta\Phi$ and ultimately the ON/OFF conductance ratio. This again, would require much more detailed MD simulations and underlines the fact, that direct molecular structure - device property relationships are difficult to deduce.

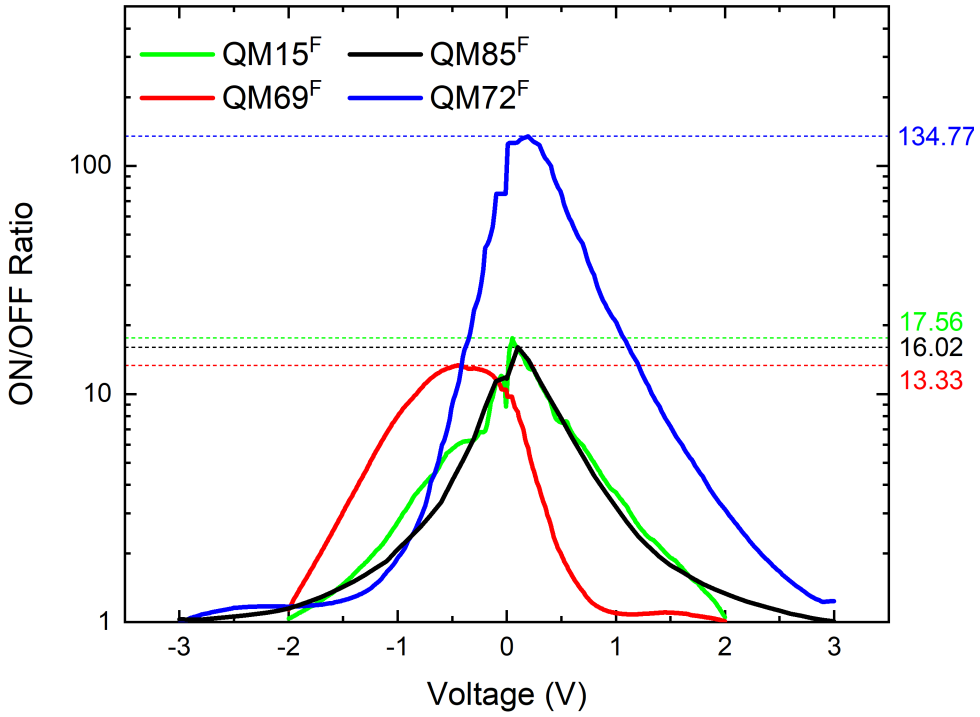

Figure 9.3.1 Comparison of ON/OFF ratios of all molecules characterized in this work. Dashed horizontal lines mark the maximum ON/OFF ratio. Color coded numbers on the right indicate the respective values.

Without much speculation, from the data presented above, it is still safe to say, that the choice of the chemical building block that constitutes the dipolar unit has the largest influence the magnitude of the hysteresis that can be observed. All other structural variations did not affect the maximum ratio in a large way.

Table 9.2 Comparison of devices based on a variety of liquid crystal inspired molecules. Definitions of the figures of merit are given in the main text. For all figures of merit, a higher number corresponds to a more desirable device function. Rectification for QM69 was calculated as 1/r, i.e., in contrast to all other molecules, magnitude of current densities at positive voltages exceeded those at negative voltages.

Compound	maximum ON/OFF ratio	rectification		retention conductance ratio	envelope ratio	
		LRS	HRS	LRS /%	LRS	HRS
QM15	17.56	1.26	0.79	1.50	-	-
QM69	13.33	1.63	11.94	20.10	0.76	0.66
QM72	134.77	6.92	8.09	9.35	0.29	0.04
QM85	16.02	2.69	5.16	65.06	0.58	0.58

As listed in Table 5.2, QM69^F comes with the largest $\Delta\Delta\Phi$ of all three molecules. At the same time, for QM69^F both HOMO and LUMO show the biggest shift between the two conformers of the molecule. Namely, the HOMO is expected to shift by 0.1 eV, while the LUMO is expected to shift by 0.19 eV. In a single molecular model, that would result in the highest ON/OFF conductance ratio. However, as the 3,5-dimethylphenylene unit was added to increase the *intra*molecular rotation barrier, the number of molecules that switch within the monolayer might be significantly decreased compared to molecules lacking this additional barrier. This in turn would decrease the average lateral dipole change and could hence counteract the intended increase in ON/OFF

ratio. In fact, QM69^F also showed the lowest decay of the LRS over time among all molecules presented here, which might also be explained by the increased rotational barrier. These results highlight the previous finding, that direct chemical design of liquid crystal inspired molecules for conductance switching ensemble molecular devices is complicated by the fact that device performance is closely connected to **inter**molecular forces within the SAM. Further MD simulations might shine some light on whether an increased rotational barrier can lead to a lower amount of switching molecules and ultimately a lower than expected on/off ratio.

The range of potential explanations for the observed transfer characteristics outlined above exemplify that relationships between the electronic structure of single molecules and hysteresis of conductance are difficult to deduce, mostly due to the fact that comparisons of charge transport in ensemble molecular devices is confounded by the interrelated differences in *inter*molecular interaction and SAM formation. However, the following trends could be observed:

- All devices with a difluorophenyl cyclohexane derivative showed a maximum ON/OFF conductance ratio of $\approx 13 - 18$, while devices with the only 4,6-difluorodibenzofurane derivative exhibited a maximum ratio of ≈ 135, i.e., ten times larger.
- Devices with molecules that were designed to feature an increased *intra*molecular rotational barrier (QM69^F) or an increased *inter*molecular barrier (QM85^F) were found to show a slower decay of the LRS as well as a smaller range of current density values per conductance state throughout 20 voltage cycles than devices that did not posses such chemical building blocks. Increasing the *inter*molecular rotational barrier by molecular design has shown to yield the lowest decay of the LRS among all tested molecules, with 65% of the initial conductance preserved after 20 min. The variation of the measured current density in each state was lowest for the molecule featuring the *intra*molecular rotational barrier. LRS values showed a maximum change of 24% while HRS values showed one of 34%.
- Devices with the molecule that exhibited the largest ON/OFF ratio at the same time showed the steepest decline in conductance over time (91% decline over 20 min) and the largest maximum sweep to sweep variation (71% and 95% variation for LRS and HRS respectively).
- Devices with an aromatic linker between headgroup and dipolar unit exhibited the largest rectification (J(1V)/J(-1V)≈12) for the HRS.

9.4 Multi-State Conductance Switching

The molecular dynamics simulations presented in Chapter 7 indicated that the average dipole moment of the QM15^F SAM in z-direction exhibits near-linear dependency on the magnitude of the previously applied electric field. This means that in ensemble molecular devices based on QM15^F, more than two conductance states should be accessible via the variation of the maximum applied voltage. It seems reasonable to assume that this would be true for molecules of very similar structure, too. To test this, a device featuring a **TiN/QM85^F/Ti/Au** stack was electrically characterized.

Current density voltage characteristics were obtained by sweeping the voltage between $\pm V_{max}$ three times, starting with a sweep in positive direction. Traces were averaged for LRS and HRS separately. This measurement was repeated for 23 different values of $V_{max} \in [2; 10]\ V$. The resulting average current densities at evaluation voltage 0.2 V for HRS and LRS were then extracted and plotted against V_{max}. A histogram of

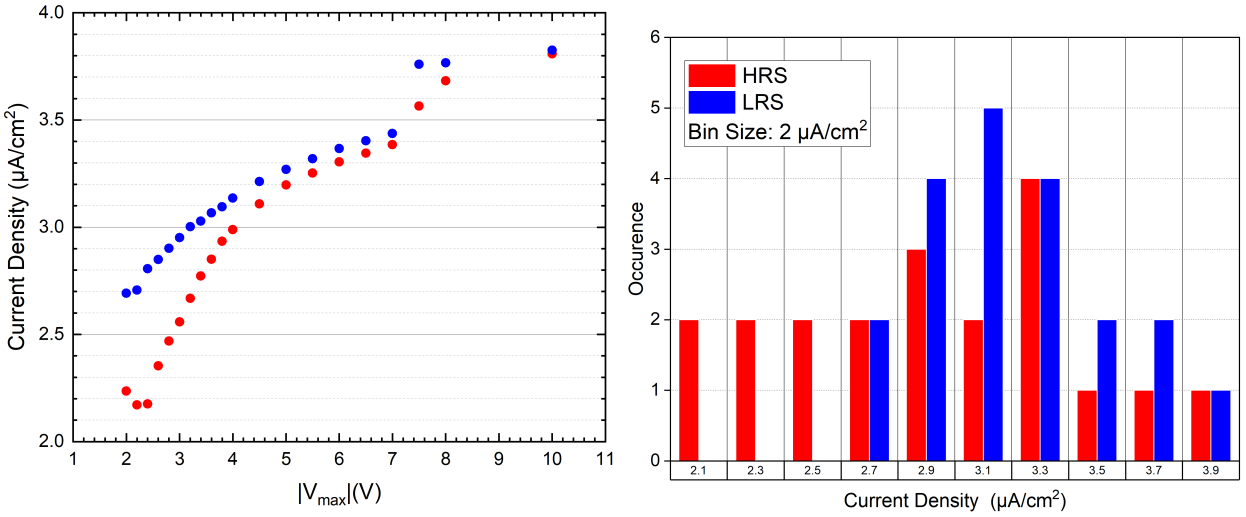

(a) (b)

Figure 9.4.1 Multi-state switching in a QM85^F device. Device area of 20 μm x 20 μm. a) Current densities of LRS (*blue*) and HRS (*red*) at evaluation voltage V= 0.2 V versus maximum magnitude of sweep voltage V_{max}, b) histogram of the current densities shown in a) with bin size 0.2 μA / cm^2. Red: value from HRS, Blue: Value from LRS. Value on the abscissa corresponds to the center value of each bin, i.e., for instance the first bin is labeled 2.1 and summarizes the occurrence of current densities from 2.0 to 2.2 μA / cm^2.

all current density values featuring a bin size of 0.2 μA/cm^2 was also calculated. The resulting graphs are displayed in Figure 9.4.1.

In a potential multi-state memory device, multiple conductance states do not need to be achieved via applying a field of opposite polarity, but instead can also be reached via applying the a voltage of same polarity but different magnitude. Calculating the ON/OFF conductance ratio is only of limited value, since the conductance states do not necessesarily have to be identified as LRS or HRS state. Figure 9.4.1 clearly indicates that an increase in V_{max} is related to an increased in the measured current density. From molecular dynamics simulations, a near-linear increase of the dipole moment in z-direction with increasing applied voltage is to be expected. The data suggests, that there are two distinct regimes, 2.2-4.0 V and 4.2-7.0 V in which this is true. However, the gradient dJ/dV_{max} differs between those two regions and the data observed for $V_{max} < 2.2$ V and $V_{max} > 7.0$ V also break with this trend.

Figure 9.4.1b shows the occurrence of current densities within 10 current density ranges of 0.2 μA / cm^2 bin size. For the chosen bin size, 10 different states of the ensemble molecular device can be observed, with each current density bin being reached by at least two states of the molecular junction. In other words, more than 3 bit of information can be stored in one such junction and each state can be reached by at least two different applied voltages. For a bin size of 0.5 μA / cm^2, the device exhibits 4 different states, which is equivalent to a 2 bit information storage. All current density states ≥ 2.6 μA / cm^2 can be reached through either a low resistive state of the junction, or a high resistive state of the junction at a higher maximum sweep voltage. The current density of the HRS at $V_{max} = 2.4$ V already exceeds the current density of the LRS at $V_{max} = 2.4$ V. This exemplifies that the HRS and LRS may become indistinguishable when V_{max} is varied, but the total number of conductance states of a junction may still increase despite of that.

9.5 Summary

Conductance switching ensemble molecular devices based on SAMs constituted of various molecules with an embedded, flexible, molecular dipole have been demonstrated. Devices that differed in both, the contacting scheme as well as the chemical design of the SAM forming molecule from the devices presented in Chapter 7 showed pronounced hysteresis. This constitutes compelling evidence for the feasibility of utilizing conformationally flexible embedded molecular dipoles for conductance switching devices and that in fact, the occurence of this hysteresis is independent of contacting scheme. It also provides further proof for the general applicability of the **TiN/../Ti/Au** contacting scheme for phosphonic acid based ensemble molecular devices, presented in Chapter 8.

Molecular design has proven to greatly influence conductance ON/OFF ratios and cycle-to-cycle variance as well as the retention of conductive states of ensemble molecular devices. Several chemical structure-device property relationships have been proposed. The potential of multi-state conductance switching, as proposed by MD simulations, has further been demonstrated.

This concludes the feasibility study regarding the utilization of electrical field controlled, dipole induced tunneling barrier height modification for conductance switching ensemble molecular devices.

10 Conclusion and Outlook

In this work, the feasibility of conductance switching ensemble molecular devices based on liquid crystal inspired molecules has been demonstrated. Specifically, the following was achieved:

- First realization of conductance switching devices based on the novel, proposed switching mechanism that builds on electrical field-controlled variation of the dipole induced tunneling barrier height via molecular reorientation in a self-assembled monolayer.
- Development of a novel contacting scheme for self-assembled monolayers of molecules with a phosphonic acid head group
- Characterization of the impact of structural variation of the SAM forming molecule on charge transfer characteristics within the novel contacting scheme
- Demonstration of multi-state conductance switching in ensemble molecular devices featuring the novel conductance switching mechanism

In the following, the major results are summed up and some potential routes towards device optimization and improvement of the measurement setup are given.

Alternative Contacting Scheme

An alternative contacting scheme to embed SAMs between two solid, metallic contacts has been developed in this work. To this end, the formation of alkylphosphonic acid (APA) monolayers on titanium nitride (TiN) has been studied in great detail. After immersing samples with a TiN surface layer in 1 mM solutions of a varierty of APAs in THF for 72 hours and subsequent annealing at 130 °C, the resulting surface were found to have changed from 66° to 97° (probed via water contact angle). AFM scratching, XPS absorption (measured at the Ti2p peak) and variable angle spectroscopic ellipsometry have revealed an increasing thickness trend with increasing molecular length, that is in good agreement with the increase of calculated layer thickness for APAs featuring 6-12 carbon atoms. For 14 and 16 carbon atoms, data remained inconclusive as to whether a double layer was formed. Fourier transform infrared spectroscopy revealed the presence of alkyl chains and potentially tri-dentate surface bound phosphonic acid on all samples. Peak positions and FWHM of the CH2 stretching vibration were found to be in ranges, typically connected to densily packed SAMs, indicating even more regularily packed SAMs than previously reported SAMs of APAs on aluminum oxide (compare also [57]). Peak positions were found at 2925-2918 cm^{-1} and FWHM was found to be in the range from 6 to 21. Peak position moved towards lower frequencies with increasing chain length, whereas the FWHM values also decreased with increasing chain length of the APA molecule. These trends are consistent with observations by others in literature.
Ensemble molecular devices with APAs of varying length were analyzed using DC voltage cycles. While several features remain yet to be explained, general trends could be observed. In particular, analyzing current

densities at a variety of evaluation voltages versus molecular chain length revealed an exponential decrease for a wide range of device areas and molecular lengths. Tunneling attenuation factors β_i and injection currents $J_{0,i}$ were also determined. β_i was found to be within the literature consensus range. Both β_i and $J_{0,i}$ were found to increase with magnitude of the evaluation voltage, which is both unexpected, from the Simmons formula alone, and at the same time in agreement with measurements made by others. It might be attributed to electrostriction. Detailed fitting of J-V traces from single devices revealed physically sound parameters for electrically active area (K = 0.1, i.e., 10%), barrier height (ϕ = 3.0eV) and ideality factor ($\alpha = 0.71 - 0.82$). Together with electrical data of liquid crystal inspired molecules contacted using this contacting scheme, and TEM crosssectional images displaying the structural integrity of all layers within one of these devices, this constitutes compelling evidence that the **TiN/../Ti/Au** contacting scheme constitutes a novel alternative of fabricating ensemble molecular devices with solid contacts, based on SAMs with a phosphonic acid headgroup.

To further improve understanding and fabrication of ensemble molecular devices with this contacting scheme, the following points should be addressed in future work:

- The need for a spacious mask alignment kit greatly limits the potential to scale this fabrication method. Consequently, moving from shadow mask evaporation towards **top contact structuring via lift-off lithography** would greatly enhance the number of chips that can be fabricated at the same time. This in turn would decrease the time needed per experiment and would increase the comparability between chips, since only then the top contact formation to multiple different monolayers could be performed with identical parameters of the physical vapor phase deposition. A lithographic step after monolayer formation would, however, also expose the SAM to additional solvents, resins and potentially UV radiation that might greatly impact its integrity.

- Another improvement would be to **downscale feature sizes further**. As of now, the minimum achievable device area is limited by the minimum feature width of the nickel shadow mask. Device area could be further decreased, for instance, if the bottom contact area alone would be decreased, yielding junctions of non-square area. Also, other suppliers of nickel masks might be able to produce masks with smaller feature sizes.

- Experiments in this work have also revealed that larger area devices show lower device yield and often seem to be dominated by non-molecular conductance channels. Future chip layouts might build on that by only placing **devices of smaller area** on the chip. If multiple rows of devices were to be designed with the same device area, the concept of shared contact pads but mutually exclusive conductance paths could be expanded across rows to safe area on the chip and ultimatly increase the number of devices of same area on the chip. This could potentially result in more statistics per device area.

- To test the universality of the novel contacting approach, it would also be beneficial to perform a series of experiments featuring alkylphosphonic acids with **different ambient facing moieties**, such as a hydroxyl, carboxyl, thiol, amino, phenyl, trifluormethyl, acide or phosphonic acid group. These compounds are all readily available through commercial sellers, such as Sigma Aldrich or Sikémia, as of today.

- Since the contacting scheme used in this work was chosen based on the assumptions that the combination of top and bottom contact material is detrimental to the structural integrity of the resulting stack, this

of course encourages to **broaden the search for contacting schemes** and consider other combinations as well. This becomes even more relevant, when expanding the study of ensemble molecular devices to potential SAM based spintronic devices. Studying them would most likely require a ferromagnetic anchoring layer. One potential combination could be that of a natural oxide covered nickel (Ni) layer as bottom contact and anchoring layer and nickel as PVD deposited top contact. Spintronic devices built on monolayers as of today are typically produced using a thin gold interlayer on top of the ferromagnetic metal (e.g., Ni). Forming SAMs directly on top of the ferromagnetic would greatly reduce fabrication complexity and, most likely, also increase device stability. First experiments to graft APAs on natural oxide covered nickel surfaces have shown promising results, as can be seen from the water contact angle measurements shown in the appendix.

Conductance Switching Ensemble Molecular Devices

Conductance switching based on electrical-field controlled reorientation of molecular dipoles within ensemble molecular devices has been demonstrated. First, monolayers of a difluorphenylcyclohexane based phosphonic acid were grafted on aluminum surfaces and devices of the molecules sandwiched between aluminum and lead were fabricated and subsequently electrically characterized. Surface analysis revealed the formation of uniform monolayers. NEXAFS measurements revealed the presence of the aromatic moiety and an average angle of the normal to the aromatic plane of $\beta = 23°$, which was found to be in agreement with MD simulations.
TEM images of FIB-cut lamellae of the devices revealed structurally intact organic layers sandwiched between the electrodes. Thickness of these layers was in range with the theoretically predicted values. DC current voltage spectroscopy revealed J-V traces with a pronounced hysteresis for the fluorinated compound, whereas the unfluorinated compound did not show such hysteresis. Average data from 6 devices of the same area revealed a low device-to-device variance and a maximum average ON/OFF conductance ratio of 303. Conductance switching remained repeatable for 100 cycles between ± 3.0 V.
Calculations on single molecule, molecular ensemble and device model provided compelling evidence, that the origin of the conductance switching was in fact the re-orientation of the dipolar unit. Single molecule rotational scans reveiled an intramolecular barrier of 1.41 kcal mol^{-1} from *anti* to *syn* and a 2.1 kcal mol^{-1} barrier from *syn* to *anti*. Molecular dynamics further revealed a disordered SAM, with tilt and orientation angles following distributions, that could be effectively shifted by applying electrical field pulses. The resulting shift in average molecular dipole in z-direction was found to increase near-linearly with the magnitude of the applied electric field. This shift was also found to change less with increasing surface density. In contrast, the remanent dipole moment change after removing the field, was found to increase with surface density. This indicates that *inter*molecular forces play a significant role in device performance. The device model, derived in this work based on a parallel capacitor combined with a tunneling formula as derived by *Gruverman et al.* [133] revealed a strong dependency of the ON/OFF conductance ratio on the effective charge carrier mass within the oxide-SAM double layer as well as on the surface density of the SAM.

Ensemble molecular devices based on LCI molecules sandwiched between TiN and Ti were electrically characterized to analyze the impact of structural variation on device performance. First, devices with the same molecule as in the above experiments were fabricated and J-V traces were compared. In-depth analysis revealed that the novel contacting scheme came with 5 orders of magnitude higher current densities, but also one order of magnitude lower ON/OFF conductance ratios. Maximum average ON/OFF conductance ratio determined

from 3 devices was found to be 13.
In short, the further variation of the structural motifs of SAM forming molecules confirmed the strong influence of intra and *inter*molecular forces on device performance, as well as the impact of the choice of dipolar unit on the ON/OFF ratio. All devices with molecules that feature a 3,4 difluorophenylcyclohexane dipolar unit showed ON/OFF ratios in the range of 13-18, while the device featuring a molecule with a difluorodibenzofurane unit exhibited an ON/OFF conductance ratio of ≈ 135.
The molecule featuring the 2,3-fluoro-6-methylphenyl cyclohexane dipolar unit with no pentyl end group exhibited the lowest degradation of the LRS, with 65% of the initial conductance being preserved after 20 min. This is in particular a stark contrast to the devices that feature almost the same molecule - apart from the additional methyl group and the removed pentyl endgroup - which only retained 1.5% of the conductance of the LRS over the course of 20 min.

One issue that may be addressed in potential future work is that the experiments conducted in this work focused on studying the feasibility of a novel contacting scheme as well as the general concept of liquid crystal-inspired molecules for conductance switching and did not include any device optimization. As outlined in the above work, the device performance is likely to depend heavily on SAM characteristics. It therefore stands to reason that it is worthwhile to investigate the process parameters of SAM formation in more detail. Potential processing parameters to optimize include:

- **Choice of solvents or solvent mixtures.** The choice of solvent or even solvent mixture have shown to influence the monolayer formation dynamics and might be a potential lever to adjust the surface density of molecules that in turn affects device performance. [286, 287]

- **Duration of the dip.** While one experiment not referenced in this work showed decreased device yield for a dip time of ≈ 24 h, decreasing the dip time from 72 h to shorter times would come with the benefit of further decreasing the time each experiment takes.

- **Temperature during and after dipcoating**. Temperature during immersion was kept at room temperature within a controlled environment (≈ 22°C) in all experiments. While this yielded functional monolayers and keeps the processing simple, increasing this temperature might speed up the self-assembly process. On the other hand increased temperatures might also lead to faster detachment of the molecules during self-assembly and decreasing processing temperature might in fact be beneficial. Since both these processes compete, it is likely, that there is an optimum processing temperature that one might subject to optimization. The heating temperature after dip coating was initially fixed at 130 °C and kept constant since it yielded functional monolayers on several types of substrates.

- **Number of different molecules within the monolayer**. Monolayers of one single type of molecule are commonly studied. Since device performance of the conductance switching SAMs in this work seems to be highly dependent on *inter*molecular forces, using molecule mixtures might be an interesting route towards optimization of device performance. Mixing electronically active molecules with alkylphosphonic acids to improve device performance have only recently begun to be studied, but already yielded some promising results. For instance, one series of studies showed that forming a mixed SAM of a rectifying molecule (based on a bipyridine unit) and a non-rectifying, alkylthiolate significantly increased rectification ratios.[288–290] A comprehensive, recent review of charge transfer in and applications of mixed self-assembled monolayers that may lend itself as a good starting point for future work is provided by *Kong et al.*. [291]

In addition to that, physical characteristics of the oxide, most notably the relative permittivity and the position of the conduction and valence band, that constitute the barrier height on one side of the asymmetric barrier, present a lever for potential optimization. This could be exploited by either adjusting adding a processing step prior to the SAM formation in order to tune the characteristics of the oxide, or even the exploration of different oxides that might have both, a high thickness to permittivity ratio as well as low barrier with respect to the contact metal.
In case of TiN as bottom electrode, the potential to tune TiN workfunction and over-/under stoichiometry present additional potential routes towards device performance optimization. The former may impact the barrier height whereas the latter may influence the permittivity of the potential oxide, which in turn influences the voltage across the SAM and the ON/OFF conductance ratio.

When it comes to the chemical design of liquid crystal inspired molecules, some variations have been explored in this work already. Electrical characterization has revealed, in particular, that only limited, direct relationships between the design of a single molecule to device performance can be drawn. Especially the dipole moment change between the two conformers of one molecule did not directly relate to the ON/OFF conductance ratio of the resulting devices. However, from the data in this work, the dipolar unit seemed to have the largest impact on ON/OFF conductance ratio. Moving forward, designing molecules with different dipolar units and testing them directly in ensemble molecular devices seems advisable. Designing molecules that feature an increased *intra*molecular barrier as well as molecules that feature chemical building blocks that increase the *inter*molecular interactions seems to increase the stability of the LRS over time as well as decrease the sweep-to-sweep variation. From the data acquired in this work, moving forward, an advisable strategy might be to focus on carefully designing molecular building blocks that vary *inter*molecular to further study the effects of these on device performance.
Also, in this work, liquid crystal inspired molecules that differ in multiple chemical building blocks have been compared to each other. Since molecules where only one building block - e.g., the linker between head group and dipolar group, as well as the alkyl chain at the tail of the molecule - is systematically varied are already available, the direct influence of this variation on device performance may be studied in future work.

As has been mentioned in the main text, the performance of conductance switching monolayers is interrelated with characteristics of the monolayer as well as the contacting scheme. This complicates modeling, but also renders comparisons to alternative conductance switching concepts almost impossible, if different contacting schemes are utilized. Some of the most prominently conductance switching ensemble molecular devices are based on bipyridines in an **Au/../EGaIn** contacting scheme. Almost identical molecules, only featuring a phosphonic acid instead of a thiol as binding group are readily available at e.g., Sikémia. These molecules might form monolayers on TiN as well and could be measured in either a **TiN/../Ti/Au** or a **TiN/../EGaIn** contacting scheme to reveal the respective advantages and disadvantages of both approaches.

Measurement Methods

Lastly, further measurement methods could be used to improve the understanding of conductance switching ensemble molecular devices.
The following electrical characteristics might be measured:

- **Electrical impedance spectroscopy (EIS) of monolayers and devices**. DC measurements can be used to determine well-established device characteristics such as the tunneling decay constant β and the injection current density J_0. To separate contributions of individual components of the junctions, e.g.,, interfaces, oxides and molecules, EIS may be employed. Electrical impedence spectroscopy is the study of the frequency response of a device via applying sinusoidal perturbations with varying frequency. It could, for instance, be used to calculate the dielectric constant of oxide and SAM, hence improving the device model. Some initial work on EIS on SAMs has already been performed by others [249] and the topic has picked up research interest very recently[292–294].

- **Current noise Spectroscopy**. By keeping the voltage across a SAM constant and sampling the current at a very high sampling frequency, noise can be measured and randomly occurring events can be recognized. While current noise spectroscopy is not very commonly employed for ensemble molecular devices to date, some initial work on it exists [295–297]. A recent, comprehensive review on noise analysis of molecular electronic devices and the potential advances in understanding of charge transport mechanisms it might provide is given by *Kim and Song* [298].

- **Short voltage pulses**. Characterizing the devices using short voltage pulses and voltage pulse sequences, device characteristics such as endurance, retention, switching speed, switching energy and variability can be measured in a recommended way, yielding device characteristics that are comparable to other material systems. [299] These measurements can be performed with the Keithley 4200 SCS parameter analyzer. Some preliminary results of measurements of **TiN/QM15^F/Ti/Au** devices using a read-set-read-reset pulse sequence and the Keithley 4200 SCS at the probestation can be found in the appendix.

- **Temperature dependent current voltage spectroscopy**. Recording J-V traces at various, lower voltages, might shine some light on the derived transport model as well as on the proposed switching mechanism. Combining these measurements with MD simulations at different temperatures might in fact also reveal the minimum energy required for a switching process.

Further, SAMs of LCI molecules on TiN might be analyzed using (polarized) FTIR to gain more insight on the molecular orientation after SAM formation. Kelvin probe AFM measurements could be employed to locally resolve the induced vacuum energy level shift of LCI SAMs. Conductive AFM might further be used to locally resolve the current density of both SAMs and devices. Cross-correlating results of both AFM measurement techniques might ultimately reveal information about the correlation between induced vacuum energy level shift and conductance change.

A NiO as Alternative Anchoring Layer

Since nickel is assumed to form a natural oxide under ambient conditions, it may lend itself as an alternative anchoring layer for alyklphosphonic acids. Nickel bottom contacts would be particularly interesting for ensemble molecular spintronic devices, since nickel is ferromagnetic. Silicon wafers with 290 nm dry oxide, 10 nm sputter deposited Ti an 100 nm sputter deposited Ni were obtained from *Siegert Wafer GmbH* (Aachen, Germany) and then cut into 8 mm x 8 mm substrates. They were then immersed in 1 mM solutions of a series of alkylphosphonic acids in THF, namely octyl- (C8), dodecyl-(C12), tetradecyl-(C14) -phosphonic acid (C16). Substrates were subsequently annealed for 1 h at 130 °C, rinsed in an ethanol stream, heated again for 2 min at 130 °C and then characterized via water contact angle. Contact angles were also measured on pristine native nickel oxide surfaces. Figure A.0.1 shows the results averaged from one chip and three measurement points per chip. Water contact angle of the APA grafted sample is clearly increased compared to the pristine surfaces, which is a first indicator that monolayers were formed.
AFM measurements of the same samples showed a RMS surface roughness of ≈ 2 nm over a 5 µm x 5 µm area.

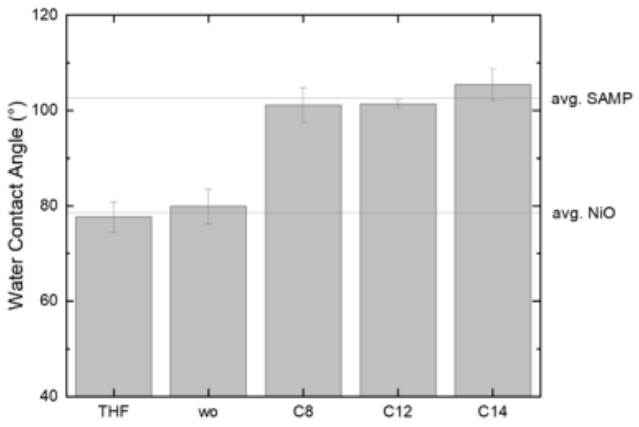

Figure A.0.1 Water contact angle of nickel surfaces covered with a natural oxide that were immersed in 1 mM solutions of different APAs. The clear increase from the pristine layer (w/o) to the APA grafted ones is a first indicator pointing towards successful APA monolayer formation on nickel surfaces.

B EGaIn Measurements of Alkyl Phosphonic Acids and Alkyl Phosphonic Bipyridines

One of the setups designed and set up during this work was an EGaIn system. The intention was to provide a well-established measurement system as a reference system. Figure B.0.1 shows an image of the final setup that was connected to a Keithley 2635 source measurement unit.
EGaIn tips were formed by pushing some EGaIn out of the capillary, making contact with a gold surface and moving the eutectic away from the surface until the now surface "bound" broke off, leaving a cone of EGaIn.

To test the setup, a series of alkylphosphonic acids was grafted on TiN surfaces and cyclic current density voltage traces were recorded for three such surfaces. Substrates covered with TiN were cleaned and immersed for 72 hours in 1 mM solutions of dodecyl-(C12), hexadecyl-(C16) and octadexyl-phosphonic acid(C18) . Substrates were subsequently annealed for 1h at 130 °C, rinsed in an ethanol stream, heated again for 2 min at 130°C and then characterized using the EGaIn setup. Each chip was contacted only once and J-V traces were recorded for voltages up to ± 1 V. The figure below displays J-V traces for all 3 devices, as well as the current density of all three devices at V = -1 V. A fit to the simplified Simmons formula was then performed, resulting in β = 0.9 nC^{-1}, which is well in range of literature consensus. Even those can only be taken as preliminary results, since only one position was measured on each chip, these results point towards the successful fabrication of **TiN/APA/EGaIn** junctions with the newly set up EGaIn setup.

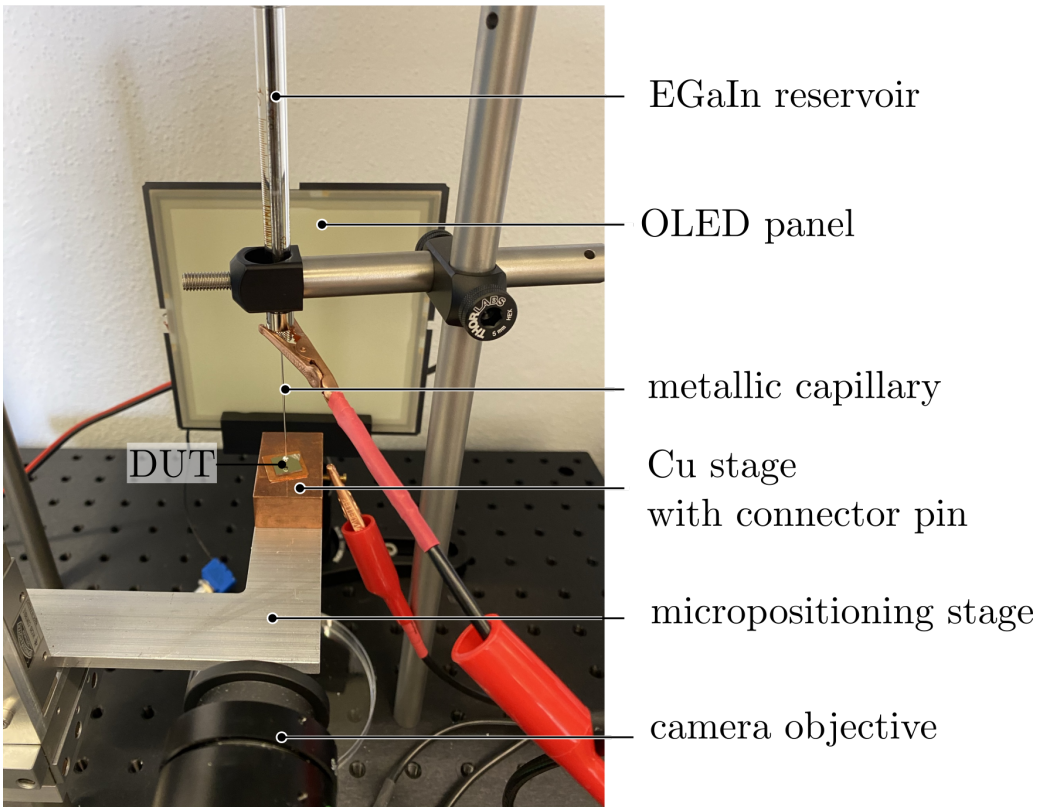

Figure B.0.1 Eutectic Gallium Indium (EGAIn) setup as developed and set up during this work. EGaIn is stored in a sealed glass syringe and pushed out of the metallic needle to perform experiments. Substrates are glued to copper plates using either EGaIn or silver paint and placed on the copper stage. SMU is connected to both, the metallic capillary and a connector pin at the Cu state.

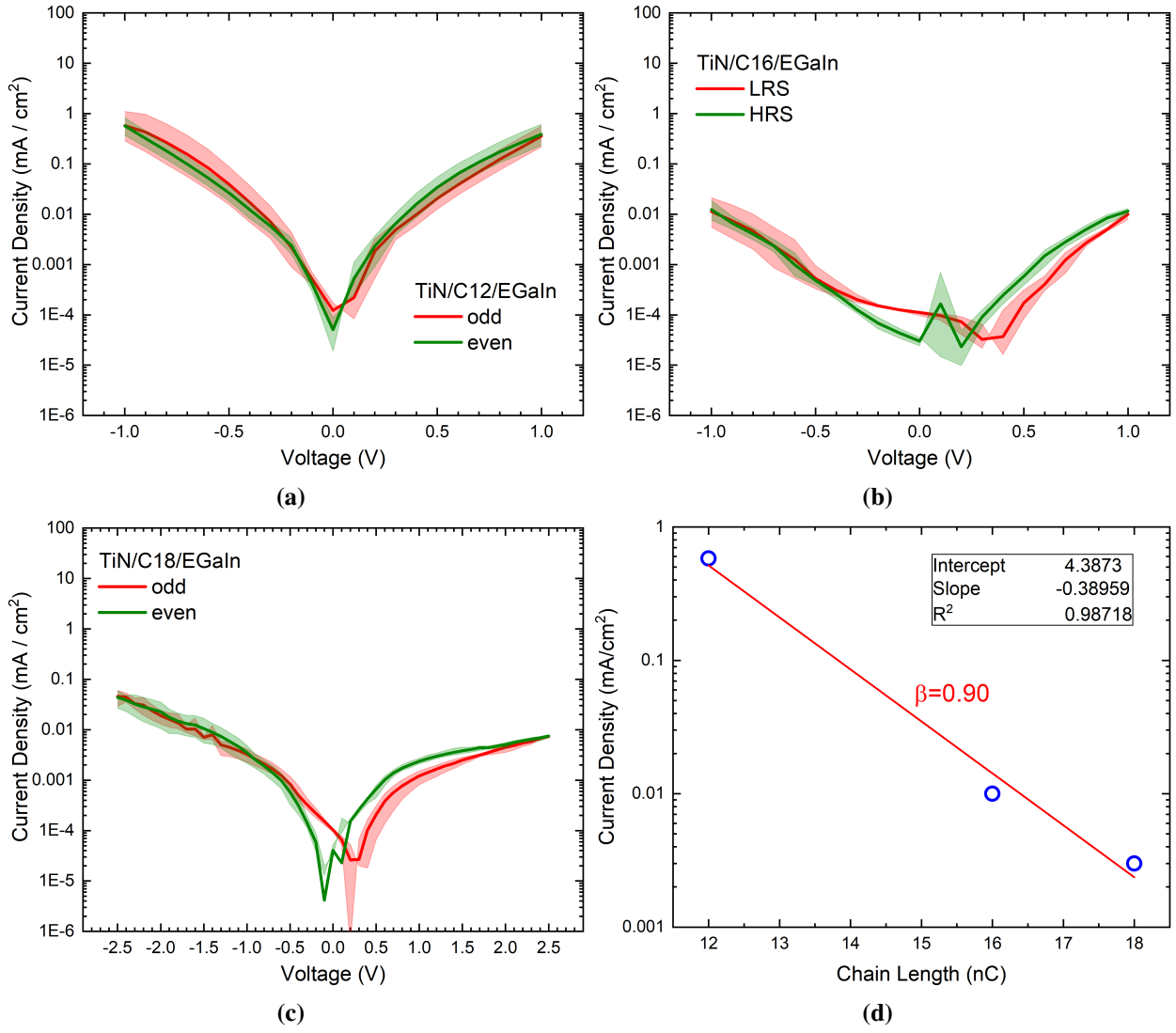

Figure B.0.2 Charge transport of individual TiN/SAM/EGaIn junctions. a)-c) Average J-V of 4 sweeps per junction for junctions with C12, C16 and C18 sandwiched between TiN and EGaIn. d) Current densities at V = -1 V versus alkyl chain length in number of carbons (nC) and fit to the simplified Simmons model.

B.1 Bipyridines

Self-assembled monolayers of molecules featuring a bipyridine unit have been shown to act as electrical-field controlled molecular switches [11, 15, 220]. In order to explore advantages and disadvantages of this system as compared to the liquid crystal-inspired molecules studied in the main part of this work, the idea was to transfer the concept outlined by Han et al. to a measurement setup that both types of molecules could be characterized in. To that end, bipyridines with two different exchange ions (Cl^- and Br^-) and a phosphonic acid anchoring group were obtained from *Sikémia* (Grabels, France). The only difference of these molecules as compared to those studied in the above cited literature are the anchoring groups. Structures of these two molecules are displayed in Figure B.1.1

The surface grafting of TiN surfaces was attempted by dip coating cleaned substrates with TiN surface in 1 mM solutions of each phosphonic acid bipyridine for 72 hrs, subsequent heating for 1 h at 130°C, EtOH rinsing and subsequent heating for 2 min at 130°C. Water contact angles of the resulting surfaces were obtained at three spots on the substrates and averaged. This resulted in water contact angles of 104° (BPy-Cl) and 92°(BPy-Br). Samples fabricated in the same fashion were measured using the previously described EGaIn setup. Voltage was cycled at one position between ± 1 hjV for a total of 7 sweeps and current densities were calculated from the diameter of the EGaIn cone in contact with the substrate. The J-V traces of these measurements are displayed in figure B.1.2. From these preliminary measurements the following behaviour could be observed: with each sweep, the conductivity of the junction seemed to decrease for both types of molecule. This is shown in Figure B.1.2.

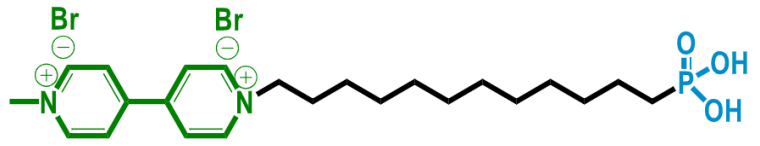

(a)

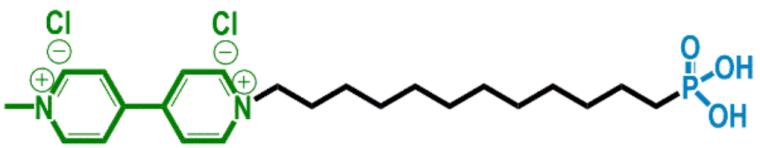

(b)

Figure B.1.1 Structures of the bipyridines. *Blue*: phosphonic acid binding group, *green*: bipyridine a) molecule with Br^- as exchange ions [(1-Methyl-4,4'-bipyridine-1,1'-diium-1'-dodecylphosphonic acid) dibromide] b) molecule with Cl^- as exchange ions [(1-Methyl-4,4'-bipyridine-1,1'-diium-1'-dodecylphosphonic acid) dichloride].

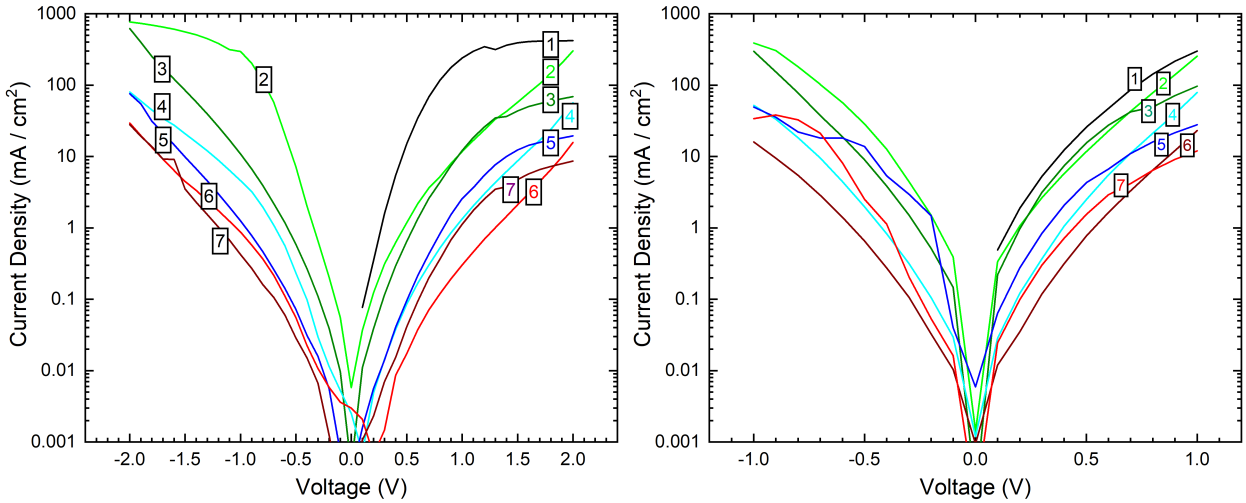

Figure B.1.2 J-V characteristics of charge transfer in TiN/BPy/EGaIn juctions. a) with Cl^- as counter ions, b) with Br^- as counter-ions. The numbers at the individual traces denote the order in which they were measured.

C Pulsed Measurements

To test whether the observed conductance switching was persistent when it was attempted with short voltage pulses, a 15 µm x 15 µm **TiN/QM15^F/Ti/Au** device fabricated as described in the main text, was measured using a Keithley 4200 Parameter analyzer at the Probestation. The read-set-read-reset cycle that was performed for a total of 0.09 s is shown in Figure C.0.1. Data from the read parts of the cycle is displayed in Figure C.0.2. Current was measured simultaneously with the applied voltage. As can be seen, the conductance switching between two distinct states also occurs when very short pulses are applied to the ensemble molecular devices. Currents of both states seem to first decrease with increasing number of pulse sequences already applied and then saturate at a saturation value. Since this was only one measurement at one device, more statistics is needed to draw any meaningful conclusion. For now, the data presented here, points towards the feasibility of using LCI molecules in conductance switching devices, even when the conductance states are addressed via few ns long pulses. In fact, the data presented here also points towards the potential retention of the conductance switching effect over $\approx 10^8$ set-reset cycles. However, a more detailed, statistical analysis to confirm this is necessary.

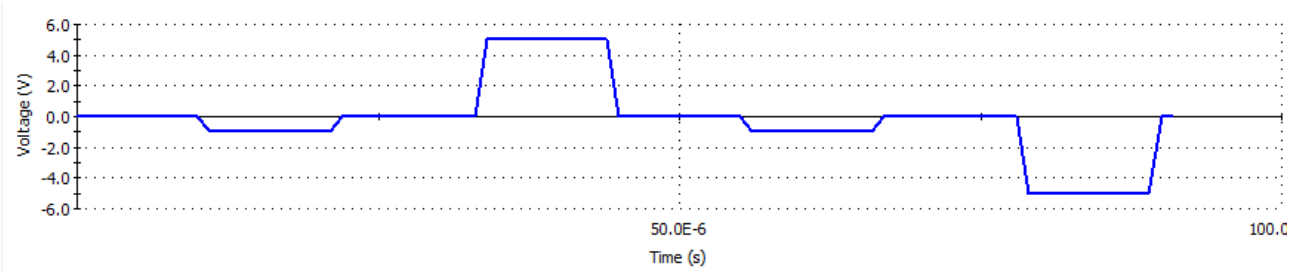

Figure C.0.1 V(t) of a single read-set-read-reset pulse cycle that was repeatedly applied to the **TiN/QM15^F/Ti/Au** device. Read pulse maximum voltage was set to 1 V. Set and reset pulse featured the same magnitude ($|V|$ = 5 V), but opposite polarity of the applied voltage. All pulse lengths, as well as time between two consecutive pulses was set to 10 ns. Rise and fall times of pulses was set to 0.1 ns. The full sequence is therefore 88 ns long. Durations and voltages were arbitrarily chosen.

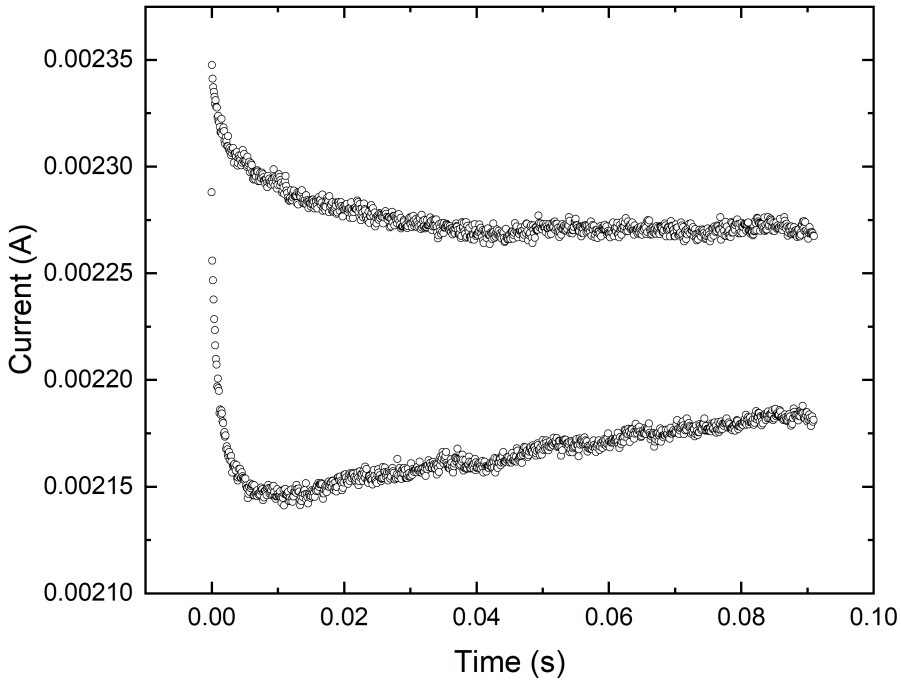

Figure C.0.2 Results of the read-set-read-reset cycle measurement. Open circles represent measured current at each read pulse. Upper curve stems from the read pulse at the beginning of the pulse sequence (after reset pulse), lower curve data stems from the read pulse after the set pulse. The measured currents for a total of $\approx 1 \cdot 10^8$ pulse sequences are displayed here.

Publications

The following journal publications and conference contributions evolved from this work:

Journal Articles and Conference Proceedings

- **Julian M. Dlugosch**, Henning Seim, Achyut Bora, Takuya Kamiyama, Itai Lieberman, Falk May, Florian Müller-Plathe, Alexei Nefedov, Saurav Prasad, Sebastian Resch, Kai Saller, Christian Seim, Maximilian Speckbacher, Frank Voges, Marc Tornow, Peer Kirsch. *Conductance switching in liquid crystal-inspired self-assembled monolayer junctions*. ACS Appl. Mater. Interfaces 14, 27, 31044–31053, 2022. DOI:10.1021/acsami.2c05264

- Domenikos Chryssikos, **Julian M. Dlugosch**, Jerry A. Fereiro, Takuya Kamiyama, Mordechai Sheves, David Cahen, Marc Tornow. *Electronic Transport Through Organophosphonate-Grafted Bacteriorhodopsin Films on Titanium Nitride*. IEEE-NANO, 21st International Conference on Nanotechnology, *online*, pp. 389-392, 2021. DOI: 10.1109/NANO51122.2021.9514351

- **Julian M. Dlugosch**, Deepthi Devendra, Domenikos Chryssikos, Sabrina Artmeier, Maximilian Speckbacher, Takuya Kamiyama, Marc Tornow. *Metallic Top Contacts to Self-Assembled Monolayers of Aliphatic Phosphonic Acids on Titanium Nitride*. IEEE-NANO, 20th International Conference on Nanotechnology, *online*, pp.29-34, 2020. DOI: 10.1109/NANO47656.2020.9183521

Conference Presentations & Poster

- **Julian M. Dlugosch**, Deepthi Devendra, Domenikos Chryssikos, Sabrina Artmeier, Maximilian Speckbacher, Takuya Kamiyama, Marc Tornow. *Metallic Top Contacts to Self-Assembled Monolayers of Aliphatic Phosphonic Acids on Titanium Nitride*. IEEE 20th International Conference on Nanotechnology (NANO), *online*, September 2020.

- **Julian Dlugosch**, Deepthi Devendra, Takuya Kamiyama, Domenikos Chryssikos, Maximilian Speckbacher, Marc Tornow *Electrical top-contacts to organophosphonate monolayers grown on TiN, poster presentation*. SPICE Workshop “Molecular Electro-Opto-Spintronics”, Mainz, Germany, October 2019.

Patents

- Peer Kirsch, Sebastian Resch, Henning Seim, Itai Lieberman, Shintaro Arai, Marc Tornow; Takuya Kamiyama, **Julian Dlugosch**, Mansour Moinpour. *Electronic Switching Device*. EP3813132A1.

- Peer Kirsch, Sebastian Resch, Henning Seim, Itai Lieberman, Marc Tornow, **Julian Dlugosch**. *Two bit memory device and method for operating the two-bit memory device and electronic component*. EP3813135A1.

Bibliography

[1] R. Stanley Williams. "What's Next? [The end of Moore's law]". In: *Computing in Science & Engineering* 19 (2 Mar. 2017), pp. 7–13. ISSN: 1521-9615. DOI: 10.1109/MCSE.2017.31.

[2] Gordon E. Moore. "Cramming more components onto integrated circuits". In: *Electronics* 38 (8 Sept. 1965), p. 144. ISSN: 1098-4232. DOI: 10.1109/N-SSC.2006.4785860.

[3] John M. Shalf and Robert Leland. "Computing beyond Moore's Law". In: *Computer* 48 (12 Dec. 2015), pp. 14–23. ISSN: 0018-9162. DOI: 10.1109/MC.2015.374.

[4] Tayfun Gokmen and Yurii Vlasov. "Acceleration of Deep Neural Network Training with Resistive Cross-Point Devices". In: (Mar. 2016). DOI: 10.3389/fnins.2016.00333.

[5] G. I. Meijer. "MATERIALS SCIENCE: Who Wins the Nonvolatile Memory Race?" In: *Science* 319 (5870 Mar. 2008), pp. 1625–1626. ISSN: 0036-8075. DOI: 10.1126/science.1153909.

[6] Ayelet Vilan, Dinesh Aswal, and David Cahen. "Large-Area, Ensemble Molecular Electronics: Motivation and Challenges". In: *Chemical Reviews* 117 (5 Mar. 2017), pp. 4248–4286. ISSN: 0009-2665. DOI: 10.1021/acs.chemrev.6b00595.

[7] Dong Xiang, Xiaolong Wang, Chuancheng Jia, Takhee Lee, and Xuefeng Guo. "Molecular-Scale Electronics: From Concept to Function". In: *Chemical Reviews* 116 (7 2016), pp. 4318–4440. ISSN: 15206890. DOI: 10.1021/acs.chemrev.5b00680.

[8] Guo Fang Zuo, Xin You Lei, and Jian Bin Zhang. "Molecular electronics on silicon based on self assembled monolayers". In: *Gongneng Cailiao yu Qijian Xuebao/Journal of Functional Materials and Devices* 16 (5 2010), pp. 429–436. ISSN: 10074252.

[9] Ritu Gupta, Priyajit Jash, and Prakash Chandra Mondal. "Nanoscale molecular layers for memory devices: challenges and opportunities for commercialization". In: *Journal of Materials Chemistry C* 9 (35 2021), pp. 11497–11516. ISSN: 2050-7526. DOI: 10.1039/D1TC01283E.

[10] Junwoo Park, Mohamad S. Kodaimati, Lee Belding, Samuel E. Root, George C. Schatz, and George M. Whitesides. "Controlled Hysteresis of Conductance in Molecular Tunneling Junctions". In: *ACS Nano* 16 (3 Mar. 2022), pp. 4206–4216. ISSN: 1936086X. DOI: 10.1021/ACSNANO.1C10155.

[11] Yingmei Han, Cameron Nickle, Ziyu Zhang, Hippolyte P.A.G. Astier, Thorin J. Duffin, Dongchen Qi, Zhe Wang, Enrique del Barco, Damien Thompson, and Christian A. Nijhuis. "Electric-field-driven dual-functional molecular switches in tunnel junctions". In: *Nature Materials* (2020). ISSN: 14764660. DOI: 10.1038/s41563-020-0697-5.

[12] Su Ying Quek, Maria Kamenetska, Michael L. Steigerwald, Hyoung Joon Choi, Steven G. Louie, Mark S. Hybertsen, J. B. Neaton, and Latha Venkataraman. "Mechanically controlled binary conductance switching of a single-molecule junction". In: *Nature Nanotechnology* 4 (4 Apr. 2009), pp. 230–234. ISSN: 1748-3387. DOI: 10.1038/nnano.2009.10.

[13] Z. J. Donhauser, B. A. Mantooth, K. F. Kelly, L. A. Bumm, J. D. Monnell, J. J. Stapleton, D. W. Price, A. M. Rawlett, D. L. Allara, J. M. Tour, and P. S. Weiss. "Conductance Switching in Single Molecules Through Conformational Changes". In: *Science* 292 (5525 June 2001), pp. 2303–2307. ISSN: 0036-8075. DOI: 10.1126/science.1060294.

[14] Sreetosh Goswami, Adam J. Matula, Santi P. Rath, Svante Hedström, Surajit Saha, Meenakshi Annamalai, Debabrata Sengupta, Abhijeet Patra, Siddhartha Ghosh, Hariom Jani, Soumya Sarkar, Mallikarjuna Rao Motapothula, Christian A. Nijhuis, Jens Martin, Sreebrata Goswami, Victor S. Batista, and T. Venkatesan. "Robust resistive memory devices using solution-processable metal-coordinated azo aromatics". In: *Nature Materials* 16 (12 2017), pp. 1216–1224. ISSN: 14764660. DOI: 10.1038/nmat5009.

[15] Sreetosh Goswami, Santi P. Rath, Damien Thompson, Svante Hedström, Meenakshi Annamalai, Rajib Pramanick, B. Robert Ilic, Soumya Sarkar, Sonu Hooda, Christian A. Nijhuis, Jens Martin, R. Stanley Williams, Sreebrata Goswami, and T. Venkatesan. "Charge disproportionate molecular redox for discrete memristive and memcapacitive switching". In: *Nature Nanotechnology* 15 (5 May 2020), pp. 380–389. ISSN: 1748-3387. DOI: 10.1038/s41565-020-0653-1.

[16] Florian Schwarz, Michael Koch, Georg Kastlunger, Heinz Berke, Robert Stadler, Koushik Venkatesan, and Emanuel Lörtscher. "Charge Transport and Conductance Switching of Redox-Active Azulene Derivatives". In: *Angewandte Chemie International Edition* 55 (39 Sept. 2016), pp. 11781–11786. ISSN: 14337851. DOI: 10.1002/anie.201605559.

[17] Stefan Wagner, Ferdinand Kisslinger, Stefan Ballmann, Frank Schramm, Rajadurai Chandrasekar, Tilmann Bodenstein, Olaf Fuhr, Daniel Secker, Karin Fink, Mario Ruben, and Heiko B. Weber. "Switching of a coupled spin

pair in a single-molecule junction". In: *Nature Nanotechnology* 8 (8 Aug. 2013), pp. 575–579. ISSN: 1748-3387. DOI: 10.1038/nnano.2013.133.

[18] Salvador Cardona-Serra, Lorena E. Rosaleny, Silvia Giménez-Santamarina, Luis Martínez-Gil, and Alejandro Gaita-Ariño. "Towards peptide-based tunable multistate memristive materials". In: *Physical Chemistry Chemical Physics* 23 (3 2021), pp. 1802–1810. ISSN: 1463-9076. DOI: 10.1039/D0CP05236A.

[19] Auke J. Kronemeijer, Hylke B. Akkerman, Tibor Kudernac, Bart J. van Wees, Ben L. Feringa, Paul W. M. Blom, and Bert de Boer. "Reversible Conductance Switching in Molecular Devices". In: *Advanced Materials* 20 (8 Apr. 2008), pp. 1467–1473. ISSN: 09359648. DOI: 10.1002/adma.200800053.

[20] Sense Jan van der Molen, Jianhui Liao, Tibor Kudernac, Jon S. Agustsson, Laetitia Bernard, Michel Calame, Bart J. van Wees, Ben L. Feringa, and Christian Schönenberger. "Light-Controlled Conductance Switching of Ordered Metal-Molecule-Metal Devices". In: *Nano Letters* 9 (1 Jan. 2009), pp. 76–80. ISSN: 1530-6984. DOI: 10.1021/nl802487j.

[21] Peter Liljeroth, Jascha Repp, and Gerhard Meyer. "Current-Induced Hydrogen Tautomerization and Conductance Switching of Naphthalocyanine Molecules". In: *Science* 317 (5842 Aug. 2007), pp. 1203–1206. ISSN: 0036-8075. DOI: 10.1126/science.1144366.

[22] Robert Lovrinčić, Olga Kraynis, Rotem Har-Lavan, Abd-Elrazek Haj-Yahya, Wenjie Li, Ayelet Vilan, and David Cahen. "A New Route to Nondestructive Top-Contacts for Molecular Electronics on Si: Pb Evaporated on Organic Monolayers". In: *The Journal of Physical Chemistry Letters* 4 (3 Feb. 2013), pp. 426–430. ISSN: 1948-7185. DOI: 10.1021/jz302153z.

[23] Hyunhak Jeong, Dongku Kim, Dong Xiang, and Takhee Lee. "High-Yield Functional Molecular Electronic Devices". In: *ACS Nano* 11 (7 2017), pp. 6511–6548. ISSN: 1936086X. DOI: 10.1021/acsnano.7b02967.

[24] Arieh Aviram and Mark A. Ratner. "Molecular rectifiers". In: *Chemical Physics Letters* 29 (2 1974), pp. 277–283. ISSN: 00092614. DOI: 10.1016/0009-2614(74)85031-1.

[25] Yuru Liu, Xinkai Qiu, Saurabh Soni, and Ryan C. Chiechi. "Charge transport through molecular ensembles: Recent progress in molecular electronics". In: *Chemical Physics Reviews* 2 (2 June 2021), p. 021303. ISSN: 2688-4070. DOI: 10.1063/5.0050667.

[26] Xinjian Feng and Lei Jiang. "Design and Creation of Superwetting/Antiwetting Surfaces". In: *Advanced Materials* 18 (23 Dec. 2006), pp. 3063–3078. ISSN: 1521-4095. DOI: 10.1002/ADMA.200501961.

[27] N. Ballav, A. Shaporenko, A. Terfort, and M. Zharnikov. "A Flexible Approach to the Fabrication of Chemical Gradients". In: *Advanced Materials* 19 (7 Apr. 2007), pp. 998–1000. ISSN: 09359648. DOI: 10.1002/adma.200602168.

[28] Nirmalya Ballav, Heidi Thomas, Tobias Winkler, Andreas Terfort, and Michael Zharnikov. "Making Protein Patterns by Writing in a Protein-Repelling Matrix". In: *Angewandte Chemie International Edition* 48 (32 July 2009), pp. 5833–5836. ISSN: 1521-3773. DOI: 10.1002/ANIE.200900950.

[29] Axel Rosenhahn, Sören Schilp, Hans Jürgen Kreuzer, and Michael Grunze. "The role of inert surface chemistry in marine biofouling prevention". In: *Physical Chemistry Chemical Physics* 12 (17 Apr. 2010), pp. 4275–4286. ISSN: 1463-9084. DOI: 10.1039/C001968M.

[30] J. Landoulsi, K. E. Cooksey, and V. Dupres. "Interactions between diatoms and stainless steel: focus on biofouling and biocorrosion". In: *Biofouling* 27 (10 Nov. 2011), pp. 1105–1124. ISSN: 1029-2454. DOI: 10.1080/08927014.2011.629043.

[31] Ilja Lange, Sina Reiter, Michael Pätzel, Anton Zykov, Alexei Nefedov, Jana Hildebrandt, Stefan Hecht, Stefan Kowarik, Christof Wöll, Georg Heimel, and Dieter Neher. "Tuning the Work Function of Polar Zinc Oxide Surfaces using Modified Phosphonic Acid Self-Assembled Monolayers". In: *Advanced Functional Materials* 24 (44 Nov. 2014), pp. 7014–7024. ISSN: 1616-3028. DOI: 10.1002/ADFM.201401493.

[32] James W. Borchert, Boyu Peng, Florian Letzkus, Joachim N. Burghartz, Paddy K.L. Chan, Karin Zojer, Sabine Ludwigs, and Hagen Klauk. "Small contact resistance and high-frequency operation of flexible low-voltage inverted coplanar organic transistors". In: *Nature communications* 10 (1 Dec. 2019). ISSN: 2041-1723. DOI: 10.1038/S41467-019-09119-8.

[33] Norbert Koch. "Energy levels at interfaces between metals and conjugated organic molecules". In: *Journal of Physics: Condensed Matter* 20 (18 Apr. 2008), p. 184008. ISSN: 0953-8984. DOI: 10.1088/0953-8984/20/18/184008.

[34] Jian Ming Chiu and Yian Tai. "Improving the efficiency of ZnO-based organic solar cell by self-assembled monolayer assisted modulation on the properties of ZnO acceptor layer". In: *ACS Applied Materials and Interfaces* 5 (15 Aug. 2013), pp. 6946–6950. ISSN: 19448244. DOI: 10.1021/AM400928N.

[35] Stefano Casalini, Carlo Augusto Bortolotti, Francesca Leonardi, and Fabio Biscarini. "Self-assembled monolayers in organic electronics". In: *Chemical Society Reviews* 46 (1 Jan. 2017), pp. 40–71. ISSN: 1460-4744. DOI: 10.1039/C6CS00509H.

[36] Edsger C. P. Smits, Simon G. J. Mathijssen, Paul A. van Hal, Sepas Setayesh, Thomas C. T. Geuns, Kees A. H. A. Mutsaers, Eugenio Cantatore, Harry J. Wondergem, Oliver Werzer, Roland Resel, Martijn Kemerink, Stephan Kirchmeyer, Aziz M. Muzafarov, Sergei A. Ponomarenko, Bert de Boer, Paul W. M. Blom, and Dago M. de Leeuw. "Bottom-up organic integrated circuits". In: *Nature* 455 (7215 Oct. 2008), pp. 956–959. ISSN: 0028-0836. DOI: 10.1038/nature07320.

[37] J. Christopher Love, Lara A. Estroff, Jennah K. Kriebel, Ralph G. Nuzzo, and George M. Whitesides. *Self-assembled monolayers of thiolates on metals as a form of nanotechnology*. Vol. 105. 2005, pp. 1103–1169. ISBN: 2172440809. DOI: 10.1021/cr0300789.

[38] Casey W. Miller and Dustin D. Belyea. "The impact of barrier height distributions in tunnel junctions". In: *Journal of Applied Physics* 105 (9 2009), pp. 1–6. ISSN: 00218979. DOI: 10.1063/1.3122600.

[39] David T. Valley, Matthew Onstott, Sergey Malyk, and Alexander V. Benderskii. "Steric hindrance of photoswitching in self-assembled monolayers of azobenzene and alkane thiols". In: *Langmuir* 29 (37 Sept. 2013), pp. 11623–11631. ISSN: 07437463. DOI: 10.1021/LA402144G.

[40] Robert L. Rowell. "Physical Chemistry of Surfaces, 6th ed." In: *Journal of Colloid and Interface Science* 208 (2 1998). ISSN: 00219797. DOI: 10.1006/jcis.1998.5823.

[41] Anna Cattani-Scholz. "Functional Organophosphonate Interfaces for Nanotechnology: A Review". In: *ACS Applied Materials and Interfaces* 9 (31 Aug. 2017), pp. 25643–25655. ISSN: 19448252. DOI: 10.1021/acsami.7b04382.

[42] Ralph G. Nuzzo, Lawrence H. Dubois, and David L. Allara. "Fundamental Studies of Microscopic Wetting on Organic Surfaces. 1. Formation and Structural Characterization of a Self-Consistent Series of Polyfunctional Organic Monolayers". In: *Journal of the American Chemical Society* 112 (2 1990), pp. 558–569. ISSN: 15205126. DOI: 10.1021/JA00158A012.

[43] Abraham Ulman. "Formation and Structure of Self-Assembled Monolayers". In: *Chemical Reviews* 96 (4 Jan. 1996), pp. 1533–1554. ISSN: 0009-2665. DOI: 10.1021/cr9502357.

[44] N. Camillone, P. Eisenberger, T. Y.B. Leung, P. Schwartz, G. Scoles, G. E. Poirier, and M. J. Tarlov. "New monolayer phases of n-alkane thiols self-assembled on Au(111): Preparation, surface characterization, and imaging". In: *The Journal of Chemical Physics* 101 (12 June 1998), p. 11031. ISSN: 0021-9606. DOI: 10.1063/1.467854.

[45] E. Barrena, C. Ocal, and M. Salmeron. "Structure and stability of tilted-chain phases of alkanethiols on Au(111)". In: *The Journal of Chemical Physics* 114 (9 Feb. 2001), p. 4210. ISSN: 0021-9606. DOI: 10.1063/1.1346676.

[46] Mehmet F. Danişman, Loredana Casalis, Gianangelo Bracco, and Giacinto Scoles. "Structural Investigation of Monolayers Prepared by Deposition of (CH3S)2 on the (111) Face of Single-Crystal Gold". In: *Journal of Physical Chemistry B* 106 (45 Nov. 2002), pp. 11771–11777. ISSN: 10895647. DOI: 10.1021/JP0257911.

[47] Frank Schreiber. "Self-assembled monolayers: from simple model systems to biofunctionalized interfaces". In: *Journal of Physics: Condensed Matter* 16 (28 July 2004), R881–R900. ISSN: 0953-8984. DOI: 10.1088/0953-8984/16/28/R01.

[48] Flavio S. Damos, Rita C.S. Luz, and Lauro T. Kubota. "Determination of thickness, dielectric constant of thiol films, and kinetics of adsorption using surface plasmon resonance". In: *Langmuir* 21 (2 Jan. 2005), pp. 602–609. ISSN: 07437463. DOI: 10.1021/LA0487038.

[49] Mirko Prato, Riccardo Moroni, Francesco Bisio, Ranieri Rolandi, Lorenzo Mattera, Ornella Cavalleri, and Maurizio Canepa. "optical characterization of thiolate self-assembled monolayers on au(111)". In: *Journal of Physical Chemistry C* 112 (10 Mar. 2008), pp. 3899–3906. ISSN: 19327447. DOI: 10.1021/jp711194s.

[50] Miao Yu, N. Bovet, Christopher J. Satterley, S. Bengió, Kevin R.J. Lovelock, P. K. Milligan, Robert G. Jones, D. P. Woodruff, and V. Dhanak. "True nature of an archetypal self-assembly system: Mobile Au-thiolate species on Au(111)". In: *Physical Review Letters* 97 (16 Oct. 2006), p. 166102. ISSN: 00319007. DOI: 10.1103/PHYSREVLETT.97.166102/FIGURES/2/MEDIUM.

[51] B.C. Haynie, A.V. Walker, T.B. Tighe, D.L. Allara, and N. Winograd. "Adventures in molecular electronics: how to attach wires to molecules". In: *Applied Surface Science* 203-204 (Jan. 2003), pp. 433–436. ISSN: 01694332. DOI: 10.1016/S0169-4332(02)00695-5.

[52] Colin D. Bain, E. Barry Troughton, Yu Tai Tao, Joseph Evall, George M. Whitesides, and Ralph G. Nuzzo. "Formation of Monolayer Films by the Spontaneous Assembly of Organic Thiols from Solution onto Gold". In: *Journal of the American Chemical Society* 111 (1 1989), pp. 321–335. ISSN: 15205126. DOI: 10.1021/JA00183A049.

[53] Mingji Wang, Kenneth M. Liechti, Qi Wang, and J. M. White. "Self-assembled silane monolayers: Fabrication with nanoscale uniformity". In: *Langmuir* 21 (5 Mar. 2005), pp. 1848–1857. ISSN: 07437463. DOI: 10.1021/LA048483Y.

[54] J. D. Le Grange, J. L. Markham, and C. R. Kurkjian. "Effects of surface hydration on the deposition of silane monolayers on silica". In: *Langmuir* 9 (7 July 1993), pp. 1749–1753. ISSN: 0743-7463. DOI: 10.1021/la00031a023.

[55] M. Auernhammer, S. J. Schoell, M. Sachsenhauser, K.-C. Liao, J. Schwartz, I. D. Sharp, and A. Cattani-Scholz. "Surface functionalization of 6H-SiC using organophosphonate monolayers". In: *Applied Physics Letters* 100 (10 Mar. 2012), p. 101601. ISSN: 0003-6951. DOI: 10.1063/1.3691919.

[56] Peter Thissen, Tatiana Peixoto, Roberto C. Longo, Weina Peng, Wolf Gero Schmidt, Kyeongjae Cho, and Yves J. Chabal. "Activation of Surface Hydroxyl Groups by Modification of H-Terminated Si(111) Surfaces". In: *Journal of the American Chemical Society* 134 (21 May 2012), pp. 8869–8874. ISSN: 0002-7863. DOI: 10.1021/ja300270w.

[57] Anshuma Pathak, Achyut Bora, Kung Ching Liao, Hannah Schmolke, Antje Jung, Claus Peter Klages, Jeffrey Schwartz, and Marc Tornow. "Disorder-derived, strong tunneling attenuation in bis-phosphonate monolayers". In: *Journal of Physics Condensed Matter* 28 (9 2016), p. 94008. ISSN: 1361648X. DOI: 10.1088/0953-8984/28/9/094008.

[58] Michael Eschner, Ralf Frenzel, Frank Simon, Dieter Pleul, Petra Uhlmann, and Hans Jürgen Adler. "ω-substituted long chain alkylphosphonic acids: their synthesis and deposition on metal oxides and subsequent functional group conversion of the deposited compounds". In: *Macromolecular Symposia* 210 (1 Mar. 2004), pp. 77–84. ISSN: 1521-3900. DOI: 10.1002/MASY.200450609.

[59] Alexandros G. Koutsioubas, Nikolaos Spiliopoulos, Dimitris L. Anastassopoulos, Alexandros A. Vradis, and George D. Priftis. "Formation of alkane-phosphonic acid self-assembled monolayers on alumina: an in situ SPR study". In: *Surface and Interface Analysis* 41 (11 Nov. 2009), pp. 897–903. ISSN: 1096-9918. DOI: 10.1002/SIA.3116.

[60] Osama El Zubir, Iain Barlow, Graham J. Leggett, and Nicholas H. Williams. "Fabrication of molecular nanopatterns at aluminium oxide surfaces by nanoshaving of self-assembled monolayers of alkylphosphonates". In: *Nanoscale* 5 (22 Oct. 2013), pp. 11125–11131. ISSN: 20403364. DOI: 10.1039/C3NR04701F.

[61] R. Hofer, M. Textor, and N. D. Spencer. "Alkyl Phosphate Monolayers, Self-Assembled from Aqueous Solution onto Metal Oxide Surfaces". In: *Langmuir* 17 (13 June 2001), pp. 4014–4020. ISSN: 07437463. DOI: 10.1021/LA001756E.

[62] Wei Gao, Lucy Dickinson, Christina Grozinger, Frederick G. Morin, and Linda Reven. "Self-assembled monolayers of alkylphosphonic acids on metal oxides". In: *Langmuir* 12 (26 Dec. 1996), pp. 6429–6435. ISSN: 07437463. DOI: 10.1021/LA9607621.

[63] Florence Brodard-Severac, Gilles Guerrero, Jocelyne Maquet, Pierre Florian, Christel Gervais, and P. Hubert Mutin. "High-field 17O MAS NMR investigation of phosphonic acid monolayers on titania". In: *Chemistry of Materials* 20 (16 Aug. 2008), pp. 5191–5196. ISSN: 08974756. DOI: 10.1021/cm8012683.

[64] G. Guerrero, P. H. Mutin, and A. Vioux. "Anchoring of phosphonate and phosphinate coupling molecules on titania particles". In: *Chemistry of Materials* 13 (11 2001), pp. 4367–4373. ISSN: 08974756. DOI: 10.1021/CM001253U.

[65] Ellen S. Gawalt, Michael J. Avaltroni, Norbert Koch, and Jeffrey Schwartz. "Self-assembly and bonding of alkanephosphonic acids on the native oxide surface of titanium". In: *Langmuir* 17 (19 2001), pp. 5736–5738. ISSN: 07437463. DOI: 10.1021/la010649x.

[66] Stephen Marcinko and Alexander Y. Fadeev. "Hydrolytic stability of organic monolayers supported on TiO2 and ZrO2". In: *Langmuir : the ACS journal of surfaces and colloids* 20 (6 Mar. 2004), pp. 2270–2273. ISSN: 0743-7463. DOI: 10.1021/LA034914L.

[67] Emanuele Smecca, Alessandro Motta, Maria Elena Fragalà, Yana Aleeva, and Guglielmo Guido Condorelli. "Spectroscopic and Theoretical Study of the Grafting Modes of Phosphonic Acids on ZnO Nanorods". In: *The Journal of Physical Chemistry C* 117 (10 Mar. 2013), pp. 5364–5372. ISSN: 1932-7447. DOI: 10.1021/jp308983p.

[68] Dongfang Liu, Wei Wu, Yongfu Qiu, Shihe Yang, Si Xiao, Qu-Quan Wang, Lu Ding, and Jiannong Wang. "Surface Functionalization of ZnO Nanotetrapods with Photoactive and Electroactive Organic Monolayers". In: *Langmuir* 24 (9 May 2008), pp. 5052–5059. ISSN: 0743-7463. DOI: 10.1021/la800074f.

[69] Eric L. Hanson, Jeffrey Schwartz, Bert Nickel, Norbert Koch, and Mehmet Fatih Danisman. "Bonding Self-Assembled, Compact Organophosphonate Monolayers to the Native Oxide Surface of Silicon". In: *Journal of the American Chemical Society* 125 (51 Dec. 2003), pp. 16074–16080. ISSN: 0002-7863. DOI: 10.1021/ja035956z.

[70] Irina Gouzman, Manish Dubey, Michael D. Carolus, Jeffrey Schwartz, and Steven L. Bernasek. "Monolayer vs. multilayer self-assembled alkylphosphonate films: X-ray photoelectron spectroscopy studies". In: *Surface Science* 600 (4 Feb. 2006), pp. 773–781. ISSN: 0039-6028. DOI: 10.1016/J.SUSC.2005.11.030.

[71] Abraham Vega, Peter Thissen, and Yves J. Chabal. "Environment-controlled tethering by aggregation and growth of phosphonic acid monolayers on silicon oxide". In: *Langmuir* 28 (21 May 2012), pp. 8046–8051. ISSN: 07437463. DOI: 10.1021/LA300709N.

[72] A. Bora, A. Pathak, K. C. Liao, M. I. Vexler, A. Kuligk, A. Cattani-Scholz, B. Meinerzhagen, G. Abstreiter, J. Schwartz, and M. Tornow. "Organophosphonates as model system for studying electronic transport through monolayers on {SiO2}/{Si} surfaces". In: *Applied Physics Letters* 102 (24 June 2013), p. 241602. ISSN: 00036951. DOI: 10.1063/1.4811441.

[73] Remi Boissezon, Julien Muller, Vincent Beaugeard, Sophie Monge, and Jean Jacques Robin. *Organophosphonates as anchoring agents onto metal oxide-based materials: Synthesis and applications*. Aug. 2014. DOI: 10.1039/c4ra05414h.

[74] Jeffrey Schwartz, Michael J Avaltroni, Michael P Danahy, Brett M Silverman, Eric L Hanson, Jean E Schwarzbauer, Kim S Midwood, and Ellen S Gawalt. "Cell attachment and spreading on metal implant materials". In: *Materials Science and Engineering: C* 23 (3 Mar. 2003), pp. 395–400. ISSN: 09284931. DOI: 10.1016/S0928-4931(02)00310-7.

[75] P. Hubert Mutin, Gilles Guerrero, and André Vioux. "Hybrid materials from organophosphorus coupling molecules". In: *Journal of Materials Chemistry* 15 (35-36 2005), p. 3761. ISSN: 0959-9428. DOI: 10.1039/b505422b.

[76] L.G. Hector Jr, S.M. Opalka, G.A. Nitowski, L. Wieserman, D.J. Siegel, H. Yu, and J.B. Adams. "Investigation of vinyl phosphonic acid/hydroxylated α-Al2O3 reaction enthalpies". In: *Surface Science* 494 (1 Nov. 2001), pp. 1–20. ISSN: 00396028. DOI: 10.1016/S0039-6028(01)01387-5.

[77] Regina Luschtinetz, Gotthard Seifert, Evelin Jaehne, and Hans Jürgen P. Adler. "Infrared spectra of alkylphosphonic acid bound to aluminium surfaces". In: vol. 254. 2007, pp. 248–253. DOI: 10.1002/masy.200750837.

[78] T. A. Lewington, M. R. Alexander, G. E. Thompson, and E. McAlpine. "Characterisation of alkyl phosphonic acid monolayers self assembled on hydrated surface of aluminium". In: *Surface Engineering* 18 (3 2002), pp. 228–232. ISSN: 02670844. DOI: 10.1179/026708401225005269.

[79] R. D. Ramsier, P. N. Henriksen, and A. N. Gent. "Adsorption of phosphorus acids on alumina". In: *Surface Science* 203 (1-2 Sept. 1988), pp. 72–88. ISSN: 0039-6028. DOI: 10.1016/0039-6028(88)90195-1.

[80] Vincent Lafond, Christel Gervais, Jocelyne Maquet, Daniel Prochnow, Florence Babonneau, and P. Hubert Mutin. "17 O MAS NMR Study of the Bonding Mode of Phosphonate Coupling Molecules in a Titanium Oxo-Alkoxo-Phosphonate and in Titania-Based Hybrid Materials". In: *Chem. Mater.* 15 (21 2003), pp. 4098–4103.

[81] Pavel B. Paramonov, Sergio A. Paniagua, Peter J. Hotchkiss, Simon C. Jones, Neal R. Armstrong, Seth R. Marder, and Jean-Luc Brédas. "Theoretical Characterization of the Indium Tin Oxide Surface and of Its Binding Sites for Adsorption of Phosphonic Acid Monolayers". In: *Chemistry of Materials* 20 (16 Aug. 2008), pp. 5131–5133. ISSN: 0897-4756. DOI: 10.1021/cm8014622.

[82] Frank Schreiber. "Structure and growth of self-assembling monolayers". In: *Progress in Surface Science* 65 (5-8 Nov. 2000), pp. 151–257. ISSN: 0079-6816. DOI: 10.1016/S0079-6816(00)00024-1.

[83] Daniel O. Hutchins, Orb Acton, Tobias Weidner, Nathan Cernetic, Joe E. Baio, David G. Castner, Hong Ma, and Alex K.-Y. Jen. "Solid-state densification of spun-cast self-assembled monolayers for use in ultra-thin hybrid dielectrics". In: *Applied Surface Science* 261 (Nov. 2012), pp. 908–915. ISSN: 01694332. DOI: 10.1016/j.apsusc.2012.09.013.

[84] Peter Thissen, Markus Valtiner, and Guido Grundmeier. "Stability of Phosphonic Acid Self-Assembled Monolayers on Amorphous and Single-Crystalline Aluminum Oxide Surfaces in Aqueous Solution". In: *Langmuir* 26 (1 Jan. 2010), pp. 156–164. ISSN: 0743-7463. DOI: 10.1021/la900935s.

[85] Xianglong Wan, Itai Lieberman, Andika Asyuda, Sebastian Resch, Henning Seim, Peer Kirsch, and Michael Zharnikov. "Thermal Stability of Phosphonic Acid Self-Assembled Monolayers on Alumina Substrates". In: *Journal of Physical Chemistry C* 124 (4 Jan. 2020), pp. 2531–2542. ISSN: 19327455. DOI: 10.1021/ACS.JPCC.9B10628.

[86] Clemence Queffelec, Marc Petit, Pascal Janvier, D. Andrew Knight, and Bruno Bujoli. "Surface modification using phosphonic acids and esters". In: *Chemical Reviews* 112 (7 July 2012), pp. 3777–3807. ISSN: 00092665. DOI: 10.1021/CR2004212.

[87] Bernhard Mann and Hans Kuhn. "Tunneling through Fatty Acid Salt Monolayers". In: *Journal of Applied Physics* 42 (11 Oct. 1971), pp. 4398–4405. ISSN: 0021-8979. DOI: 10.1063/1.1659785.

[88] Elena Gorenskaia, Kelly L. Turner, Santiago Martin, Pilar Cea, and Paul J. Low. "Fabrication of metallic and non-metallic top electrodes for large-area molecular junctions". In: *Nanoscale* (2021). ISSN: 2040-3364. DOI: 10.1039/d1nr00917f.

[89] Sabyasachi Mukhopadhyay, Sidney R. Cohen, Debora Marchak, Noga Friedman, Israel Pecht, Mordechai Sheves, and David Cahen. "Nanoscale electron transport and photodynamics enhancement in lipid-depleted bacteriorhodopsin monomers". In: *ACS nano* 8 (8 Aug. 2014), pp. 7714–7722. ISSN: 1936-086X. DOI: 10.1021/NN500202K.

[90] D. J. Wold and C. D. Frisbie. "Fabrication and Characterization of Metal-Molecule-Metal Junctions by Conducting Probe Atomic Force Microscopy". In: *Journal of the American Chemical Society* 123 (23 2001), pp. 5549–5556. ISSN: 00027863. DOI: 10.1021/JA0101532.

[91] X. D. Cui, A. Primak, X. Zarate, J. Tomfohr, O. F. Sankey, A. L. Moore, T. A. Moore, D. Gust, G. Harris, and S. M. Lindsay. "Reproducible measurement of single-molecule conductivity". In: *Science (New York, N.Y.)* 294 (5542 Oct. 2001), pp. 571–574. ISSN: 0036-8075. DOI: 10.1126/SCIENCE.1064354.

[92] X. D. Cui, X. Zarate, J. Tomfohr, O. F. Sankey, A. Primak, A. L. Moore, T. A. Moore, D. Gust, G. Harris, and S. M. Lindsay. "Making electrical contacts to molecular monolayers". In: *Nanotechnology* 13 (1 Feb. 2002), pp. 5–14. ISSN: 0957-4484. DOI: 10.1088/0957-4484/13/1/302.

[93] E. P. Honig. "D.C. conduction in Langmuir-Blodgett films with various electrode materials". In: *Thin Solid Films* 33 (2 Apr. 1976), pp. 231–236. ISSN: 0040-6090. DOI: 10.1016/0040-6090(76)90083-3.

[94] Yoram Selzer, Adi Salomon, and David Cahen. "The Importance of Chemical Bonding to the Contact for Tunneling through Alkyl Chains". In: *Journal of Physical Chemistry B* 106 (40 Oct. 2002), pp. 10432–10439. ISSN: 10895647. DOI: 10.1021/JP026324M.

[95] Yoram Selzer, Adi Salomon, Jamal Ghabboun, and David Cahen. "Voltage-driven changes in molecular dipoles yield negative differential resistance at room temperature". In: *Angewandte Chemie - International Edition* 41 (5 Mar. 2002), pp. 827–830. ISSN: 14337851. DOI: 10.1002/1521-3773(20020301)41:5<827::AID-ANIE827>3.0.CO;2-N.

[96] Nobuhiro Gemma, Koichi Mizushima, Akira Miura, and Makoto Azuma. "The transport mechanism of stearic acid LB films on metal and semiconductor substrates". In: *Synthetic Metals* 18 (1-3 Feb. 1987), pp. 809–814. ISSN: 0379-6779. DOI: 10.1016/0379-6779(87)90983-0.

[97] S. Sha, T. Hisatsune, T. Moriizumi, K. Ogawa, H. Tamura, N. Mino, Y. Okahata, and K. Ariga. "Electrical evaluation of ultrathin organic films on solid substrates". In: *Thin Solid Films* 179 (1-2 Nov. 1989), pp. 277–282. ISSN: 0040-6090. DOI: 10.1016/0040-6090(89)90194-6.

[98] Michael D. Dickey, Ryan C. Chiechi, Ryan J. Larsen, Emily A. Weiss, David A. Weitz, and George M. Whitesides. "Eutectic Gallium-Indium (EGaIn): A Liquid Metal Alloy for the Formation of Stable Structures in Microchannels at Room Temperature". In: *Advanced Functional Materials* 18 (7 Apr. 2008), pp. 1097–1104. ISSN: 1616301X. DOI: 10.1002/adfm.200701216.

[99] Ryan C. Chiechi, Emily A. Weiss, Michael D. Dickey, and G.M. Whitesides. "Eutectic Gallium-Indium (EGaIn): A Moldable Liquid Metal for Electrical Characterization of Self-Assembled Monolayers". In: *Angewandte Chemie International Edition* 47 (1 Jan. 2008), pp. 142–144. ISSN: 14337851. DOI: 10.1002/anie.200703642.

[100] Christian A. Nijhuis, William F. Reus, Jabulani R. Barber, Michael D. Dickey, and George M. Whitesides. "Charge transport and rectification in arrays of SAM-based tunneling junctions". In: *Nano letters* 10 (9 Sept. 2010), pp. 3611–3619. ISSN: 1530-6992. DOI: 10.1021/NL101918M.

[101] Henrry M. Osorio, Pilar Cea, Luz M. Ballesteros, Ignacio Gascón, Santiago Marqués-González, Richard J. Nichols, Francesc Pérez-Murano, Paul J. Low, and Santiago Martín. "Preparation of nascent molecular electronic devices from gold nanoparticles and terminal alkyne functionalised monolayer films". In: *Journal of Materials Chemistry C* 2 (35 Aug. 2014), pp. 7348–7355. ISSN: 2050-7534. DOI: 10.1039/C4TC01080A.

[102] Evangelina Pensa, Emiliano Cortés, Gastón Corthey, Pilar Carro, Carolina Vericat, Mariano H. Fonticelli, Guillermo Benítez, Aldo A. Rubert, and Roberto C. Salvarezza. "The chemistry of the sulfur-gold interface: in search of a unified model". In: *Accounts of chemical research* 45 (8 Aug. 2012), pp. 1183–1192. ISSN: 1520-4898. DOI: 10.1021/AR200260P.

[103] Masato M. Maitani, David L. Allara, Douglas A.A. Ohlberg, Zhiyong Li, R. Stanley Williams, and Duncan R. Stewart. "High integrity metal/organic device interfaces via low temperature buffer layer assisted metal atom nucleation". In: *Applied Physics Letters* 96 (17 Apr. 2010), p. 173109. ISSN: 0003-6951. DOI: 10.1063/1.3377044.

[104] Gabriel Puebla-hellmann, Koushik Venkatesan, Marcel Mayor, and Emanuel Lörtscher. "Metallic nanoparticle contacts for high-yield, ambient-stable molecular-monolayer devices". In: *Nature* (2018). ISSN: 1476-4687. DOI: 10.1038/s41586-018-0275-z.

[105] Luz M. Ballesteros, Santiago Martín, Javier Cortés, Santiago Marqués-González, Francesc Pérez-Murano, Richard J. Nichols, Paul J. Low, and Pilar Cea. "From an Organometallic Monolayer to an Organic Monolayer Covered by Metal Nanoislands: A Simple Thermal Protocol for the Fabrication of the Top Contact Electrode in Molecular Electronic Devices". In: *Advanced Materials Interfaces* 1 (9 Dec. 2014), p. 1400128. ISSN: 2196-7350. DOI: 10.1002/ADMI.201400128.

[106] Ruben Ezquerra, Samantha G. Eaves, Sören Bock, Brian W. Skelton, Francesc Pérez-Murano, Pilar Cea, Santiago Martín, and Paul J. Low. "New routes to organometallic molecular junctions via a simple thermal processing protocol". In: *Journal of Materials Chemistry C* 7 (22 June 2019), pp. 6630–6640. ISSN: 2050-7534. DOI: 10.1039/C9TC01305A.

[107] W. F. Van Dorp and C. W. Hagen. "A critical literature review of focused electron beam induced deposition". In: *Journal of Applied Physics* 104 (8 Oct. 2008), p. 081301. ISSN: 0021-8979. DOI: 10.1063/1.2977587.

[108] Soraya Sangiao, Santiago Martín, Alejandro González-Orive, César Magén, Paul J. Low, José M. De Teresa, and Pilar Cea. "All-Carbon Electrode Molecular Electronic Devices Based on Langmuir-Blodgett Monolayers". In: *Small* 13 (7 Feb. 2017), p. 1603207. ISSN: 1613-6829. DOI: 10.1002/SMLL.201603207.

[109] Amin Morteza Najarian, Akhtar Bayat, and Richard L. McCreery. "Orbital control of photocurrents in large area all-carbon molecular junctions". In: *Journal of the American Chemical Society* 140 (5 Feb. 2018), pp. 1900–1909. ISSN: 15205126. DOI: 10.1021/JACS.7B12577.

[110] Paul A. Van Hal, Edsger C. P. Smits, Tom C. T. Geuns, Hylke B. Akkerman, Bianca C. De Brito, Stefano Perissinotto, Guglielmo Lanzani, Auke J. Kronemeijer, Victor Geskin, Jerome Cornil, Paul W. M. Blom, Bert De Boer, and Dago M. De Leeuw. "Upscaling, integration and electrical characterization of molecular junctions". In: *Nature Nanotechnology* 3 (12 Dec. 2008), pp. 749–754. ISSN: 1748-3387. DOI: 10.1038/nnano.2008.305.

[111] Alexander B. Neuhausen, Ali Hosseini, Joseph A. Sulpizio, Christopher E.D. Chidsey, and David Goldhaber-Gordon. "Molecular junctions of self-assembled monolayers with conducting polymer contacts". In: *ACS Nano* 6 (11 2012), pp. 9920–9931. ISSN: 19360851. DOI: 10.1021/nn3035183.

[112] Hylke B. Akkerman, Paul W M Blom, Dago M. De Leeuw, and Bert De Boer. "Towards molecular electronics with large-area molecular junctions". In: *Nature* 441 (1 2006), pp. 69–72. ISSN: 14764687. DOI: 10.1038/nature04699.

[113] Hylke B. Akkerman, Ronald C.G. Naber, Bert Jongbloed, Paul A. Van Hal, Paul W.M. Blom, Dago M. De Leeuw, and Bert De Boer. "Electron tunneling through alkanedithiol self-assembled monolayers in large-area molecular junctions". In: *Proceedings of the National Academy of Sciences of the United States of America* 104 (27 2007), pp. 11161–11166. ISSN: 00278424. DOI: 10.1073/pnas.0701472104.

[114] Gunuk Wang, Hana Yoo, Seok In Na, Tae Wook Kim, Byungjin Cho, Dong Yu Kim, and Takhee Lee. "Electrical conduction through self-assembled monolayers in molecular junctions: Au/molecules/Au versus Au/molecule/PEDOT:PSS/Au". In: *Thin Solid Films* 518 (2 Nov. 2009), pp. 824–828. ISSN: 0040-6090. DOI: 10.1016/J.TSF.2009.07.094.

[115] A. M. Nardes, M. Kemerink, and R. A.J. Janssen. "Anisotropic hopping conduction in spin-coated PEDOT:PSS thin films". In: *Physical Review B - Condensed Matter and Materials Physics* 76 (8 Aug. 2007), p. 085208. ISSN: 10980121. DOI: 10.1103/PHYSREVB.76.085208/FIGURES/6/MEDIUM.

[116] Michael J. Preiner and Nicholas A. Melosh. "Creating large area molecular electronic junctions using atomic layer deposition". In: *Applied Physics Letters* 92 (21 2008), pp. 1–4. ISSN: 00036951. DOI: 10.1063/1.2917870.

[117] Sameer Patwardhan, Duyen H. Cao, George C. Schatz, and Alex B.F. Martinson. "Atomic Layer Deposition Nucleation on Isolated Self-Assembled Monolayer Functional Groups: A Combined DFT and Experimental Study". In: *ACS Applied Energy Materials* 2 (7 July 2019), pp. 4618–4628. ISSN: 25740962. DOI: 10.1021/acsaem.8b02202.

[118] Ayelet Vilan. "Analyzing molecular current-voltage characteristics with the Simmons tunneling model: Scaling and linearization". In: *Journal of Physical Chemistry C* 111 (11 2007), pp. 4431–4444. ISSN: 19327447. DOI: 10.1021/jp066846s.

[119] A. Vilan. "Revealing tunnelling details by normalized differential conductance analysis of transport across molecular junctions". In: *Phys. Chem. Chem. Phys.* 19 (2017), pp. 27166–27172. ISSN: 1463-9076. DOI: 10.1039/C7CP05536F.

[120] Emily A. Weiss, Jennah K. Kriebel, Maria Anita Rampi, and George M. Whitesides. "The study of charge transport through organic thin films: mechanism, tools and applications". In: *Philosophical transactions. Series A, Mathematical, physical, and engineering sciences* 365 (1855 June 2007), pp. 1509–1537. ISSN: 1364-503X. DOI: 10.1098/RSTA.2007.2029.

[121] Alvar R. Garrigues, Lejia Wang, Enrique Del Barco, and Christian A. Nijhuis. "Electrostatic control over temperature-dependent tunnelling across a single-molecule junction". In: *Nature Communications 2016 7:1* 7 (1 May 2016), pp. 1–7. ISSN: 2041-1723. DOI: 10.1038/ncomms11595.

[122] Julie Bonkerud, Christian Zimmermann, Philip Michael Weiser, Lasse Vines, and Eduard V. Monakhov. "On the permittivity of titanium dioxide". In: *Scientific Reports 2021 11:1* 11 (1 June 2021), pp. 1–5. ISSN: 2045-2322. DOI: 10.1038/s41598-021-92021-5.

[123] Elias Burstein. *Tunneling Phenomena in Solids*. Springer US, 1969. DOI: 10.1007/978-1-4684-1752-4.

[124] John G. Simmons. "Generalized Formula for the Electric Tunnel Effect between Similar Electrodes Separated by a Thin Insulating Film". In: *Journal of Applied Physics* 34 (6 June 1963), pp. 1793–1803. ISSN: 00218979. DOI: 10.1063/1.1702682.

[125] William F. Reus, Christian A. Nijhuis, Jabulani R. Barber, Martin M. Thuo, Simon Tricard, and George M. Whitesides. "Statistical tools for analyzing measurements of charge transport". In: *Journal of Physical Chemistry C* 116 (11 Mar. 2012), pp. 6714–6733. ISSN: 19327447. DOI: 10.1021/JP210445Y.

[126] Christian A. Nijhuis, William F. Reus, Jabulani R. Barber, and George M. Whitesides. "Comparison of SAM-based junctions with Ga 2O 3/EGaIn top electrodes to other large-area tunneling junctions". In: *Journal of Physical Chemistry C* 116 (26 July 2012), pp. 14139–14150. ISSN: 19327447. DOI: 10.1021/JP303072A.

[127] Emily A. Weiss, Ryan C. Chiechi, George K. Kaufman, Jennah K. Kriebel, Zhefeng Li, Marco Duati, Maria A. Rampi, and George M. Whitesides. "Influence of defects on the electrical characteristics of mercury-drop

junctions: Self-assembled monolayers of n-alkanethiolates on rough and smooth silver". In: *Journal of the American Chemical Society* 129 (14 Apr. 2007), pp. 4336–4349. ISSN: 00027863. DOI: 10.1021/JA0677261.

[128] R. E. Holmlin, R. Haag, M. L. Chabinyc, R. F. Ismagilov, A. E. Cohen, A. Terfort, M. A. Rampi, and G. M. Whitesides. "Electron transport through thin organic films in metal-insulator-metal junctions based on self-assembled monolayers". In: *Journal of the American Chemical Society* 123 (21 2001), pp. 5075–5085. ISSN: 0002-7863. DOI: 10.1021/JA004055C.

[129] Felice Carlo Simeonea and Maria Anita Rampiab. "Test-beds for Molecular Electronics: Metal-Molecules-Metal Junctions Based on Hg Electrodes". In: *CHIMIA* 64 (6 June 2010), p. 362. ISSN: 0009-4293. DOI: 10.2533/chimia.2010.362.

[130] Yannick J. Dappe. "Attenuation factors in molecular electronics: Some theoretical concepts". In: *Applied Sciences (Switzerland)* 10 (18 Sept. 2020), pp. 1–18. ISSN: 20763417. DOI: 10.3390/APP10186162.

[131] Felice C. Simeone, Hyo Jae Yoon, Martin M. Thuo, Jabulani R. Barber, Barbara Smith, and George M. Whitesides. "Defining the value of injection current and effective electrical contact area for egain-based molecular tunneling junctions". In: *Journal of the American Chemical Society* 135 (48 2013), pp. 18131–18144. ISSN: 00027863. DOI: 10.1021/ja408652h.

[132] W. F. Brinkman, R. C. Dynes, and J. M. Rowell. "Tunneling conductance of asymmetrical barriers". In: *Journal of Applied Physics* 41 (5 1970), pp. 1915–1921. ISSN: 00218979. DOI: 10.1063/1.1659141.

[133] A. Gruverman, D. Wu, H. Lu, Y. Wang, H. W. Jang, C. M. Folkman, M. Ye Zhuravlev, D. Felker, M. Rzchowski, C. B. Eom, and E. Y. Tsymbal. "Tunneling electroresistance effect in ferroelectric tunnel junctions at the nanoscale". In: *Nano letters* 9 (10 Oct. 2009), pp. 3539–3543. ISSN: 1530-6992. DOI: 10.1021/NL901754T.

[134] Michael Gärtner, Eric Sauter, Giulia Nascimbeni, Andreas Petritz, Adrian Wiesner, Martin Kind, Tarek Abu-Husein, Michael Bolte, Barbara Stadlober, Egbert Zojer, Andreas Terfort, and Michael Zharnikov. "Understanding the Properties of Tailor-Made Self-Assembled Monolayers with Embedded Dipole Moments for Interface Engineering". In: *Journal of Physical Chemistry C* 122 (50 Dec. 2018), pp. 28757–28774. ISSN: 19327455. DOI: 10.1021/ACS.JPCC.8B09440.

[135] Andrii Kovalchuk, Tarek Abu-Husein, Davide Fracasso, David A. Egger, Egbert Zojer, Michael Zharnikov, Andreas Terfort, and Ryan C. Chiechi. "Transition voltages respond to synthetic reorientation of embedded dipoles in self-assembled monolayers". In: *Chemical Science* 7 (1 2016), pp. 781–787. ISSN: 20416539. DOI: 10.1039/c5sc03097h.

[136] Andrii Kovalchuk, David A. Egger, Tarek Abu-Husein, Egbert Zojer, Andreas Terfort, and Ryan C. Chiechi. "Dipole-induced asymmetric conduction in tunneling junctions comprising self-assembled monolayers". In: *RSC Advances* 6 (73 2016), pp. 69479–69483. ISSN: 20462069. DOI: 10.1039/c6ra10471a.

[137] Bert De Boer, Afshin Hadipour, M. Magdalena Mandoc, Teunis Van Woudenbergh, and Paul W.M. Blom. "Tuning of Metal Work Functions with Self-Assembled Monolayers". In: *Advanced Materials* 17 (5 Mar. 2005), pp. 621–625. ISSN: 1521-4095. DOI: 10.1002/ADMA.200401216.

[138] Hisao Ishii, Kiyoshi Sugiyama, Eisuke Ito, and Kazuhiko Seki. "Energy Level Alignment and Interfacial Electronic Structures at Organic/Metal and Organic/Organic Interfaces". In: *Advanced Materials* 11 (8 1999). <m:note><m:bold>From Duplicate 2 (</m:bold><m:bold><m:italic>Energy Level Alignment and Interfacial Electronic Structures at Organic/Metal and Organic/Organic Interfaces</m:italic></m:bold><m:bold> - Ishii, Hisao; Sugiyama, Kiyoshi; Ito, Eisuke; Seki, Kazuhiko)<m:linebreak/></m:bold><m:linebreak/><m:linebreak/><m:linebreak/></m:note>, pp. 605–625. ISSN: 1521-4095.

[139] Andika Asyuda, Michael Gärtner, Xianglong Wan, Ines Burkhart, Torben Saßmannshausen, Andreas Terfort, and Michael Zharnikov. "Self-Assembled Monolayers with Embedded Dipole Moments for Work Function Engineering of Oxide Substrates". In: *The Journal of Physical Chemistry C* 124 (16 Apr. 2020), pp. 8775–8785. ISSN: 1932-7447. DOI: 10.1021/acs.jpcc.0c00482.

[140] Xiaoping Chen, Hongting Hu, Jorge Trasobares, and Christian A. Nijhuis. "Rectification Ratio and Tunneling Decay Coefficient Depend on the Contact Geometry Revealed by in Situ Imaging of the Formation of EGaIn Junctions". In: *ACS Applied Materials and Interfaces* 11 (23 2019), pp. 21018–21029. ISSN: 19448252. DOI: 10.1021/acsami.9b02033.

[141] José M. Soler, Emilio Artacho, Julian D. Gale, Alberto García, Javier Junquera, Pablo Ordejón, and Daniel Sánchez-Portal. "The SIESTA method for ab initio order-N materials simulation". In: *Journal of Physics: Condensed Matter* 14 (11 Mar. 2002), p. 2745. ISSN: 0953-8984. DOI: 10.1088/0953-8984/14/11/302.

[142] Carlos Fiolhais, Miguel A. L. Marques, and Fernando Nogueira, eds. *A Primer in Density Functional Theory*. 1st ed. Vol. 1. Springer-Verlag Berlin Heidelberg, 2003.

[143] P. J. Stephens, F. J. Devlin, C. F. Chabalowski, and M. J. Frisch. "Ab Initio Calculation of Vibrational Absorption and Circular Dichroism Spectra Using Density Functional Force Fields". In: *The Journal of Physical Chemistry* 98 (45 Nov. 1994), pp. 11623–11627. ISSN: 0022-3654. DOI: 10.1021/j100096a001.

[144] Chengteh Lee, Weitao Yang, and Robert G. Parr. “Development of the Colle-Salvetti correlation-energy formula into a functional of the electron density”. In: *Physical Review B* 37 (2 Jan. 1988), pp. 785–789. ISSN: 0163-1829. DOI: 10.1103/PhysRevB.37.785.

[145] A. D. Becke. “Density-functional exchange-energy approximation with correct asymptotic behavior”. In: *Physical Review A* 38 (6 Sept. 1988), pp. 3098–3100. ISSN: 0556-2791. DOI: 10.1103/PhysRevA.38.3098.

[146] Axel D. Becke. “Density-functional thermochemistry. III. The role of exact exchange”. In: *The Journal of Chemical Physics* 98 (7 Apr. 1993), pp. 5648–5652. ISSN: 0021-9606. DOI: 10.1063/1.464913.

[147] M. Paulsson. “Non Equilibrium Green’s Functions for Dummies: Introduction to the One Particle NEGF equations”. In: (Oct. 2002). DOI: 10.48550/arxiv.cond-mat/0210519.

[148] Kurt Stokbro, Jeremy Taylor, Mads Brandbyge, and Pablo Ordejón. “TranSIESTA: a spice for molecular electronics”. In: *Annals of the New York Academy of Sciences* 1006 (2003), pp. 212–226. ISSN: 0077-8923. DOI: 10.1196/ANNALS.1292.014.

[149] Nick Papior, Nicolás Lorente, Thomas Frederiksen, Alberto García, and Mads Brandbyge. “Improvements on non-equilibrium and transport Green function techniques: The next-generation transiesta”. In: *Computer Physics Communications* 212 (Mar. 2017), pp. 8–24. ISSN: 0010-4655. DOI: 10.1016/J.CPC.2016.09.022.

[150] Eric Paquet and Herna L. Viktor. “Molecular dynamics, monte carlo simulations, and langevin dynamics: A computational review”. In: *BioMed Research International* 2015 (2015). ISSN: 23146141. DOI: 10.1155/2015/183918.

[151] Daan Frenkel and Berend Smit. *Understanding Molecular Simulation*. Elsevier, 2002. ISBN: 9780122673511. DOI: 10.1016/B978-0-12-267351-1.X5000-7.

[152] Andrew Leach. *Molecular Modelling - Principles and Applications*. 2nd ed. 2001.

[153] L. Martinez, R. Andrade, E. G. Birgin, and J. M. Martínez. “PACKMOL: a package for building initial configurations for molecular dynamics simulations”. In: *Journal of computational chemistry* 30 (13 2009), pp. 2157–2164. ISSN: 1096-987X. DOI: 10.1002/JCC.21224.

[154] Julian Matthias Dlugosch, Henning Seim, Achyut Bora, Takuya Kamiyama, Itai Lieberman, Falk May, Florian Müller-Plathe, Alexei Nefedov, Saurav Prasad, Sebastian Resch, Kai Saller, Christian Seim, Maximilian Speckbacher, Frank Voges, Marc Tornow, and Peer Kirsch. “Conductance Switching in Liquid Crystal-Inspired Self-Assembled Monolayer Junctions”. In: *ACS Applied Materials & Interfaces* 14.27 (2022). PMID: 35776551, pp. 31044–31053. DOI: 10.1021/acsami.2c05264.

[155] G. Binnig, C. F. Quate, and Ch. Gerber. “Atomic Force Microscope”. In: *Physical Review Letters* 56 (9 Mar. 1986), pp. 930–933. ISSN: 0031-9007. DOI: 10.1103/PhysRevLett.56.930.

[156] Dror Sarid. “Review of scanning force microscopy”. In: *Journal of Vacuum Science &Technology B: Microelectronics and Nanometer Structures* 9 (2 Mar. 1991), p. 431. ISSN: 0734211X. DOI: 10.1116/1.585585.

[157] Bruker Corporation. “Bruker Dimension V - Instruction Manual”. 2011.

[158] Eugene Hecht. *Optik*. De Gruyter, Dec. 2018. ISBN: 9783110526653. DOI: 10.1515/9783110526653.

[159] Douglas B. Murphy and Michael W. Davidson. *Fundamentals of Light Microscopy and Electronic Imaging*. John Wiley & Sons, Inc., Sept. 2012. ISBN: 9781118382905. DOI: 10.1002/9781118382905.

[160] David B. Williams and C. Barry Carter. *Transmission Electron Microscopy*. Springer Science+Business Media New York, 1996. ISBN: 978-0-306-45324-3. DOI: 10.1007/978-1-4757-2519-3.

[161] Rainer Waser. “Nanoelectronics and Information Technology”. In: *Nanoelectronics and Information Technology* (2012). ISSN: 3527409270.

[162] William A. McGahan, Blaine Johs, and John A. Woollam. “Techniques for ellipsometric measurement of the thickness and optical constants of thin absorbing films”. In: *Thin Solid Films* 234 (1-2 Oct. 1993), pp. 443–446. ISSN: 00406090. DOI: 10.1016/0040-6090(93)90303-7.

[163] Karsten Hinrichs, Klaus Jochen Eichhorn, Gerhard Ertl, Douglas L. Mills, and Hans Lüth. *Ellipsometry of Functional Organic Surfaces and Films*. Vol. 52. 2014. ISBN: 9783642401275. DOI: 10.1007/978-3-642-40128-2.

[164] C. M. Herzinger, B. Johs, W. A. McGahan, J. A. Woollam, and W. Paulson. “Ellipsometric determination of optical constants for silicon and thermally grown silicon dioxide via a multi-sample, multi-wavelength, multi-angle investigation”. In: *Journal of Applied Physics* 83 (6 1998), pp. 3323–3336. ISSN: 00218979. DOI: 10.1063/1.367101.

[165] J.A. Woollam Co. “CompleteEase Software Manual, Version 4.63”. In: (2011).

[166] Terri Lichtenstein. *Handbook of Thin Film Materials*. College of Engineering and Applied Science, University of Rochester, 1979.

[167] Abraham Ulmann, ed. *An Introduction to Ultrathin Organic Films: From Langmuir-Blodgett to Self-Assembly*. Elsevier, 1991. ISBN: 9780080926315. DOI: 10.1016/C2009-0-22306-3.

[168] Maria Losurdo, Michael Bergmair, Giovanni Bruno, Denis Cattelan, Christoph Cobet, Antonello De Martino, Karsten Fleischer, Zorana Dohcevic-mitrovic Norbert, Esser Melanie, Kurt Hingerl, and Josef Humlicek. “Spectroscopic ellipsometry and polarimetry for materials and systems analysis at the nanometer scale : state-of-the-art , potential , and perspectives”. In: (2009), pp. 1521–1554. DOI: 10.1007/s11051-009-9662-6.

[169] Maurizio Canepa, Giulia Maidecchi, Chiara Toccafondi, Ornella Cavalleri, Mirko Prato, Vijay Chaudhari, and Vladimir A. Esaulov. "Spectroscopic ellipsometry of self assembled monolayers: Interface effects. the case of phenyl selenide SAMs on gold". In: *Physical Chemistry Chemical Physics* 15 (27 2013), pp. 11559–11565. ISSN: 14639076. DOI: 10.1039/c3cp51304a.

[170] Mirko Prato, Riccardo Moroni, Francesco Bisio, Ranieri Rolandi, Lorenzo Mattera, Ornella Cavalleri, and Maurizio Canepa. "Optical Characterization of Thiolate Self-Assembled Monolayers on Au (111)". In: (111 2008), pp. 3899–3906. DOI: 10.1021/jp711194s.

[171] J.N. Hilfiker, B. Johs, C.M. Herzinger, J.F. Elman, E. Montbach, D. Bryant, and P.J. Bos. "Generalized spectroscopic ellipsometry and Mueller-matrix study of twisted nematic and super twisted nematic liquid crystals". In: *Thin Solid Films* 455-456 (May 2004), pp. 596–600. ISSN: 00406090. DOI: 10.1016/j.tsf.2004.01.031.

[172] Kazuya Goda, Yasuo Toko, Ryouhei Takahashi, Taiju Takahashi, Munehiro Kimura, and Tadashi Akahane. "Characterization of bistable hybrid-twisted nematic liquid crystal mode by means of renormalized transmission spectroscopic ellipsometry". In: *Japanese Journal of Applied Physics* 50 (5 PART 1 May 2011), p. 056601. ISSN: 00214922. DOI: 10.1143/JJAP.50.056601/XML.

[173] Hans Kuzmany. *Solid-state spectroscopy: An introduction*. Springer Berlin Heidelberg, 2009, pp. 1–554. ISBN: 9783642014789. DOI: 10.1007/978-3-642-01479-6.

[174] R. A. MacPhail, H. L. Strauss, R. G. Snyder, and C. A. Elliger. "Carbon-hydrogen stretching modes and the structure of n-alkyl chains." In: *The Journal of Physical Chemistry* 88 (3 Feb. 1984), pp. 334–341. ISSN: 0022-3654. DOI: 10.1021/j150647a002.

[175] R.G. Snyder and H.L. Strauss. "C-H Stretching Modes and the Structure of n-Alkyl Chains". In: *J. Phys.Chem* 86 (1982), pp. 5145–5150.

[176] John Coates. "Interpretation of Infrared Spectra, A Practical Approach". In: *Encyclopedia of Analytical Chemistry* (2006), pp. 10815–10837. DOI: 10.1002/9780470027318.a5606.

[177] John T. Reilly, John M. Walsh, Michael L. Greenfield, and Marc D. Donohue. "Analysis of FT-IR spectroscopic data: The Voigt profile". In: *Spectrochimica Acta Part A: Molecular Spectroscopy* 48 (10 1992), pp. 1459–1479. ISSN: 05848539. DOI: 10.1016/0584-8539(92)80154-O.

[178] Tery L. Barr. *Modern ESCA*. CRC Press, Nov. 2020. ISBN: 9781003069041. DOI: 10.1201/9781003069041.

[179] Michael C. Burrell and John J. Chera. "Charge correction of the binding energy scale in XPS analysis of polymers using surface deposition of PDMS". In: *Surface and Interface Analysis* 27 (9 Sept. 1999), pp. 811–815. ISSN: 0142-2421. DOI: 10.1002/(SICI)1096-9918(199909)27:9<811::AID-SIA636>3.0.CO;2-W.

[180] M. P. Seah and W. A. Dench. "Quantitative electron spectroscopy of surfaces: A standard data base for electron inelastic mean free paths in solids". In: *Surface and Interface Analysis* 1 (1 Feb. 1979), pp. 2–11. ISSN: 0142-2421. DOI: 10.1002/sia.740010103.

[181] John F. Watts and John Wolstenholme. *An Introduction to Surface Analysis by XPS and AES*. John Wiley & Sons, Ltd, Mar. 2003. ISBN: 9780470867938. DOI: 10.1002/0470867930.

[182] Paul E. Laibinis, Colin D. Bain, and George M. Whitesides. "Attenuation of photoelectrons in monolayers of n-alkanethiols adsorbed on copper, silver, and gold". In: *The Journal of Physical Chemistry* 95 (18 Sept. 1991), pp. 7017–7021. ISSN: 0022-3654. DOI: 10.1021/j100171a054.

[183] Xavier Wallart, Catherine Henry de Villeneuve, and Philippe Allongue. "Truly Quantitative XPS Characterization of Organic Monolayers on Silicon: Study of Alkyl and Alkoxy Monolayers on H-Si(111)". In: *Journal of the American Chemical Society* 127 (21 June 2005), pp. 7871–7878. ISSN: 0002-7863. DOI: 10.1021/ja0430797.

[184] Gianangelo Bracco and Bodil Holst, eds. *Surface Science Techniques*. Vol. 51. Springer Berlin Heidelberg, 2013. ISBN: 978-3-642-34242-4. DOI: 10.1007/978-3-642-34243-1.

[185] Joachim Stöhr. *NEXAFS Spectroscopy*. Vol. 25. Springer Berlin Heidelberg, 1992. ISBN: 978-3-642-08113-2. DOI: 10.1007/978-3-662-02853-7.

[186] Jinxuan Liu, Björn Schüpbach, Asif Bashir, Osama Shekhah, Alexei Nefedov, Martin Kind, Andreas Terfort, and Christof Wöll. "Structural characterization of self-assembled monolayers of pyridine-terminated thiolates on gold". In: *Physical Chemistry Chemical Physics* 12 (17 2010), p. 4459. ISSN: 1463-9076. DOI: 10.1039/b924246p.

[187] Christoph Partes, Eric Sauter, Michael Gärtner, Martin Kind, Andika Asyuda, Michael Bolte, Michael Zharnikov, and Andreas Terfort. "Reestablishing Odd-Even Effects in Anthracene-Derived Monolayers by Introduction of a Pseudo-C2v Symmetry". In: *The Journal of Physical Chemistry C* 123 (33 Aug. 2019), pp. 20362–20372. ISSN: 1932-7447. DOI: 10.1021/acs.jpcc.9b05299.

[188] Alexei Nefedov and Christof Wöll. *Advanced Applications of NEXAFS Spectroscopy for Functionalized Surfaces*. 2013. DOI: 10.1007/978-3-642-34243-1_10.

[189] Iris Hehn, Swen Schuster, Tobias Wächter, Tarek Abu-Husein, Andreas Terfort, Michael Zharnikov, and Egbert Zojer. "Employing X-ray Photoelectron Spectroscopy for Determining Layer Homogeneity in Mixed Polar Self-Assembled Monolayers". In: *The Journal of Physical Chemistry Letters* 7 (15 Aug. 2016), pp. 2994–3000. ISSN: 1948-7185. DOI: 10.1021/acs.jpclett.6b01096.

[190] Hannah Aitchison, Rodrigo Ortiz de la Morena, Raphael Peifer, Suhad Omar, Hao Lu, Stephen M. Francis, Michael Zharnikov, Andreas Grohmann, and Manfred Buck. "Self-Assembly of Di(pyrazol-1-yl)pyridine-benzoic Acid on Underpotentially Deposited Ag from Solution". In: *Langmuir* 34 (33 Aug. 2018), pp. 9654–9664. ISSN: 0743-7463. DOI: 10.1021/acs.langmuir.8b01734.

[191] Hai-Tao Rong, Stefan Frey, Yong-Jie Yang, Michael Zharnikov, Manfred Buck, Mario Wühn, Christof Wöll, and Günter Helmchen. "On the Importance of the Headgroup Substrate Bond in Thiol Monolayers: A Study of Biphenyl-Based Thiols on Gold and Silver". In: *Langmuir* 17 (5 Mar. 2001), pp. 1582–1593. ISSN: 0743-7463. DOI: 10.1021/la0014050.

[192] Eric Sauter, Giulia Nascimbeni, Daniel Trefz, Sabine Ludwigs, Egbert Zojer, Florian von Wrochem, and Michael Zharnikov. "A dithiocarbamate anchoring group as a flexible platform for interface engineering". In: *Physical Chemistry Chemical Physics* 21 (40 2019), pp. 22511–22525. ISSN: 1463-9076. DOI: 10.1039/C9CP03306H.

[193] Prashant Waske, Tobias Wächter, Andreas Terfort, and Michael Zharnikov. "Nitro-Substituted Aromatic Thiolate Self-Assembled Monolayers: Structural Properties and Electron Transfer upon Resonant Excitation of the Tail Group". In: *The Journal of Physical Chemistry C* 118 (45 Nov. 2014), pp. 26049–26060. ISSN: 1932-7447. DOI: 10.1021/jp507265k.

[194] Philipp Werner, Tobias Wächter, Andika Asyuda, Adrian Wiesner, Martin Kind, Michael Bolte, Lothar Weinhardt, Andreas Terfort, and Michael Zharnikov. "Electron Transfer Dynamics and Structural Effects in Benzonitrile Monolayers with Tuned Dipole Moments by Differently Positioned Fluorine Atoms". In: *ACS Applied Materials & Interfaces* 12 (35 Sept. 2020), pp. 39859–39869. ISSN: 1944-8244. DOI: 10.1021/acsami.0c10513.

[195] P. E. Batson. "Carbon 1 s near-edge-absorption fine structure in graphite". In: *Physical Review B* 48 (4 July 1993), pp. 2608–2610. ISSN: 0163-1829. DOI: 10.1103/PhysRevB.48.2608.

[196] E. Hoque, J. A. DeRose, P. Hoffmann, H. J. Mathieu, B. Bhushan, and M. Cichomski. "Phosphonate self-assembled monolayers on aluminum surfaces". In: *The Journal of Chemical Physics* 124 (17 May 2006), p. 174710. ISSN: 0021-9606. DOI: 10.1063/1.2186311.

[197] Igal Levine, Stephanie M. Weber, Yishay Feldman, Tatyana Bendikov, Hagai Cohen, David Cahen, and Ayelet Vilan. "Molecular length, monolayer density, and charge transport: Lessons from Al-AlOx/alkyl-phosphonate/Hg junctions". In: *Langmuir* 28 (1 2012), pp. 404–415. ISSN: 07437463. DOI: 10.1021/la2035664.

[198] D. Adam Hook, Shannon J. Timpe, Michael T. Dugger, and Jacqueline Krim. "Tribological degradation of fluorocarbon coated silicon microdevice surfaces in normal and sliding contact". In: *Journal of Applied Physics* 104 (3 Aug. 2008), p. 034303. ISSN: 0021-8979. DOI: 10.1063/1.2960567.

[199] Merlin Bruening, Rami Cohen, Jean François Guillemoles, Tamar Moav, Jacqueline Libman, Abraham Shanzer, and David Cahen. "Simultaneous control of surface potential and wetting of solids with chemisorbed multifunctional ligands". In: *Journal of the American Chemical Society* 119 (24 June 1997), pp. 5720–5728. ISSN: 00027863. DOI: 10.1021/JA964434Z.

[200] P. G. de Gennes. *Wetting: Statistics and Dynamics*. 1985.

[201] D. Y. Kwok and A. W. Neumann. "Contact angle measurement and contact angle interpretation". In: *Advances in Colloid and Interface Science* 81 (3 Sept. 1999), pp. 167–249. ISSN: 0001-8686. DOI: 10.1016/S0001-8686(98)00087-6.

[202] W. A. ZISMAN. "Relation of the Equilibrium Contact Angle to Liquid and Solid Constitution". In: (Jan. 1964), pp. 1–51. DOI: 10.1021/BA-1964-0043.CH001.

[203] S. Tosatti, R. Michel, M. Textor, and N. D. Spencer. "Self-Assembled Monolayers of Dodecyl and Hydroxy-dodecyl Phosphates on Both Smooth and Rough Titanium and Titanium Oxide Surfaces". In: *Langmuir* 18 (9 Apr. 2002), pp. 3537–3548. ISSN: 07437463. DOI: 10.1021/LA011459P.

[204] Doris M. Spori, Nagaiyanallur V. Venkataraman, Samuele G.P. Tosatti, Firat Durmaz, Nicholas D. Spencer, and Stefan Zürcher. "Influence of alkyl chain length on phosphate self-assembled monolayers". In: *Langmuir* 23 (15 July 2007), pp. 8053–8060. ISSN: 07437463. DOI: 10.1021/LA700474V.

[205] Stephen M. Rossnagel. "Magnetron sputtering". In: *Journal of Vacuum Science & Technology A* 38 (6 Dec. 2020), p. 060805. ISSN: 0734-2101. DOI: 10.1116/6.0000594.

[206] Angel Yanguas-Gil. *Growth and Transport in Nanostructured Materials*. 2017, p. 128. ISBN: 978-3-319-24670-3.

[207] Tina Wahl, Jonas Hanisch, and Erik Ahlswede. "Comparison of the Al back contact deposited by sputtering, e-beam, or thermal evaporation for inverted perovskite solar cells". In: *Journal of Physics D: Applied Physics* 51 (13 2018). ISSN: 13616463. DOI: 10.1088/1361-6463/aab0d8.

[208] Zhongping Wang and Zengming Zhang. *Electron Beam Evaporation Deposition*. Sept. 2016. DOI: 10.1002/9783527696406.ch2.

[209] Keiji Ono, Hiroshi Shimada, Shun-ichi Kobayashi, and Youiti Ootuka. "A New Fabrication Method for Ultra Small Tunnel Junctions". In: *Jpn. J. Appl. Phys* 35 (1996), pp. 2369–2371.

[210] Mandar M. Deshmukh, D. C. Ralph, M. Thomas, and J. Silcox. "Nanofabrication using a stencil mask". In: *Applied Physics Letters* 75 (11 1999), pp. 1631–1633. ISSN: 00036951. DOI: 10.1063/1.124777.

[211] Chris Mack. *Fundamental Principles of Optical Lithography*. John Wiley & Sons, Ltd, Nov. 2007. ISBN: 9780470723876. DOI: 10.1002/9780470723876.

[212] Peer Kirsch and Matthias Bremer. "Nematic liquid crystals for active matrix displays: Molecular design and synthesis". In: *Angewandte Chemie - International Edition* 39 (23 2000), pp. 4216–4235. ISSN: 14337851. DOI: 10.1002/1521-3773(20001201)39:23<4216::AID-ANIE4216>3.0.CO;2-K.

[213] Matthias Bremer, Peer Kirsch, Melanie Klasen-Memmer, and Kazuaki Tarumi. "The TV in your pocket: Development of liquid-crystal materials for the new millennium". In: *Angewandte Chemie - International Edition* 52 (34 2013), pp. 8880–8896. ISSN: 14337851. DOI: 10.1002/anie.201300903.

[214] Hiroaki Iino, Takayuki Usui, and Jun Ichi Hanna. "Liquid crystals for organic thin-film transistors". In: *Nature Communications 2015 6:1* 6 (1 Apr. 2015), pp. 1–8. ISSN: 2041-1723. DOI: 10.1038/ncomms7828.

[215] Hiroaki Iino and Jun Ichi Hanna. "Liquid crystalline organic semiconductors for organic transistor applications". In: *Polymer Journal 2017 49:1* 49 (1 Oct. 2016), pp. 23–30. ISSN: 1349-0540. DOI: 10.1038/pj.2016.101.

[216] Shahar Kvatinsky, Guy Satat, Nimrod Wald, Eby G. Friedman, Avinoam Kolodny, and Uri C. Weiser. "Memristor-based material implication (IMPLY) logic: Design principles and methodologies". In: *IEEE Transactions on Very Large Scale Integration (VLSI) Systems* 22 (10 2014), pp. 2054–2066. ISSN: 10638210. DOI: 10.1109/TVLSI.2013.2282132.

[217] Wenhua Zhang, Alexei Nefedov, Michael Naboka, Liang Cao, and Christof Wöll. "Molecular orientation of terephthalic acid assembly on epitaxial graphene: NEXAFS and XPS study". In: *Physical Chemistry Chemical Physics* 14 (29 2012), p. 10125. ISSN: 1463-9076. DOI: 10.1039/c2cp23748b.

[218] D. Fuhrmann, D. Wacker, K. Weiss, K. Hermann, M. Witko, and Ch. Wöll. "The adsorption of small hydrocarbons on Cu(111): A combined He-atom scattering and x-ray absorption study for ethane, ethylene, and acetylene". In: *The Journal of Chemical Physics* 108 (6 Feb. 1998), pp. 2651–2658. ISSN: 0021-9606. DOI: 10.1063/1.475652.

[219] M Giza, P Thissen, and G Grundmeier. "Adsorption Kinetics of Organophosphonic Acids on Plasma-Modified Oxide-Covered Aluminum Surfaces". In: 141 (12 2008), pp. 8688–8694.

[220] Lee Belding, Samuel E. Root, Yuan Li, Junwoo Park, Mostafa Baghbanzadeh, Edwin Rojas, Priscilla F. Pieters, Hyo Jae Yoon, and George M. Whitesides. "Conformation, and Charge Tunneling through Molecules in SAMs". In: *Journal of the American Chemical Society* (ii 2021). ISSN: 15205126. DOI: 10.1021/jacs.0c12571.

[221] J. Hölzl and F. K. Schulte. "Work function of metals". In: (1979), pp. 1–150. DOI: 10.1007/BFB0048919.

[222] Gregory N. Derry, Megan E. Kern, and Eli H. Worth. "Recommended values of clean metal surface work functions". In: *Journal of Vacuum Science & Technology A: Vacuum, Surfaces, and Films* 33 (6 Oct. 2015), p. 060801. ISSN: 0734-2101. DOI: 10.1116/1.4934685.

[223] Herbert B. Michaelson. "The work function of the elements and its periodicity". In: *Journal of Applied Physics* 48 (11 Nov. 1977), pp. 4729–4733. ISSN: 0021-8979. DOI: 10.1063/1.323539.

[224] T. V. Perevalov, V. A. Gritsenko, and V. V. Kaichev. "Electronic structure of aluminum oxide: ab initio simulations of α and γ phases and comparison with experiment for amorphous films". In: *The European Physical Journal Applied Physics* 52 (3 Dec. 2010), p. 30501. ISSN: 1286-0042. DOI: 10.1051/epjap/2010159.

[225] I. Costina and R. Franchy. "Band gap of amorphous and well-ordered Al2O3 on Ni3Al(100)". In: *Applied Physics Letters* 78 (26 June 2001), pp. 4139–4141. ISSN: 0003-6951. DOI: 10.1063/1.1380403.

[226] Rui Guo, Lingling Tao, Ming Li, Zhongran Liu, Weinan Lin, Guowei Zhou, Xiaoxin Chen, Liang Liu, Xiaobing Yan, He Tian, Evgeny Y. Tsymbal, and Jingsheng Chen. "Interface-engineered electron and hole tunneling". In: *Science Advances* 7 (13 2021), pp. 1–9. ISSN: 23752548. DOI: 10.1126/sciadv.abf1033.

[227] W. Martienssen and H. Warlimont. "Springer Handbook of Condensed Matter and Materials Data". In: *Springer Handbook of Condensed Matter and Materials Data* (2005). DOI: 10.1007/3-540-30437-1.

[228] Richard C. Hatch, David L. Huber, and Hartmut Höchst. "HOMO band structure and anisotropic effective hole mass in thin crystalline pentacene films". In: *Physical Review B - Condensed Matter and Materials Physics* 80 (8 Aug. 2009), p. 081411. ISSN: 10980121. DOI: 10.1103/PHYSREVB.80.081411/FIGURES/4/MEDIUM.

[229] Radu Berdan, Takao Marukame, Kensuke Ota, Marina Yamaguchi, Masumi Saitoh, Shosuke Fujii, Jun Deguchi, and Yoshifumi Nishi. "Low-power linear computation using nonlinear ferroelectric tunnel junction memristors". In: *Nature Electronics* 3 (May 2020). ISSN: 25201131. DOI: 10.1038/s41928-020-0405-0.

[230] Alexander Serb, Johannes Bill, Ali Khiat, Radu Berdan, Robert Legenstein, and Themis Prodromakis. "Unsupervised learning in probabilistic neural networks with multi-state metal-oxide memristive synapses". In: *Nature Communications 2016 7:1* 7 (1 Sept. 2016), pp. 1–9. ISSN: 2041-1723. DOI: 10.1038/ncomms12611.

[231] Julian M. Dlugosch, Deepthi Devendra, Domenikos Chryssikos, Sabrina Artmeier, Maximilian Speckbacher, Takuya Kamiyama, and Marc Tornow. "Metallic top contacts to self-assembled monolayers of aliphatic phosphonic acids on titanium nitride". In: *Proceedings of the IEEE Conference on Nanotechnology* 2020-July (2020), pp. 29–34. ISSN: 19449380. DOI: 10.1109/NANO47656.2020.9183521.

[232] J. Evertsson, F. Bertram, F. Zhang, L. Rullik, L. R. Merte, M. Shipilin, M. Soldemo, S. Ahmadi, N. Vinogradov, F. Carlà, J. Weissenrieder, M. Göthelid, J. Pan, A. Mikkelsen, J. O. Nilsson, and E. Lundgren. "The thickness

of native oxides on aluminum alloys and single crystals". In: *Applied Surface Science* 349 (2015), pp. 826–832. ISSN: 01694332. DOI: 10.1016/j.apsusc.2015.05.043.

[233] Michael Geiger, Marion Hagel, Thomas Reindl, Jürgen Weis, R. Thomas Weitz, Helena Solodenko, Guido Schmitz, Ute Zschieschang, Hagen Klauk, and Rachana Acharya. "Optimizing the plasma oxidation of aluminum gate electrodes for ultrathin gate oxides in organic transistors". In: *Scientific Reports* 11 (1 Dec. 2021), p. 6382. ISSN: 2045-2322. DOI: 10.1038/s41598-021-85517-7.

[234] N. Cabrera and N. F. Mott. "Theory of the oxidation of metals". In: *Reports on Progress in Physics* 12 (1 1949), pp. 163–184. ISSN: 00344885. DOI: 10.1088/0034-4885/12/1/308.

[235] Lester D. Grant. *LEAD AND COMPOUNDS*. Mar. 2020. DOI: 10.1002/9781119438922.ch17.

[236] Gagan Flora, Deepesh Gupta, and Archana Tiwari. "Toxicity of lead: a review with recent updates". In: *Interdisciplinary Toxicology* 5 (2 Nov. 2012), pp. 47–58. ISSN: 1337-9569. DOI: 10.2478/v10102-012-0009-2.

[237] Miriam Beatriz Virgolini and Michael Aschner. *Molecular mechanisms of lead neurotoxicity*. 2021. DOI: 10.1016/bs.ant.2020.11.002.

[238] A. Vilan and D. Cahen. "Soft Contact Deposition onto Molecularly Modified GaAs. Thin Metal Film Flotation: Principles and Electrical Effects". In: *Advanced Functional Materials* 12 (1112 Dec. 2002), pp. 795–807. ISSN: 1616301X. DOI: 10.1002/adfm.200290009.

[239] Hossam Haick, Marianna Ambrico, Teresa Ligonzo, and David Cahen. "Discontinuous molecular films can control metal/semiconductor junctions". In: *Advanced Materials* 16 (23-24 2004), pp. 2145–2151. ISSN: 09359648. DOI: 10.1002/adma.200400923.

[240] Sohyeon Seo, Misook Min, Junghyun Lee, Takhee Lee, Sung-Yool Choi, and Hyoyoung Lee. "Solution-Processed Reduced Graphene Oxide Films as Electronic Contacts for Molecular Monolayer Junctions". In: *Angewandte Chemie International Edition* 51 (1 Jan. 2012), pp. 108–112. ISSN: 14337851. DOI: 10.1002/anie.201105895.

[241] Frederick Chesneau, Andreas Terfort, and Michael Zharnikov. "Nickel deposition on fluorinated, aromatic self-assembled monolayers: Chemically induced cross-linking as a tool for the preparation of well-defined top metal films". In: *Journal of Physical Chemistry C* 118 (22 June 2014), pp. 11763–11773. ISSN: 19327455. DOI: 10.1021/jp5025334.

[242] Christina A. Hacker, Curt A. Richter, Nadine Gergel-Hackett, and Lee J. Richter. "Origin of differing reactivities of aliphatic chains on H-Si(111) and oxide surfaces with metal". In: *Journal of Physical Chemistry C* 111 (26 2007), pp. 9384–9392. ISSN: 19327447. DOI: 10.1021/jp072216u.

[243] Xi Yu, Robert Lovrinčić, Olga Kraynis, Gabriel Man, Tal Ely, Arava Zohar, Tal Toledano, David Cahen, and Ayelet Vilan. "Fabrication of Reproducible, Integration-Compatible Hybrid Molecular/Si Electronics". In: *Small* (Aug. 2014), n/a–n/a. ISSN: 16136810. DOI: 10.1002/smll.201400484.

[244] Marc Wittmer. "Properties and microelectronic applications of thin films of refractory metal nitrides". In: *Journal of Vacuum Science & Technology A: Vacuum, Surfaces, and Films* 3 (4 July 1985), pp. 1797–1803. ISSN: 0734-2101. DOI: 10.1116/1.573382.

[245] Gul Zeb and Xuan Tuan Le. "Grafting of Aminoethylphosphonic Acid Monolayers on Titanium Nitride : The Effect of Surface Pretreatments through Electrochemical-Assisted Oxidation". In: (2017). DOI: 10.1002/admi.201600827.

[246] Sidharam P. Pujari, Luc Scheres, Antonius T M Marcelis, and Han Zuilhof. "Covalent surface modification of oxide surfaces". In: *Angewandte Chemie - International Edition* 53 (25 2014), pp. 6322–6356. ISSN: 15213773. DOI: 10.1002/anie.201306709.

[247] Masato M. Maitani and David L. Allara. *Issues and Challenges in Vapor-Deposited Top Metal Contacts for Molecule-Based Electronic Devices*. 2011. DOI: 10.1007/128_2011_177.

[248] Maria A. Rampi, Olivier J.A. Schueller, and George M. Whitesides. "Alkanethiol self-assembled monolayers as the dielectric of capacitors with nanoscale thickness". In: *Applied Physics Letters* 72 (14 June 1998), p. 1781. ISSN: 0003-6951. DOI: 10.1063/1.121183.

[249] C. S.Suchand Sangeeth, Albert Wan, and Christian A. Nijhuis. "Equivalent circuits of a self-assembled monolayer-based tunnel junction determined by impedance spectroscopy". In: *Journal of the American Chemical Society* 136 (31 Aug. 2014), pp. 11134–11144. ISSN: 15205126. DOI: 10.1021/JA505420C.

[250] Vincent B. Engelkes, Jeremy M. Beebe, and C. Daniel Frisbie. "Length-Dependent Transport in Molecular Junctions Based on SAMs of Alkanethiols and Alkanedithiols: Effect of Metal Work Function and Applied Bias on Tunneling Efficiency and Contact Resistance". In: *Journal of the American Chemical Society* 126 (43 Nov. 2004), pp. 14287–14296. ISSN: 00027863. DOI: 10.1021/JA046274U.

[251] D.K. Aswal, S. Lenfant, D. Guerin, J.V. Yakhmi, and D. Vuillaume. "Self assembled monolayers on silicon for molecular electronics". In: *Analytica Chimica Acta* 568 (1-2 May 2006), pp. 84–108. ISSN: 00032670. DOI: 10.1016/j.aca.2005.10.027.

[252] Asim Bhaumik and Shinji Inagaki. “Mesoporous Titanium Phosphate Molecular Sieves with Ion-Exchange Capacity”. In: *Journal of the American Chemical Society* 123 (4 Jan. 2001), pp. 691–696. ISSN: 0002-7863. DOI: 10.1021/ja002481s.

[253] Anshuma Pathak. *Structural and electronic properties of organophosphonate monolayers on alumina and silicon oxide*. Vol. 1. Verlag Dr. Hut, München, 2015.

[254] Marc D. Porter, Thomas B. Bright, David L. Allara, and Christopher E. Chidsey. “Spontaneously Organized Molecular Assemblies. 4. Structural Characterization of n-Alkyl Thiol Monolayers on Gold by Optical Ellipsometry, Infrared Spectroscopy, and Electrochemistry”. In: *Journal of the American Chemical Society* 109 (12 1987), pp. 3559–3568. ISSN: 15205126. DOI: 10.1021/ja00246a011.

[255] A. Szwajca, J. Wei, M. I. Schukfeh, and M. Tornow. “Self-assembled monolayers of alkyl-thiols on InAs: A Kelvin probe force microscopy study”. In: *Surface Science* 633 (Mar. 2015), pp. 53–59. ISSN: 00396028. DOI: 10.1016/j.susc.2014.11.023.

[256] Michael P. Danahy, Michael J. Avaltroni, Kim S. Midwood, Jean E. Schwarzbauer, and Jeffrey Schwartz. “Self-assembled Monolayers of α,ω-Diphosphonic Acids on Ti Enable Complete or Spatially Controlled Surface Derivatization”. In: *Langmuir* 20 (13 June 2004), pp. 5333–5337. ISSN: 0743-7463. DOI: 10.1021/la036084h.

[257] Ayelet Vilan, Orner Yaffe, Ariel Biller, Adi Salomon, Antoine Kahn, and David Cahen. “Molecules on Si: Electronics with chemistry”. In: *Advanced Materials* 22 (2 2010), pp. 140–159. ISSN: 09359648. DOI: 10.1002/adma.200901834.

[258] Gunuk Wang, Yonghun Kim, Minhyeok Choe, Tae-Wook Kim, and Takhee Lee. “A New Approach for Molecular Electronic Junctions with a Multilayer Graphene Electrode”. In: *Advanced Materials* 23 (6 2011), pp. 755–760. ISSN: 09359648. DOI: 10.1002/adma.201003178.

[259] Hylke B. Akkerman and Bert De Boer. “Electrical conduction through single molecules and self-assembled monolayers”. In: *Journal of Physics Condensed Matter* 20 (1 2008). ISSN: 09538984. DOI: 10.1088/0953-8984/20/01/013001.

[260] Adi Salomon, Dvora Berkovich, and David Cahen. “Molecular modification of an ionic semiconductor-metal interface: ZnO/molecule/Au diodes”. In: *Applied Physics Letters* 82 (7 Feb. 2003), p. 1051. ISSN: 0003-6951. DOI: 10.1063/1.1543638.

[261] Omer Yaffe, Luc Scheres, Lior Segev, Ariel Biller, Izhar Ron, Eric Salomon, Marcel Giesbers, Antoine Kahn, Leeor Kronik, Han Zuilhof, Ayelet Vilan, and David Cahen. “Hg/Molecular Monolayer-Si Junctions: Electrical Interplay between Monolayer Properties and Semiconductor Doping Density”. In: *The Journal of Physical Chemistry C* 114 (22 June 2010), pp. 10270–10279. ISSN: 1932-7447. DOI: 10.1021/jp101656t.

[262] Michael J. Hostetler, Jennifer J. Stokes, and Royce W. Murray. “Infrared spectroscopy of three-dimensional self-assembled monolayers: N-alkanethiolate monolayers on gold cluster compounds”. In: *Langmuir* 12 (15 1996), pp. 3604–3612. ISSN: 07437463. DOI: 10.1021/la960249n.

[263] Ragnar Holm. *Electric Contacts*. Springer Berlin Heidelberg, 1967. ISBN: 978-3-642-05708-3. DOI: 10.1007/978-3-662-06688-1.

[264] J.A. Greenwood and J.B.P. Williamson. “Contact of nominally flat surfaces”. In: *Proceedings of the Royal Society of London. Series A. Mathematical and Physical Sciences* 295 (1442 Dec. 1966), pp. 300–319. ISSN: 0080-4630. DOI: 10.1098/rspa.1966.0242.

[265] Krzysztof Slowinski, Harold K.Y. Fong, and Marcin Majda. “Mercury-mercury tunneling junctions. Electron tunneling across symmetric and asymmetric alkanethiolate bilayers”. In: *Journal of the American Chemical Society* 121 (31 Aug. 1999), pp. 7257–7261. ISSN: 00027863. DOI: 10.1021/JA991613I.

[266] Hyunwook Song, Hyoyoung Lee, and Takhee Lee. “Intermolecular chain-to-chain tunneling in metal-alkanethiol-metal junctions”. In: *Journal of the American Chemical Society* 129 (13 Apr. 2007), pp. 3806–3807. ISSN: 00027863. DOI: 10.1021/JA068875M.

[267] Krzysztof Slowinski, Richard V. Chamberlain, Renata Bilewicz, and Marcin Majda. “Evidence for inefficient chain-to-chain coupling in electron tunneling through liquid alkanethiol monolaver films on mercury”. In: *Journal of the American Chemical Society* 118 (19 1996), pp. 4709–4710. ISSN: 00027863. DOI: 10.1021/JA9601191.

[268] M. J. D. Powell. *A Direct Search Optimization Method That Models the Objective and Constraint Functions by Linear Interpolation*. 1994. DOI: 10.1007/978-94-015-8330-5_4.

[269] Michael Celestin, Subramanian Krishnan, Shekhar Bhansali, Elias Stefanakos, and D Yogi Goswami. “A review of self-assembled monolayers as potential terahertz frequency tunnel diodes”. In: 7 (5 2014), pp. 589–625.

[270] Bert de Boer, Martin M. Frank, Yves J. Chabal, Weirong Jiang, Eric Garfunkel, and Zhenan Bao. “Metallic Contact Formation for Molecular Electronics: Interactions between Vapor-Deposited Metals and Self-Assembled Monolayers of Conjugated Mono- and Dithiols”. In: *Langmuir* 20 (5 Mar. 2004), pp. 1539–1542. ISSN: 0743-7463. DOI: 10.1021/la0356349.

[271] M. Zharnikov. “Ultrathin metal films on top of SAMs”. In: *Encyclopedia of Interfacial Chemistry: Surface Science and Electrochemistry* 3 (2018), pp. 375–380. DOI: 10.1016/B978-0-12-409547-2.14169-1.

[272] Y. Tai, A. Shaporenko, W. Eck, M. Grunze, and M. Zharnikov. "Abrupt change in the structure of self-assembled monolayers upon metal evaporation". In: *Applied Physics Letters* 85 (25 Dec. 2004), pp. 6257–6259. ISSN: 0003-6951. DOI: 10.1063/1.1842361.

[273] Li Jiang, C. S.Suchand Sangeeth, Albert Wan, Ayelet Vilan, and Christian A. Nijhuis. "Defect scaling with contact area in EGaIn-based junctions: Impact on quality, Joule heating, and apparent injection current". In: *Journal of Physical Chemistry C* 119 (2 Jan. 2015), pp. 960–969. ISSN: 19327455. DOI: 10.1021/JP511002B.

[274] C. S. Suchand Sangeeth, Li Jiang, and Christian A. Nijhuis. "Bottom-electrode induced defects in self-assembled monolayer (SAM)-based tunnel junctions affect only the SAM resistance, not the contact resistance or SAM capacitance". In: *RSC Advances* 8 (36 2018), pp. 19939–19949. ISSN: 2046-2069. DOI: 10.1039/C8RA01513A.

[275] Domenikos Chryssikos, Julian M. Dlugosch, Jerry A. Fereiro, Takuya Kamiyama, Mordechai Sheves, David Cahen, and Marc Tornow. "Electronic Transport Through Organophosphonate-Grafted Bacteriorhodopsin Films on Titanium Nitride". In: IEEE, July 2021, pp. 389–392. ISBN: 978-1-6654-4156-8. DOI: 10.1109/NANO51122.2021.9514351.

[276] L.P.B. Lima, J.A. Diniz, I. Doi, and J. Godoy Fo. "Titanium nitride as electrode for MOS technology and Schottky diode: Alternative extraction method of titanium nitride work function". In: *Microelectronic Engineering* 92 (Apr. 2012), pp. 86–90. ISSN: 01679317. DOI: 10.1016/j.mee.2011.04.059.

[277] F. Fillot, T. Morel, S. Minoret, I. Matko, S. Maîtrejean, B. Guillaumot, B. Chenevier, and T. Billon. "Investigations of titanium nitride as metal gate material, elaborated by metal organic atomic layer deposition using TDMAT and NH3". In: *Microelectronic Engineering* 82 (3-4 Dec. 2005), pp. 248–253. ISSN: 01679317. DOI: 10.1016/j.mee.2005.07.083.

[278] David R. Lide, ed. *CRC Handbook of Chemistry and Physics*. 88th. Vol. 130. Jan. 2008, pp. 12–140. DOI: 10.1021/ja077011d.

[279] Yongxun Liu, Shinya Kijima, Etsuro Sugimata, Meishoku Masahara, Kazuhiko Endo, Takashi Matsukawa, Kenichi Ishii, Kunihiro Sakamoto, Toshihiro Sekigawa, Hiromi Yamauchi, Yoshifumi Takanashi, and Eiichi Suzuki. "Investigation of the TiN Gate Electrode With Tunable Work Function and Its Application for FinFET Fabrication". In: *IEEE Transactions On Nanotechnology* 5 (6 Nov. 2006), pp. 723–730. ISSN: 1536-125X. DOI: 10.1109/TNANO.2006.885035.

[280] C. Ren, B.B. Faizhal, D.S.H. Chan, M.-F. Li, Y.-C. Yeo, A.D. Trigg, N. Balasubramanian, and D.-L. Kwong. "Work function tuning of metal nitride electrodes for advanced CMOS devices". In: *Thin Solid Films* 504 (1-2 May 2006), pp. 174–177. ISSN: 00406090. DOI: 10.1016/j.tsf.2005.09.081.

[281] J. Westlinder, T. Schram, L. Pantisano, E. Cartier, A. Kerber, G.S. Lujan, J. Olsson, and G. Groeseneken. "On the thermal stability of atomic layer deposited TiN as gate electrode in MOS devices". In: *IEEE Electron Device Letters* 24 (9 Sept. 2003), pp. 550–552. ISSN: 0741-3106. DOI: 10.1109/LED.2003.816579.

[282] Arrigo Calzolari and Alessandra Catellani. "Controlling the TiN Electrode Work Function at the Atomistic Level: A First Principles Investigation". In: *IEEE Access* 8 (2020), pp. 156308–156313. ISSN: 2169-3536. DOI: 10.1109/ACCESS.2020.3017726.

[283] John Robertson. "Band offsets of wide-band-gap oxides and implications for future electronic devices". In: *Journal of Vacuum Science & Technology B: Microelectronics and Nanometer Structures* 18 (3 2000), p. 1785. ISSN: 0734211X. DOI: 10.1116/1.591472.

[284] J. Robertson. "High dielectric constant oxides". In: *The European Physical Journal Applied Physics* 28 (3 Dec. 2004), pp. 265–291. ISSN: 1286-0042. DOI: 10.1051/epjap:2004206.

[285] Yong Xu and Martin A.A. Schoonen. "The absolute energy positions of conduction and valence bands of selected semiconducting minerals". In: *American Mineralogist* 85 (3-4 Mar. 2000), pp. 543–556. ISSN: 0003-004X. DOI: 10.2138/am-2000-0416.

[286] Hanno Dietrich and Dirk Zahn. "Molecular Mechanisms of Solvent-Controlled Assembly of Phosphonate Monolayers on Oxide Surfaces". In: *Journal of Physical Chemistry C* 121 (33 2017), pp. 18012–18020. ISSN: 19327455. DOI: 10.1021/acs.jpcc.7b05750.

[287] Xin Chen, Erwann Luais, Nadim Darwish, Simone Ciampi, Pall Thordarson, and J. Justin Gooding. "Studies on the effect of solvents on self-assembled monolayers formed from organophosphonic acids on indium tin oxide". In: *Langmuir* 28 (25 2012), pp. 9487–9495. ISSN: 07437463. DOI: 10.1021/la3010129.

[288] Gyu Don Kong, Miso Kim, Soo Jin Cho, and Hyo Jae Yoon. "Gradients of Rectification: Tuning Molecular Electronic Devices by the Controlled Use of Different-Sized Diluents in Heterogeneous Self-Assembled Monolayers". In: *Angewandte Chemie International Edition* 55 (35 Aug. 2016), pp. 10307–10311. ISSN: 14337851. DOI: 10.1002/anie.201604748.

[289] Gyu Don Kong, Junji Jin, Martin Thuo, Hyunsun Song, Joonyoung F. Joung, Sungnam Park, and Hyo Jae Yoon. "Elucidating the Role of Molecule–Electrode Interfacial Defects in Charge Tunneling Characteristics of Large-Area Junctions". In: *Journal of the American Chemical Society* 140 (38 Sept. 2018), pp. 12303–12307. ISSN: 0002-7863. DOI: 10.1021/jacs.8b08146.

[290] Junji Jin, Gyu Don Kong, and Hyo Jae Yoon. “Deconvolution of Tunneling Current in Large-Area Junctions Formed with Mixed Self-Assembled Monolayers”. In: *The Journal of Physical Chemistry Letters* 9 (16 Aug. 2018), pp. 4578–4583. ISSN: 1948-7185. DOI: 10.1021/acs.jpclett.8b01997.

[291] Gyu Don Kong, Seo Eun Byeon, Sohyun Park, Hyunsun Song, Seo-Yeon Kim, and Hyo Jae Yoon. “Mixed Molecular Electronics: Tunneling Behaviors and Applications of Mixed Self-Assembled Monolayers”. In: *Advanced Electronic Materials* 6 (2 Feb. 2020), p. 1901157. ISSN: 2199-160X. DOI: 10.1002/aelm.201901157.

[292] Priyajit Jash, Ranjeev Kumar Parashar, Claudio Fontanesi, and Prakash Chandra Mondal. “The Importance of Electrical Impedance Spectroscopy and Equivalent Circuit Analysis on Nanoscale Molecular Electronic Devices”. In: *Advanced Functional Materials* 32 (10 Mar. 2022), p. 2109956. ISSN: 1616-301X. DOI: 10.1002/adfm.202109956.

[293] Jaismon Francis, S A Bassam, and C S Suchand Sangeeth. “Importance of impedance spectroscopy in self-assembled monolayer-based large-area tunnel junctions”. In: *Journal of Physics D: Applied Physics* 55 (7 Feb. 2022), p. 075301. ISSN: 0022-3727. DOI: 10.1088/1361-6463/ac30fc.

[294] Xiaoping Chen and Christian A. Nijhuis. “The Unusual Dielectric Response of Large Area Molecular Tunnel Junctions Probed with Impedance Spectroscopy”. In: *Advanced Electronic Materials* 8 (2 Feb. 2022), p. 2100495. ISSN: 2199-160X. DOI: 10.1002/aelm.202100495.

[295] Youngsang Kim, Hyunwook Song, Dongwoo Kim, Takhee Lee, and Heejun Jeong. “Noise Characteristics of Charge Tunneling via Localized States in Metal-Molecule-Metal Junctions”. In: *ACS Nano* 4 (8 Aug. 2010), pp. 4426–4430. ISSN: 1936-0851. DOI: 10.1021/nn100255b.

[296] Nicolas Clément, David Guérin, Stéphane Pleutin, Sylvie Godey, and Dominique Vuillaume. “Role of Hydration on the Electronic Transport through Molecular Junctions on Silicon”. In: *The Journal of Physical Chemistry C* 116 (33 Aug. 2012), pp. 17753–17763. ISSN: 1932-7447. DOI: 10.1021/jp3018106.

[297] Mingyu Jung, Shashank Shekhar, Duckhyung Cho, Myungjae Yang, Jeehye Park, and Seunghun Hong. “Dipolar Noise in Fluorinated Molecular Wires”. In: *Nanomaterials* 12 (8 Apr. 2022), p. 1371. ISSN: 2079-4991. DOI: 10.3390/nano12081371.

[298] Youngsang Kim and Hyunwook Song. “Noise spectroscopy of molecular electronic junctions”. In: *Applied Physics Reviews* 8 (1 Mar. 2021), p. 011303. ISSN: 1931-9401. DOI: 10.1063/5.0027602.

[299] Mario Lanza, H. S.Philip Wong, Eric Pop, Daniele Ielmini, Dimitri Strukov, Brian C. Regan, Luca Larcher, Marco A. Villena, J. Joshua Yang, Ludovic Goux, Attilio Belmonte, Yuchao Yang, Francesco M. Puglisi, Jinfeng Kang, Blanka Magyari-Köpe, Eilam Yalon, Anthony Kenyon, Mark Buckwell, Adnan Mehonic, Alexander Shluger, Haitong Li, Tuo Hung Hou, Boris Hudec, Deji Akinwande, Ruijing Ge, Stefano Ambrogio, Juan B. Roldan, Enrique Miranda, Jordi Suñe, Kin Leong Pey, Xing Wu, Nagarajan Raghavan, Ernest Wu, Wei D. Lu, Gabriele Navarro, Weidong Zhang, Huaqiang Wu, Runwei Li, Alexander Holleitner, Ursula Wurstbauer, Max C. Lemme, Ming Liu, Shibing Long, Qi Liu, Hangbing Lv, Andrea Padovani, Paolo Pavan, Ilia Valov, Xu Jing, Tingting Han, Kaichen Zhu, Shaochuan Chen, Fei Hui, and Yuanyuan Shi. “Recommended Methods to Study Resistive Switching Devices”. In: *Advanced Electronic Materials* 5 (1 2019), pp. 1–28. ISSN: 2199160X. DOI: 10.1002/aelm.201800143.

Acknowledgements

At this point, I would like to thank all those who have accompanied me during my time as a scientific assistant at the Technical University of Munich - without whom this work would not have been possible in this way.

First and foremost I am grateful for the opportunity to perform the research at the **Professorship for Molecular Electronics** at the Technical University of Munich. I would like to thank Prof. Dr. Marc Tornow for the guidance where needed as well as the freedom and trust to explore own ideas and the patience to wait for results until I was comfortable to provide a complete picture. Additionally, I am grateful for the opportunity to be heavily involved in the acquisition and set up of several characterization tools as well as the general handling of the challenges of the COVID-19 pandemic.

I am deeply grateful for the very close collaboration, fruitful scientific discussions and inspiring conversations with the scientists at **Merck KGaA**: Prof. Dr. Peer Kirsch, Dr. Itai Lieberman, Dr. Sebastian Resch, Dr. Henning Seim, Dr. Frank Voges and Dr. Falk May. At Merck KGaA I would also like to thank Simon Schwarzkopf for developing the measurement software for the Keithley 2635 and continuously integrating helpful features. I would like to thank Dr. Henning Seim - for the very close collaboration when setting up measurement and analysis protocols as well as during the set up of the probe station in Darmstadt. I am also grateful for funding by Merck KGaA.
I would like to thank my mentor Prof. Dr. Peer Kirsch for abundant inspiration, continued support in pursuing my own ideas and providing me with the opportunity to get a glimpse into the inner workings of a chemical company in form of a shadowing day, as well as for continuosly investing valuable time to give career advice.

Furthermore, extend my gratitude to **my collegues at TUM** - in particular those who welcomed me with open arms into the group and with whom I enjoyed joyful discussions, coffee breaks and visits to the local beer gardens, in particular Dr. Maximilian Speckbacher, Dr. Simon Pfaehler, Dr. Quoc Hung Nguyen, Dr. Kai Saller and Dr. Takuya Kamiyama. Many thanks go also to the rest of the molecular electronics group, namely Domenikos Chryssikos, Sabrina Artmeier, Jonathan Rojas Rojas and Daniel Reiser.
I would like to especially thank the students that decided to work on their theses under my supervision, Maria Kallergi and Deepthi Devendra; as well as Til Friebe for his pionieering work on EGaIn measurements of APAs on TiN.
I would also like extend my gratitude towards **my collegues at WSI and ZNN**, especially to Felix Eckmann, Andreas Zeidler, Dr. Alexander Henning and Dr. Mattheo Bessone for the friendly working atmosphere, fruitful discussions during coffee breaks and providing helping hands whenever necessary.
Additionally, I am very thankful for the support of **our technical support staff** that kept the things running at the labs. First and foremost I am grateful for the support by Peter Weiser who almost single-handedly kept things running at ZNN until his retirement. I am also grateful for the assistance at the 'Obere Technologie' lab at WSI by Claudia Paulus. I would also like to thank Anika Kwiatkowsky for wafer dicing and continued

support with her expertise when it comes to the usage, transport and storage of chemicals. I also thank Rosi Mittermeier. I am very grateful for IT support by Hans Ranke and Tobias Baur.
I am also grateful for the support in operating and maintaining the Balzers PVD system. In particular I would like to thank Prof. Dr. Markus Becherer and Rainer Emling for keeping a >60 year old PVD system alive.

I would also like to thank friends at **TEDxTUM**, in particular Sami Affifi, Dr. Maria Littmann, Dr. Richard Littmann, Dr. Susanne Sölch, Michael Schwarz, Monika Wirthl, Emiliano Ordonez, Thuna Dinh, Agnese Barreza, Sanika Joshi.

Furthermore, I would like to extend my gratitude to the "morning crew" at **Athletikstube** - Claudi, Karin, Max and Nico - for a motivating distraction during challenging times as well as the always welcoming, supportive atmosphere.

I would also like to thank my friends, in particular Dr. David Prakash and Dr. Max von Blankenburg for honest exchanges about the challenges of pursuing a PhD in different domains and inspiring conversations over the last years.

I would also extend my gratitude to my former academic supervisors Prof. Uli Lemmer, Dr. Stefan Höfle, Dr. Joshua Fragoso Garcia, Dr. Alexander Colsmann, Dr. Daniel Riedel and Dr. Thomas Wehlus for motivating encouragement to pursue a PhD and for providing me with some exceptional opportunities to hone my scientific skills and to follow my curiosity in a variety of scientific fields.

Finally, I would like to express a big and heart-felt thank you' to my parents Susanne and Roland as well as to my brother Johannes, for supporting me in good and difficult times during my studies and during my PhD. Without your constant support, all this would not have been possible.

Last but definitely not least I would like to thank my partner Dr. Dora Dzvonyar: Thank you for your understanding, your patience, your never-ending encouragement and for constantly inspiring me to become a better person.